Department
Of
Mechanical
Engineering.

Measurement of Surface Deflection in Rolling Bearing by Ultrasonic Reflection

Emir Avcioglu

February 2018

A thesis submitted in partial fulfilment of the requirements for the degree of Doctor of Philosophy

ABSTRACT

One of the main reasons contributing to the growth of the wind industry is the effort placed on improving designs and on reducing the operating and maintenance costs to make wind energy more cost competitive. Operations and maintenance is in fact estimated to contribute to 20-25% of the levelised cost of energy for wind energy. Studies have shown that while the gearbox is responsible for a substantial portion of the downtime incurred during the lifetime of a wind turbine, the initial point of failure is generally attributed to the bearings within. Given this scenario, the main aim of this project is to study the applicability of ultrasound techniques as a non-destructive monitoring technique that enables detection of problems in the bearings prior to failure. The downtime can therefore be reduced by avoiding catastrophic failure and by enabling more efficient scheduled maintenance.

In this study a focused immersion transducer has been used to emit and collect ultrasonic waves aimed at, and reflected off, the outer race of a bearing. Any changes in the reflected waves convey information on the outer race displacements, which in turn provide information on the health of the bearing.

A new approach was developed for the construction of cylindrical roller bearing outer race surface displacement curves by employing a focused immersion transducer. The proposed technique is based on measurement of the first reflected wave specifically defined by the zero-crossing point while the bearing is in operation. It is clearly observed that as the rolling element goes through the investigated area the distance between transducer and bearing outer race is shortened resulting in a time shift of the first reflection. Time shift measurements were subsequently converted into bearing outer race deflection by using time-of-flight technique. Moreover, it has been shown that real time monitoring of the time shift is possible at a low resolution.

The study shows how the bearing outer race deflection curves provide information about the ongoing contact events within the bearing. This information can be used to identify an unhealthy component, since when any of the components contains a defect, an anomaly in the bearing outer race deflection curves is observed. Such discontinuities have been characterized by two parameters: peak height and duration and the relationship

between these parameters and load, defect location, defect severity and defect size has been explored.

It was found that the proposed method is able to distinguish which of the components is defective, detect line defects larger than 0.36 mm, assess the severity of the defects and pin-point the location of the defect with respect to the sensor as long as it falls within the identified measurable range.

ACKNOWLEDGEMENTS

I would like to offer my most sincere gratitude to Professor Robert Dwyer-Joyce for offering me the opportunity to work on this project and for the guidance and support given throughout the duration of the studies. I would also like to thank my second supervisor Dr Hui Long for her assistance on the project.

I am very grateful to Professor Mahmut Ozbay and Professor Metin U. Salamci for their encouragement to pursue a PhD in the United Kingdom and to the Turkish Ministry of Education for making it possible by providing financial assistance. I would also like to thank Professor Nizami Akturk and Associate Professor Tuncay Karacay for recommending the field of study and for offering very helpful tribological discussions.

The help and assistance offered by Dr Robin Mills, Dr Tom Howard, Dr Henry Brunskill and Dr Juan Zhu is very much appreciated. Special thanks goes to Dr Andrew Hunter for developing the LabVIEW interface used in the study and for his constant support and suggestions throughout the study. I would also like to show my gratitude towards Mr. Dave Butcher for helping me in the test rig modifications and to Mr. Geoffrey Hildebrand for preparing the defects on the bearing components.

I would like to thank my mother for inciting me to pursue a PhD and Mr. and Mrs. Hopkins for their support and encouragement. I am also grateful to my friends.

Finally, special thanks goes to my partner Lynne Hopkins for her love and endless support, patience and encouragement in this important stage of my life.

TABLE OF CONTENTS

List of Figures

List of Tables

Nomenclature

Roman Symbols

A	Decayed sound wave amplitude, Decibels
a	Reliability factor
A_0	Initial wave amplitude, Decibels
a_{iso}	Life modification factor
$A_m(f)$	Spectral amplitude of ultrasonic reflection
$A_{ref}(f)$	Reference spectral amplitude
B	Bulk modulus, N/m^2
b	Line contact semi-width, m
BD	Roller diameter, m
C	Dynamic load capacity, N
c	Speed of sound, m/s
C_u	Fatigue load limit
D	Element diameter, m
$d_{deflection}(t)$	The deflection at a time t, m
d_m	Bearing pitch diameter, m
dp	Pressure change
du	Compression displacement
$d\vartheta$	Volume change of the fluid
d_{wp}	Water path distance, m
E	Modulus of elasticity of the material, N/m^2
e_C	Contamination factor
E^*	Reduced elastic modulus, N/m^2
F	Focal length, m
f	Frequency, Hertz
f_{ir}	Inner race defect frequency, Hz
f_m	Resonant frequency, Hz
f_{or}	Outer race defect frequency, Hz
F_r	Applied radial load, N
f_{re}	Rolling element defect frequency, Hz
f_s	Shaft rotation frequency, Hz
G	Shear modulus of the material, N/m^2
h	Oil film thickness, m
K	Interfacial stiffness, N/m
k	Stiffness coefficient
K_b	Bearing stiffness matrix
K_t	Load-deflection factor
L	Rolling element length, m
L_{10}	Bearing rating life
L_{na}	Adjusted rating life

L_{nm}	Modified rating life
M	The number of selected data
m	Mode number
N	Near field length, m
n	Revolution per minute, rpm
n_r	Rolling element rotation speed, rpm
P	Standardised dynamic equivalent load, N
p	Life equation exponent
PD	Pitch diameter, m
p_{max}	Maximum pressure at contact, N/m^2
R	Reflection
R	Radius of the contacting surfaces, m
R^*	Reduced radius, m
R(f)	Experimentally obtained reflection coefficient
R_{ref}	Reference interface reflection coefficient
R_x	Effective radius in x direction, m
T	Transmission
t_{td}	Time difference between incident pulse and first reflection, s
$t_{timeshift}$	The time shift at a time t, s
V	Linear velocity, m/s
ϑ	Volume of the fluid, m^3
W_{max}	Applied maximum load, N
WP	Water path, m
$x[\,]$	Input data for moving average filter
$y[\,]$	Output data from moving average filter
Z	Acoustic impedance, Ns/m^3
Z	Number of rolling elements

Greek Symbols

α	Attenuation coefficient, cm^{-1}
β	Contact angle
δ_{max}	Maximum radial deflection, m
κ	Viscosity ratio
λ	Wavelength of ultrasound, m
v	Poisson's ratio
ω	Angular frequency, rad/s
θ_1	Incident wave angle
θ_2	Refracted wave angle
ξ	Simplified integral,
ρ	Density, kg/m^3

Subscripts

c	Subscript c refers to centre
i	Subscript i refers to inner race
$longitudinal$	Subscript longitudinal refers to sound waves type
o	Subscript o refers to outer race
pzt	Subscript pzt refers to piezoelectric element
$shear$	Subscript shear refers to sound waves type
tm	Subscript tm refers to material thickness
w	Subscript w refers to water
1	Subscript 1 refers to medium 1
2	Subscript 2 refers to medium 2

Abbreviations

ABMA	American Bearing Manufacturers
AE	Acoustic Emission
CBM	Condition Based Monitoring
CNC	Computer Numerical Control
CRB	Cylindrical Roller Bearing
EDM	Wire-Cut Electrical Discharge
EX	Expansion Type Bearing
FFPI	Fiber Fabry Perot Interferometer
FFT	Fast Fourier Transform
FIR	Finite Impulse Response
FMS	Film Measurement System
GR	Fixed Type Bearing
GWEC	Global Wind Energy Council
HFRT	High Frequency Resonance Technique
HIT	Acoustic Burst Emission
IRENA	The International Renewable Energy Agency
ISO	International Organisation for Standardisation
KPMG	Klynveld Peat Marwick Goerdeler
LCOE	Levelised Cost of Energy
NDT	Non-Destructive Testing
O&M	Operations and Maintenance
PCI	Peripheral Component Interconnecting
PODS	Portable Oil Diagnostic Systems
PRR	Pulser Repetition Rate
PW	Pulse Width
PZT	Lead Zirconate Titanate
RE	Rolling Element
RMS	Root Mean Square
SCADA	Supervisory Control and Data Acquisition

SKF	Svenska Kullagerfabriken AB
STFT	Short Time Fourier Transform
STO	Safe Torque-Off
TDMS	Technical Data Management Streaming
ToF	Time of Flight
TRB	Tapered Roller Bearing
UPR	Ultrasound Pulser-Receiver

1 INTRODUCTION

1.1 Background

The wind power industry has been experiencing growth since its naissance. According to the statistical reports prepared by the Global Wind Energy Council (GWEC) in the past five years, capacity generation has increased by a factor of two, reaching 486 GW by the end of 2016 as shown in the Figure 1.2 (GWEC, 2016). This translates to about 5% of the global electricity production in 2016 (*Global Energy Statistical Year Book*, 2017). China holds the largest share, 34.7% of installed wind capacity followed by the United States (16.9%), Germany (10.3%), India (5.9%), Spain (4.7%) and the United Kingdom (3%) (as of December, 2016). Establishing itself as one of the most cost competitive sources of energy, in addition to being a clean and reliable source, predictions are that the industry will continue to grow in the coming years (GWEC, 2016).

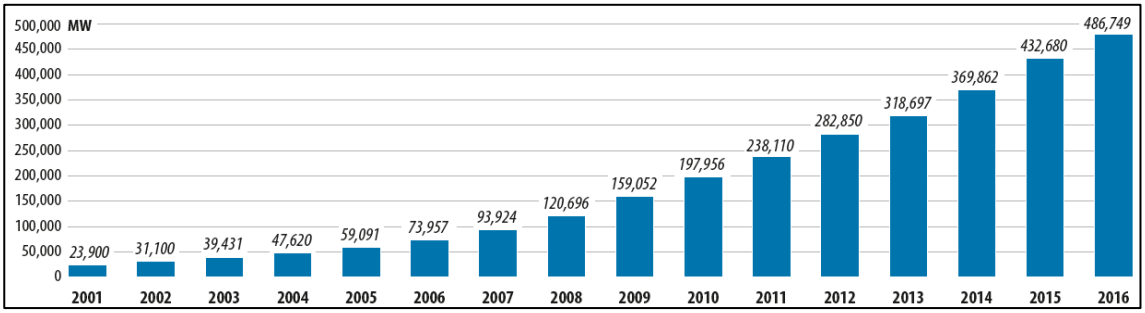

Figure 1.1 Installed wind energy capacity between 2001-2016 (GWEC, 2016)

The industry growth has most certainly been fuelled by governmental aid and incentives, which are issued to help the countries attain their renewable energy targets. An example is the Europe 2020 package whereby the energy produced from renewables in EU countries must reach 20% by 2020 (European Parliament, 2009). As an aid to investors, companies and other entities, KPMG issued a report in 2015 compiling all the incentives and policies all over the world (KPMG, 2015).

However, since the 1980s, the industry has matured, enabling lower investment costs and higher capacity factors that have substantially reduced the price of wind energy to unprecedented levels. In fact, the levelised cost of energy (LCOE) for onshore wind power in certain markets has decreased so much it is nowadays one of the most competitive sources of energy, even when compared to fossil fuels as illustrated in the Figure 1.2 (IRENA, 2015).

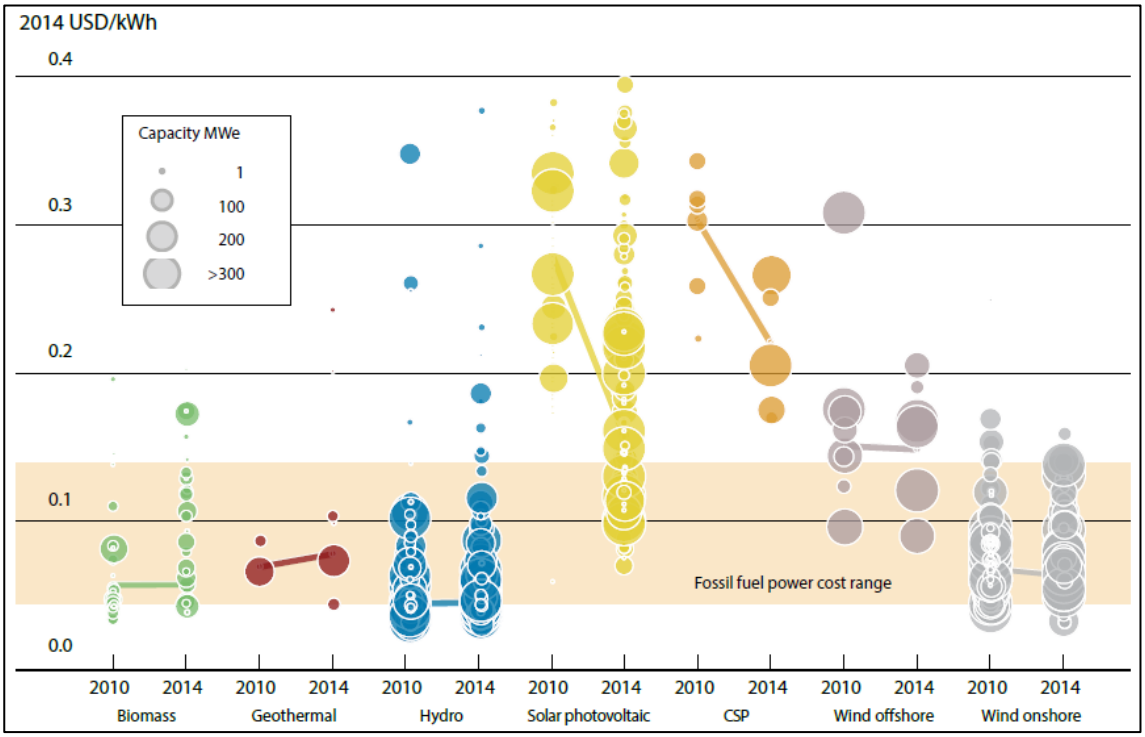

Figure 1.2 The levelised cost of electricity from utility-scale renewable technologies, 2010 and 2014 (IRENA, 2015)

Although Operations and Maintenance (O&M) costs are estimated to contribute to 20-25% of the LCOE, studies on the running costs and failure modes of operating wind turbines are very scarce. Despite this lack of information, the industry keeps evolving by improving designs on all levels and reducing operational and maintenance costs to make wind energy more efficient and less expensive (Echavarria *et al.*, 2008).

A recent remarkable study by Reder *et al.* (2016) has focused on wind turbine component failures and downtime. Involving over 4300 onshore wind turbines within 230 wind farms, of power ranging from 300kW to 3MW, the authors analysed failure logbooks from different manufacturers for 3 operational years covering over 7000 failures. The

failure rates represent the normalized component failure per turbine and year and the downtime represents the component contribution to overall downtime.

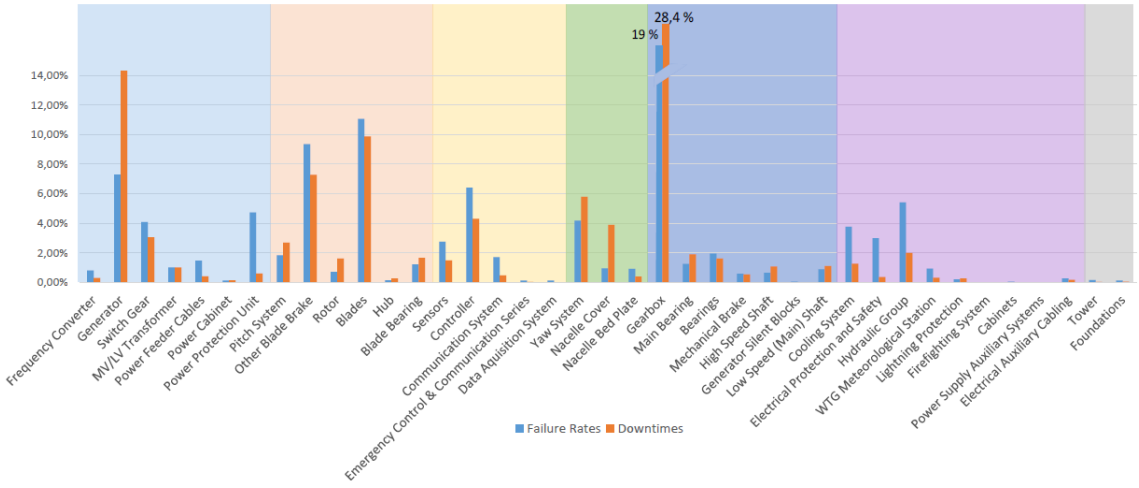

Figure 1.3 Normalised failure rates and downtimes for geared G < 1MW Turbines (Reder *et al.*, 2016)

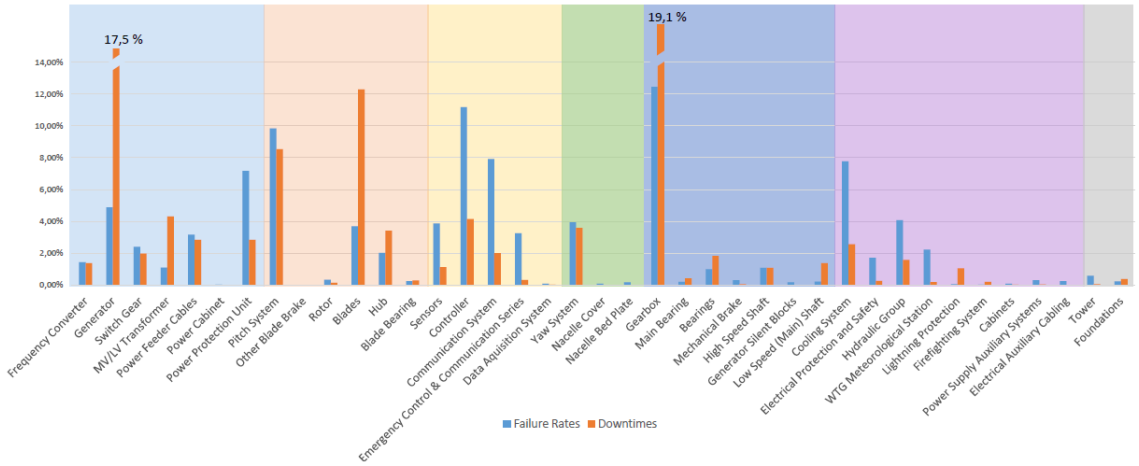

Figure 1.4 Normalised failure rates and downtimes for geared G ≥ 1MW Turbines (Reder *et al.*, 2016)

Other older studies (Hahn *et al.*, 2007; Ribrant and Bertling, 2007) are less detailed than the one described above, however there is consensus that the gearbox represents a failure mode that is responsible for a substantial amount of downtime.

In order to detect the failures in wind turbine components shown in Figure 1.3 and 1.4, Condition Monitoring Systems (CMS) have been developed. These systems use a variety of different types of sensors to monitor critical wind turbine components. There are two types of wind turbine CMS: those that are purpose-designed to monitor a particular component or the more general and extensive Supervisory Control and Data Acquisition that is commonly referred to as SCADA (Yang *et al.,* 2014). The widely employed SCADA systems monitor gearbox, bearings and lubricant temperature, vibration level of bearings and gearbox, tower and drive train acceleration. The system monitors wind turbines inputs such as wind speed, wind deviations and outputs rotor speed, blade angle and output active and reactive power to diagnose wind turbine condition, prevent additional cost, minimise downtime and increase the wind turbine reliability (Salameh *et al.,* 2018).

These condition monitoring systems consist of an integration of several sensors such as temperature, vibration, acoustic emission, and ultrasound transducers. The temperature of bearings, lubricant, generator, converter, nacelle and transformer is monitored by thermocouples. A substantial increase in temperature could be indicative of a late-stage fault, however, an increase in temperature could also be the result of a change in the operating conditions of surrounding components. The vibration level of the main shaft, main bearing, gearbox, generator, nacelle, tower, blade and foundation is monitored by vibration sensors. Component degradation, poor bearing installation, precession of bearing and faulty bearing components result in an increase of the level of vibration. This makes vibration monitoring is a suitable method to diagnose wind turbine components. Although, acoustic emission sensors are also capable to detect defects in wind turbine components as sensitively as vibration sensors, due to high cost, high noise and high data storage requirement, their application is not common. Ultrasound transducers were employed in commercialised condition monitoring techniques to detect tower defects and wind turbine blade defects in their early stages. In this method, elastic high frequency sound waves propagate in the material and interaction with a defect will cause the waves to be fully or partially reflected depending on the defect and material properties involved. By monitoring emitted and received ultrasound waves, localisation and imaging of surface and subsurface defects as well as severity analysis can be performed (Tchakoua *et al.,* 2013)

On the other hand, ultrasound has been proven to determine the stress and oil film thickness in the bearing contacts (Quinn *et al.*, 2002 and Dwyer-Joyce *et al.*, 2003). The work of Howard (2016), has shown how lubricant breakdown can be monitored by ultrasound and how this can provide information about incipient bearing failure. The bearing load and bearing outer race displacement have been monitored by ultrasound time-of-flight measurements by Ibrahim 2012 and Chen 2016, respectively. Although there is no commercialised ultrasound condition monitoring system, the mentioned works have shown the potential of ultrasound techniques as a CMS application. In this project, bearing outer race surface displacement and defect detection capabilities of ultrasound transducers were examined.

The condition monitoring methods which were discussed briefly above, are mainly employed to monitor wind turbine gearboxes and bearings within the drive train. Figures 1.5 and 1.6 illustrate the bearings that can be found in a wind turbine and in a wind turbine gearbox respectively.

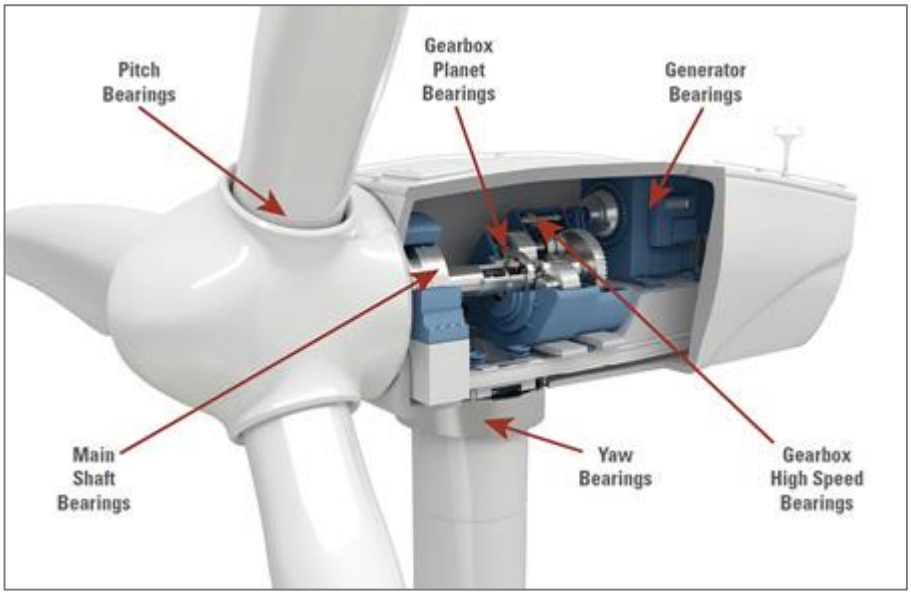

Figure 1.5 Bearings in the wind turbine (Fierro, 2016)

The wind turbine nacelle connects the tower to blades and rotor. It consists of three main parts: the main shaft, the gearbox and the generator. Bearings can be found in various locations throughout the nacelle. Pitch bearings are generally large, rolling element bearings or slewing bearings. They connect the blades and the rotor hub, which in turn are connected to the gearbox via the main shaft. Spherical roller bearings or tapered roller bearings (TRB) in combination with cylindrical roller bearings (CRB) are commonly used to support the main shaft (Dvorak, 2017). Within the gearbox, planet bearings and arrangements of CRBs, TRBs, and ball bearings can be found. These can be in multi-row or full complement versions to sustain high radial loads. The bearings in the generator, ball bearings or CRBs, require current insulation to prevent damage from passing current. Finally, the yaw system connecting the nacelle to the tower would include angular contact ball bearing or tapered roller bearings due to their compact and high load capacity properties (Yagi, 2004).

As studies show that the gearbox is responsible for substantial downtime, the bearings within the gearbox are generally the initial point of failure of the gearbox (Musial *et al*., 2007). The study by Musial *et al*., (2007) has identified certain bearing locations as being the most critical after having been reported to incur the most application failures irrespective of size, brand or model. These locations are those for the planet bearings, intermediate shaft-locating bearings and high-speed location bearings.

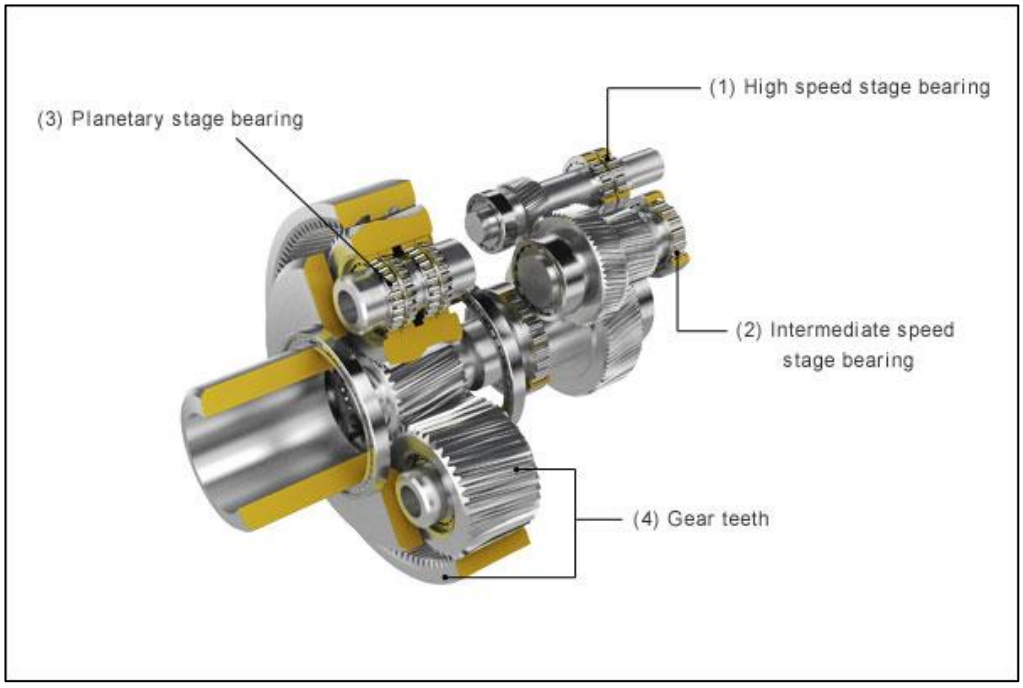

Figure 1.6 Wind turbine gearbox (Olympus, 2017)

The bearings within a gearbox must sustain a varying load operating environment as the wind ranges from a breeze to gusts of winds. This makes the acting loads difficult to predict possibly leading to the application of an inadequate bearing. One of the aims of this study is to develop a monitoring system to measure the applied load on the bearings. The same monitoring method can be used for defect detection – whereby problems with bearings can be detected prior to failure, hence avoiding catastrophic failures, enabling scheduled maintenance based on weather conditions rather than on remaining life-time, more efficient use of cranes and replacement of bearings before substantial degradation, whereby particles carried away by the oil start affecting other components. This project therefore proposes a monitoring system with the aim of reducing downtime and hence increase wind turbine reliability.

Although the method would be applicable to any bearing with rotating inner races, such as the main bearing and other bearings within the gearbox, the bearing employed in this study is a Cooper split bearing – which with respect to non-split bearings has the advantages of easier mounting or replacement due to lower handling weights and because it can be fitted around the shaft, hence reducing costs and downtime.

1.2 Aim and objectives

Since bearing related faults are generally catastrophic and costly, monitoring of the bearings is a necessity. The main aim of this project is to study the applicability of ultrasound techniques as a means of obtaining bearing health information, in a non-destructive manner, for bearings used in wind turbines.

The benefits of employing an ultrasound transducer as opposed to the widely employed vibration sensors would be twofold:

- Ultrasound transducers are not in contact with the casing, whereas vibration sensors are seismic devices that are affected by the total motion of the structure (casing vibration).

- In vibration-based condition monitoring applications, the vibration data of the bearing is first stored, then analysed in frequency domain. The proposed method is able to detect defect, analyse the source of defect and diagnose the defect severity in real time for low rotation speed applications.

To achieve the above aim, the objectives are:

1. Assess the applicability of an ultrasound transducer as a proximity sensor. As the outer race of a bearing in operation undergoes cyclic deflection, the outer race outer surface distance relative to a fixed-position transducer changes. The first step is to evaluate whether an ultrasound transducer can be employed to detect this deflection in the outer race and to what resolution.

2. Investigate the deflection curves obtained from the outer race using an ultrasound transducer. The effects of the number of rolling elements and shaft rotation speeds affect the deflection curves is investigated.

3. Detect defects from the deflection curves. This includes the determination of the faulty component (inner race, outer race or rolling elements) and assessment of the defect severity and location.

4. Develop signal processing software for both real time and post signal processing to enable bearing monitoring.

1.3 Thesis layout

Since the nature of this study is relatively complex and involves both bearing theory, ultrasound theory and post processing signal analysis the literature review extends over three chapters: Chapters 2,3 and 4. This was necessary to give the reader a basic understanding of the concepts involved. Subsequently, Chapter 5 explains the experimental procedures followed, and Chapters 6, 7 and 8 discuss the findings.

Chapter 2 introduces the reader to ultrasound theory: definitions and ultrasound wave propagation and reflection as determined by the material acoustic properties. Some measurement techniques, their principles, the transducer types employed, structure and functions of main components are explained briefly. Finally, the application of ultrasound techniques to bearing outer race displacements are discussed.

Chapter 3 discusses the bearing outer race force-deflection relationship and compares various bearing deformation theories.

In Chapter 4, the last literature review chapter, bearings – the failure modes, bearing life prediction approaches and existent defect diagnosis methods are reviewed. The latter include the types of transducers and data processing techniques that are most commonly employed for defect assessment.

Chapter 5 then introduces the test rig used in this study. Its main components, including the transducer instrumentation is presented and the data acquisition systems that were developed to record ultrasound reflections are explained.

Chapter 6 deals with outer race deflection measurements by using an ultrasound immersion transducer. The proposed bearing outer race deflection measurement method is explained in detail, starting from data acquisition and signal processing techniques. Finally, the effects of shaft rotation speed, load and the number of rolling elements on the deflection magnitude are examined.

Defects on the rolling elements and inner race of the bearing are discussed in Chapter 7. Deflection curves obtained from bearings having differently sized line defects incised on rolling elements and inner races are analysed and defect detection, location and size are evaluated.

Ensuing in Chapter 8 is an analysis of defects on the outer race. Defect detection and characterization (size and location) on the critically loaded part of the outer race is explored. Moreover, the effect of loading conditions on the deflection pattern of a defected outer race is investigated.

Finally, Chapter 9 draws the main points deduced from this research and gives some recommendations for future research.

2 ULTRASOUND BACKGROUND

Within the wind turbine market, condition monitoring systems incorporating ultrasound transducers have been employed as structural integrity monitoring systems for components such as blades and towers. Although the potential of ultrasound transducers in some bearing condition monitoring applications has been investigated, such systems have not yet been applied commercially. Hence, this study attempts to pursue further this area of study by evaluating the abilities of ultrasound transducers for bearing monitoring systems. Also, since the abilities of non-contact transducers (eddy-current, fibre optic) have been confirmed to be able to monitor bearing health, the possibility of using an ultrasound transducer as a non-contact sensor is evaluated.

This chapter introduces ultrasound and behavior of ultrasonic waves as they interact with different media. Also, it provides information about the theory behind ultrasonic condition monitoring techniques which are used to detect bearing defects by monitoring the change of bearing outer race shape (deflection and deformation). Finally, applied signal processing techniques to determine measurements from the ultrasound data will be introduced.

2.1 Ultrasound

Sound is a mechanical vibration that requires a medium to propagate. The frequency of vibration can range up to 100 GHz as illustrated in Figure 2.1. Ultrasound waves are sound waves with a frequency that surpasses the sonic region, i.e. the limit of the human hearing (20 kHz), but that is less than 10 GHz. This considerably high vibration frequency can be obtained by vibrating the piezo electric element by means of piezoelectric effect.

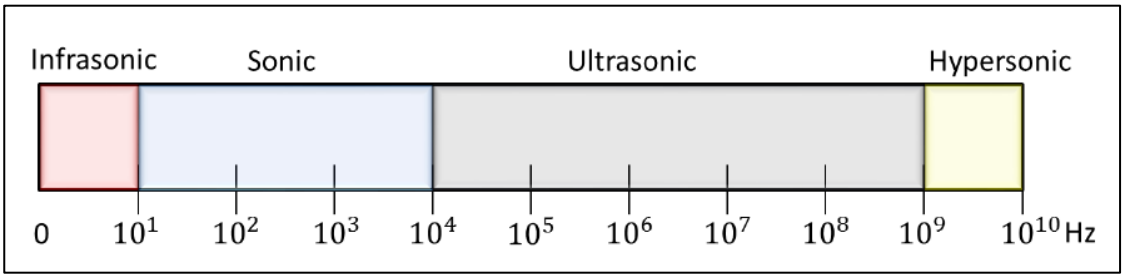

Figure 2.1 The frequency range of sound (Kinsler *et al.*, 1999)

When ultrasound interacts with a medium, the wave can be fully reflected or partially reflected and partially transmitted, depending on the acoustic impedance of the material(s). Digital imaging is performed by measuring the reflected and transmitted sound wave energies and comparing them to the incident wave.

This penetrating nature of the ultrasound wave enables non-destructive testing and monitoring of materials. Ultrasound testing offers a higher safety, less expensive and lower frequency solution when compared with X-rays, but also provides a higher spatial resolution than other non-destructive methods. These distinctive, superior features lead to extensive usage in many non-destructive testing applications in many different fields such as veterinary and human medicine, medical scanners and non-destructive testing (NDT) of structures. Usage of ultrasound became more popular in the 20th century because of the development of computers that facilitate signal processing capabilities.

2.1.1 Ultrasound propagation and wave types

All materials are composed of atoms connected via elastic bonds, which at small deflections behave similar to a spring, as shown in the Figure 2.2. When the individual particles are exposed to oscillation, this vibration force is transmitted to the adjacent particle through the elastic bonds. Propagation of the oscillation through the rest of the particles in the material will result in a sound wave.

In the media sound waves propagate via four different oscillation modes: longitudinal, shear, surface, and plate waves, depending on particles oscillations and wave propagation direction. In industrial ultrasonic testing applications, longitudinal and shear waves are more commonly employed. Within this work, longitudinal waves were studied.

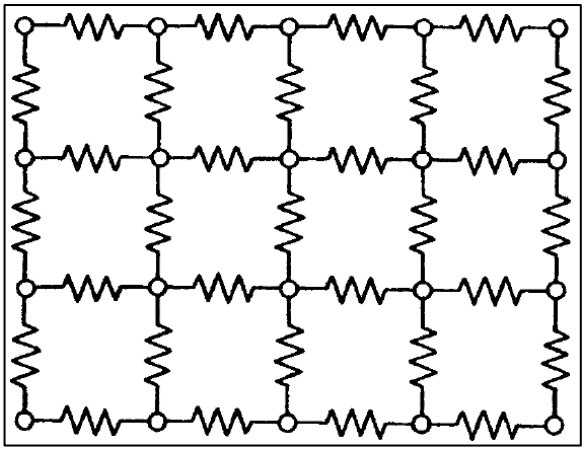

Figure 2.2 Spring-like elastic bonding between atoms-models of an elastic body (Kräutkramer and Kräutkramer, 1987)

In the longitudinal waves, which are also known as compression or pressure waves, particle displacement (oscillation) occurs parallel to the wave propagation direction. Figure 2.3 shows a section of a host material body where a longitudinal wave is propagating. As can be seen from the Figure, the material oscillates left to right and the induced sound wave propagates to the right. The sound waves propagate at a constant speed with uniform intervals to the right. Distance between oscillation cycles represents the wavelength of the soundwave, λ, which is related to the host material's elastic modulus and density.

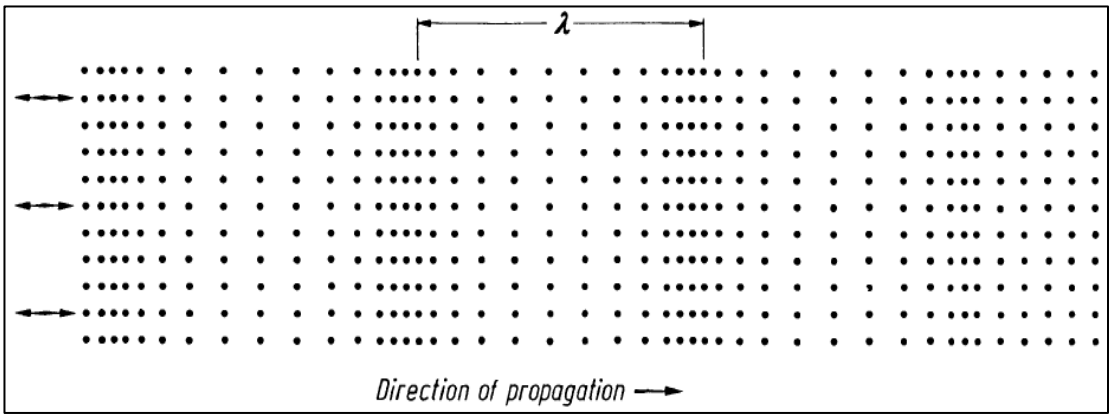

Figure 2.3 Longitudinal wave propagation (Kräutkramer and Kräutkramer, 1987)

On the other hand, in the shear waves, the oscillation of the particles within the host material is perpendicular to the wave propagation direction as shown in Figure 2.4.

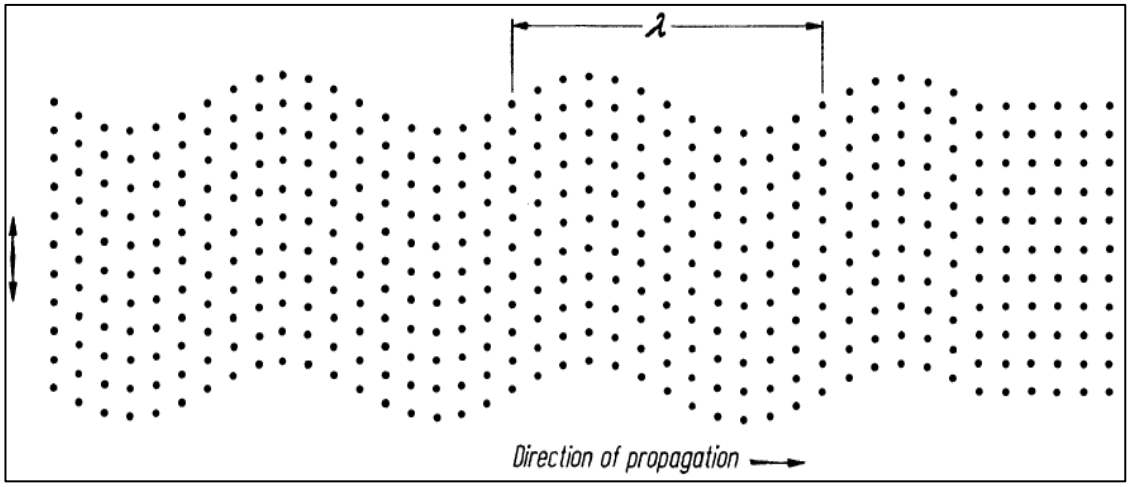

Figure 2.4 Shear wave propagation (Kräutkramer and Kräutkramer, 1987)

Shear sound waves enter the media at a moderate angle which can be created from angle beam transducers and ultrasonic shear transducers.

2.1.2 Material acoustic properties effects on ultrasound wave propagation

When sound waves interact with a dissimilar medium, the sound transmission rate will be affected by medium's acoustic properties. The relationship between the ultrasonic wave propagation and the material's acoustic properties will be discussed in more detail within the section.

2.1.2.1 Speed of sound

The speed of sound can be simply described as the travelled distance by the sound wave divided by the elapsed time. It depends on the host material and the working environment properties.

As explained in § 2.1.1, materials consist of atoms and/or molecules which are inter-connected to each other with the electrostatic bonds that determine the elastic modulus. This structure can be modelled as balls, representing particles, which are linked by springs, representing the bonds. The speed of sound through the material depends on material density, (where in the ball structure analogy density is represented by the

number of balls), and the elastic modulus of material (represented by the stiffness of the springs).

Stronger bonds transfer sound more quickly, just like stiffer springs transmit energy more rapidly. For instance, although nickel and bronze have same density, sound will travel 1.59 times faster in nickel than bronze due to high elastic modulus of nickel. The elastic modulus is directly proportional to the compressibility; hence, it follows, that the harder it is to compress a material, the higher is its elastic modulus and the faster the sound wave transmission. For example, sound is transmitted faster in solid media than liquid ones (Project Gutenberg, 2017).

On the other hand, the higher the density of the material, the slower is the transmission of the sound wave. For instance, gold and aluminum have similar elastic moduli, however sound travels twice as fast in aluminium than in gold, because gold is denser (NDT Resource Center, 2018).

Also, the speed of sound depends on the sound waves type; longitudinal waves travel faster than shear waves – for example, longitudinal waves travels 2.01 times faster than shear waves in nickel. The Equation 2.1 and 2.2 express the speed of sound for longitudinal and shear waves:

$$c_{longitudinal} = \sqrt{\frac{E(1-v)}{\rho\,(1+v)(1-2v)}} \tag{2.1}$$

$$c_{shear} = \sqrt{\frac{G}{\rho}} \tag{2.2}$$

Where c is the speed of sound, E is the modulus of elasticity of the material, G is the shear modulus, v is the Poisson's ratio and ρ is the material density. The speed of sound is also related to the ultrasound wavelength at a given frequency as illustrated by Equation 2.3.

$$c = f\lambda \tag{2.3}$$

Environmental conditions such as temperature, pressure, fluid flow velocity and moisture content (for gas) also affect the speed of sound. The variation of the speed of sound in water with temperature is shown in the Table 2.1.

	Temperature (ºC)	**Speed of sound** (m/s)
Water	0	331.4
	10	337.5
	20	343
	30	349.7
	40	355

Table 2.1 The speed of sound in water vs temperature (NDT Resource Center, 2017)

As the speed of sound and penetration rate are affected by many material parameters, any changes in these parameters will affect either one or both of the sound wave's properties. Hence, monitoring the speed of sound and penetration rate enables monitoring of many material characteristics in a non-destructive way.

The speed of sound in different materials can be found in Tables (such as Table 2.2 that has been adapted from RF Cafe (2017)), but it can also be measured by simple time of flight measurements. In these tests, an ultrasound wave travels across a material of known thickness and when it reaches the material's boundary, some of the wave energy is transmitted, and some of it is reflected back to the transducer.

By measuring the time elapsed between the wave generation and the received first reflection, the speed of sound can be obtained as shown in the Equation 2.4.

$$c = \frac{2(known\ thickness)}{elapsed\ time} \tag{2.4}$$

In this work, time of flight measurements were performed to study displacements; changes in the distance between the transducer face and the bearing outer race outer surface, where the wave is travelling through a fluid (water) and the speed of sound in the fluid is not varied. This distance (between the immersion transducer face and the bearing outer race outer surface) changes while the bearing is in operation and the rolling elements pass the monitored area.

	Material	**Speed of sound** $(\boldsymbol{m/s})$
Gases	Carbon Dioxide	259
	Helium	965
	Oxygen	316
	Nitrogen	334
	Air	331
Liquids	Glycerol	1904
	Sea Water	1535
	Water	1493
	Methyl Alcohol	1103
Solids	Diamond	12000
	Glass	5640
	Iron	5960
	Aluminum	5100
	Brass	4700
	Copper	4760
	Gold	3240
	Lead	2160
	Rubber	1550

Table 2.2 Speed of sound in various materials (longitudinal wave) (RF Cafe, 2018)

2.1.2.2 Acoustic impedance

The acoustic impedance of a material is attained from the product of density and the speed of sound. In the Equation 2.5, acoustic impedance is denoted by (Ns/m^3), the speed of sound in the material, c (m/s) and density, ρ,(kg/m^3). The acoustic impedance of the various materials is shown in the Table 2.3.

$$Z = \rho c \tag{2.5}$$

Material	Longitudinal wave acoustic impedance ($MRayls$)
Aluminum	17.1
Beryllium	23.5
Bismuth	21.4
Brass	36.7
Bronze	31.28
Copper	41.61
Cadmium	24.02
Gold	62.6
Iron	45.43
Lead	24.62
Nickel	49.99
Silver	37.8
Steel	45.4
Water	1.483
Air	0.000429

Table 2.3 Acoustic impedance table of various materials (NDT Resource Center, 2012)

Impedance affects the penetration and reflection of the sound wave at an interface. When the acoustic impedance difference between two consecutive materials is high, reflection of an incident wave is higher than transmission. This principle is the basis of ultrasonic crack detection (discontinuity source); when an ultrasonic wave encounters a crack, it is fully reflected due to the high acoustic impedance difference between the solid and the air within the crack.

In this work, generated ultrasound pulses first propagate in water, then encounter the interface of the bearing outer race, which is hardened bearing steel (100Cr6). Most of the sound energy, 87.7 per cent is reflected back to the transducer whilst the rest of it is transmitted through the bearing.

2.1.2.3 Attenuation

Attenuation is the decay rate of the amplitude of an ultrasound wave as it travels through the medium. The diminishing ratio of the wave is dependent on the host material properties: travelled distance and sound frequency. An example of diminishing of ultrasonic reflections is shown in the Figure 2.5. This reduction in ultrasonic energy can occur for various reasons some of which are radiation, absorption, and scattering.

The sound wave amplitude's decay can be expressed by Equation 2.6:

$$A = A_0 e^{-\alpha x} \tag{2.6}$$

Where, A is the decayed wave amplitude after the sound wave passed through a material of thickness x. A_0 is the initial wave amplitude and α is the attenuation coefficient (Kräutkramer and Kräutkramer, 1987).

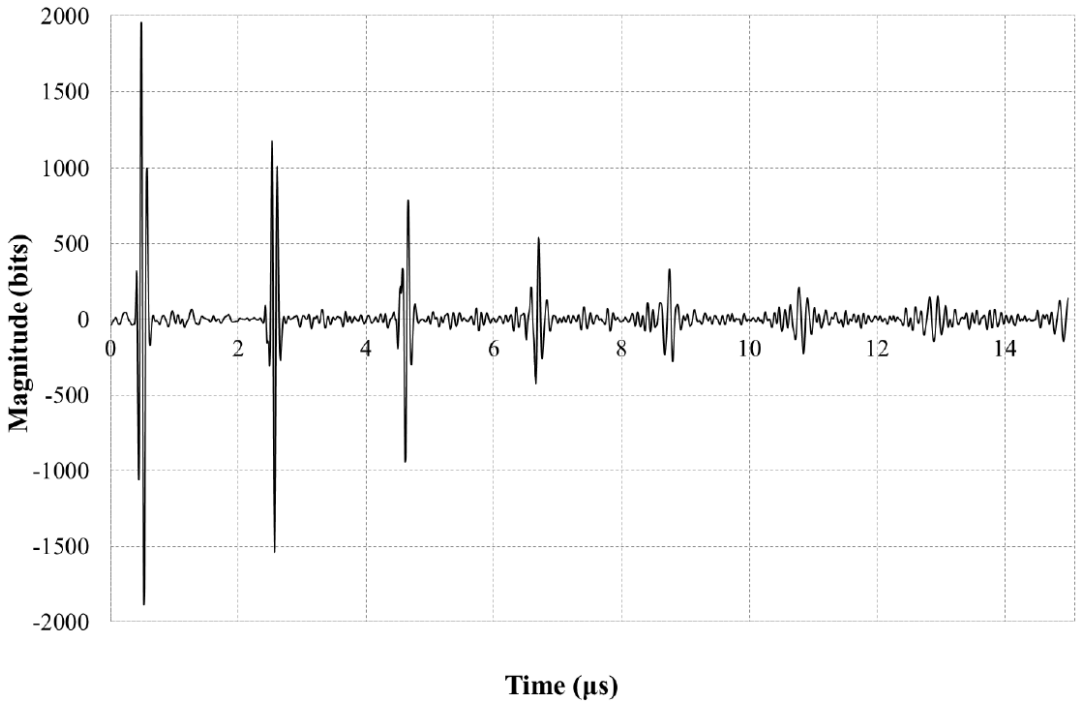

Figure 2.5 Ultrasonic reflections amplitudes diminish in time domain (Brunskill, 2013)

2.1.2.3.1 Radiation

Radiation is the decreasing of the sound wave energy due to spreading of the ultrasound wave. An ultrasound wave diverges as it propagates as a consequence of the transducer and interface geometries, transducer frequency and the speed of sound within the host medium (Figure 2.6 (a)) (NDT Resource Center, 2018).

For focused immersion transducers, low frequency and a very small active element diameter will result in excessive beam divergence (Figure 2.6 (b)). On the other hand, high frequencies cause less divergence irrespective of element diameter (Figure 6c) (NDT Resource Center, 2018).

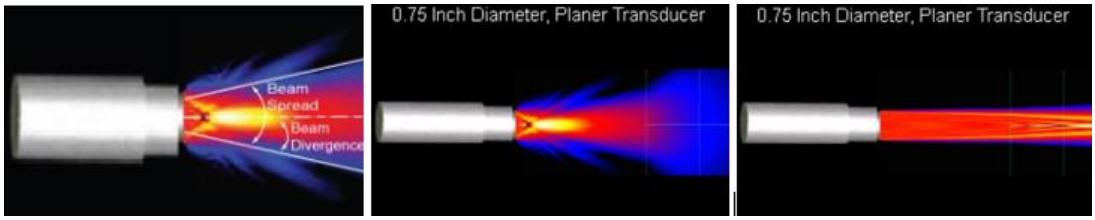

Figure 2.6 (a) Beam Divergence (b)1 MHz planar transducer's beam divergence (c) 9 MHz planar transducer's beam divergence (NDT Resource Center, 2018)

2.1.2.3.2 Absorption

Ultrasound wave propagation within media depends on particle oscillation. Some of the vibrational energy is converted into another form of energy; it changes to frictional heat, which means the energy is absorbed by the media. The loss of energy is directly proportional to the propagated sound wave frequency; therefore, high frequencies incur the highest energy losses.

2.1.2.3.3 Scattering

As the sound wave propagates in a medium, any discontinuities, inhomogeneities and other microstructural variations it encounters in the material will cause the wave to scatter. Such microscopic defects can affect propagation direction and frequency content, however, the attenuation of the sound wave amplitude is very small.

When the size of inhomogeneity is equal to or greater than the wavelength of the incident ultrasound wave, the scattering effect will cause a problem. In this work, the probability of attenuation by scattering is very low, because the wavelength of the used ultrasound wave is around 0.5 mm which is believed to be bigger than the steel discontinuities found in the used 100Cr6 high quality hardened steel bearing.

2.1.3 Ultrasonic transducers

The transducer is an electrical device which is capable of converting a physical quantity into another form of energy or vice versa. In ultrasonic transducers, the reversible conversion of energy from electrical energy to mechanical energy in the form of sound, is carried out via a piezoelectric active element. The energy conversion process can be explained briefly as follows: when the piezoelectric element is electrically charged, its atoms start vibrating at high frequency – thereby converting electrical energy into an inaudible sound wave, that propagates. Ultrasonic transducers can be used for both sound wave emission and receipt as the conversion is reversible.

Different kinds of ultrasonic transducers are available for clinical and machine element condition monitoring applications; depending on the required wave type, assembly conditions and focused or not focused properties. A classification of ultrasound transducers is given in Figure 2.7 in the form of a tree diagram.

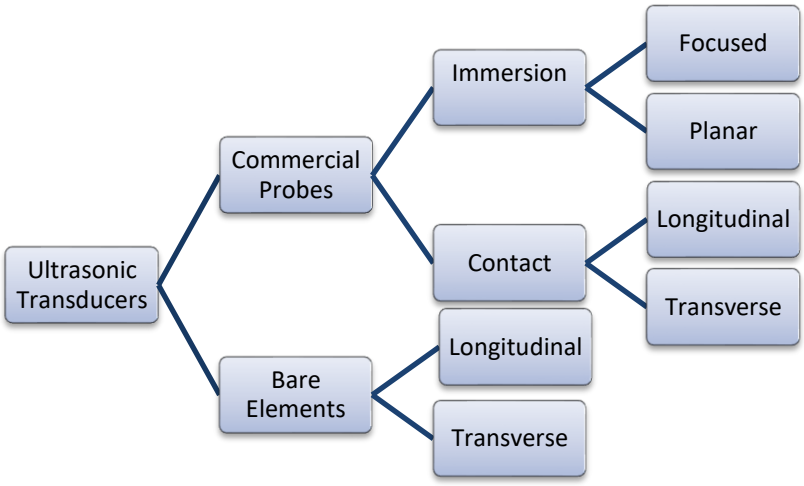

Figure 2.7 Ultrasound transducer types

Transducer type selection is the most important part of non-destructive testing of materials. The points to be considered when selecting the transducers can be summarized as follows;

- Required wavelength: Defects that are smaller than half the wavelength are difficult to detect. Hence, the ultrasound transducer wavelength, which is inversely proportional to the transducer frequency, must be chosen large enough to detect the defects under investigation.

- Sound propagation type and direction: Each wave type can be used for different applications for different measurements. Also wave propagation direction is important to detect flaws; whereas in most applications the wave direction is perpendicular to the surface of the investigated part, in some applications a wedge transducer is used to emit an ultrasound wave that hits the interface at some critical angle.

- Sound beam width: In some applications like bearing oil film thickness measurements, the ultrasound beam must fall within the contact region between the rolling elements and the races to obtain more precise results. The small contact width in bearing applications depends on the bearing material and geometry.

In this work, a cost effective commercial probe, of spherical and focused type was selected due to its ability to monitor outer race displacement by using simple time of flight measurements.

2.1.3.1 The structure of the ultrasonic transducers

The typical single element ultrasonic transducer which has one piezoelectric element, transmits and receives the ultrasound waves. Examples of such transducers are: immersion transducers, contact transducers, angle beam (wedge) transducers and delay line transducers. The main components of such single element commercial ultrasonic transducers are; piezoelectric elements, electrodes, backing (damping) material, protector wear plate, external and internal housing, RF connector and electrical connections and circuitry, as is illustrated in Figure 2.8.

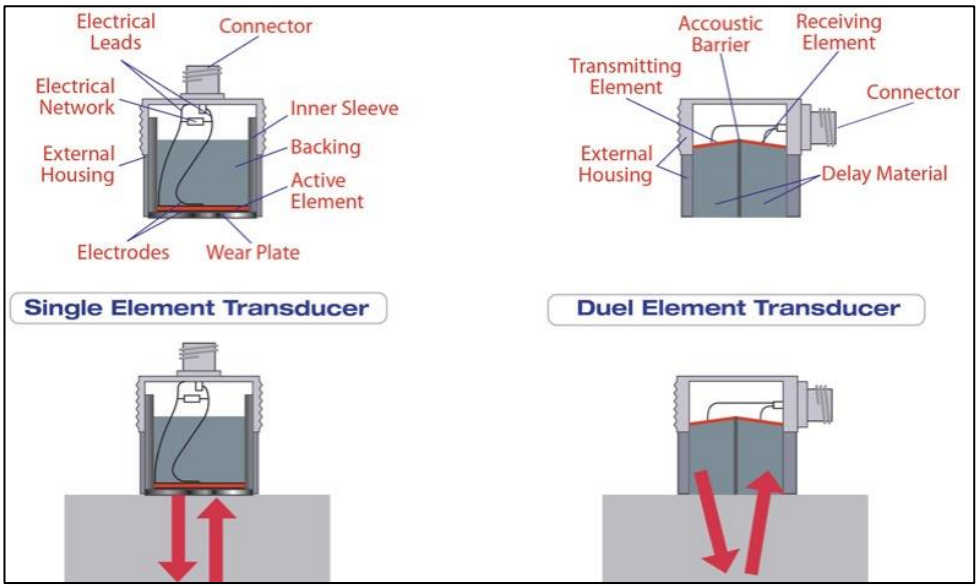

Figure 2.8 Composition of standard commercial ultrasound transducers (Olympus, 2006)

The active element of ultrasonic transducers consists of a piezoelectric ceramic or piezocomposite, in the shape of a thin disc, rectangle or square, which is sandwiched between two electrodes. When these electrodes are electrically connected, electrical energy is converted to mechanical energy through particle oscillations, and vice versa. Bare piezoelectric elements consist of this basic structure; other transducers' structure is a bit more complex.

The electrodes, which are made up of highly conductive materials such as silver or gold, cause the active element to polarize when these are electrically excited. As the molecules of the piezoelectric element align themselves, the dimensions of the element change, resulting in a displacement. These displacements can be controlled and repeated by applying an oscillating electric field to the active element to generate required sound waves.

The wear plate is located at the edge of the transducer, next to the electrodes and active element assembly to protect it from damage. An acoustic lens could also be attached to obtain a focusing effect and extra protection. The backing material which is acoustically matched with the piezoelectric element, mechanically supports the active element and helps to dampen the vibrations coming from active element. This prevents reverse

propagation and long resonance times. The use of dense and highly attenuating material enables a wide bandwidth, which gives a high sensitivity. Also, the backing material enables short pulses, as opposed to having a continuous signal.

A radio frequency co-axial connector provides voltage to oscillate the active element and carry the transducer voltage signals that are converted from the reflected sound waves to the data acquisition system. A metal external case covers all the electronics inside and protect from external damage.

2.1.3.2 Bare Piezoelectric Elements

Several types of ultrasound transducers have been used to monitor bearings. Examples include immersion ultrasound transducers (focused and unfocused) and bare piezo disc transducers. In this study, the immersion transducers used have been bought, whilst the piezo disc transducers have been made.

Bare piezoelectric discs have a very basic structure: the piezoelectric element is sandwiched between two electrodes to provide an external wiring area to apply electrical energy, as illustrated in Figure 2.9.

The lower electrode – located between the active element and the investigated machine element– partly envelopes the active element to facilitate wiring (as shown in Figure 2.9). The upper electrode covers almost entirely the active element, but is separated from the small overlapping part of lower electrode. A differential voltage can be applied to active element via the non-contacting electrodes.

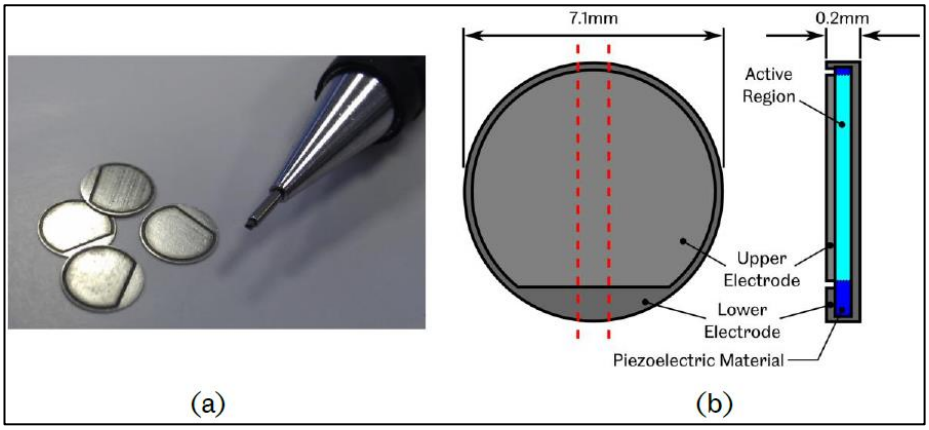

Figure 2.9 Piezo disc (1 mm slice) (Howard, 2016)

Standard longitudinal piezodiscs of 7.1 mm diameter and 0.2 mm thickness provide 10 MHz sound waves. This can be calculated from Equation 2.7 which shows that there is an inversely proportional relationship between the transducer's centre frequency and the thickness of the active element; the thinner piezodisc provides a higher frequency sound wave.

$$fc = \frac{c_{pzt}}{t} \tag{2.7}$$

In the formula, c_{pzt} is the speed of sound in piezoelectric element, and for PZTA1, this is 2000 m/s. t is the active element thickness, 0.2 mm, and fc is the centre frequency of the transducer. Thus, the frequency of the sound waves produced is 10 MHz.

The width of the ultrasonic beam generated depends on the size of the piezo disc (Howard, 2016). To monitor small areas, such as bearing contacts, which are in the order of millimeters, the piezo disc will need to be cut. It is important to cut the piezo disc in such a way that it includes both upper and lower electrodes (as shown in the Figure 2.9).

2.1.3.3 Immersion transducers

Immersion transducers, as the name suggests, do not come into contact with the inspected component, but are immersed in its liquid environment. They can be categorised in three different configurations: unfocused, spherically focused and cylindrically focused (Figure 2.10). The main tests of the project were performed by using a spherically focused ultrasound transducer.

Figure 2.10 Commercial immersion ultrasound transducers (Olympus, 2006)

Focused transducers are generally used where higher sensitivity and higher resolution is required as such focusing means concentrating longitudinal sound waves into a small region, thereby providing a small, concentrated high energy point (spherically focused) or line shaped sound beam (cylindrically focused) as illustrated in Figure 2.11. Focusing also modifies the near-field effects and enhances the sound beam coupling into curved test object surfaces. This focusing effect can be provided by either curving the active element/s or by adding a concave lens.

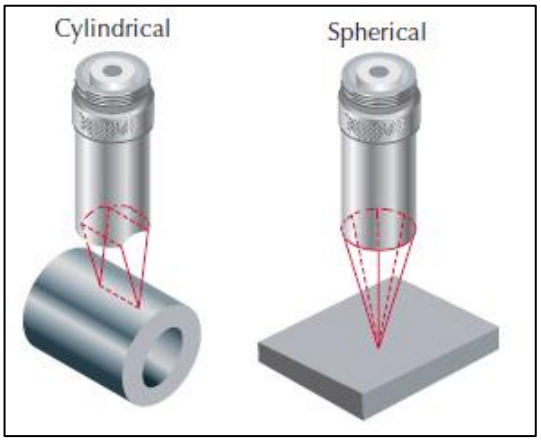

Figure 2.11 Cylindrical and spherical focused immersion transducer (Olympus, 2006)

The use of a concave lens and a flat transducer is the more common alternative due to the nature of the pulse similarity between sound and light. Spherically focused transducers are good solutions for improved sensitivity of small flaws on curved materials such as bearings, whilst the cylindrical focused version is more suitable for line shaped inspection, which is required in certain machine elements such as tubing or bar stock. The application of a spherically focused transducer on bearing systems can be seen in the Figure 2.12.

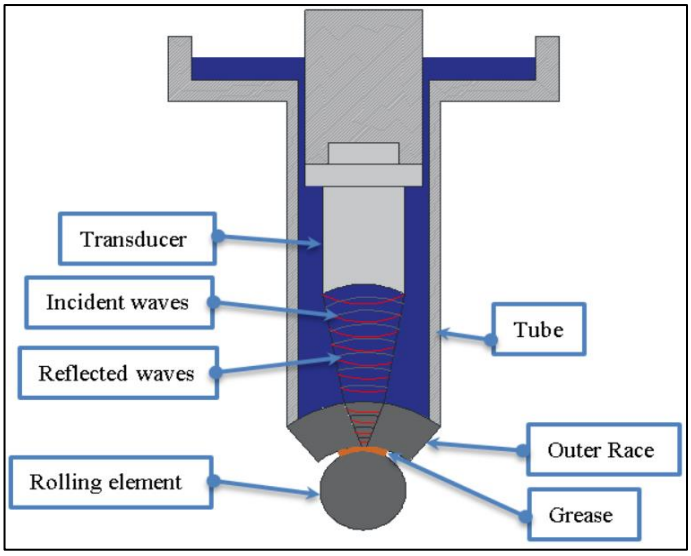

Figure 2.12 Spherically focused immersion transducer focusing effect on bearing application

On the other hand, unfocused transducers are more commonly used in more generic applications or for thick material applications where precision is not necessary.

To perform more precise measurements, focus ultrasound transducer instrumentation parameters such as water path and focal spot diameter should be adjusted suitably for the experiment. The water path distance can be described as a distance between the transducer face and the inspected component surface. The focal spot diameter is the narrowest diameter of the sound beam at focal point, where the highest sound beam pressure is observed.

In this work, although deflection measurements were not affected significantly by the water path distance, to obtain accurate measurements the inspected component was positioned in the focal zone where the narrowest and strongest sound beams befall.

2.1.3.3.1 Sound propagation of a spherically focused immersion transducer

Contactless transducers need a liquid environment between the test object and the transducers to get rid of huge acoustic mismatch. Water, because of its structure is the best candidate for longitudinal sound wave propagation.

The soundfield of a focused ultrasound transducer is divided into two zones: the near field (Fresnel zone) and the far field (Fraunhofer zone). The near field region starts from the surface of the transducer to the focal point – where other than having the narrowest diameter and highest energy, the echo signal is reduced to – 6 dB of its peak value. In this region, the longitudinal sound wave beam diameter narrows as the distance from the transducer increases. Soundfield pressure and echo amplitude increase until the far field region starts. Beyond this point, the sound waves diverge; sound field pressure drops to zero and the beam diameter starts increasing. The transducer frequency and the crystal diameter affect the divergence of the beam in the far field region in an inversely proportional manner. The best inspection results can be obtained within the focal zone region, in the section where the beam diameter decreases from twice the diameter at the focal point, to the focal point and increases again to twice the minimum, as indicated by Figure 2.13 (Advanced NDT Systems, 2004; Olympus, 2006).

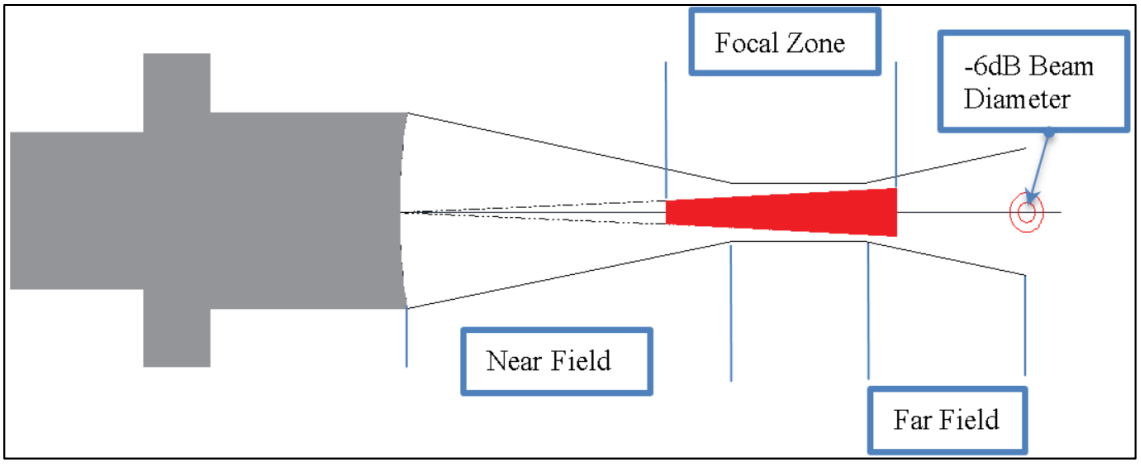

Figure 2.13 Sound field of a focused transducer

2.1.3.3.2 Water path

The distance between face of the transducer and the inspected components is called the water path. This distance is crucial for reliable results and is dependent on the inspected material thickness, speed of sound in water and the involved material (ex. steel) and also on the focal length, the latter of which is 0.8 times the near field length for a point target focus. The water path is additionally affected by frequency and diameter of the transducer as a result of the relationship between focal length and nearfield.

The near field distance can be calculated using Equation 2.8 or measured experimentally. It can also be found in catalogues provided by many transducer manufacturers.

$$N = \frac{D^2 f}{4c} \tag{2.8}$$

Where N is the near field length in water, D is element diameter, f transducer frequency and c is speed of sound in water.

In this work, this approach has been adopted in addition to comparing the obtained results to other work in literature that made use of the same sensor (Dwyer-Joyce *et al.*, 2003).

Center Frequency (MHz)	**Bandwidth (-6dBpoints) (MHz)**	**Element Diameter (mm)**	**Focal Length in water (mm)**	**Spot Size in water (mm)**
10	4 – 17	12.7	76	0.921

Table 2.4 Sensor properties in water (Dwyer-Joyce *et al.*, 2003)

The transducer is able to make accurate position measurements between the minimum and maximum focus distances. For the employed transducer these distances are 2.54cm and 20.32 cm respectively (Olympus (2006), Advanced NDT Systems (2004)). While the bearing outer race movement measurements are performed, the distance between bearing outer race and transducer should be within these limits. On the other hand, in the oil film thickness measurements, since the oil between rolling element and bearing outer race is thin and narrow, the emitted sound beam size is critical and should be smaller than the size of the oil in the contact area. For this reason, the transducer should be placed at the focal zone, where the narrowest sound beam can be obtained.

.

The focal length of a transducer is specified for water but it is effectively shortened in solid material due to speed of sound difference between the media as shown in Figure 2.14. Most of the solid materials which are inspected have higher sound velocities than water which results in a shortening of the focal length due to refraction.

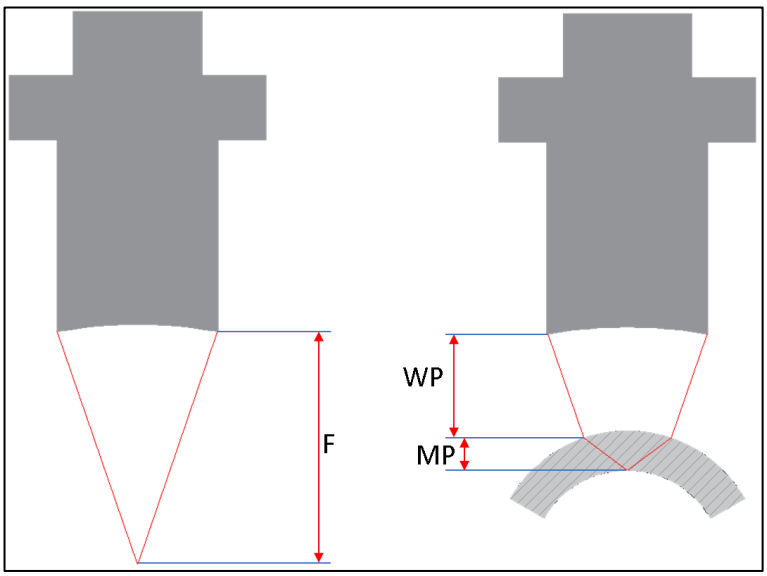

Figure 2.14 Focal length shortening

In the Equation 2.9, where F is focal length in water, MP is inspected material thickness, c_{tm} and c_w are speed of sound in testing material and water respectively, can be used to determine the water path that involves two different media.

$$WP = F - MP\left(\frac{c_{tm}}{c_w}\right) \tag{2.9}$$

After specific test conditions were applied to the Equation 2.9, the water path was calculated to be 54.5mm.

2.1.3.3.3 Focal spot diameter

The focal spot is the point which exhibits the narrowest beam diameter and highest sound field pressure within the focal zone. At this point, the sound field pressure drops to 50% (-6 dB). The focal spot diameter is dependent upon the transducer's characteristic properties as well as the propagated media's acoustic properties and can be calculated from Equation 2.10 Silk (1984).

$$d_f(-6dB) = 1.025\frac{F_w c_w}{fD} \tag{2.10}$$

Where F_w is the focal length of transducer in water, c_w is the speed of sound in the water, D is the diameter of focus transducer piezoelectric element, f is the transducer frequency. In this work, the narrowest diameter for the used transducer was calculated to be 0.921 mm in water applications.

2.2 Ultrasonic interactions at boundaries

Behaviour of longitudinal waves at the boundaries and how this is applied to the bearing environment are described in this section. Ultrasound waves, in some ways behave in a similar manner to light waves; as the sound waves propagate in the media, Snell's law of reflection and refraction is observed. When the ultrasound waves strike an interface at an inclined angle, the transmitted sound waves are bended due to sound wave propagation speed difference between the two consecutive media as illustrated in the Figure 2.15. However, unlike light waves, an incident ultrasound wave energy is distributed into longitudinal and shear waves as it overcomes a boundary.

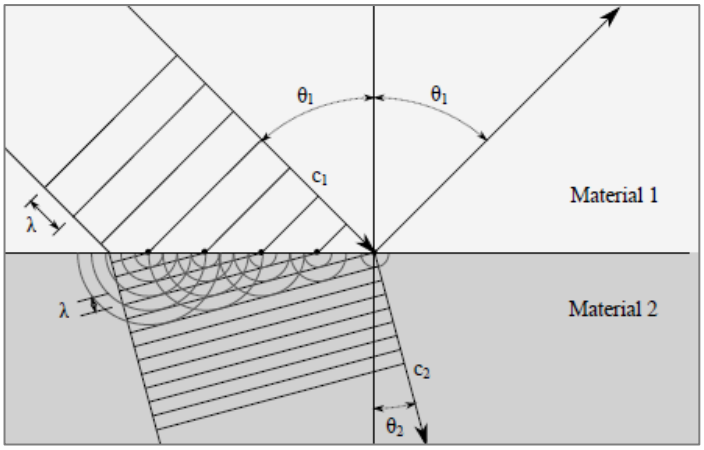

Figure 2.15 Application of Snell refraction law to the ultrasound waves (Brunskill, 2013)

When an incident sound beam hits an interface at some angle, some of the wave energy is reflected with the same angle of incident wave; the rest of the energy is transmitted into the next material and is refracted at a different angle. This angle can be calculated by using Snell's law of refraction as shown in the Equation 2.11.

$$\frac{c_1}{c_2} = \frac{sin\theta_1}{sin\theta_2} \tag{2.11}$$

Where c_1 and c_2 are the speed of sound in the media, θ_1 is the incident wave angle and θ_2 is the refracted wave angle.

On the other hand, a generated ultrasound wave hitting an interface normally, incurs no refraction, but is partially reflected back, and partially transmitted through the material. The amount of reflection depends on the acoustic impedances of the concerned media and is defined by the ultrasound reflection coefficient, *R*, given by Equation 2.12. Figure 2.16 shows a schematic of this theory.

$$R = \frac{z_2 - z_1}{z_2 + z_1} \tag{2.12}$$

The reflection coefficient can also be expressed in terms of the function of transmission, T as illustrated by Equation 2.13:

$$R = 1 - T \tag{2.13}$$

In practical ultrasound measurements, R can be obtained, by measuring instantaneous reflection and dividing it by the reference reflection as shown by Equation 2.14. In bearing oil film thickness measurement applications, while the rolling element is not in contact, the point which is being investigated, is assumed to be the reference and the expected interface is steel-air. However, when contact occurs beneath the transducer, oil film thickness gets thinner and a steel oil interface is observed. In the latter case, reflection amplitudes are lower.

$$R = \frac{Measured\ Ref.(Roller\ in\ contact\ with\ outer\ race\ under\ the\ sensor)}{Reference\ (not\ in\ contact)} \tag{2.14}$$

The ultrasonic reflection coefficient varies between -1 and 1, where $R = 1$ denotes 100% reflection, as in a solid to air environment case. $R = 0$ represents an identical material environment where the entire ultrasonic energy is transmitted. The sign of the value denotes the phase of the reflected ultrasound wave.

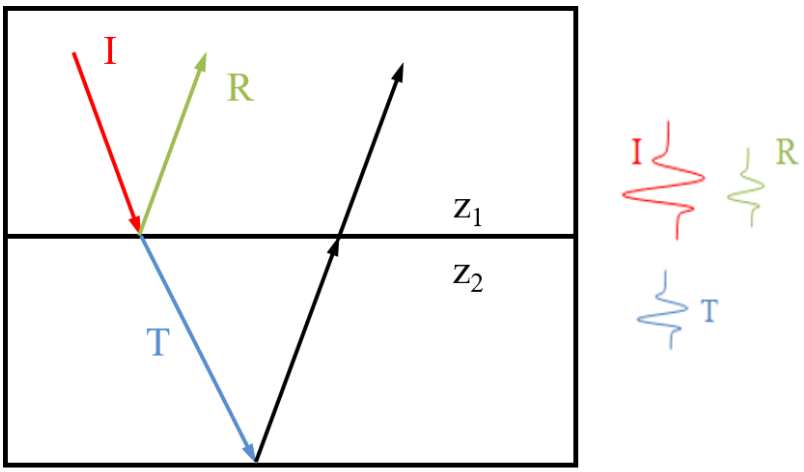

Figure 2.16 Incident, reflected and transmitted pulses at perfect boundaries

2.2.1 Ultrasonic Interactions at Real Engineering Contacts

Surface profiles of real engineering contacts are never as perfect as illustrated in Figure 2.17 (a). Surfaces have asperities that behave like a spring when two mating surfaces are pressed against each other. Such asperities, which prevent perfect contact, result in an interfacial stiffness, K (Gpa) (Tattersall, 1973). Hence, taking into consideration these contact imperfections, the ultrasound reflection coefficient vector formula must be modified to include the interfacial stiffness as shown in the Equation 2.15.

$$R = \frac{z_2 - z_1 + i\omega\left(\frac{z_2 z_1}{K}\right)}{z_2 + z_1 + i\omega\left(\frac{z_2 z_1}{K}\right)} \tag{2.15}$$

In the Equation 2.15, z represents the concerned media acoustic impedances and ω is the ultrasonic waves' angular frequency ($\omega = 2\pi f$). This relation is named the 'spring model' and is used commonly in ultrasonic contact monitoring applications. In bearing contact applications, the interfacial stiffness is replaced by the lubricant stiffness, because the lubricant increases separation between the contacts and makes the imperfections (asperities) effect negligible.

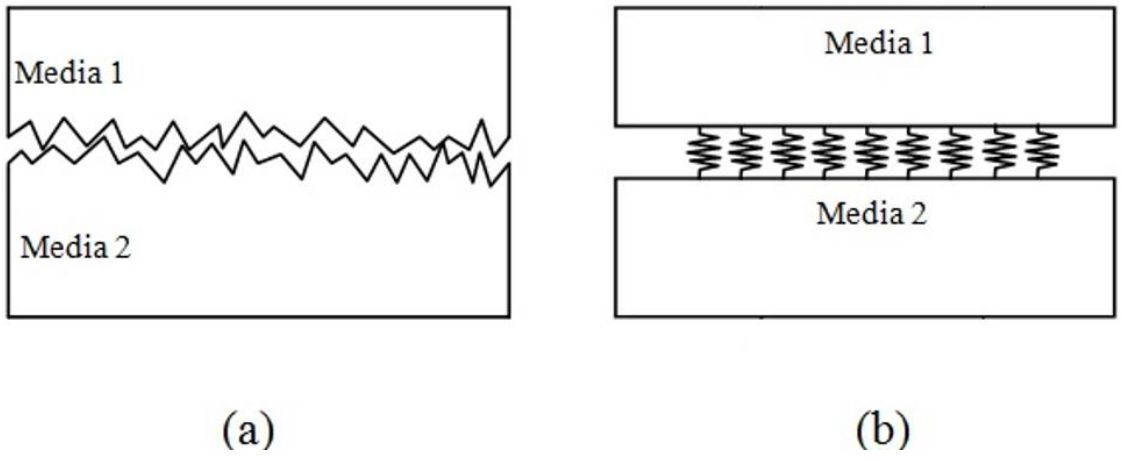

Figure 2.17 (a) Asperities in real contact (b) Spring Model as a consequence of contact roughness

In Equation 2.15, the reflection coefficient vector has an imaginary component i that represents both phase and amplitude. In practical applications, the reflection coefficient magnitude is usually measured and Pythagoras' theorem is applied to the Equation 2.15 to obtain the Equation 2.16 which enables the calculation of the absolute value of the reflection coefficient (Tattersall, 1973).

$$|R| = \sqrt{\frac{(z_2 - z_1)^2 + \frac{\omega^2 z_2^2 z_1^2}{K^2}}{(z_2 + z_1)^2 + \frac{\omega^2 z_2^2 z_1^2}{K^2}}} \tag{2.16}$$

2.2.2 Ultrasonic interactions and measurements at bearing contacts

In this section, the behavior of ultrasonic waves in bearing contacts and the theory of measurement techniques will be explained. A discussion of the different techniques and their capabilities follows towards the end of the section.

Ultrasonic measurements can be performed by using one of the following three approaches: time of flight method, the resonance technique, the spring model in bearing contacts. Each approach can be used for bearing lubricant thickness measurements, but the measurable range of each method is different. When the lubricant layer thickness is equal to or higher than 40 micrometers (µm), the ultrasound wavelength time of flight method can be used. If the measuring lubricant thickness is equal to the ultrasound wavelength, the resonance method, for which the lowest limit of lubricant film thickness must be around 10 µm, can be employed. When the measuring oil film thickness is in the nanometer range and is hence smaller than the ultrasound wavelength, the spring model can be used (Suzuki, 2016).

2.2.2.1 Basic concepts of the spring model

In engineering applications where a fluid (e.g. oil) is squeezed between two solid media (as in for example piston-cylinder interfaces and bearing applications) (Mills *et al.*, 2015; Howard, 2016), ultrasonic reflection was found to be related to the effective fluid stiffness, *K*, which in turn, is related to the compressibility (change in volume due to a change in pressure) of the fluid. In bearing applications, lubricants are trapped between the outer race and the rolling element. The oil layer stiffness describes the resistance to the compression of the layer with applying pressure as shown by Equation 2.17.

$$K = -\frac{dp}{du} \tag{2.17}$$

Where u is the compression displacement and dp is the pressure change.

Stiffness of the liquid is also related to the bulk modulus of the layer and layer thickness as illustrated in Equation 2.18.

$$K = \frac{B}{h} \tag{2.18}$$

In Equation 2.18, oil layer bulk modulus is defined by B, and h is the oil film thickness. Bulk modulus determines how compressible the fluid is. It shows how the density of a fluid changes when the fluid is subjected to pressure as illustrated by Equation 2.19.

$$B = -\left(\frac{\vartheta}{d\vartheta}\right) d\rho \tag{2.19}$$

Where ϑ is the volume of the fluid, $d\vartheta$ is the volume change of the fluid due to compression, $d\rho$ is the subjected pressure.

However, the bulk modulus can also be determined by Equation 2.20 that relates the lubricant density and speed of sound through the lubricant film under ambient temperature to the bulk modulus.

$$B = \rho c^2 \tag{2.20}$$

Hence, substituting Equation 2.20 into Equation 2.18, the lubricant film thickness can be determined from fluid parameters.

$$K = \frac{\rho c^2}{h} \tag{2.18}$$

To obtain a relationship between oil film thickness and reflection coefficient, Equation 2.18 can be substituted in Equation 2.16:

$$h = \frac{pc^2}{\omega z_2 z_1} \sqrt{\frac{|R\,|^2 (z_2 + z_1)^2 - (z_2 - z_1)^2}{1 - |R\,|^2}} \tag{2.21}$$

If the lubricant is trapped between identical materials, as in bearing applications, the lubricant film thickness formula can be expressed easily by Equation 2.22 (Howard, 2016).

$$h = \frac{2\rho c^2}{\omega z} \sqrt{\frac{|R|^{\,2}}{1 - |R|^2}} \tag{2.22}$$

The reflection coefficient can be obtained experimentally as shown by Equation 2.23.

$$R(f) = \frac{A_m(f)}{A_{ref}(f)} R_{ref} \tag{2.23}$$

Where $A_m(f)$ is the spectral amplitude of ultrasonic reflection from the oil layer, $A_{ref}(f)$ is the reference spectral amplitude, and R_{ref} is the reflection coefficient of the reference interface.

2.2.2.2 Basic concepts of the time of flight method

Sufficiently thick lubricant film thicknesses which are greater than the wavelength of the used transducer, can be measured by using the time of flight method. Thus, the measurable lowest lubricant film thickness is defined by the centre frequency of the ultrasound transducer. For steel applications ultrasound frequencies are limited to 60 MHz because attenuation increases significantly with frequency. Consequently, the lowest measurable thickness limit is 40 μm (Suzuki, 2016).

Within this method, related reflections must be located discretely in the time domain without overlap. Subsequently, the time difference between related reflections gives the time of flight.

The thickness of the lubricant layer can be calculated by using the known speed of sound in the layer and measured time of flight. As is expressed in Equation 2.24 for thickness calculation, the time of flight, t, must be divided by two because the elapsed time covers transmission and reflection of ultrasound waves.

$$h = \frac{ct}{2} \tag{2.24}$$

Where h is the measured distance, c is the speed of sound, and t is the elapsed time.

This work employs the ToF method to calculate the distance between the focus immersion transducer and the bearing outer race. Also, the distance changes caused by the outer race displacement was monitored via the same technique. The bearing outer race, whilst sustaining a radial load, is bent when the rolling element passes under the transducer. This phenomenon results in a shortened distance, and consequently, the travel time of the sound wave also shortens (Ibrahim, 2012). A detailed explanation of the method and signal processing techniques will be discussed in outer race displacement chapter.

2.2.2.3 Basic concepts of resonance method

When the layer to be measured has a thickness that is equal to the wavelength of the employed transducer, the resonant dip technique is applicable. In this technique, the lubricant layer is resonated by ultrasound waves and these resonances can be seen as drops to zero in the reflection coefficient spectrum, as shown in the figure below. If the speed of sound, c, in the layer is known, and if the reflection coefficient spectrum in the frequency domain is obtained, the layer thickness, h, can be calculated by using Equation 2.25:

$$h = \frac{cm}{2f_m} \tag{2.25}$$

Where m is the mode number (first, second, third…etc) of the resonant frequency and f_m is the corresponding resonant frequency (Zhang *et al.*, 2006).

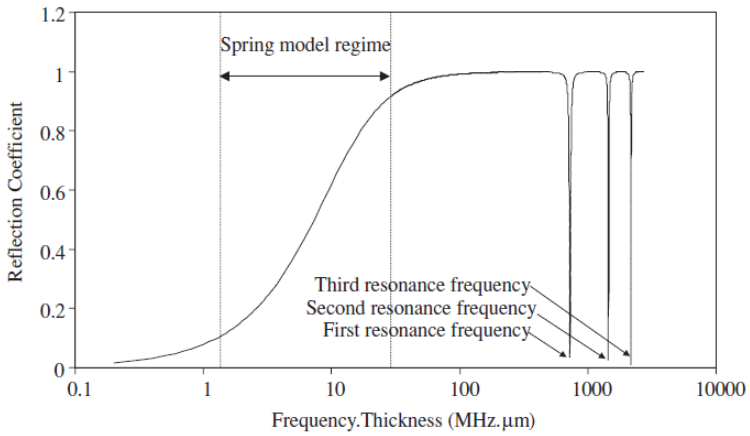

Figure 2.18 Prediction of the reflection-coefficient spectrum from a layer of mineral oil between two steel half spaces (Zhang *et al.*, 2006)

This technique, like ToF, is restricted by the frequency of used transducer, due to high attenuation. The work of (Zhang *et al.*, 2006) shows that in an application of oil of type Shell Turbo T68 trapped between EN24 steel parts, the thinnest possible measurable oil layer thickness is 7 µm.

2.3 Conclusion

This chapter gives some general background about ultrasound. Some measurement techniques and their theory have also been discussed, with more detail given about those employed in this research. The main points discussed by the chapter are:

- Ultrasound definition and the generation of ultrasound wave physics
- Wave types and the effects of the acoustic properties of a medium on the wave propagation
- Ultrasound transducer types, structure and the function of the main components. The transducers employed in this work have been discussed in some detail.
- Ultrasound wave behavior when waves encounter boundaries for example bearing contacts
- The main approaches for lubricant film thickness and outer race displacement measurements by using reflected ultrasound signals: spring layer model, time of flight and resonant layer model. The former methods, since they have been employed in this work, have been given in greater detail.

3 BEARING OUTER RACE SURFACE DEFLECTION

This chapter discusses some bearing outer race deflection theories and very briefly the principle of bearing outer race deflection measurement which has been employed in this research.

3.1 Bearing force-deflection relationship

Machine elements, such as rolling element bearings, contain locations that need to have a lubricant to separate the mating surfaces sustaining a force. In the case of a bearing, such contacting surfaces would be in between the races and rolling elements. The lubricant thickness depends on bearing operating conditions, such as the applied forces. When the lubricant thickness is too thin, the bearing contacts experience elastohydrodynamic lubrication conditions, meaning, that the applied forces are able to deform the bearing surfaces elastically (Hamrock and Anderson, 1983).

Applied forces and moments in a bearing, cause elastic deformation and a corresponding displacement in the direction in which the forces are exerted. The relationship between the applied load and the obtained displacement is non-linear, as illustrated in the following figure.

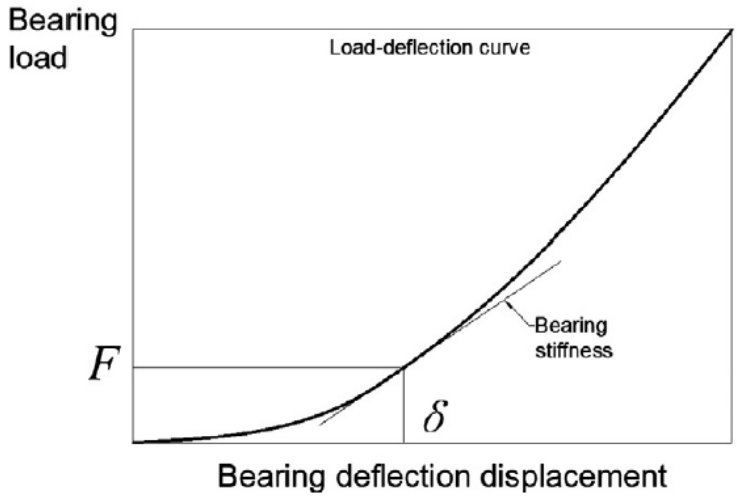

Figure 3.1 Rolling bearing load-deflection curve (Bhushan, 2000)

Moreover, the slope of the load-deflection curve at any point gives the bearing stiffness which is a multi-dimensional characteristic of bearing. The bearing stiffness matrix can be described mathematically as a 5×5 symmetric matrix (Lim and Singh, 1990).

$$K_b = \begin{bmatrix} k_{xx} & k_{xy} & k_{xz} & k_{x\theta_x} & k_{x\theta_y} \\ k_{yx} & k_{yy} & k_{yz} & k_{y\theta_x} & k_{y\theta_y} \\ k_{zx} & k_{zy} & k_{zz} & k_{z\theta_x} & k_{z\theta_y} \\ k_{\theta_x x} & k_{\theta_x y} & k_{\theta_x z} & k_{\theta_x \theta_x} & k_{\theta_x \theta_y} \\ k_{\theta_y x} & k_{\theta_y y} & k_{\theta_y z} & k_{\theta_y \theta_x} & k_{\theta_y \theta_y} \end{bmatrix}$$

The matrix consists of the ratios of exerted forces and moments over the related displacement in all directions. The matrix depends on the applied load, bearing geometric and kinematic parameters, number of rolling elements, radial clearance, contact angle at unloaded case, Hertzian stiffness constant.

3.2 Bearing deflection calculation approaches

Several approaches have been proposed to calculate the bearing deflection, however, each approach gives a different value for the elastic displacement acting under the same operating conditions. In this section, some of these equations and approaches will be presented.

The first attempt at elastic deformation calculation of a point and of a rectangular contact was performed by Hertz (1881). Pressure distribution and applied stress effects on the deformation were studied and boundary conditions were determined. The assumptions and derived equations in this study are the basis of present day contact mechanics. Another early attempt at deformation calculation of semi-infinite elastic surfaces at point loaded contact conditions was conducted by Boussinesq (1885). Rectangular contact elastic deformation formulations can be derived by using the elastic deformation equations of point loading conditions.

Although these early attempts laid the foundations of the elastic deformation fundamentals, they were not enough to determine surface deflection in a bearing precisely and there was a need for more accurate equations to be developed. However, since the elasticity of contacted and compressed surfaces is still based on Hertzian contact theory, the main terms should be explained before discussing bearing contact deformation.

3.2.1 Bearing internal load distribution

An applied radial force is sustained by the rolling elements, and its distribution is such that the rolling element located on the same radial direction of the applied load carries the highest load. The load carried by the other rolling elements decreases with increase in angle between the rolling element centre and the applied force direction. Figure 3.2 depicts an example of a 200N load distribution on the rolling elements in a bearing.

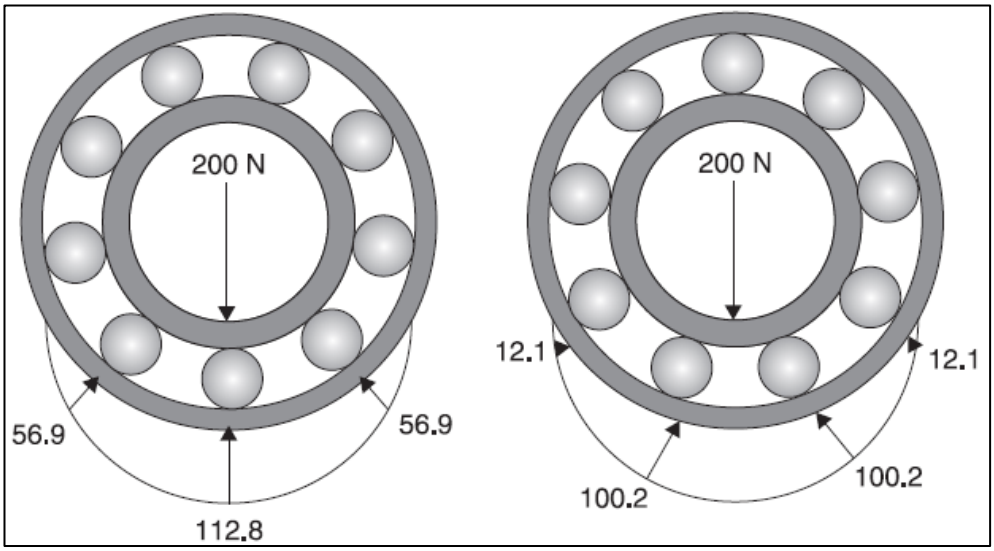

Figure 3.2 The example of load distribution of the bearing (Wardle, 2015)

The load on the maximum loaded rolling element for line contacts can be calculated by using the Equation 3.1.

$$W_{max} = \frac{5F_r}{Z} \tag{3.1}$$

Where in equation, W_{max} is the applied maximum load, F_r is applied radial load, Z is number of rolling elements (Harris and Kotzalas, 2006).

It follows that the bearing incurs maximum deflection at the point sustaining maximum load and hence, in this work, the immersion probe that measures deflection was located at this point: i.e. along the direction of the radial load applied.

3.2.2 Hertzian line contact theory

The applied load on the contacted elastic bodies results in local stress and elastic deformation at the mating surfaces (i.e. on the outer races and rolling element surfaces). The shape of the contact are between a spherical rolling element and the races is elliptic, whilst that between the cylindrical rolling element and races it is rectangular (line contact) as indicated in Figure 3.3.

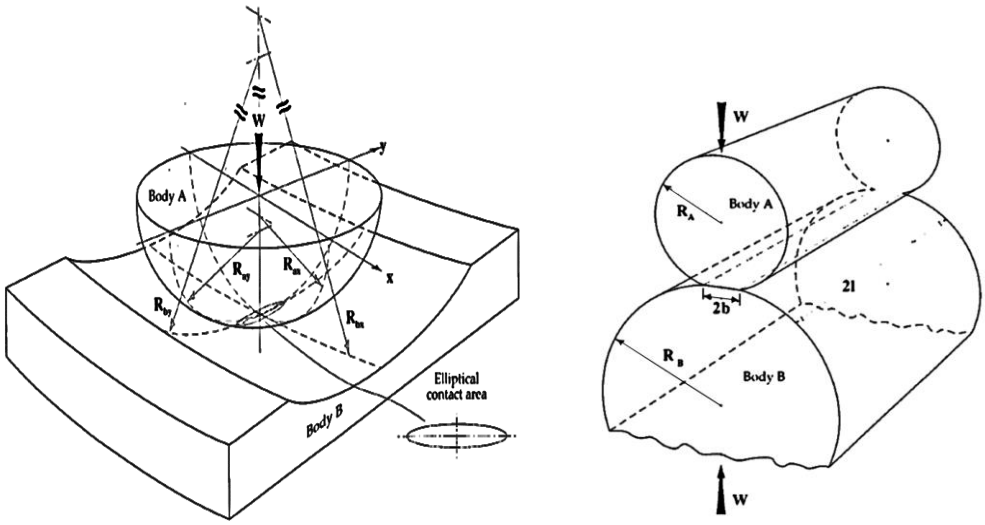

Figure 3.3 Elliptic contact and rectangular (line) contact (Stachowiak and Batchelor, 2013)

The rectangular shape of contact has width $2b$ and length L (rolling element length). The semi-width b of the contact depends on many parameters, such as the applied load, W_{max}, the radii of the contacting surfaces (R_1 and R_2), poisson ratio v and the elastic modulus E as illustrated by Equation 3.2. It is assumed that the applied load is distributed equally across the rolling element length.

$$b = \sqrt{\frac{4W_{max}R^*}{L\pi E^*}} \tag{3.2}$$

Where E^* is the reduced elastic modulus which depends on the poisson ratios and elastic moduli of related media; R^* is the reduced radius, and can be found from Equation 3.3:

$$\frac{1}{R^*} = \frac{1}{R_A} + \frac{1}{R_B} \tag{3.3}$$

Where R_A is the rolling element radius and R_B is the radius of outer race or inner race. If the rectangular line contact between the outer race and rolling element is being analysed, R_B is negative because the contact is concave, whereas if the contact between inner race and rolling element is analysed R_B carries a positive sign.

The pressure, p_{max}, is distributed across the rectangular contact and can be found by using Equation 3.4:

$$p_{max} = \frac{2W_{max}}{L\pi b} \tag{3.4}$$

3.2.3 Line contact elastic deformation

The elastic deformation of a line contact has been studied by many researchers and consequently there are many equations that are slightly different from each other. The textbook by Harris and Kotzalas (2006), cites the equations developed by Lundberg and Sjoval (1958) and the simpler, more practical version derived later by Palmgren (1959) as illustrated by Equation 3.5.

$$\delta = \frac{2W_{max}(1-v^2)}{\pi E l} \ln\left[\frac{\pi E l^2}{W_{max}(1-v^2)\left(1 \pm \frac{D}{d_m}\right)}\right] \tag{3.5}$$

Where D is the rolling element diameter and d_m is the pitch diameter, which is the distance between two oppositely located rolling element centers (Lundberg and Sjoval, 1958).

Generally, rolling elements are crowned (as shown in Figure 3.4) to avoid high stress at the edges and protection from slight misalignment. The more practical formula developed by Palmgren (1959) as shown in Equation 3.6 , was derived by observing the contact deformation obtained from testing a range of crowned cylindrical roller bearings under different operating conditions.

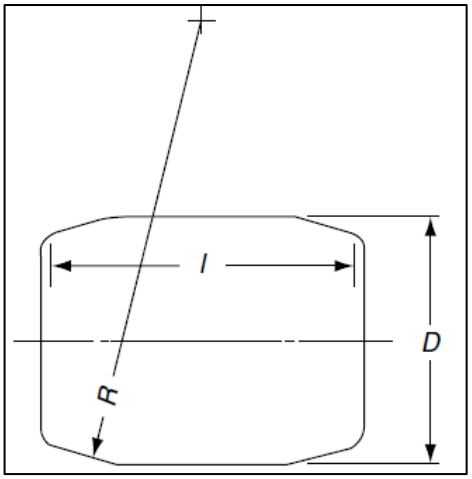

Figure 3.4 Crowned cylindrical rolling element (exaggerated scale)(Harris and Kotzalas, 2006)

$$\delta_{max} = 3.84 \times 10^{-5} \frac{W_{max}^{0.9}}{l^{0.8}} \tag{3.6}$$

Where l is the length of the roller in mm, and W_{max} is the load of heavily loaded rolling elements in Newtons. The radial deflection value which is calculated from the equation includes both the cylindrical rolling element and raceway radial elastic deformation amount.

Changsen (1991) modified Palmgren's formula for deflection as Equation 3.7 and 3.8;

$$\delta_{max} = K_t W_{max}^{0.9} \tag{3.7}$$

$$K_t = 3.81 \left[\frac{1 - v_1^2}{\pi E_1} + \frac{1 - v_2^2}{\pi E_2} \right]^{0.9} \frac{1}{l^{0.8}} \tag{3.8}$$

It should be emphasised that there are many different equations in literature for the determination of maximum deflection. The work of Houpert (2001) outlines this point. In this study, the values given from different equations were compared to published experimental work conducted under the same working conditions, and eventually, a new equation was proposed. The same exercise was repeated for different loading conditions. The difference in the deflection values given by the equations studied by Houpert (2001) reveal discrepancies of up to 27%, which is quite significant.

Q/L (kN/m)	Tripp (1985)	Zantopulos (1988)	Eschmann, *et al.* (1985)	Houpert (2001)
10	0.74 µm	0.99 µm	0.86 µm	0.75 µm
100	6.49 µm	8.54 µm	7.26 µm	6.34 µm
1000	52.8 µm	72.1 µm	61.1 µm	53.7 µm

Table 3.1 Three different loading conditions calculated deformations by using different approaches (reproduced from Houpert, 2001)

Different studies have developed equations to calculate the total cylindrical bearing outer race deformations. The ensuing table shows some more of these equations (more detail can be found in the given references). The existence of a variety of formulas shows that the calculation of bearing outer race elastic deformation is neither clear, nor standardized. From the point of view of the author, the total elastic deformation of bearing components, may also depend on the thickness and shape of the bearing outer race and the distance between rolling elements.

(Hamrock and Anderson, 1983)	$\delta = \frac{2WR_x}{\pi}\left[\frac{2}{3} + \ln\left(\frac{4r_{ax}}{b}\right) + \ln\left(\frac{4r_{bx}}{b}\right)\right]$
(Hamrock and Anderson, 1995)	$\delta = \frac{2WR_x}{\pi}\left[\ln\left(\frac{4r_{ax}}{b}\right) + \ln\left(\frac{4r_{bx}}{b}\right) - 1\right]$
(Schmid, *et al.*, 2014)	$\delta = \frac{2W'R_x}{\pi}\left[\ln\left(\frac{2\pi}{W'}\right)\right]$
(Bhushan, 2000)	$\delta = \frac{Wl}{\pi}\left[\frac{2}{E'}\ln\left(\frac{\pi E' R_e}{2Wl}\right) - \frac{(1+v_1)v_1}{E_1} + \frac{(1+v_2)v_2}{E_2}\right]$
(Stachowiak and Batchelor, 2013)	$\delta = \bar{\xi}_i\left[\left(\frac{4.5}{\bar{\xi}_i R_i'}\right)\left(\frac{W}{\pi \bar{k}_i E'}\right)^2\right]^{1/3} + \bar{\xi}_o\left[\left(\frac{4.5}{\bar{\xi}_o R_o'}\right)\left(\frac{W}{\pi \bar{k}_o E'}\right)^2\right]^{1/3}$

Table 3.2 Cylindrical rolling element bearing total elastic deformation calculation formulas

3.3 The principle of the outer race deflection measurement

In this study, a technique that makes use of ultrasound waves for the measurement of deflection of the outer race has been employed. The principle of operation is quite straight forward – emitted ultrasound waves that encounter an interface will partly be reflected and partly be transmitted. Hence, when incident waves are directed onto a series of interfaces, the transducer will receive a series of reflections – depicted in Figure 3.5 – that within a time domain will reveal distances travelled in each medium.

Within this study, the immersion transducer is fitted on a steel rod, within a tube that is located in line with the shaft center of the bearing and the roller element position that incurs the highest load. The tube provides water that enables transmission of ultrasound waves to the outer race. Incident ultrasound waves are directed onto the outer race outer surface and upon impingement, some of the waves are reflected back to the transducer, whilst the rest of the energy is transmitted through the outer race. The transmitted waves subsequently encounter another interface – that of the outer race inner surface.

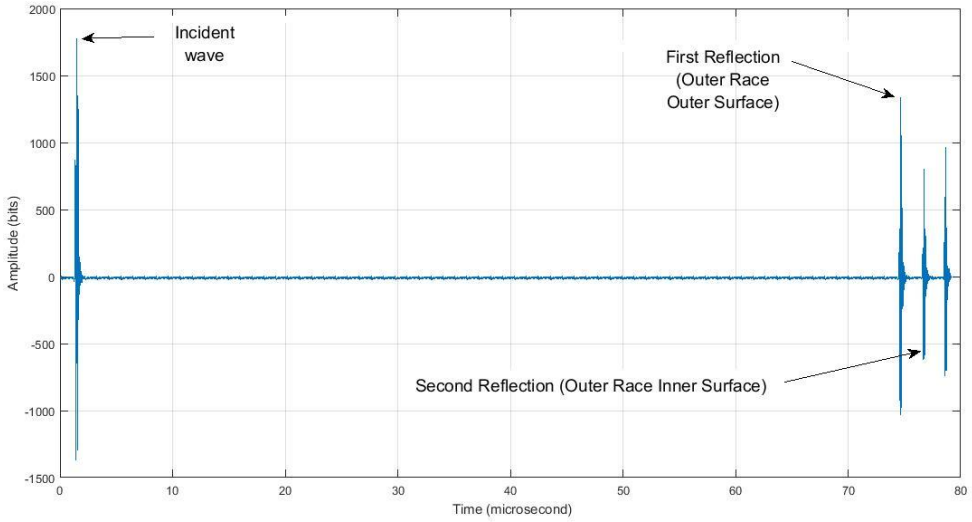

Figure 3.5 Ultrasound reflections in bearing interface

However, this interface is also the point where contact between the outer race and rolling elements occurs, and with the passing of each rolling element, a time shift was observed in the reflected waves.

When a rolling element is directly under the focus transducer, the outer race is compressed and pushed in the direction of the probe and hence the water path is shortened. Figure 3.6 illustrates this event. Once the rolling element passes the examined area, the outer race is reinstated back to its previous, normal position. This deflection event has been observed clearly because the investigated area is partially unsupported due to the 14 mm diameter hole in the cartridge that was required to accommodate the ultrasound immersion transducer. The deflection of the outer race and the consequent water path distance shortening means that the reflection from the water-outer race surface interface will occur before (less distance to be travelled by the waves to get to the interface) and hence, this is exhibited by the reflections in a leftward shift in the time domain.

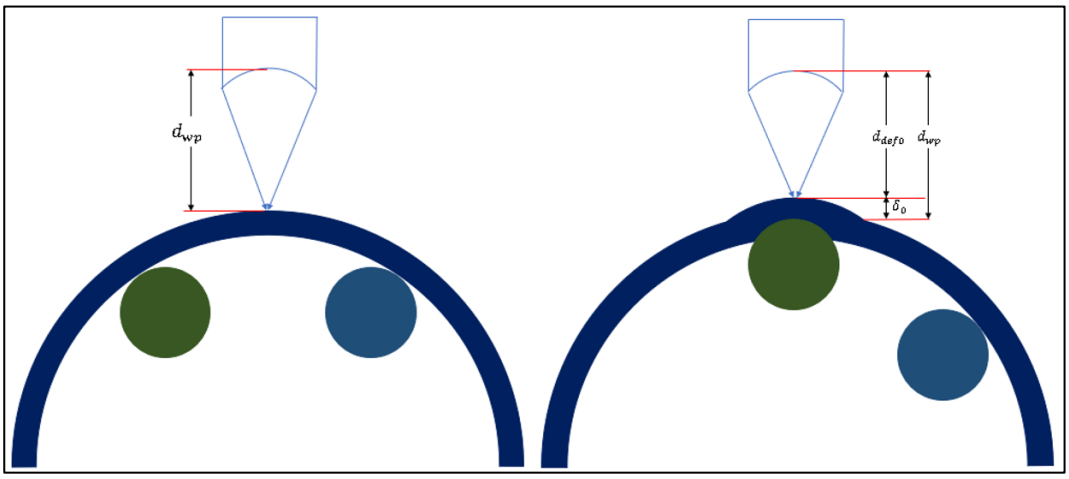

Figure 3.6 Bearing outer race deflection schematic

In this work, it has been found that the amount of outer race displacement is directly related to the applied load – when the bearing is healthy and without micro subsurface cracks. Impurities and invisible cracks weaken the outer race which would result in the race incurring higher displacements.

The reason why a race sustains deflection lies in a changing load distribution: the stress distribution within the outer race changes with the passing rolling elements. An applied radial load on the bearing compresses the outer race, but while the rolling element is at the contact point, a normal force in the reverse direction is exerted on the outer race. Since the rolling elements are constantly rotating within the bearing, these deflections occur cyclically, subjecting the outer race to fatigue.

Knowing the speed of sound in water and the time shift of the first reflection, the outer race deflection can be calculated. Since the first reflection travels only through water, these calculations are not affected by the acousto-elastic effect – which is a change in the speed of sound in a material under stress. This independence from the acousto-elastic effect is a characteristic that makes the measurements of the bearing outer race surface displacement less complex.

3.3.1 Reflection wave time-shift determination in time domain

A series of reflections within a time domain, such as those in Figure 3.5 is referred to as an A-scan. Time-shift measurements consist of determining the amount of movement of the reflections in the time domain of the A-scan data, where most of the information about the outer race deflection can be obtained from the first and second reflection waves.

The time difference between the incident pulse and first reflection can be used to find the distance between transducer and bearing outer race as illustrated by Equation 3.9. This measurement is also used for calibration of transducer, because this distance and the speed of sound in water are both known.

$$d_{wp} = 0.5ct_{td} \tag{3.9}$$

Where in formula d_{wp} is the water path distance, c is the speed of sound in the water, and t_{td} is the time difference between incident pulse and first reflection.

After calibrating the immersion transducer, the occurring time shifts can be calculated using time-of-flight measurements. There are several methods to perform these measurements, example of which are: sing-around, pulse-overlap, peak-to-peak, cross-correlation, phase spectral method, Hilbert transformed and zero-crossing method (Mason and Thurston, 1964; Thompson and Chimenti, 2012). In this research, the most precise and most sensitive method, the zero crossing method, has been employed for the measurements.

3.3.1.1 ToF and time shift determination by Zero-Crossing method

The time difference between two consecutive reflections in an A-Scan can be calculated by determining the difference between the two points which cross the zero amplitude line after the first crest of the reflection waves. As can be seen from the following figure, these points are in the same phase. The first data point which intersects the horizontal zero line after first crest of the first reflection is identified as the starting point of the ToF (time of flight) distance, and the corresponding zero crossing point of the second reflection is referred to as the finishing point of ToF distance.

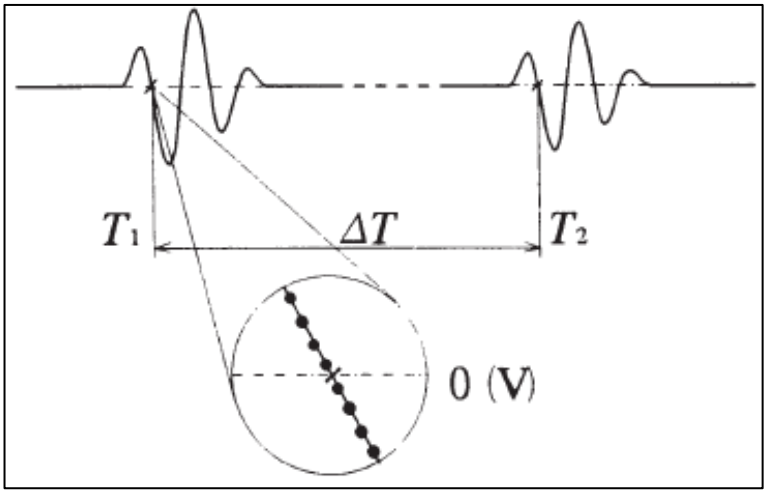

Figure 3.7 Zero-crossing method (Fujii and Kawashima, 1995)

3.4 Conclusion

This chapter commences by a review of bearing force-deformation relationship. This is followed by an in-detail discussion and comparison of bearing deformation theories. Finally, the principle of the proposed method to measure bearing outer race surface displacement is introduced briefly.

4 ROLLING ELEMENT BEARING FAILURE MECHANISMS AND DETECTION METHODS

In this section, bearing failure modes and their causes will be presented. This shall be followed by a comparison of the currently available bearing condition monitoring methods and their defect severity detection capabilities. Finally, the monitoring method under investigation in this project shall be evaluated and compared against the already existing methods.

4.1 Bearing failure analysis

The bearing is often a key component in the assembly in which it is located and its failure can lead to a catastrophic failure of the whole system, which other than the obvious economic consequences, may also lead to serious accidents. It is thus easy to understand why a lot of work has been done in failure mode analysis in an attempt to help identify the cause of the failure and subsequently, to prevent its reoccurrence.

Amongst the various bearing failure mode analysis guides that are readily available (as most bearing manufacturers provide their own guide), is the ISO 15243 (International Organisation for Standardisation, 2017), first drawn in 2004, but which has been superseded in 2017. In this document, in service failure modes are classified into 6 different modes, each with subdivisions. Definitions, characteristics, images and possible root causes are provided. The following table, compiled by ISO 15243 aptly summarizes this standard.

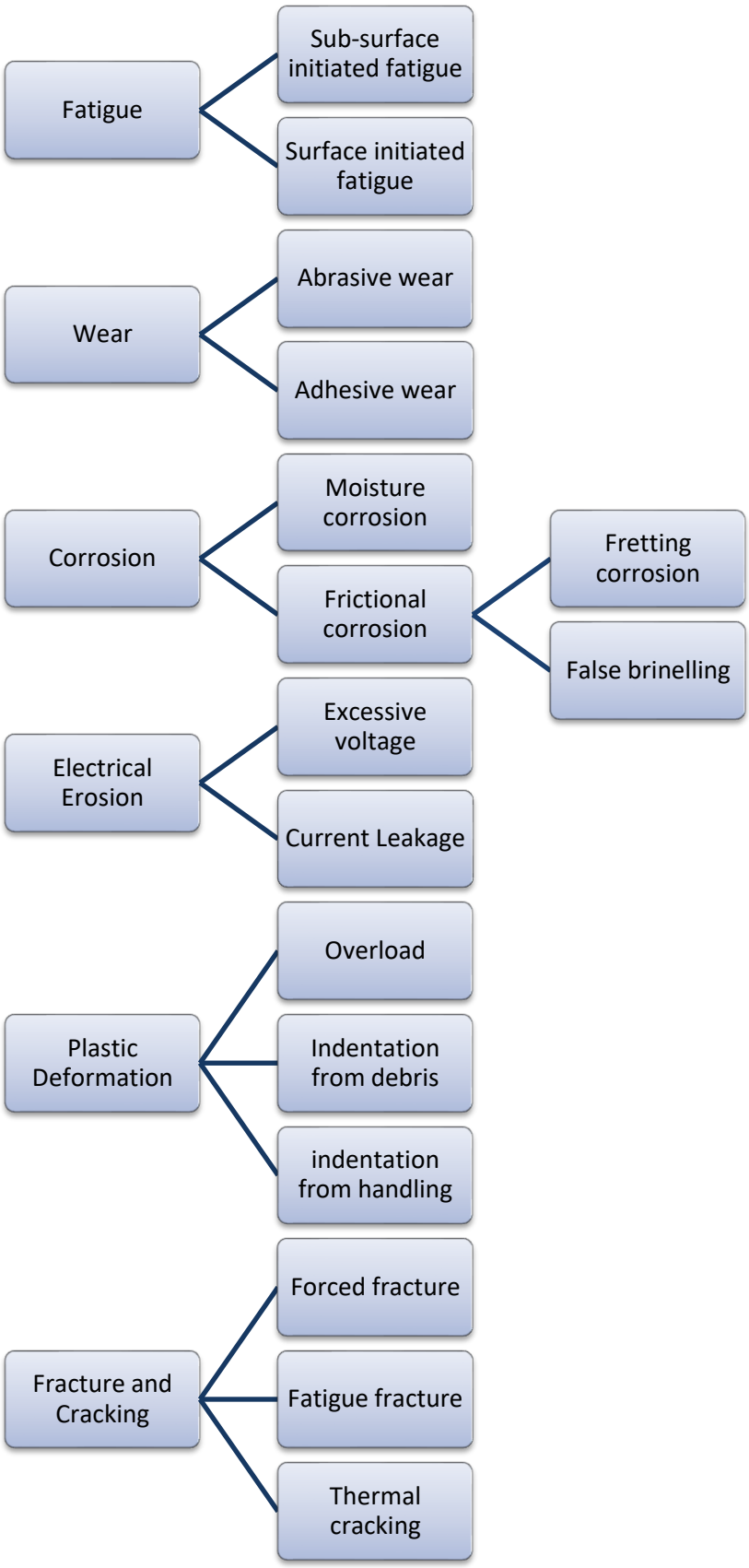

Table 4.1 Bearing damage classification (International Organisation for Standardisation, 2017)

4.1.1 Rolling contact fatigue

The repeated stresses incurred by the contacting surfaces of the bearing (inner raceway, outer raceway or balls) can result in fatigue failure, which generally manifests in spalling, i.e. the removal of material from the surface.

A fatigue failure may have its initiation point at the surface or at a subsurface point. In the latter, as explained by the Hertzian theory, a microcrack can develop below the surface as a result of a build-up of plastic strain that is accumulated from repeated loading cycles. Spalling occurs once the crack propagates to the surface. Since the load incurred by the bearing would have been considered during the design stage, a subsurface crack in practice, is unlikely unless the bearing experiences some abnormal loading. A more probable scenario is the formation of a microcrack that is caused by an impurity in the steel.

On the other hand, a surface initiated crack can form when the surface is distressed. In many instances, this occurs as a consequence of inadequate lubrication; when the lubricating film fails to prevent contact of the asperities of the mating surfaces, plastic deformation which would lead to microcracking and eventually spalling will be incurred. In instances when the lubrication is sound surface initiated fatigue may take place when indentations in the surface – caused by foreign particles, extreme loads or handling, have protrusions that exceed the oil film thickness, and hence come into contact with the asperities from the interacting surface.

4.1.2 Wear

Wear is damage, in the form of material removal, which is incurred by a contacting surface as a result of the acting mechanical forces. It is generally divided into two classes: adhesive or abrasive.

4.1.2.1 Abrasive wear

Abrasive wear is material removal from a surface through the action of hard particles – which can be contaminants or oxidised spalled fragments from the same surface – ploughing through the softer material. Depending on the nature of the particles, the surfaces usually become dull, however, a polishing effect may prevail if the particles are very fine. The affected areas are generally the raceways, rolling elements and the cage as indicated in Figure 4.1.

Figure 4.1 Abrasive wear on the bearing inner race (Timken, 2011)

4.1.2.2 Adhesive wear

Under loading conditions, the contacting asperities are under high stress conditions and deform, increasing the contact area, until the load can be supported. An interfacial bond that is stronger than any of the interacting materials may form and any further movement (sliding) can cause shearing away from the (welded) interface, thereby resulting in material transfer, temporary or permanent, from one of the surfaces to the other.

Smearing is a form of severe adhesive wear and occurs because of inadequate lubrication. It is typically observed between rolling elements and raceways, but can also take place in other locations such as rib faces, and at the ends of the rollers. Figure 4.2 shows an example of smearing on an outer raceway. Even the slight movement (creep) of the bearing with respect to its seating may lead to smearing on the bearing bore and housing seat, if lubrication is not sufficient. Scuffing (smearing) can occur suddenly and may result in seizure of the bearing.

Figure 4.2 Adhesive wear on the inner race (Tallian, 2006)

4.1.3 Corrosion

Corrosion is the deterioration of material through chemical action. It falls into two broad categories: moisture corrosion and frictional corrosion, the latter of which further subdivides in fretting corrosion and false brinelling.

4.1.3.1 Moisture corrosion

Condensation from atmosphere, water from lubricants (or degraded lubricants), or contamination, enable moisture and other aggressive media to come into contact with bearing components. Subsequent to such exposure, oxidation or other chemical reactions, such as the formation of rust can take place, resulting in pitting and eventually spalling.

The bearing is most susceptible to corrosion when it is at a standstill and the water settles around the rolling elements. Hence, as shown in Figure 4.3 deep-seated rust tends to show in dark greyish streaks across the raceways, in distances corresponding to rolling element positions.

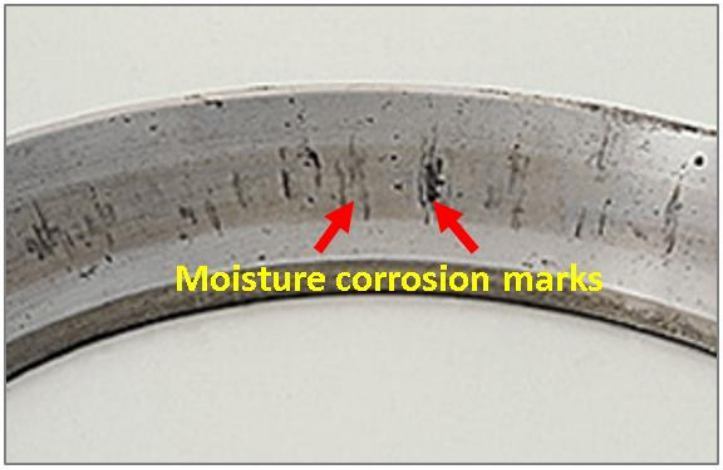

Figure 4.3 Moisture corrosion on the outer race of bearing (NTN Corporation, 2001)

4.1.3.2 Frictional corrosion

Frictional corrosion is a chemical reaction that occurs at contacting surfaces when the bearing is stationary (not rotating). Small relative motions, such as vibrations, cause the mating surfaces to oxidize, resulting in loss of material in powdery particles.

4.1.3.2.1 Fretting corrosion:

Fretting corrosion is damage incurred by contacting surfaces undergoing oscillating micromovements whilst transmitting loads. For example, fretting corrosion can be found

between bearing rings and shafts or housings when the fit is too loose. Typically unlubricated, the leading corrosion mechanism is oxidation and for steel components this yields reddish debris and similarly coloured rubbing surfaces.

4.1.3.2.2 False brinelling:

False brinelling, like fretting corrosion, occurs as a consequence of small oscillatory movement, however, unlike fretting corrosion, it takes place at the rolling element-raceway interfaces, where under certain conditions, the lubricant is prevented from providing adequate lubrication, resulting in corrosion. The raceway hence incurs discoloured depressions that replicate the shape and pitch of the rolling elements as illustrated in Figure 4.4.

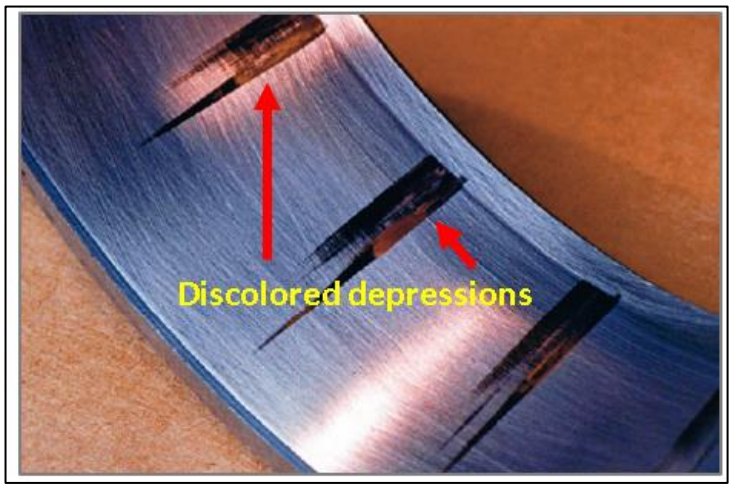

Figure 4.4 False brinelling and fretting corrosion on the bearing outer race (Errichello, 2004)

4.1.4 Electrical erosion

Electrical erosion is defined as material removal or incurred changes in microstructure as a result of a damaging electrical current. Such a current may be a singular incident of an excessive current magnitude, or of a smaller size but over a prolonged period in the form of a current leak. Damage caused by electrical erosion on an outer raceway and ball bearing can be seen in Figure 4.5.

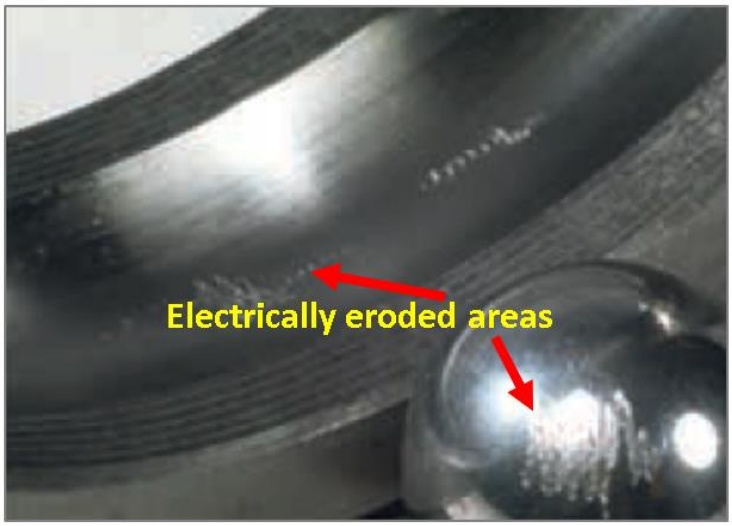

Figure 4.5 Electrical erosion on the outer race and ball bearing (International Organisation for Standardisation, 2017)

4.1.4.1 Excessive current erosion

When an electric current passes from one ring to another through the rolling elements, it is passing through a small contact area, causing localized heat in a very short time interval. The magnitude of the current will determine the heat incurred, which start being damaging upon exceeding 200°C – at which temperature annealing of the rings and rolling elements start occurring, leading to loss in hardness and the eventual premature bearing failure.

In extreme cases, heating may cause the contact area to melt and weld, resulting in a series of craters of diameters up to 500µm (electrical pitting). Such damage usually manifests on both rolling elements and raceways.

4.1.4.2 Current leakage erosion

In the presence of a continual flow of current, even if this has a low intensity, many shallow craters of microscopic dimensions form in very close proximity to each other. Eventually, these will develop into fluting (parallel ridges and grooves) on the raceways (Figure 4.6) and rolling elements. Ball bearings do not form flutes, but show discolouration which under microscopic inspection reveal craters.

An electric current also damages the lubricant; which will darken in colour, harden in consistency, and fail to provide adequate lubrication – leading to other forms of failure already discussed.

The extent of the damage caused depends on factors such as current intensity and duration, bearing load and speed, and the lubricant.

Figure 4.6 Fluting on the inner race (Humbert, 2008)

4.1.5 Plastic deformation

Plastic deformation is the permanent deformation or change that is incurred by a material under the action of some load, after the yield strength has been exceeded.

A bearing can incur such a failure on two different levels: on a macroscopic scale – when the load incurred by the rolling element and raceway contact is excessive, or on a microscopic scale – when a foreign particle gets rolled over between the ring and the rolling element and yielding occurs within the contact area.

4.1.5.1 Overload deformation

This type of deformation tends to occur more when the bearing is stationary, and is often the result of severe impact (ex. dropping bearing), incorrect mounting (ex. using a hammer), or excessive preloading. Figure 4.7 shows an example of heavy impact on the bearing. Whenever the load sustained by the bearing is large enough to exceed the elastic limit of the raceways, plastic deformation occurs at the contact areas, leaving depression marks in positions corresponding to the rolling elements. This form of damage is also referred to as true brinelling and distinguishes itself from false brinelling or electrical fluting from the surface finish or residual machining marks within the indents.

On the other hand, an excessive load incurred during operation manifests itself in different ways, depending on the particulars of the case. For example, an instantaneous overload can form flutes with additional individual, non-symmetrical and extended marks or it can form depressions in a pitch corresponding to that of the rolling elements. In contrast, when the excessive load is constant, plastic deformation occurs macroscopically across all of the overloaded area of the ring.

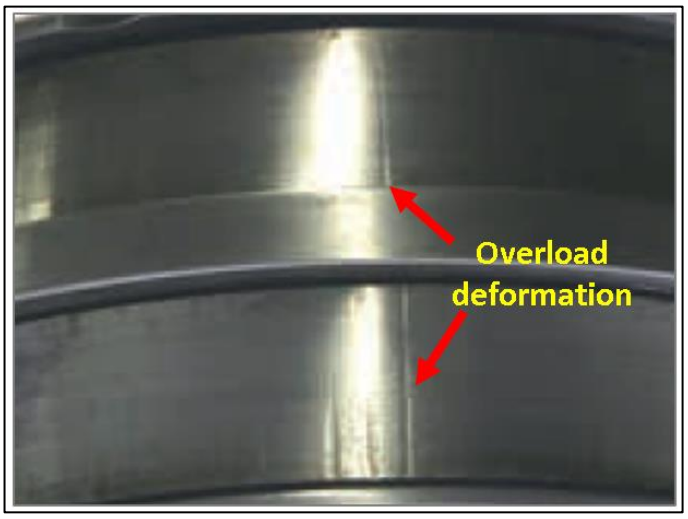

Figure 4.7 Overload deformation (International Organisation for Standardisation, 2017)

4.1.5.2 Indentation from particles

Over-rolled particles from debris or oil film contamination will plastically deform the raceway and rolling elements during contact – as can be seen in the raceway shown in Figure 4.8. The resulting indentation depends upon the nature of the particles, whereby the harder the particles, the more severe the damage. Moreover, fatigue and subsequent

spalling may also be incurred as indentation shoulders incur a reduction in film thickness and higher load concentrations.

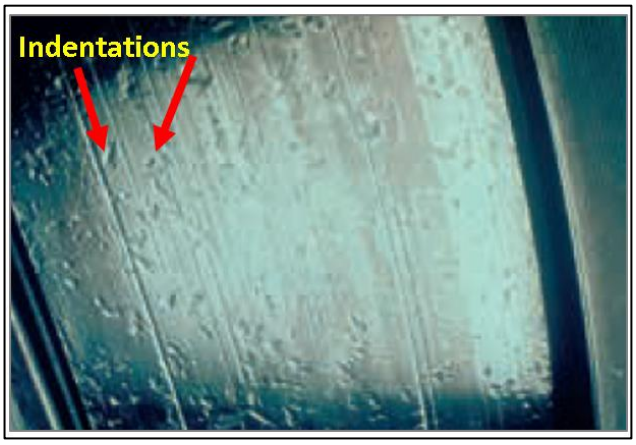

Figure 4.8 Indentation scars on the bearing outer race (International Organisation for Standardisation, 2017)

4.1.6 Cracking and fracture

Cracks initiate at points of high stress concentrations and propagate, i.e. advance within the material, until the component fails by fracture, which is a term that is used to signify separation of the body into two or more parts. An example of such a crack can be seen in Figure 4.9. The ISO standard subdivides fractures in bearings into 3 kinds: forced fracture, fatigue fracture and thermal cracking.

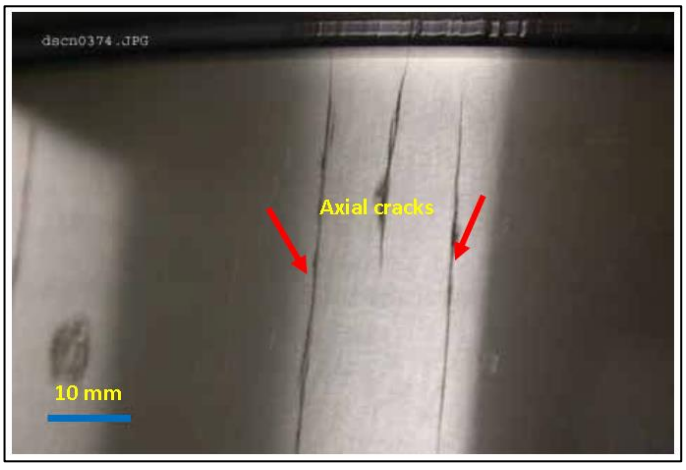

Figure 4.9 Axial crack on the inner race (Tallian, 2006)

4.1.6.1 Forced fracture

A forced fracture is the result of a stress concentration that exceeds the tensile strength of the material. In other words, it occurs when the bearing is subjected to excessive loads / stress. Most commonly, such over-stressing happens as a consequence for rough handling (impact) during mounting or dismounting. Another example that can lead to fracture is excessive interference fit.

4.1.6.2 Fatigue fracture

In components experiencing bending, tension or torsion, cracks can develop at some high stress point. Such a crack would propagate in increments with each additional stress cycle and upon exceeding a critical crack size, crack propagation accelerates significantly and the component, typically a ring or cage, fails by fracture.

4.1.6.3 Thermal cracking

Sliding motion on the inner or outer ring of a bearing gives rise to high frictional heat. In such situations cracks perpendicular to the sliding direction appear on the contacting surfaces. Hardened steels are especially susceptible to such form of cracking due to the generated heat affecting their heat treatment, causing local rehardening and residual stresses. Sliding can result from incorrect seating that would allow certain components, such as the backing rings or the end caps to turn and slide against the rings.

4.2 Wind Turbine Bearings Damage Types

The most commonly observed types of failures in wind turbine bearings are axial cracking, spalling, flaking, smearing and micro pitting (Herr and Heidenreich, 2014). These failures result in material loss (removal) in bearing components and eventually catastrophic failure. The proposed method can detect the defects when the material loss propagates in an axial direction (form of line) and when the size of the defect exceeds the detectable minimum defect size of the method (0.36 mm). The employed method in the project may therefore detect defects at early stages since sub-millimeter sized defects are accepted as incipient defects (Tra *et al.*, 2017)

Figure 4.10 (a) and (b) show how axial cracks and spalling develop into line shaped defects. Figure 4.10 (c) shows a simulated defect representing such defects.

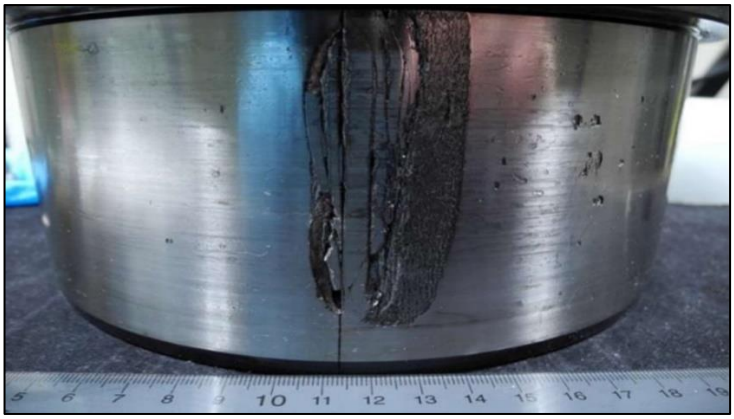

a) Crack initiation and develop in wind turbine high speed bearing inner race

b) Spalling develop into line shape (230/600 series spherical roller bearing inner race) (Kotzalas and Doll , 2010)

c) Simulated line defect

Figure 4.10 Real bearing defects and simulated defect

4.3 The bearing life

The life of a bearing can be described by the how many revolutions can be performed before the first evidence of failure develops. The *basic life* of a bearing, as defined by ISO 281 is a measure that gives the total number of revolutions that 90% of apparently identical bearings can undertake or exceed without failure under the same working conditions. This figure is also known as the L_{10} life, because 10% of the population of bearings are estimated to fail before reaching this value as shown by Equation 4.1 (International Organisation for Standardisation, 2007).

$$L_{10} = (C/P)^p \tag{4.1}$$

Where L_{10} is the *bearing rating life* (or *basic life*), at 90% reliability, in one million revolutions; C is the basic dynamic load capacity, for a rating fatigue life of one million rotations; P is the standardised dynamic equivalent load (combination of axial and radial load) of the bearing; and p is the life equation exponent, which is $10/3$ for a cylindrical rolling element bearing. The equation, which forms the basis of prediction of the bearing life has been developed by Palmgren and Lundberg (1947).

However, extensive studies on the fatigue life of a bearing have that the basic life rating equation required improving: material quality, effects of operating conditions and lubrication needed to be taken into consideration to make bearing life estimation more accurate as illustrated by Equation 4.2. Hence, a statistical model based on a vast amount of experimental data was developed (Zaretsky, 1992; Jendzurski, T. and Moyer, 1997; Harnoy, 2003).

$$L_{na} = a_1 a_2 a_3 L_{10} \tag{4.2}$$

Where L_{na} is the adjusted rating life and a_1, a_2 and a_3 are the reliability factor, material factor and environment factor, respectively.

The reliability factor , a_1, converts L_{10} values to different reliability percentage values, if this is desired. For example if a reliability of 99% is required, a_1, assumes the value of 0.21. Other values for a_1 and the corresponding reliability percentages are given in Table 4.2.

Reliability (%)	L_n	a_1
90	L_{10}	1
95	L_5	0.62
96	L_4	0.53
97	L_3	0.44
98	L_2	0.33
99	L_1	0.21

Table 4.2 Reliability for factor a_1, reproduced from (NTN Corporation, 2001)

Material factor a_2, is related to the bearing materials' metallurgical properties, production method, material purity, applied heat treatments and coatings which directly affect the bearing fatigue life.

Environment factor a_3, relates to bearing operational conditions such as rotation speed, applied load, operation temperature, lubricant properties such as lubricant thickness, contamination and viscosity (Khonsari and Booser, 2008; Harnoy, 2003).
American Bearing Manufacturers (ABMA), SKF (Svenska Kullagerfabriken AB), and the International Organization for Standardization (ISO) are all examples of bodies that have published bearing life prediction standards. However, the latter is the most extensive and gives in depth consideration for lubrication, contamination, load and fatigue stress limit. For this reason, it shall be explained briefly.

ISO 281, provides Equation 4.3 for the *modified rating life* L_{nm}, whereby the material factor and the environment factor were replaced by the *life modification factor*, a_{iso};

$$L_{nm} = a_1 a_{iso} L_{10} \tag{4.3}$$

The life modification factor (a_{iso}) as shown by Equation 4.4 shows a relationship that includes the contamination factor, e_C, viscosity ratio, κ, fatigue load limit, C_u, and dynamic equivalent load, P. It is the consideration of these variables that make the

modified rating life a more accurate prediction than the basic life. The document explains how each of these Figures can be derived.

$$a_{iso} = f\left(\frac{e_C C_u}{P}, \kappa\right) \tag{4.4}$$

The standard also provides a table (reproduced as Table 4.3) with values for the reliability modification factor, a_1, which converts the L_{10} values into figures of higher reliability levels, should this be desired.

Reliability (%)	**L_{nm}**	**a_1**
90	L_{10m}	1
95	L_{5m}	0.64
96	L_{4m}	0.55
97	L_{3m}	0.47
98	L_{2m}	0.37
99	L_{1m}	0.25
99.2	$L_{0.8m}$	0.22
99.4	$L_{0.6m}$	0.19
99.6	$L_{0.4m}$	0.16
99.8	$L_{0.2m}$	0.12
99.9	$L_{0.1m}$	0.093
99.92	$L_{0.08m}$	0.087
99.94	$L_{0.06m}$	0.080
99.95	$L_{0.05m}$	0.077

Table 4.3 Life modification factor for reliability, a_1,(International Organisation for Standardisation, 2007)

4.4 Bearing condition monitoring methods

Bearings are vital machine components in many industrial applications such as wind turbines, motors, heavy machinery, automotive and railway applications. Such extensive usage of bearings added weight to the reliability issues incurred, because any engineering system's integrity relies on the robustness of its components. This stimulated advancement in the techniques which are used to monitor bearing conditions. To assess a bearing's health, parameters that significantly affect damage occurrence and propagation, such as critical elements' temperatures, vibration, lubricating oil conditions and displacements can be monitored through the use of different kinds of sensors. In this section, a review of bearing failure detection sensors and development of their diagnostic capabilities by signal processing methods will be introduced.

4.4.1 Temperature monitoring

Machine elements whose function involves contacting surfaces that slide or roll against each other, such as gears and bearings, incur frictional forces which generate heat and a consequent rise in temperature. In bearings, the temperature is generally maintained constant through the use of a lubricant of micrometer sized thickness that reduces the friction coefficient and asperity interactions between the mating surfaces. A bearing would experience a rise in temperature in instances when: an increase in friction force between the contacting surfaces takes place, bearing components interact with the cage, or lubricant hydrodynamic resistance or seal friction are high (Stolarski and Tobe, 2000).

The main reason for an increase in the friction force is depletion of the lubricant in the contact are that results in the conversion of elastohydrodynamically lubricated contacts to boundary conditions (steel-to-steel) contacts. After lubricant break down, the asperities on the mating surfaces of the bearing components come into contact and the bearing temperature starts increasing at local areas (Nagaraj *et al.*, 1978).

Monitoring of bearing temperature can therefore give information about bearing health but the method's diagnostic abilities are limited, because only well developed defects, often just before catastrophic consequences, can be detected by using the method. Detection an impending failure is difficult (Watson *et al.*, 2007; Randall and Antoni, 2011). On the other hand, the method is standardized; it is able to detect anomalies and

it can be used as a secondary verification failure detection method (complementary tool) (Jammu and Kankar, 2011; Moussa, 2014).

There are two types of sensors to measure bearing components' temperature; direct sensors and indirect sensors. Direct sensors, such as resistance temperature detectors and thermocouples, are required to mount to the monitoring components as close as possible to measure temperature. Thus, bearing housing equipment needed to be disrupted to provide surface for sensor mounting and this situation result in weakening of bearing structural integrity and decreasing bearing load carrying capacity. Examples of studies that have monitored bearing conditions by using thermocouples are those of (Read and Flack, 1987; Glavatskih, 2004).

On the other hand, indirect sensors such as thermal and infrared cameras, are non-contact temperature measurement devices. They detect heat (infrared) energy and convert it to electronic signals. Processed signals compose the thermal image of the monitored component and temperature can thus be calculated. Although, defect existence has been detected using thermal imaging of bearings via the infrared techniques, physical bearing damage severity and lubricant failures have not yet been diagnosed very well. This is because bearing temperature varies with bearing working conditions such as speed, load, ambient temperature and runtime; for this reason, bearing temperature increases could not be related to just bearing failure and lubricant problems. Addressing an increase of temperature would therefore not be easy. However, some recent works (Kim *et al.*, 2012; Singh *et al.*, 2014; Moussa, 2014), believe the method has promising potential for detecting failures.

4.4.2 Lubricant properties and wear debris in lubricants monitoring

The lubricant in rotary machine elements such as gears and bearings, separates the contacts, thereby reduces friction force, wear and the associated consequent local point temperatures. Moreover, oil circulation and filtration enables the removal of any wear debris that would normally cause further harm. The lubricant therefore plays a vital role in bearing and rotary machines. However, after a certain amount of running time, the lubricant gets degraded and its physical and chemical properties, such as viscosity, density, acid content, and contamination (metal, water…etc), change making it more difficult to maintain separate the contacts. Thus, a deteriorated lubricant leads to

deterioration of the bearing and vice versa. Monitoring oil property changes and contamination levels can therefore give information about bearing health conditions and the remaining useful time of the bearing.

Ensuing is an outline of observable lubrication oil parameters and the monitoring methods that can be employed.

Viscosity Monitoring: Viscosity can be simply defined as liquid's resistance to flow. Oil strength and contact separation abilities are directly related to oil film viscosity, whereby high viscosity oil prevents adequate flow, and low viscosity oil struggles to separate the contacts. Hence oil aging can be determined from its thinning or thickening, where even relatively small changes, like 10-20%, effect significantly oil degradation (Wang and Gao, 2006). Viscosity measurements can be performed by viscometers or rheometers. Portable oil diagnostic systems (PODS)(offline) in addition to viscosity measurement, can also measure wear debris concentration and oil temperature. Furthermore, recent studies have shown that viscosity can be measured by using ultrasonic sound waves (Schirru, 2017).

Acid Content: Acid content in the lubricants results from the usage of a wrong type of oil, the existence of acidic contaminants, oxidation, and alkaline reserve depletion. Acidity triggers corrosion and this leads to increased wear rates. The acid portion in a lubricant can be measured by offline titration tests and viscometers (Appleby, 2010).

Oil Contaminant/Wear Debris Monitoring: Wear particles can appear in bearing lubricant after any part of bearing component is degraded. Monitoring of wear particles in lubricant can give information about bearing health conditions and remaining useful time of bearing (Wang and Zhang, 2005).

Wear debris monitoring is generally employed as a complementary method in conjunction with other monitoring techniques. There are various debris monitoring sensors and techniques that can be used for machine element condition monitoring; some of these are spectrographic analysis, inductive and capacitive sensors, magnetic plugs, ferrography, and ultrasonic and acoustic techniques. These methods focus on determining wear particle morphology and concentration in order to assess the machine element failure. They differ from one another in measurable size limitations (size of particles detected), sampling methods, working environment and applicable area. The following table, summarizes and compares the different sensors on these grounds (Dan, 2013).

Product	In-line/On-line	Technology used	Measure
Smart® Zapper Electric Chip Detector	In-Line, On-Line	Magnetic collection/grip	Particles ≥ 100 μm
QDM® (Quantitative Debris Monitor)	In-Line, On-Line	Magnetic flux	Particles ≥ 50 μm
TechAlert™ 30	On-Line	Magnetic flux	Particles > 1 μm
TechAlert™ 20	In-Line, On-Line	Magnetic flux	Particles > 1 μm
TechAlert™ 10	In-Line, On-Line	Magnetic inductance	Particles > 50 μm
TechAlert™ TA Diviner	In-Line	-	Water
MetalSCAN	In-Line	Magnetic inductance, magnetic flux	Part. ferro ≥100 μm Part. No-ferro ≥500 μm. Total contamination
PATROL®	In-Line	Magnetic inductance, magnetic flux	Particles ≥ 25 μm
MIDAS	On-line, off-line	Magnetic inductance, magnetic flux	Ferrous Particles
Grid Switch®	On-Line	Magnetic collection switch/grip	Wear Particles
ANALEXrs Oil Condition Sensor	On-Line	Dielectric loss factor	Oil condition
ANALEXrs Particle Content Sensor	On-Line	Inductive coil	Particle content
ANALEXrs Total Ferrous Debris Sensor	On-Line	Magnetic inductance	Ferrous debris
Lubrigard Oil Condition Sensor	On-Line	Dielectric loss factor	Soot, Oxidation products, Water, Glycol, Metallic wear particles, Changes in TBN
FluidScan	On-Line	FTIR	TAN,TBN; oxidation, water, glycol, soot, nitration, sulfatation, additives AO, AW and contamination with other oils
OILPro	On-line	X-ray, IR,	TAN, TBN, Cleanliness, oxidation, Viscosity, water, fuel, wear metal
Debritect DT100/200/300	On-line	Magnetic	Submicron and greater / Water and Moisture
Continental TEMIC	In-line	Dielectric	Oil temperature, level and quality
Fraunhofer Munich	In-line	Dielectric	TAN, TBN, oil quality
Fraunhofer Munich	On-line	Mid-IR	Water
Fraunhofer Munich	On-line	UV	Detection of fluids, gas and solids
MSC	Off-line	-	Water, wear, particle count and wear debris analysis
EESIFLO	On-line	Dielectric	Water
TRANSLUME	On-line	Optic	Oil quality
On-line Model 600T-LP	In-Line	X-ray fluorescence XRF	N/A
Laser Net Fines	On-Line/Off line	Laser imaging	Counters >5 μm. Shape classifier >20 μm
Oil-Line Sensor	In-Line, On-Line	Electrostatic collection	Particles ≥ 20 μm
CPD-DAQ Sensor and Software	Off-Line	Blotter analysis	N/A
RULER	Off-Line	Voltammetry	AO concentration
Rockwell Automation	On-line	Pore blockage	Viscosity, wear particles
Malvern	Off -line	Microscope	Measure size 0.5 to 1000 μm and identify shape
Schubert & Salzer	In-line	Ultrasonic	Particle detection

Table 4.4 Lubricant condition monitoring sensor types (Dan, 2013)

Wear debris monitoring is a useful method to identify failure of machine elements. The relationship between wear particle features and wear characteristics such as wear rate, type, severity, and source can be established (Roylance and Raadnui, 1994).

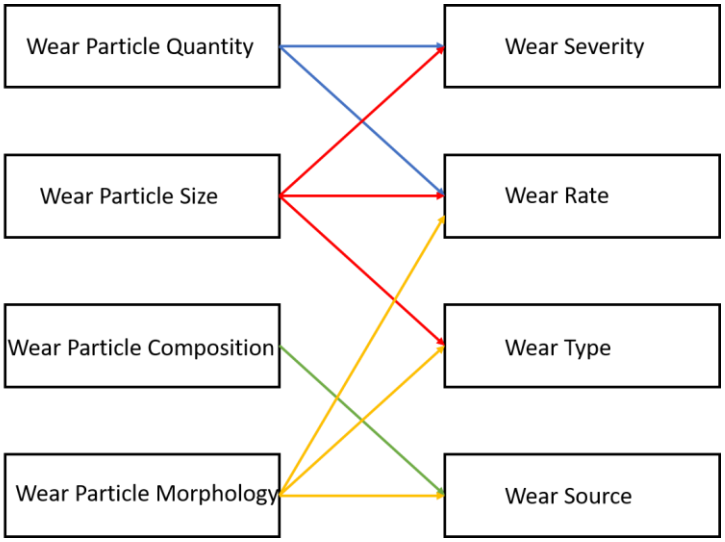

Figure 4.11 The connection between wear particle properties and wear characteristics (Roylance and Raadnui, 1994)

Although monitoring of wear debris in lubricants has been proven to be a highly informative technique that provides component health conditions and residual life expectancies, the method is time consuming due to the off-site and/or on-site laboratory work it involves. Moreover, when comparing the sensors employed to those used in vibration, acoustic emission and ultrasound methods, not only are latter less complex, but also allow automated online monitoring and data analysis more easily than wear debris monitoring ones.

In this section, temperature, oil and wear debris monitoring – all of which are complementary bearing condition monitoring methods, have been briefly discussed. In the next sections, the more major monitoring methods of vibration, acoustic emission and ultrasound shall be discussed in more detail.

4.4.3 Vibration monitoring

Vibration can be defined as an oscillatory movement of the bearing due to internal load distribution change while rolling elements pass the loaded area. There are several reasons why vibration in the bearing could increase; typically, manufacturing faults (surface imperfections), installation faults, defect existence and degradation of the bearing (Lacey, 2008). It has been proven that bearing vibration monitoring is a successful method for bearing defect detection, diagnosis and prognosis for many industrial applications, especially in wind turbines. (For instance, SCADA wind turbine condition monitoring). Moreover, vibration monitoring can be used for monitoring of other wind turbine components such as gearbox, shaft and blade health monitoring (Tautz-Weinert and Watson, 2017).

Vibration sensors, convert the physical movement of bearing, into electrical signals. The bearing's movement can be measured from acceleration, velocity or displacement. In most industrial vibration monitoring applications, the accelerometer is the most widely employed vibration sensor due to its wide frequency response. The sensor mounting position is a key point of the method and a sensor for each vibration direction expected must be installed. Generally, two sensors are employed, but when 3-D monitoring is required, 3-axis accelerometers are used.

A lot of effort has been made by researchers to develop signal processing techniques that obtain useful information, such as defect detection, assessment and remaining life prognosis from raw vibration data. These signal processing methods can be classified into three main groups: time domain, frequency domain and time-frequency domain.

Time domain signal processing methods analyse vibration data properties change in time; frequency domain methods analyse frequency content of the signal; and time-frequency domain signal processing techniques analyse the variation of the frequency content of vibration data in time.

These techniques are generally represented as shown in Figure 4.12. The fundamentals of these signal processing methods will be discussed briefly, since all the techniques are equally applicable to both vibration and acoustic emission data.

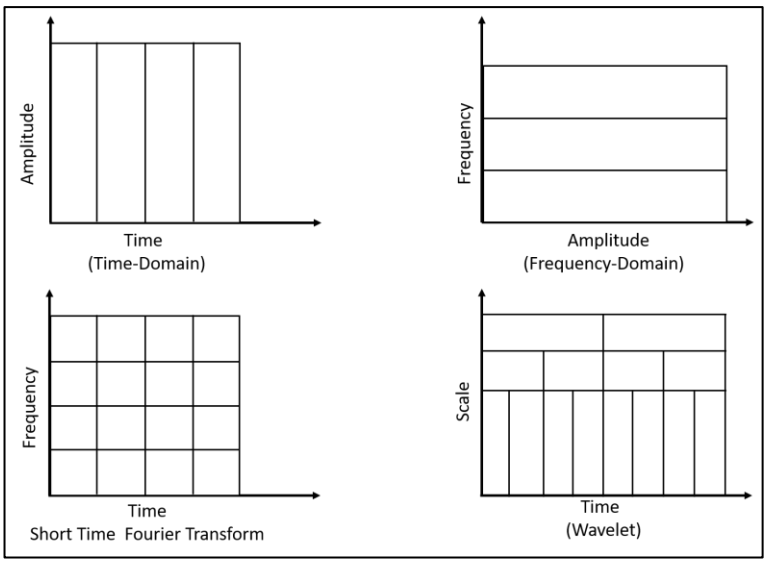

Figure 4.12 Representation of each type of domain

4.4.3.1 Time domain signal processing techniques

Time domain analysis demonstrates how the sensor data 'signal' changes over time. In the graphs, while one axis shows time, the other axis shows variations of physical signals. In the domain analysis, the signal is analysed statistically to find anomalies that would eventually result in bearing failure. A signal's statistical features, such as root mean square (RMS), peak value, kurtosis, and crest factor, change according to bearing health conditions. Also, shock pulse method analysis can be performed in the time domain: the impingements in the bearing contacts, trigger the transducer to oscillate at its resonant frequency. Thus, by monitoring the shock pulses, information on the health of the contacts can be obtained (Patidar and Soni, 2013; Vaishakh, 2015; Devendiran, 2016).

4.4.3.2 Frequency domain signal processing techniques

While the time domain graph shows a signal as it changes over time, frequency domain graphs exhibit the frequency content of the signal. It can be viewed as a conversion of the time function into a sum of sine waves at different frequencies as illustrated in Figure 4.13.

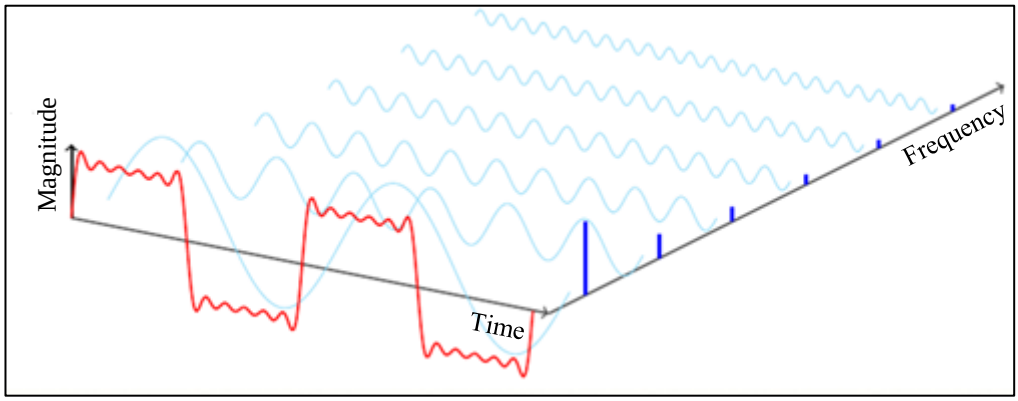

Figure 4.13 Time-frequency domain of the signal

The main reason for monitoring the frequency spectrum of a vibration signal, is to identify when and which of the bearing components has developed a defect from the short vibration pulse burst that is given off when the faulty bearing element impinges onto the mating surface.

Characteristic defect frequencies: Each bearing component has a different rotation frequency which depends on bearing geometry (number of rolling elements, contact angle) and operating conditions (shaft rotation speed). This characteristic enables identification of defected bearing components because these defects would product defect frequencies that show up as harmonics in the frequency domain graph of the component. The bearing elements defect frequencies can be calculated from Equation 4.5, 4.6 and 4.7.

$$f_{ir} = \frac{n}{2} f_s \left(1 + \frac{BD}{PD} cos\beta\right) \tag{4.5}$$

$$f_{or} = \frac{n}{2} f_s \left(1 - \frac{BD}{PD} cos\beta\right) \tag{4.6}$$

$$f_{re} = \frac{BD}{PD} f_s \left(1 + \left(\frac{PD}{BD}\right)^2 cos\beta\right) \quad (4.7)$$

Where f_{ir}, f_{or}, f_{re} are inner race defect frequency, outer race defect frequency, rolling element defect frequency, respectively; n is the number of rolling elements; f_s is the shaft rotation frequency; and BD, PD, β are roller diameter, bearing pitch diameter and contact angle between rolling element and mating surface respectively (Tandon and Choudry, 1999; Harris and Kotzalas, 2006). In order to find the frequencies, harmonics and periodicities of the defects, signals need to be processed by frequency domain methods such as the High Frequency Resonance Technique (HFRT), Cepstrum Method.

4.4.3.3 Time-frequency domain signal processing techniques

Although, a signal is assumed stationary in a Fourier transform analysis, it is non-stationary, and it comprises of time-varying frequency contents. This nature of the signal requires time-frequency analysis to obtain more comprehensive information from the vibration data (Singh, 2016). The time-frequency domain signal processing techniques can be classified as Short Time Fourier Transform (STFT), Wavelet Analysis.

4.4.4 Acoustic emission monitoring

This section provides general information about Acoustic Emission (AE) fundamentals and technology. It explains the capabilities of AE transducers for bearing defect diagnosis, common AE test parameters, AE features that are generally observed during tests and how these can be linked to defect size. Post processing methods applied to vibration signals are equally applicable to AE signals and since these have already been discussed, they shall not be reviewed again in this section.

Acoustic Emission is one of the non-destructive testing methods (NDT) which is being used increasingly in the structural integrity assessment field and in a vast number of industrial applications to detect, locate and assess the defects. Acoustic emissions are sound waves of a frequency that is over the audible range, between 100 kHz – 1 MHz, that spread from solid materials as a result of impact or structural integrity deterioration. In bearing applications, transient elastic waves can be detected from the interaction of a defected bearing component and its mating surface as it generates vibration (impact), or

from the rapid release of energy from bearing components which are under structural deformation (structural integrity deterioration) (Pao *et al.*,1979).
The transient elastic waves are received by piezoelectric transducers that convert the waves into measurable electric signals. These signals are then recorded, pre-processed and post-processed by computers.

A healthy bearing's raw acoustic emission data gives a steady trend (Figure 4.14 (a)), but while the bearing is deteriorating; i.e. whilst it is experiencing subsurface crack growth, dislocation, grain boundary sliding, precipitates or inclusion mechanisms, a burst emission (also called HIT), which has a start and an end point, with a significantly larger peak than steady signal data, is observed (Figure 4.14 (b)). Anomalies in AE data that arise from friction and bearing components' defect impingement can also be detected. For instance, a groove defect in the inner race will result in periodic acoustic bursts, at the frequency associated with the inner race, in the raw acoustic emission data (Jena *et al.*, 2012).

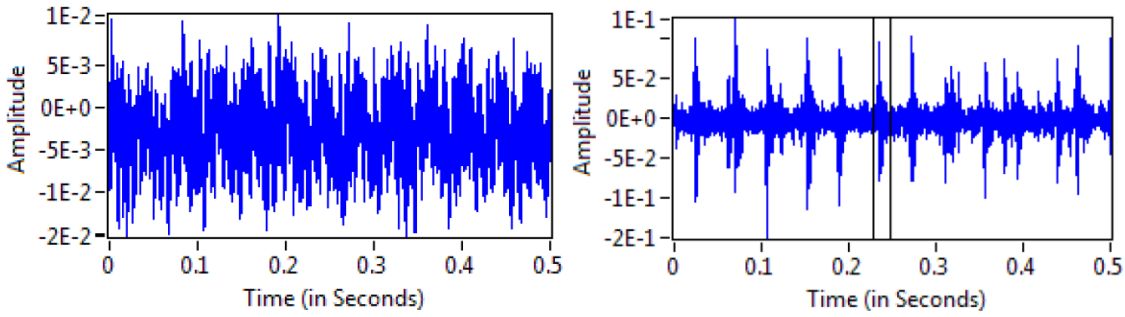

Figure 4.14 Acoustic emission raw data (a) Healthy bearing (b) Inner race groove (width 2.1 mm depth 1mm) (Jena *et al.*, 2012)

While the former type of anomalies, (i.e. those intrinsic to the material) are called primary AE sources, the latter, (i.e. those not originating from the material) are called secondary AE sources. By monitoring anomalies in AE data in the time domain and in the frequency domain, bearing defects can be detected and located, defect severity can be diagnosed and the bearing remaining useful time can be predicted. The post signal processing techniques which are used for vibration data analysis can be equally applied to the AE data for bearing monitoring. Moreover, AE burst characteristics such as rise time, decay time, ring down counts, burst amplitude, energy and duration (shown in Figure 4.14) can give additional information about bearing health condition (Caesarendra, 2015).

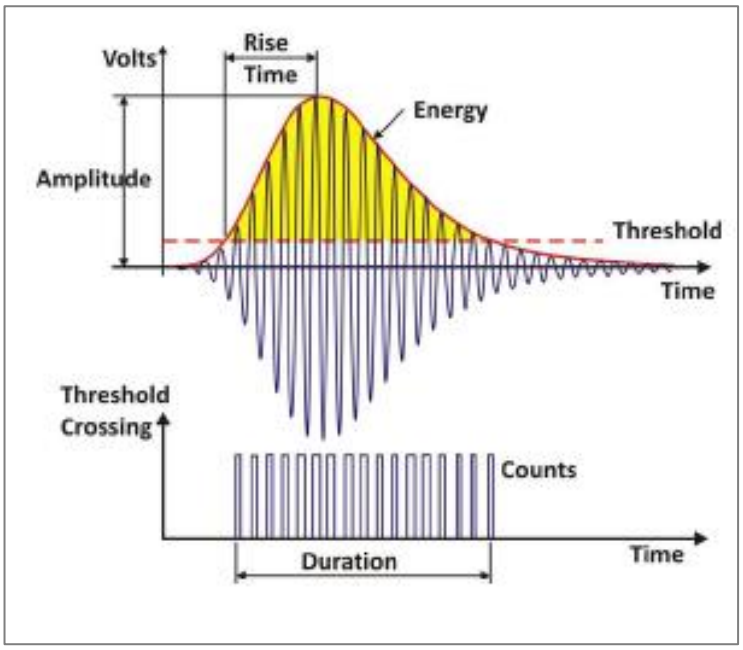

Figure 4.15 AE burst (HIT) characteristic properties representation (Caesarendra, 2015)

AE data containing anomalies, comprises of a superimposition of a continuous AE waveform and an AE burst. The latter can be described in several parameters (amplitude, ring down counts, duration, rise time, decay, and energy) all of which depend on the threshold – which is the background noise of the test rig. The amplitude is the peak of value of the AE hit, while the ring down counts are the number of times the threshold is exceeded in an event. The duration is the time difference between the first and the last threshold crossings. The rise time is the time difference between first threshold cross and the peak amplitude and the decay time is the time difference between the duration and the rise time. Finally, the energy can be defined as the area of the AE hit over the threshold (NDT Resource Center, 2017).

Researchers in this area have mainly focused on early stage defect detection (minimum detectable defect size), defect size correlation between AE parameters, and defect location determination by using AE sensors. Some of the studies compared AE and vibration sensors' defect diagnosis abilities for monitoring of natural bearing fatigue and artificially defected bearings. The relationship between defect size and burst duration has been validated only for outer race defects (Al-Ghamdi *et al.*, 2004; Al-Ghamd and Mba, 2006; Elforjani and Mba, 2010).

With regards to which of AE or vibration is the more sensitive method for defect detection, literature can be found to be confusing as there is disagreement between the few studies that have been conducted. For instance, while some researchers (Hawman and Galinaitis, 1988; James Li and Li, 1995; Nohal and Vaculka, 2017; Al-Ghamd and Mba, 2006; Mba and Rao, 2006; Tandon *et al.*, 2007) agree that AE is more sensitive than vibration, the studies of some researchers show that vibration sensors are more sensitive and can also detect smaller defects (Shiroishi *et al.*, 1997; Williams *et al.*, 2001). On the other hand, other studies have found that not only can acoustic emission sensors detect and measure defects at an early stage, but they can also determine a defect's location by measuring the signal's arrival time from source/s to multiple AE sensors at a known AE wave velocity (Yoshioka *et al.*, 1998; Elforjani and Mba, 2008).

More recent studies have focused on trying to develop signal processing methods (most of which had already been applied to vibration sensors), to increase sensor detection capabilities and obtain more precise defect size measurements, more accurate defect position determination and more accurate remaining useful time predictions. The aim has been to develop methods that could be applied across different working conditions (rotation speeds, subjected loads…etc). Also some research has been studying the feasibility of applying artificial intelligence systems to make decisions (e.g. to shut down the monitored bearing) based on the results of the collected and processed data.

Acoustic emission is a very good method to monitor bearing health conditions, as is evidenced by the advantages given above. However, its widespread applicability to wind turbine condition monitoring has been detained form its disadvantages of noise, high data storage requirements and high computational power requirement for signal processing.

4.4.5 Displacement monitoring

A body's shape varies (incurs displacements) when subjected to a force, and in a bearing environment, such displacements occur when the outer race is subjected to a radial and/or axial load, and a rolling element passes over the outer race. Displacements occur at the contact region, as indicated in the Figure 4.16.

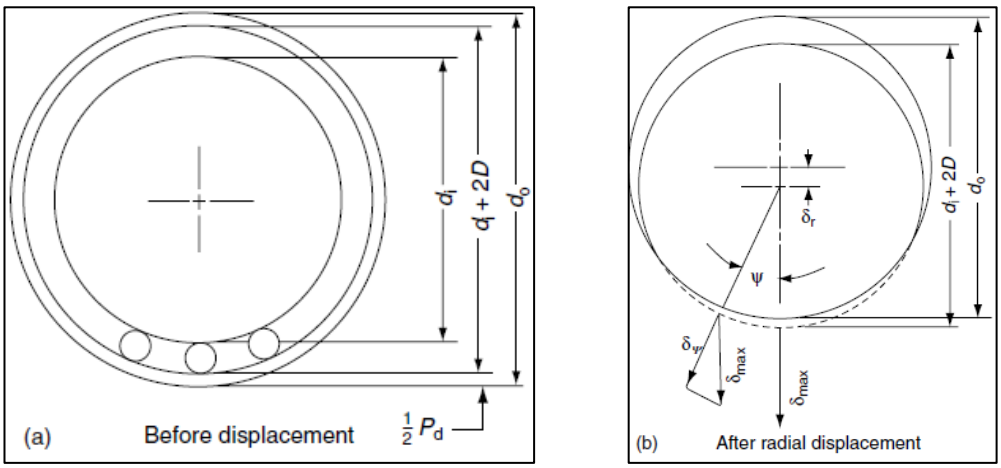

Figure 4.16 Bearing displacement (Harris and Kotzalas, 2006)

In bearing applications, outer race displacement can be measured by using non-contacting measuring devices (transducers) of which there are many kinds. For example eddy current transducers (Harker and Sandy, 1989; Yu *et al.*, 2002), fiber optics transducers (Juarez *et al.*, 2002; Conkey *et al.*, 2003), capacitance transducers (Yang *et al.*, 1999; Yang *et al.*, 2000) and piezoelectric load transducers (Holm-Hansen and Gao, 2000) have all been utilized in research studies. Each of these shall be discussed briefly in this section, however, more detail will be given to the eddy current type, because of its capability to detect defects and its similarity to the transducer used in this work.

A fibre optic transducer consists of an optical fibre which has two internal dielectric mirrors separated by a known distance, L as illustrated in Figure 4.16. When chirped laser light is directed onto the mirrors, it gets reflected back from the mirror which is closer to the bearing outer race (R2). The phase of the reflected light waves shifts with the outer race displacement incurred when a rolling element passes the investigated area. This means that by measuring the phase shift, the displacements of the outer race can be measured (Conkey *et al.*, 2003).

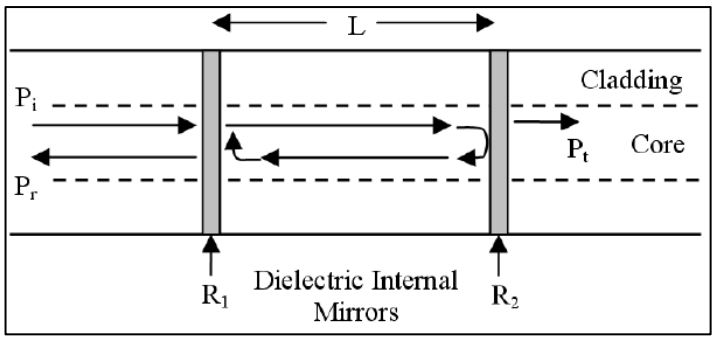

Figure 4.17 FFPI structure (Conkey *et al.*, 2003)

The work of (Conkey *et al.*, 2003), utilizes such a type of transducer (Fiber Fabry Perot Interferometer-FFPI). It was positioned within a transverse hole in the bearing housing, in close proximity to the bearing outer race. The rolling element passage profile obtained gives peaks for ball and sensor alignment, and troughs for when the sensor is in between balls, as is shown in the figure below. The frequency sampling rate employed was 1200 Hz, which is relatively lower than the frequencies using in this work (8500 Hz – 12000 Hz) (Conkey *et al.*, 2003).

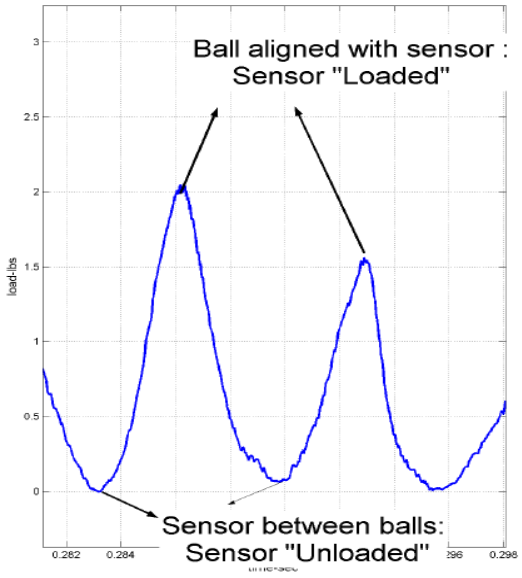

Figure 4.18 Ball passage waveform, adapted from (Conkey *et al.*, 2003)

The researcher was able to obtain information about the load and its distribution on the rolling elements. It was found that at low loading conditions, the non-uniformity caused by the shaft misalignment can be detected (refer to Figure 4.19).

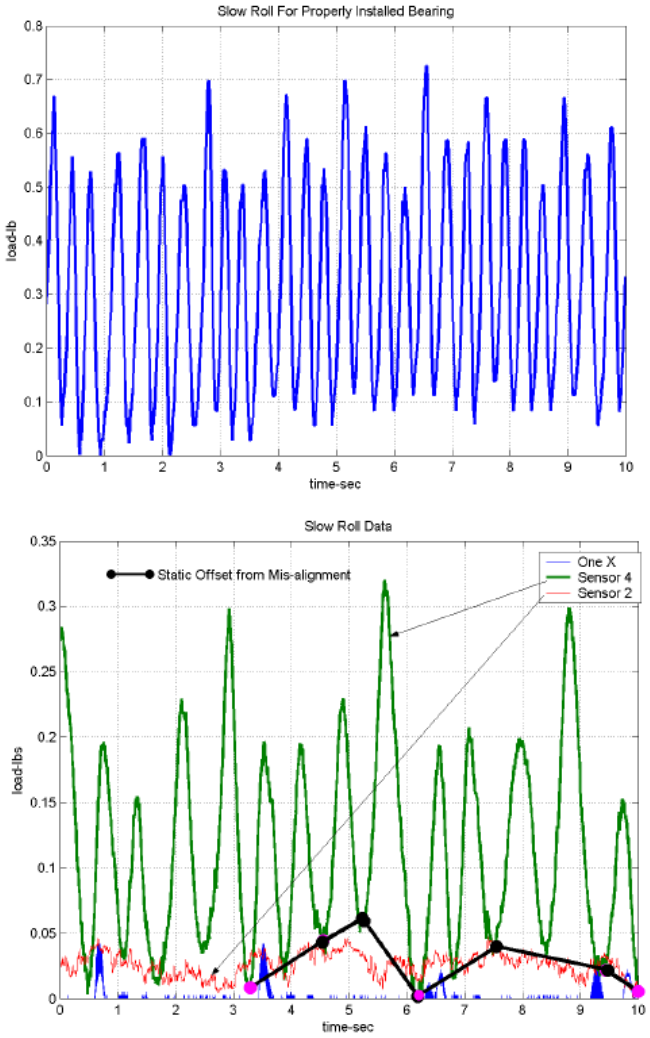

Figure 4.19 a) Uniform loading of rolling elements b) Misalignment Detection (Conkey *et al.*, 2003)

Bearing outer race displacement measurements have also been performed using capacitance measurement. The capacitive sensor, referred to as a Kevin probe, measures the contact potential difference between two dissimilar metals. One of the capacitor plates is positioned above the moving surface, which in a bearing scenario this means the probe is positioned above the outer race (as shown in Figure 4.20), and the other plate is electrically connected to the investigated surface, i.e. the other plate is electrically connected to the outer race. Displacements in the outer race will generate an electric current that varies with the magnitude of the displacement (Yang *et al.*, 1999).

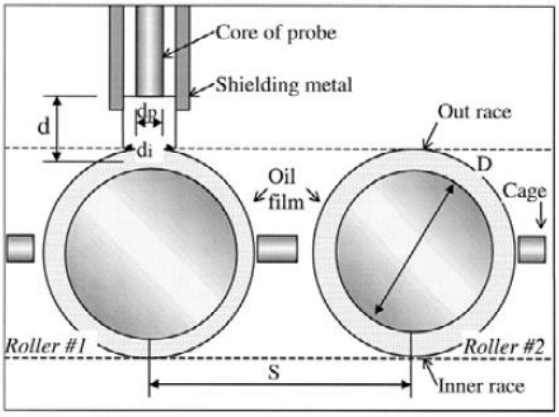

Figure 4.20 Capacitive probes application (Yang *et al.*, 1999)

This capacitance measurement technique has been successfully employed in studies that investigated relatively small (0.25mm x 0.25mm) defects on rolling elements and missing rolling elements (Yang *et al.*, 1999) – even if no relationship between the defect size and signal features has been established. They were also used to measure rolling element skewness (Yang *et al.*, 2000).

Piezoelectric sensors can be used to measure outer race displacements through the piezoelectric effect that has been explained in Chapter 2. In the studies that employed this method, the piezoelectric sensor has been embedded into a slot located at the outer race, outer surface as shown in Figure 4.21. Thus, the outer race was modelled as a beam of varying cross-section, with the sensor giving a change in voltage measurement when the shape is changed (Holm-Hansen and Gao, 2000).

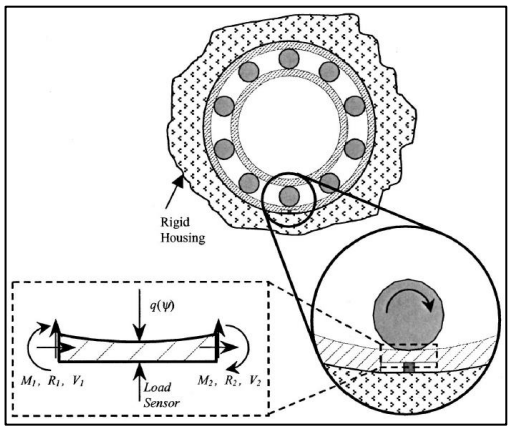

Figure 4.21 Modified bearing outer race and sensor positioning (Holm-Hansen and Gao, 2000)

The outer race cross section changes every time a rolling element passes over the slot and hence, plotting the voltage output over time shows the displacements and bearing load of the outer race whilst it is in operation. Figure 4.22 shows the output given by the sensor compared to a simulated finite element model output (Holm-Hansen and Gao, 2000).

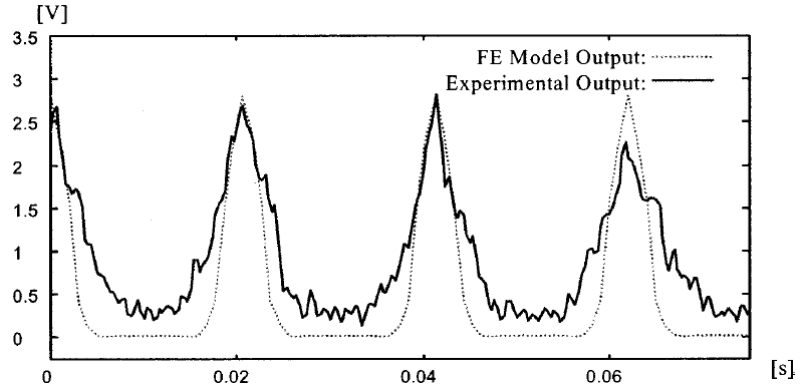

Figure 4.22 Sensor output and finite element model output (Holm-Hansen and Gao, 2000)

Each pulse in the figure, represents each rolling element pass over the sensor's slot and the pulse width is determined by the slot length (beam length). Although the method is able to determine the load and bearing outer race deflection, implementation of the sensor weakens the bearing and thus bearing load carrying capacity is lowered. This shortcoming, reduces the applicability of the method for bearing condition monitoring.

The bearing outer race displacement has also been measured with non-contact Eddy Current transducers. In the study conducted by Yu *et al.* (2002), the transducer was placed in a hole in the housing, leaving a specific distance between the transducer tip and the bearing outer race. When this distance changed, the voltage output changes as a result of the variation in the magnetic field interactions.

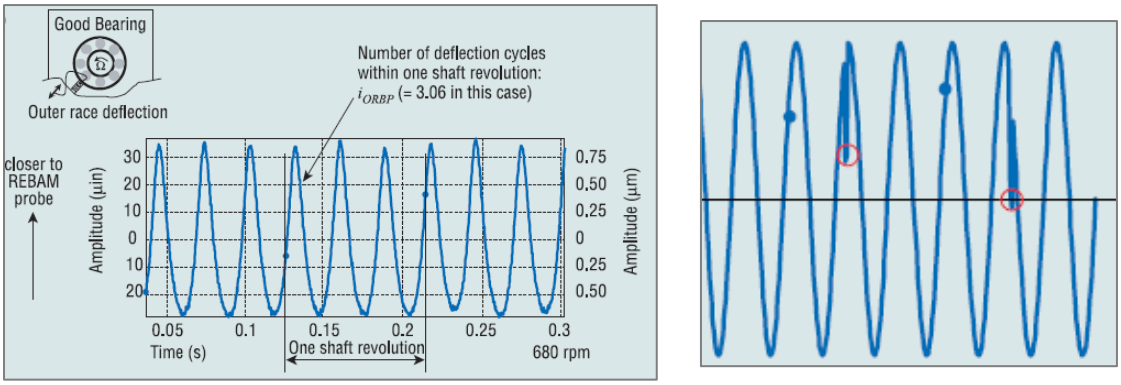

Figure 4.23 (a) Outer race deflection measurement by using eddy current; (b) Spikes resulting from defects (Yu *et al.*, 2002)

The distance between transducer tip and the conductive target (bearing outer race) changes according to rolling element positions; while rolling elements pass over the measured area, the outer race gets closer to the probe, and after contact occurs, the outer race goes back to its previous position. The voltage changes would reflect these changes in displacement.

When the defects in the bearing components fall in line with the contact area beneath the probe, spikes appear in the deflection curve as shown in Figure 4.23 (b). The amplitudes of these spikes gives an indication of defect severity – although no correlation between the spike size and defect size has been established. Also, from the components' pass frequency, it is possible to identify which of the components is the one that is defected as the harmonics of the defect pass frequencies could be observed in the frequency domain analysis.

Another type of transducer that was employed to measure bearing outer race surface displacement is the ultrasound immersion transducer. In the work of Ibrahim (2012), a 25 MHz spherically focused ultrasonic immersion transducer was employed to examine the surface displacement of a deep groove bearing. As the rolling elements passed underneath the transducer, the first reflection shifted as a result of a decrease in the distance between the bearing outer race and the ultrasound transducer. Although in this work the time shift of the first reflection and a displacement in the outer race surface have been observed, cyclic bearing outer race deflection curves were not obtained. Figure 4.24 shows how the outer race surface displacement increased with the applied load while one ball was passing the underneath the transducer.

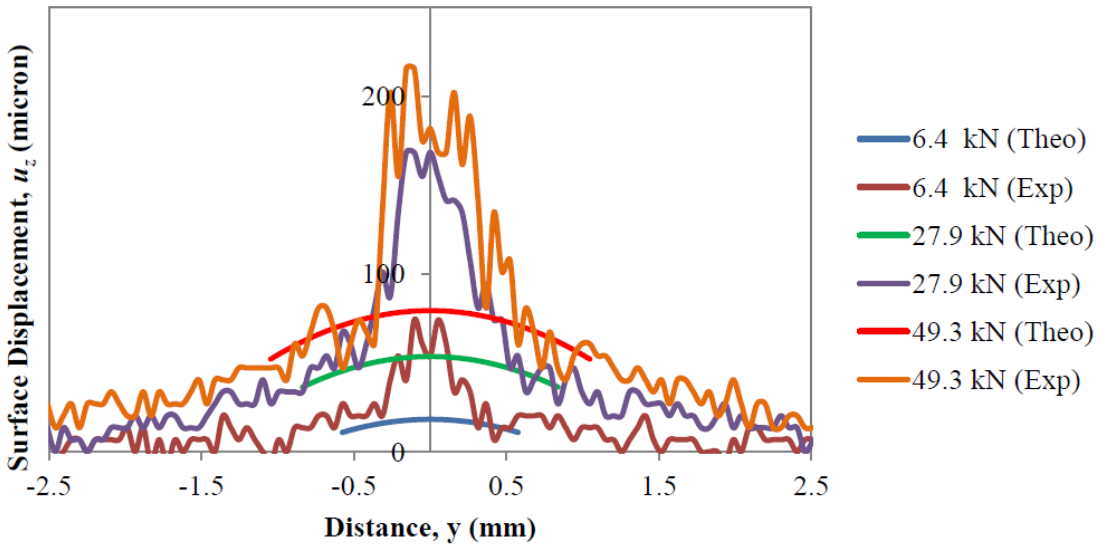

Figure 4.24 The surface displacement of the contact as a ball is passing (Ibrahim, 2012)

The above discussion has shown how different types of transducers can be applied for bearing outer race displacement measurements. The difference between the different kinds, other than in the working principles, lies in the defect resolution (horizontal), deflection magnitude resolution (vertical), in the sensitivity to the working environment, and the ease of positioning the transducer. For instance, the capacitance probe has a vertical resolution (showing magnitude of the deflection) of 0.25mm (MTI instruments), that for the fibre optic is 2µm, and eddy current transducers have a resolution of 0.2nm (Micro epsilon catalogue). On the other hand, the horizontal resolution for the eddy current transducer (which is directly related to sample rate) is much lower than that for the fibre optic transducer because. This is because an eddy current transducer records real time measurements and does not collect sampled data as the fibre optic transducer.

The works reviewed have also shown that: (a) the bearing outer race surface displacement curves obtained from eddy current transducers can detect defect and evaluate defect severity on the components of bearings (Yu *et al.*, 2002); and (b) that focused ultrasonic transducers are able to measure the deflection of an outer race surface of a bearing (Ibrahim, 2012). Hence, this work undertook the task of using a focused immersion ultrasonic transducer as a proximity transducer to study the bearing outer race surface deflection to greater detail than the previous work and by using superior data processing methods.

In addition, since an ultrasound transducer provides both high vertical and horizontal resolution data due to the sampling nature of the ultrasound wave, the defects on bearing components were examined with the aim of determining defect severity by the use of this type of transducer.

4.5 Conclusion

In the chapter, bearing failure characteristics, bearing life prediction and bearing defect analysis methods have discussed.

- Possible bearing failure reasons and failure modes were discussed.
- Different approaches for bearing life prediction were compared and the evaluation of the bearing life rating formula was presented.
- The methods, transducers and data processing techniques employed for bearing defect diagnosis were compared and discussed in some detail.
- The displacement monitoring techniques have been examined in detail due to the resemblance of these methods to that employed in this research.

5 EXPERIMENTAL DESIGN AND SENSOR INSTRUMENTATION

This chapter discusses the instrumentation used in this project, starting off from the overall design of the test rig and the properties of the bearings used. It gives details on the setup and other parameters of the transducer employed. Finally, it discusses the ultrasound wave acquisition system used to collect reflections off the bearing outer race and very briefly explains the post processing methods used to analyse the obtained signals. (The latter are discussed in more detail in Chapter 6).

5.1 Bearing test machine

The test rig, which was located in the Swift Laboratory within the Mechanical Engineering Department of the University of Sheffield, has been designed and constructed by Cooper Bearing Ltd. Any modifications required by the bearing parts and housing units, such as the attachment of ultrasonic sensors, strain gauges and thermocouples, have been conducted by the university's workshop. Such modifications were required to enable monitoring of the bearings.

The test rig consisted of the motor, driving belt, gearbox, two bearing pillow blocks, main shaft, monitored bearing, shaft speed controller, load cell, radial loading unit and the steel block through which the load was applied and measured. Figure 5.1 shows a schematic of this assembly.

The inner race of the bearing under study, a Cooper Split Roller Bearing, was bore-mounted to the shaft and rotated in correspondence to the constant shaft speed. The radial load was applied to the stationary outer race which was fixed to the cartridge unit by pins. This test rig simulates the operational mode of some of the wind turbine bearings such as the main bearing and the intermediate and high-speed stage bearings. These bearings have a rotating inner race and a fixed outer race.

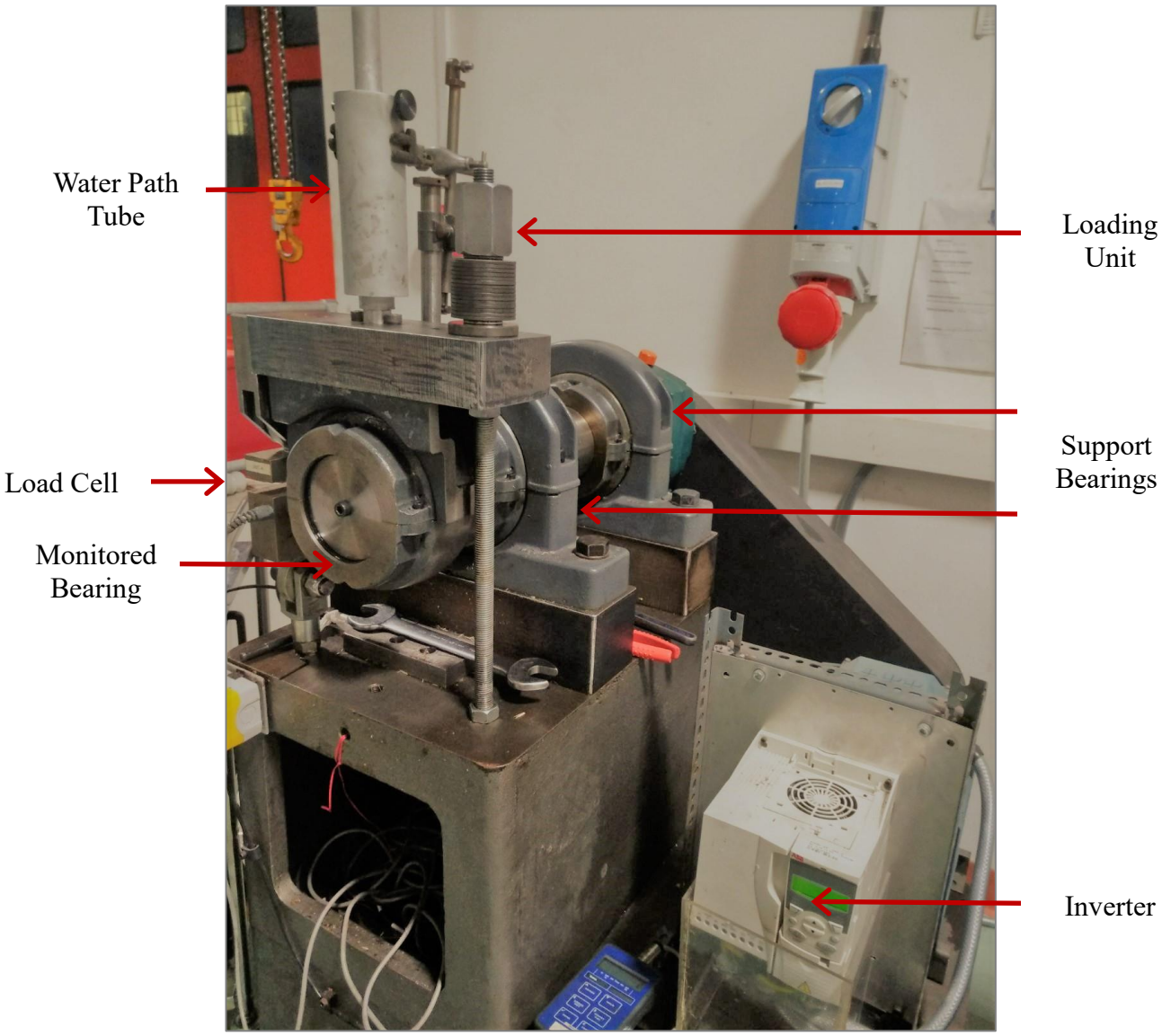

Figure 5.1 The bearing test rig

This test bearing inner raceway was driven by a 7.5 kW, 3000 rpm ABB electric motor via a 5:1 gearbox reduction and a 3.45:1 pulley stage. The ABB ACS 355 shaft speed controller enabled a range of shaft speeds up to a maximum of 175 rpm. The bearing could be loaded up to a radial load of 4000 kg, which could be adjusted by tightening the custom-made nut located at the right side of the steel block.

At the other end of the steel block sat a load cell from which the applied load could be read off as shown in Figure 5.2. The test bearing shaft was fixed by two bolt base pedestals through the shaft. The bearing was lubricated with Alvania EP(LF)2 grease.

The rotation speed of the main shaft of the test rig was set to low levels (12.5rpm and 25rpm) in order to obtain high resolution bearing outer race deflection curves. The applied radial load was not set to values exceeding 3000 kg to avoid further damaging the artificially defected bearing components.

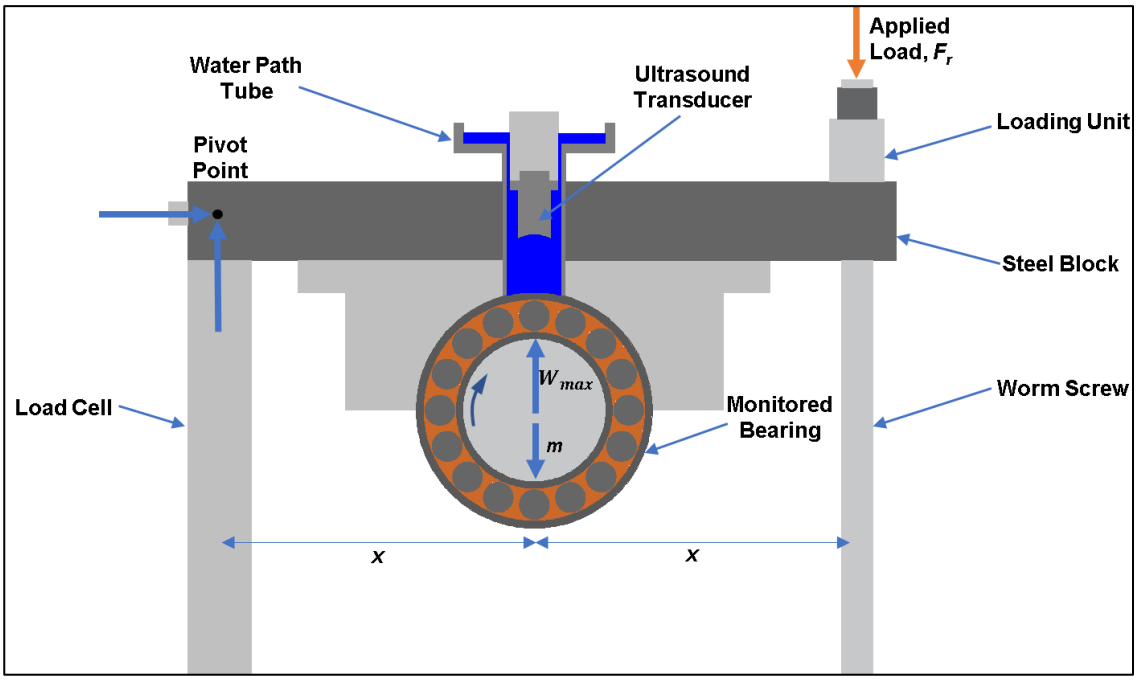

Figure 5.2 Schematic diagram of the bearing test rig

5.1.1 Test bearing

The use of a Cooper Split bearing in this project is prompted by some of its prominent advantages and its applicability to direct drive wind turbine main shafts. Cooper Bearings produce split bearings, i.e. bearings of which components such as inner and outer races and cage are split, as shown in the Figure 5.3. This makes assembly and disassembly easy and reduces downtime, installation expenses and power consumption. It also allows for easy inspection.

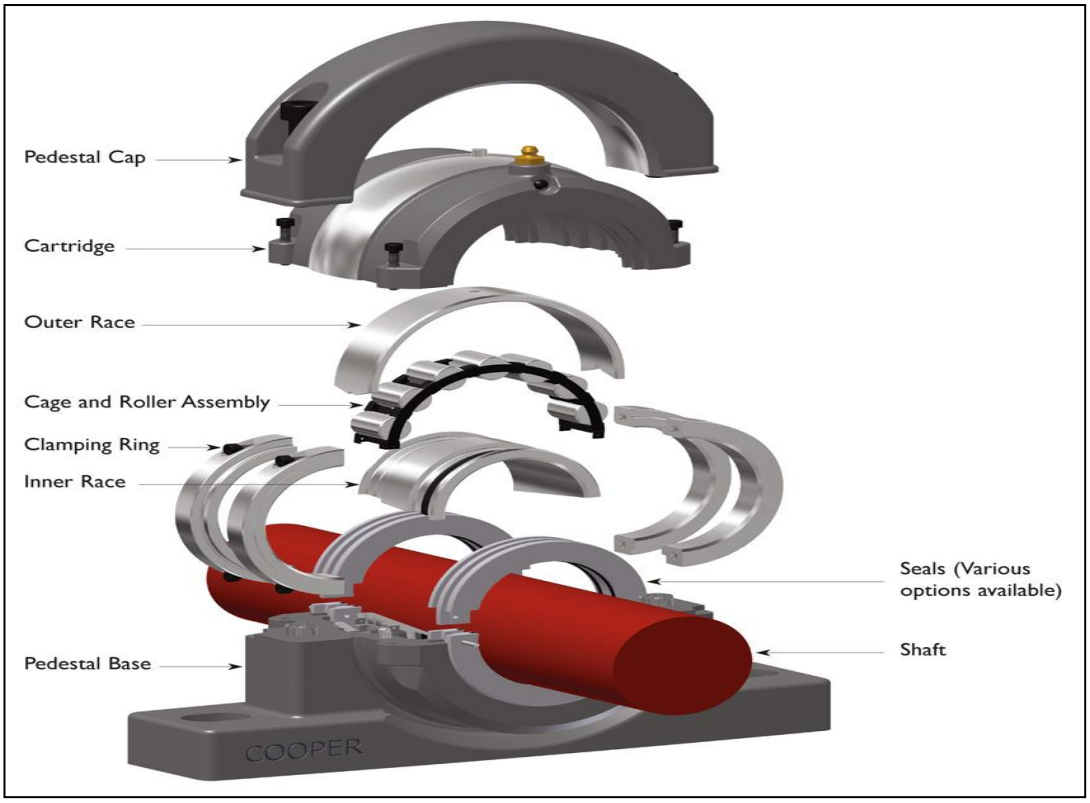

Figure 5.3 Cooper split bearing components (Cooper Bearing, 2015)

The used bearing is referenced *01E B 400EX* and is mounted on a 101.6 mm shaft diameter. For this kind of bearing there are two types outer races: Fixed Type bearing 'GR', which has a shoulder to carry axial and radial loads; and Expansion Type bearings 'EX', which does not have shoulder and takes radial loads only as shown in the Figure 5.4 (Cooper Bearing, 2015). The latter could move axially when expansion or contraction occurs on the shaft. Shoulders on the GR type outer race give more durability.

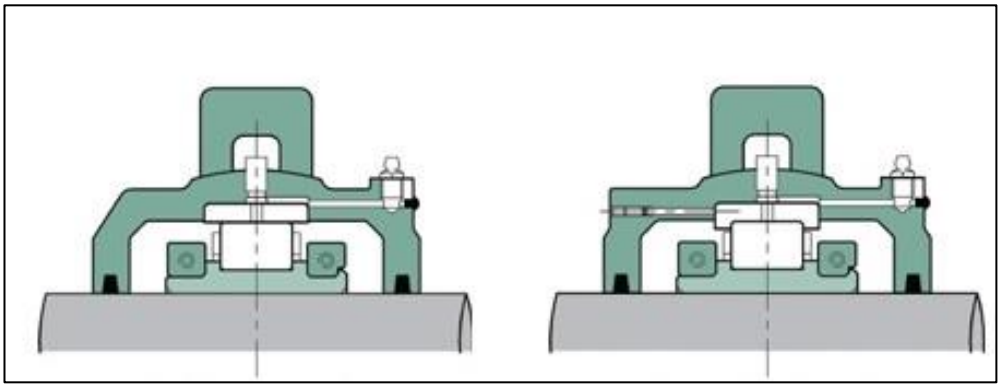

Figure 5.4 EX Type and GR Type bearing outer race (Cooper Bearing, 2015)

A technical drawing for the EX type Split Cooper bearing that has been used more predominantly in these tests is shown in Figure 5.5. Some of its key specifications are outlined in Table 5.1.

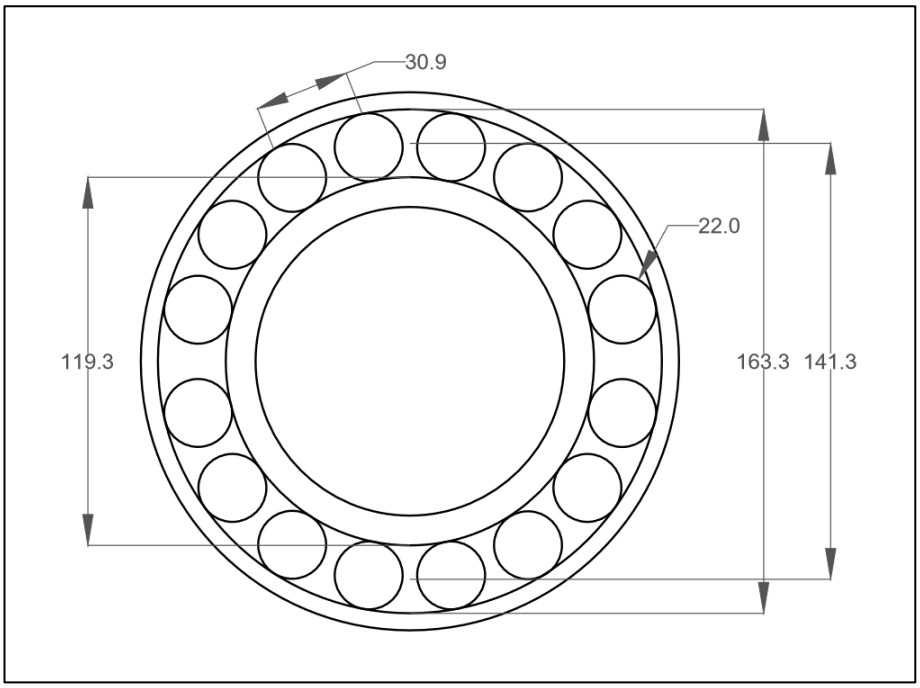

Figure 5.5 Technical drawing for EX type split cooper bearing

Radial dynamic load rating (Cr)	320 kN
Basic static load rating (Cor)	421 kN
Axial dynamic load rating (Ca)	19.6 kN
Pitch diameter (PD)	141.3 mm
Roller Diameter (BD)	22 mm
No. of Rollers	8 / 16
Contact angle	0

Table 5.1 Bearing specification (Cooper Bearing, 2015)

5.1.2 Test Lubricant (Shell Alvania EP(LF)2 Grease)

In this research, Shell's Alvania EP (LF)2 grease, a lubricant designed for heavy duty bearings, shock loading in wet environments and high temperature is used. It contains mineral oil as a base oil and is thickened by lithium soap. Also, special additives give it the capability to withstand heavy and shock loads, water wash-out resistance, oxidation stability and corrosion protection (Shell, 2007).

5.1.3 Inverter

The test rig shaft speed is controlled by an ABB ACS 355 inverter. The shaft, which is fixed to the inner race, can achieve 175 rpm rotation speed in 0.1 increments. Other advantageous features include:

- Compact drives and uniform design
- Sensorless vector control
- Built-in braking chopper
- Torque memory for lifting applications
- Common DC bus
- 600 Hz maximum output frequency

This inverter is equipped with state of the art health and safety measures. For instance, it is possible connect the emergency stop button of the rig to the inverter for accident prevention. Also, it has a Safe Torque-Off (STO) function which shuts down itself immediately in the event of failure, where the shaft requires more torque than the specified maximum. This measure not only protects against health hazards but also prevents damage to shaft, gearbox and motor (ABB, 2013).

5.2 Simulation of the bearing component defect

The complexity of life estimation of the bearings incited researchers to develop condition based monitoring (CBM) for life estimation of bearings. In such CBM applications, changes in the specific properties of the bearings which may be related to fatigue, are monitored to estimate the bearing remaining useful time.

In the first part of this study, the outer race deflection curve patterns obtained from a brand-new Cooper Split EX type bearing has been examined under different operating conditions.

The second part of this research involves the use of an ultrasound transducer to monitor outer race deflection with the aim of analysing certain typical bearing defects. Since the defect onset process can take a long time, defects of known size in the form of line defects with different widths, were artificially introduced to bearing outer races, inner races and rolling elements as illustrated in Figure 5.6. In order to assess the measurement

capabilities of the proposed method, these defects needed to be of submillimeter dimensions. Since the bearing components were composed of hardened 100Cr6 steel, machining the defects with Computer Numerical Control (CNC) to the required high precision was not possible and instead, Wire-Cut Electrical Discharge machining (EDM) was employed. The smallest wire diameter is 0.1 mm, hence line width sizes as small as several hundred micrometres could be cut in different bearing components. These submillimetre size defects were accepted as simulated defects of the very early stages of the possible defects in a bearing as shown in § 4.2.

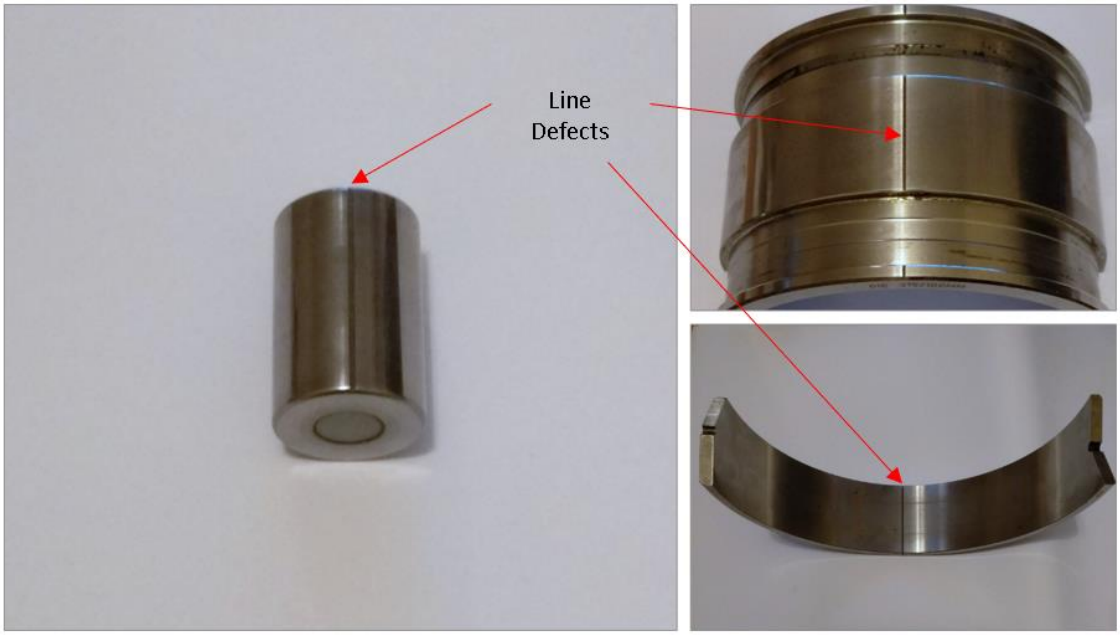

Figure 5.6 Bearing components artifical defects by EDM (Rolling element,inner race, outer race)

5.3 Sensor implementation

Detailed information on the general properties and applications of ultrasound transducers has been given in previous chapters. In this part, the implementation of the spherically focused immersion transducer within the testing equipment will be discussed.

Sensor implementation is of vital importance for testing: the sensor's physical presence, cables, connections and other requirements such as water paths need to be taken into consideration during the test rig design stage, depending on the sensor's requirements. For instance, while piezo-disc sensors with their adjustable small size disrupt the housing only slightly, other sensors such as immersion transducers need a water path which

enables sound wave transmission. This means that the housing needs to include a hole, of specific diameter within the range of 3.175 mm to 28.5 mm to accommodate their circular case geometry (as illustrated in the Figure 5.7) and water path.

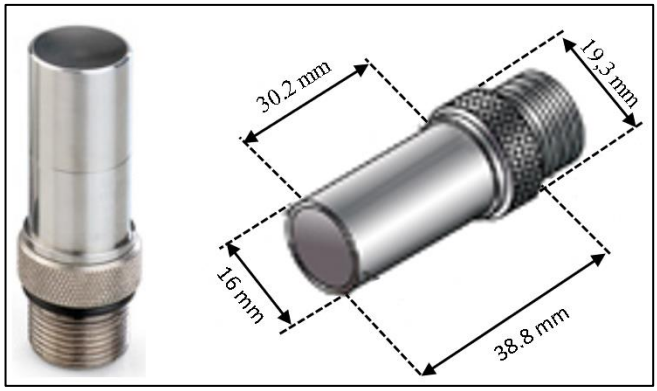

Figure 5.7 Focus ultrasound transducer and dimensions

The main tests of the project were performed by using a spherically focused ultrasound transducer. Holes of diameter 14 mm and 24 mm were drilled through the cartridge and test rig's steel block, respectively, to accommodate both the sensor and water path as shown in the Figure 5.2.

In this work, the bearing inner race was fixed to the main shaft and the cage held together the rolling elements between the inner and outer races. The outer race was fixed to the cartridge by pins to prevent rotation. Through the steel block a measured radial load was applied to the bearing. Both cartridge and steel block have been drilled all along to accommodate the sensor and water path as shown in the Figure 5.2. Dimensions of the test rig in this sketch have been exaggerated for illustrative purposes.

Ultrasound waves were aimed onto the bearing outer race from the transducer located vertically above it. The transducer does not need to be in contact with the component it will monitor: it emits waves and collects reflections from its fixed position. The ultrasound transducer positioning propagated and reflected waves can be seen in the Figure 5.8.

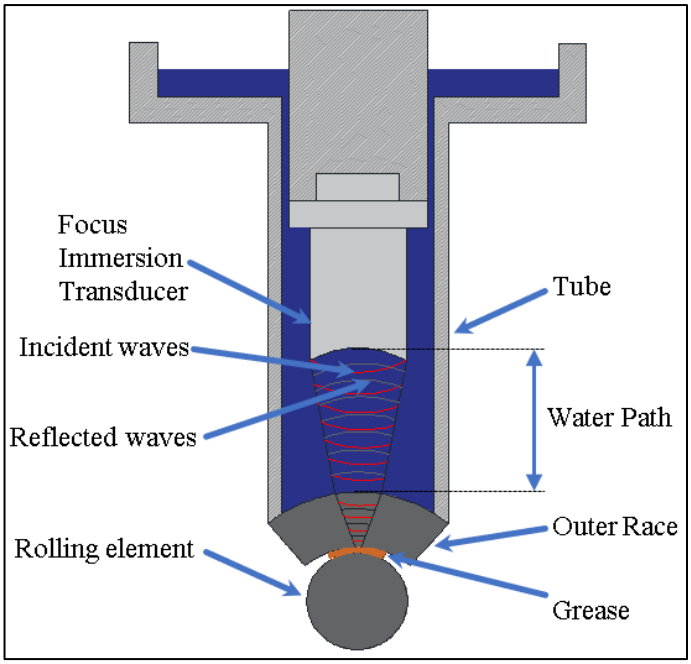

Figure 5.8 Immersion transducer positioning, wave propagation and reflection

The most critical parameter for the focus immersion ultrasound transducer is the adjustment of the water path distance – which is the distance between the face of the immersion transducer and the bearing outer race outer surface, as illustrated in the Figure 5.8. This parameter affects the ultrasound beam diameter and the transmitted ultrasound wave energy as has been explained in detail in § 2.1.3.3. The smaller the beam diameter and the highest the energy of the transmitted waves to the bearing outer race, the more accurately can the movement of the investigated are be observed. This condition can be obtained when the bearing outer race is positioned within the focal zone of the transducer.

For the setup of these tests, the water path distance has been calculated from the Equation 2.9 which was given in § 2.1.3.3.2.

$$WP = F - MP\left(\frac{c_{tm}}{c_w}\right) \tag{2.9}$$

Also, the water path can be more precisely determined through empirical measurement. This can be done by changing the distance between the face of the focused immersion transducer and the bearing outer race outer surface in small increments and analysing the differences in the ultrasonic reflections obtained.

The first reflection comes from the bearing outer race outer surface, and the amplitude of this signal indicates the power of the reflection, which is affected by the water path. The optimum water path distance is that at which the highest amplitude can be obtained. Hence, by collecting and comparing the amplitudes of the first reflections from different distances, the water path distance can be determined.

As discussed in § 2.1.3.3.2 the employed focus immersion transducer is able to make accurate measurements within the minimum and maximum focus distances: 25.4 mm and 203.2 mm, respectively. Figure 5.9 shows that the measured highest reflection amplitudes occurred at a water path distance of 54 mm. This is where the most sensitive measurements can be performed.

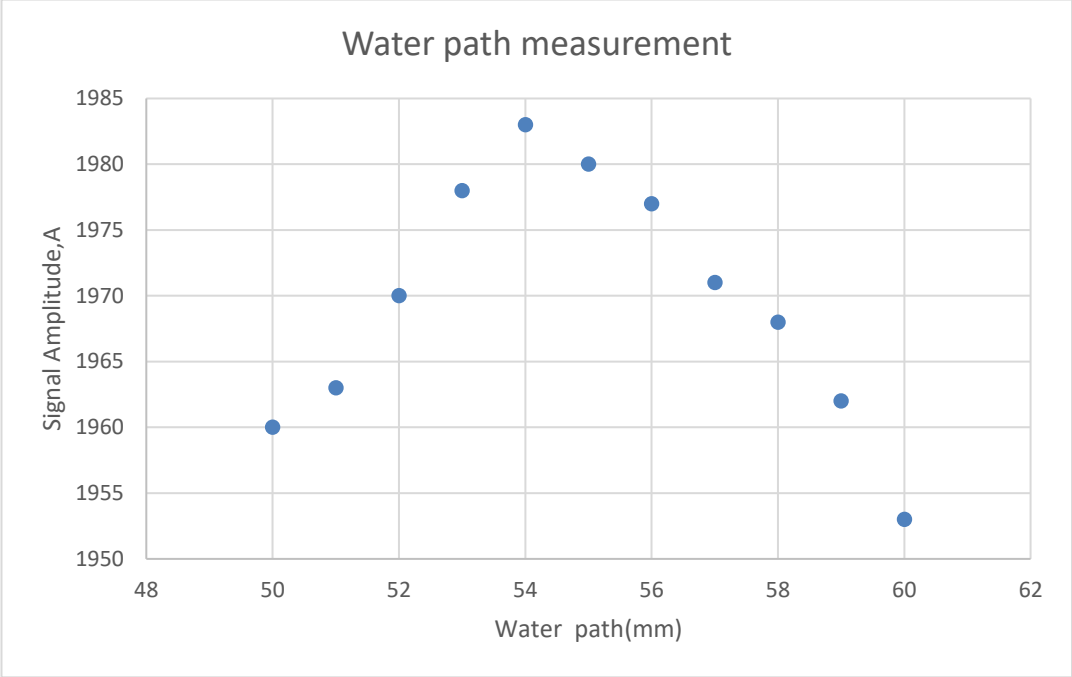

Figure 5.9 Variation water path with peak amplitude of reflections

5.4 Data acquisition and the basic principles of the post signal processing

In this project, a computer-based ultrasonic data acquisition system, called Film Measurement System (FMS), was used to perform the analysis of ultrasonic data. The system is made up of two Peripheral Component Interconnecting (PCI) cards – the digitiser and the UPR – to perform ultrasonic measurements, as shown in the Figure 5.10.

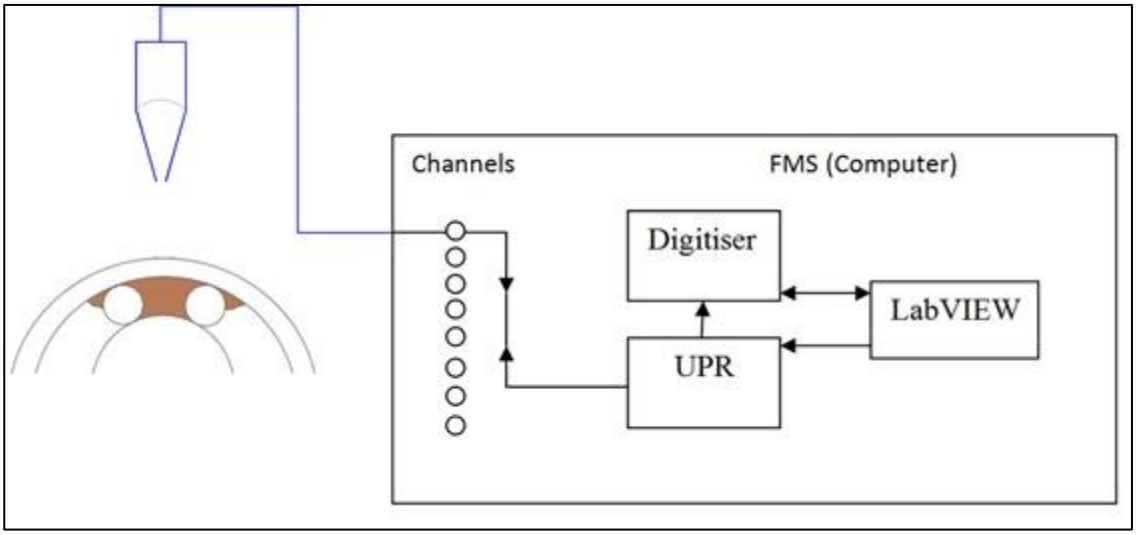

Figure 5.10 Ultrasonic measurements apparatus

The Ultrasonic pulse-receiver (UPR) generates voltage pulses to excite the piezoelectric elements within the transducer, which in turn, when induced, these piezoelectric elements produce ultrasonic waves. The UPR unit has eight channels and could deliver excitation pulses up to 300 volts. Short duration pulses could be generated at a LabVIEW control interface at a selected rate of up to 80 kHz. This frequency is called the "Pulser Repetition Rate" (PRR) and controls the rate at which the pulser fires. The pulse width (PW) can be varied from 50 to 1000 nanosecond.

The generated ultrasonic waves travel through water, interact with the bearing's outer race and are reflected back onto the transducer. These reflected ultrasonic waves are converted to a voltage response signal and passed on to the UPR. Subsequently, the analogue response is converted to a digital one by the digitiser, an operation which is required to enable further computer processing and storage. The digitiser has a digitizing rate of 100 MHZ at a resolution of 12 bits (Howard, 2016).

The vertical resolution of the signal is determined by digitiser resolution and it represents the number of voltage steps that construct the signal. In the case of a 12-bit digitiser, the signal is divided into 4096 (2^{12}) vertical digital discrete steps. Small magnitude changes of the signal can be efficiently determined by such a high-resolution digitiser. A 12-bit digitiser is sufficient for the majority of applications (Brunskill, 2013).

In ultrasound testing, sound wave incidence is of paramount importance, if an adequate reflection is to be obtained. Incident wave properties such as pulse voltage, pulse repetition rate, variable gain, length of signal and pulse width can all be adjusted via the LabVIEW control interface. Furthermore, the software allows the user to "window" the reflection of interest by adjusting the "Delay" and "Range" of the waveform. Adjusted and selected pulses can be recorded as a Technical Data Management Streaming (TDMS) file or binary file for post processing techniques. The frequency and duration of the recorded data can be adjusted from the developed interface.

The required reflections have been recorded in a stacked ultrasonic data stream form. By knowing the Pulser Repetition Rate (PRR) and pulse range, post signal processing methods could be applied to the data stream to obtain the required information.

In these studies, incident ultrasound pulses and consecutive reflections have been monitored. The first and second reflections have been recorded in same window with a sampling rate of 11200 Hz. These were analysed to determine the deflection of the outer race under different circumstances (different number of rolling elements and different main shaft rotation speed).

For the second part of the project, where the aim was to detect defects in the inner race, outer race and rolling elements, the first and second reflections were again recorded together using the same sampling rate as in previous experiments.

The idea behind the use of ultrasound transducers and post signal processing for this project can be explained simply as follows: ultrasound transducers are not only able to measure the thickness of material and detect defects within the material non-destructively, but also are able to determine the distance between the transducer and the examined material when the transducer is positioned at a distance from the inspected

material, like for example in the case of the immersion transducer. Moreover, immersion ultrasound transducers are able to quantify any movement of the inspected material with respect to their fixed position, as such movement would result in a time shift in the reflected waves. Hence, by analysing the time shifts of the first reflection wave emitted off the bearing outer race, the movements undergone by the outer race could be observed. For the signals to be correlated to the deflection of the outer race, the zero-cross and time-of-flight post processing methods have been employed.

5.5 Conclusion

This chapter describes the equipment used in this project, which very broadly consists of:

- the test rig;
- the transducer instrumentation; and
- the data acquisition system.

Details of each of these components and their role has been discussed to enable a better understanding of the subsequent chapters. In addition, the chapter provides an outline of the study.

6 BEARING OUTER RACE SURFACE DEFLECTION MEASUREMENTS

In this chapter, the methodology of the proposed method to measure bearing outer race deflection by using ultrasound immersion probe is discussed in detail. In other words, the recording of the required ultrasound reflections and signal processing techniques of the data will be explained thoroughly. Finally, the effects of the operating conditions and the number of rolling elements on the outer race surface displacement will be discussed.

6.1 Data acquisition

In order to perform post-signal processing techniques to obtain cyclic load-dependent bearing outer race displacement data, ultrasound reflections need to be identified and recorded. ToF measurements cannot be applied to the incident wave because its shape is not similar to that of the reflections (In Figure 6.1 the incident wave looks similar because the signal was rectified for illustrative purposes). Also, the number of data points recorded for the incident pulse and first reflection set is between 30-35 times larger than that recorded for the first and second reflections – which creates a data size problem. Moreover, not using the incident wave, is not an issue, because the time shift of first reflection – which is reflected from the outer race's outer surface, is enough to extract information to show the deflection of the bearing outer race.

On the other hand, the second reflection's raw data stream shows very clearly the passing of rolling elements – which is not so evident in the first reflection's raw data stream. Hence, recording of both first and second reflections together enables an acceptable data size that gives a clear identification of the passing rolling elements in the raw ultrasonic data stream and outer race deflection change with varying load.

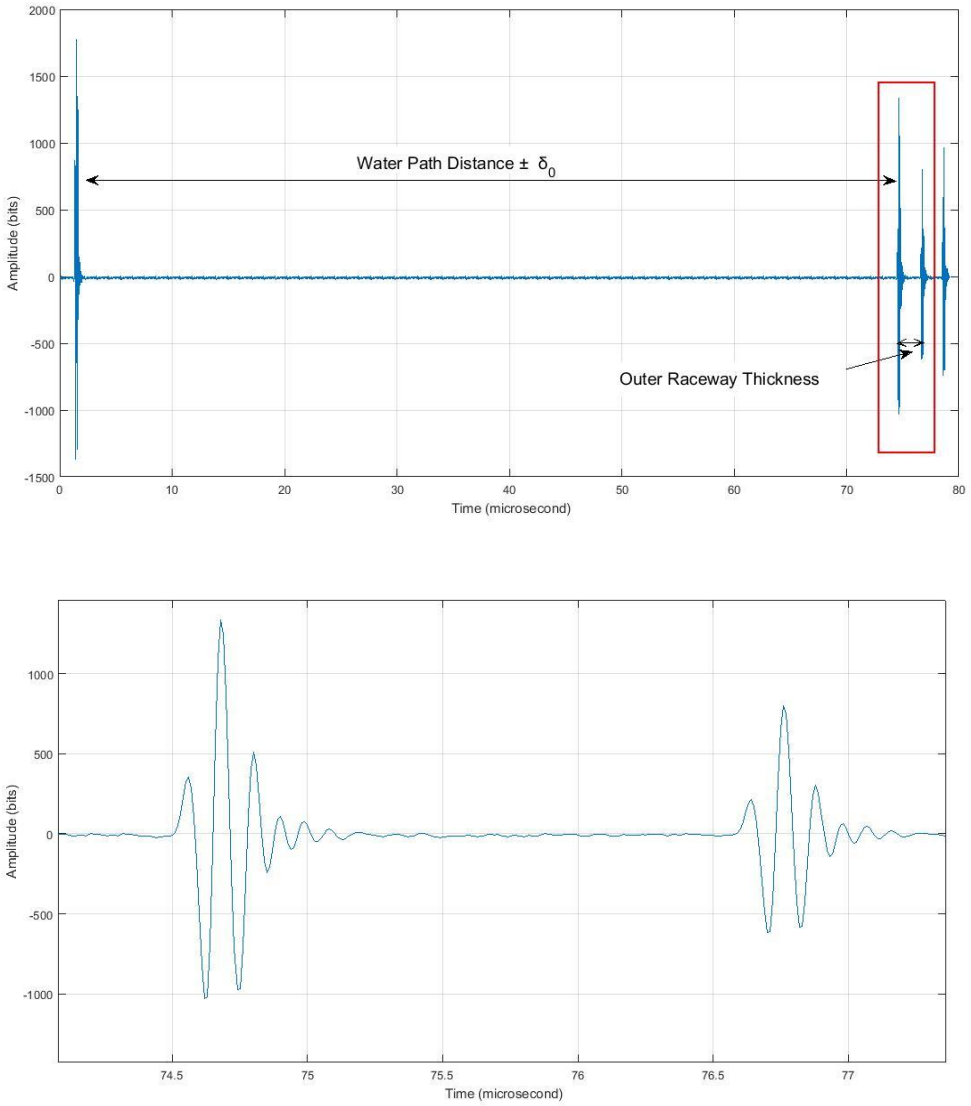

Figure 6.1 Windowing of the interested reflections- 1st-2nd reflections

The data acquisition interface software connected to the ultrasound pulser-receiver unit has been developed within LabVIEW environment. Other than the visualization of the incident wave and a series of reflections, it also enables the user to record (termed, window) parts of interest of the signal at the desired pulse repetition rate (PRR), pulse width and duration. The first and second reflections can be seen windowed in Figure 6.1 The pulses of interest can be windowed by arranging the delay and range.

The pulse repetition rate (PRR) controls the generation frequency of the specified window, which in this case includes the first and second reflections (Figure 6.2). The number of data points in the ultrasound raw data stream is the multiplication of the PRR, window size and duration of the recording time. The recorded first and second reflection can be seen in a stacked ultrasonic data stream form as shown in Figures 6.2 and 6.3.

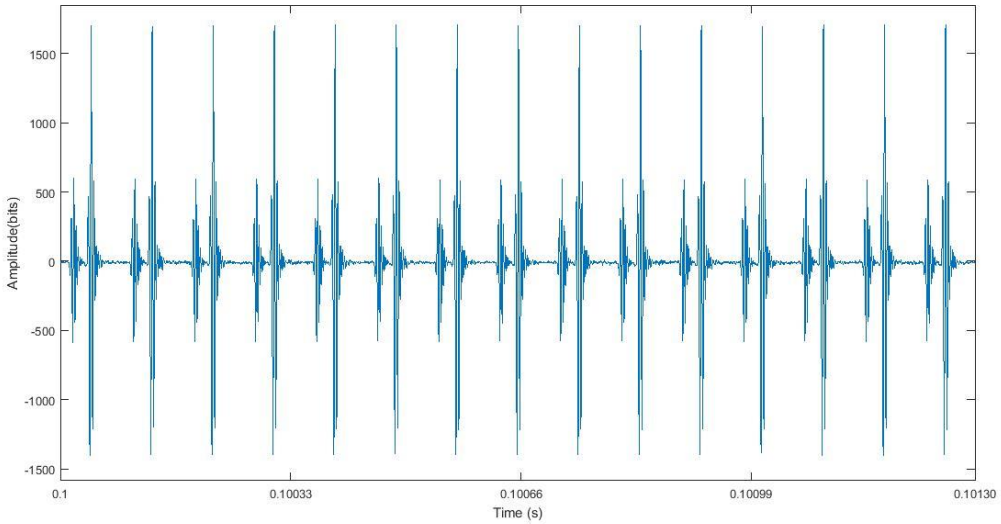

Figure 6.2 Recording of the 1st and 2nd reflections with desired PRR

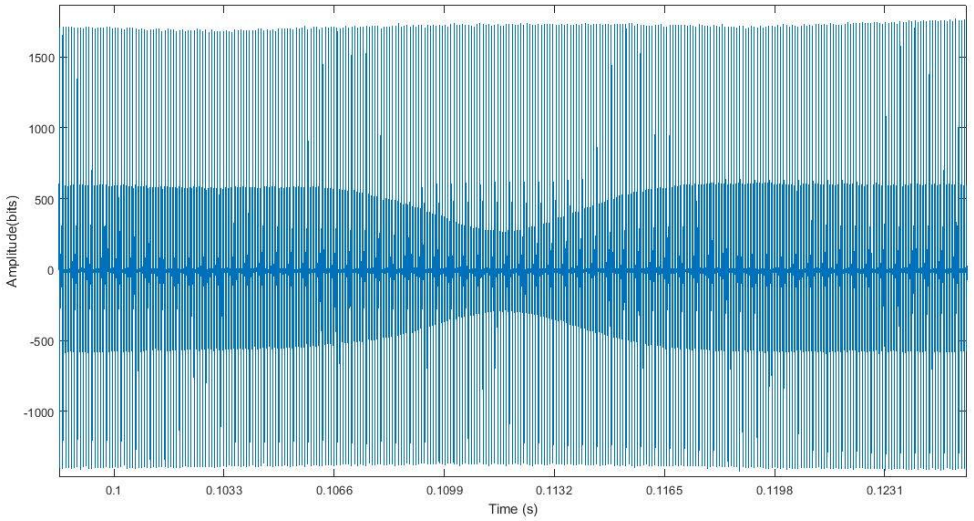

Figure 6.3 Raw ultrasound data stream, (rolling element pass evident in 2nd reflection)

6.2 Post signal processing

The first stage of post signal processing involves reading the consecutive pulses from the binary files by using the known signal configuration information, such as window length and the pulse lengths. The captured signal window is thus extracted and pulse movements can now be analysed.

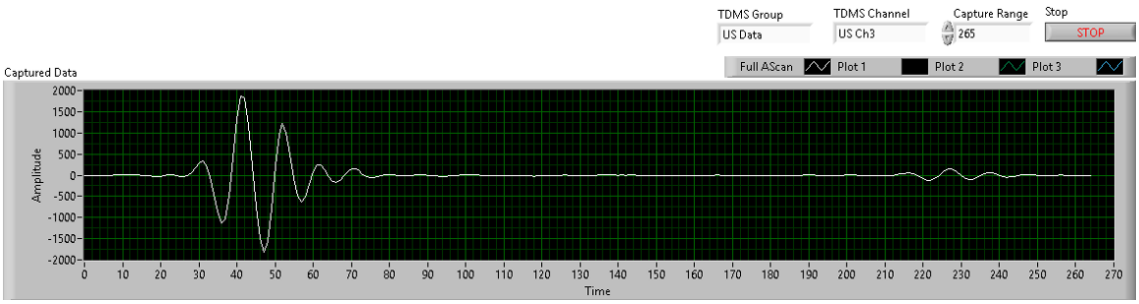

Figure 6.4 1st and 2nd reflection (Defined window)

The window in this study consisted of 265 data points (as shown in Figure 6.4), which is equivalent to 2650ns. This window size multiplied by the PRR and collection time, gives the total number of data points for the whole data stream.

Each pulse that is emitted, reflected and collected, provides information about the status of the interfaces; for example, the first reflection gives information about the outer race position relative to the fixed position of the transducer. Hence, each pulse reflection set (where a reflection set consists of the first and second reflections) has to be analysed separately. To do this, each reflection is windowed by selecting the appropriate 'index' and 'Ascan Length' – software parameters that define the window starting point and length, respectively. Subsequently, to enable the software to pick the correct point for zero crossing the pulses are likened to each other by normalization and an appropriate threshold level is defined. This latter parameter, helps the software to locate the first crest – the tail of which is used to locate the zero crossing point (shown in Figure 6.5). However, the zero crossing point that follows the highest peak in the reflection signal may also be used for time shift analysis.

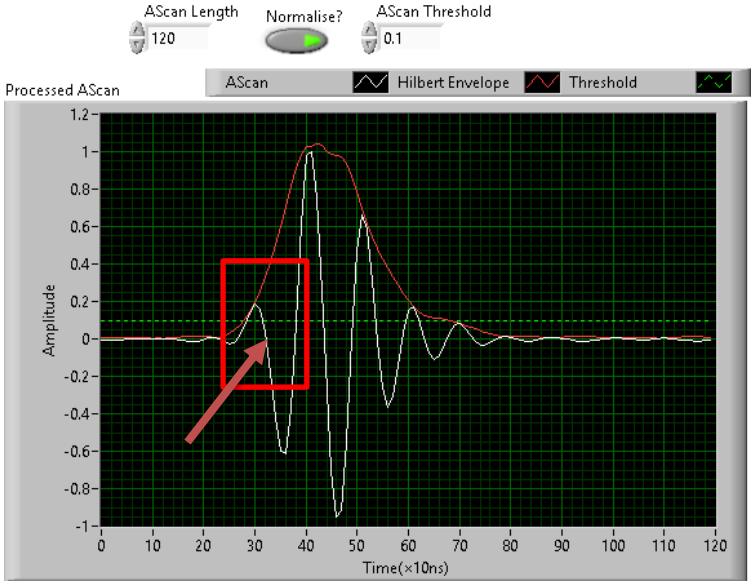

Figure 6.5 1st reflection window-first crest highlighted

Each pulse will provide one zero crossing value, and when these are plotted against time, the movement of the first reflection can be visualized. The minima of the resulting curve show when the outer race's outer surface is closest to the probe and the maxima show when the surface is farthest away.

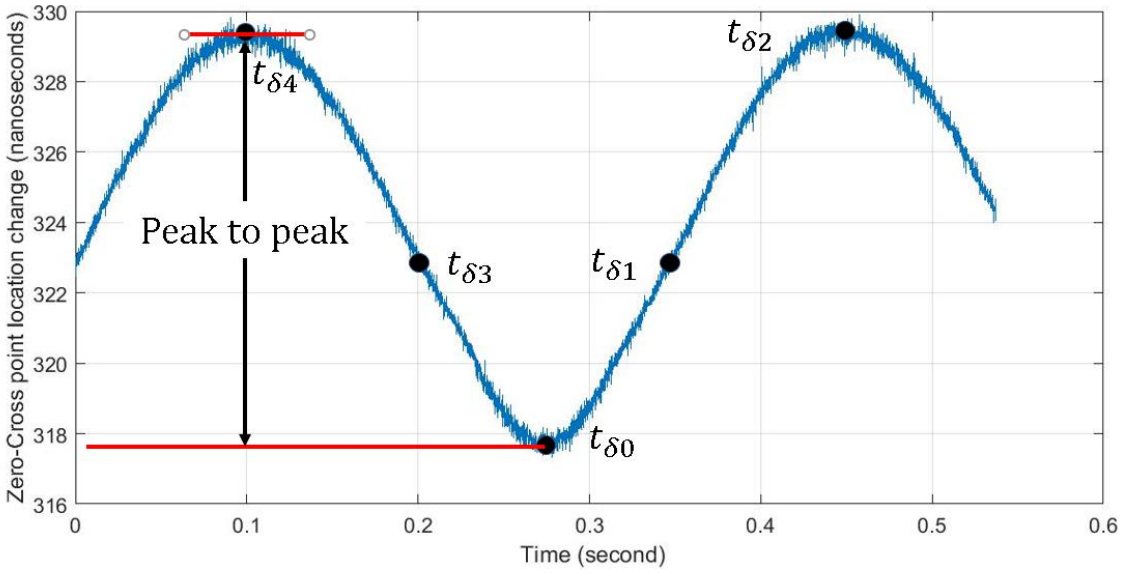

Figure 6.6 One rolling element pass time-shift graph (3000 kg-25rpm shaft speed-16RE-EX)

Figure 6.6 shows the time-shift graph for the 16 rolling element EX type bearing (under the action of a 3000 kg radial load and a shaft speed of 25 rpm), whilst one rolling element passes through the investigated area. The rolling element positions shown can be translated to positions on the time shift curve as follows. The lowest points on the time shift curve represent the moment a rolling element passes beneath the focus immersion transducer. At the point, the water path distance is shortened, with the consequence that the first reflection is shifted in the leftward direction. At that moment, the zero-crossing point of the reflection is t_{δ_0}, and the distance between outer race and transducer is d_{δ_0}. In terms of the example shown in Figure 6.4, the selected window delay is 8075 data points (meaning that the part of interest starts after 8075 data points (corresponding to 80750 nanosecond)). The lowest point of the deflection curve as determined from the zero crossing, occurs around the 31.7th data point. Adding the delay and the zero crossing point (80750 + 317), gives the ToF, which in this case is 8106.7 data points – or 81067 nanoseconds, between the transducer and the outer race outer surface. The peak point on the time shift curve represents the moment the transducer is in between the two consecutive rolling elements. At that moment the zero-crossing point of the first reflection is t_{δ_2} and the distance between outer race and transducer is d_{δ_2}. For the given case, zero crossing point occurs around the 32.8th data point, and hence, gives a ToF value of 8107.8 data points (81078 nanoseconds).

In order to find maximum bearing outer race surface displacement, the zero crossing point of the second case is subtracted from the first and the basic ToF formula is applied as shown by Equation 6.1:

$$\Delta d = d_{\delta_2} - d_{\delta_0} = 0.5\left(t_{\delta_2} - t_{\delta_0}\right) \tag{6.1}$$

The net time shift curve can be obtained by subtracting the minimum value of the curve from every data point (hence, the minima assume the value of zero, and the peaks becomes the maximum time shift) as shown in the Figure 6.7. From this curve, the net deflection at every point can be obtained as shown in the Figure 6.8 by applying the time of flight formula as shown in Equation 6.2:

$$d_{deflection}(t) = 0.5ct_{nettimeshift}(t) \tag{6.2}$$

Where $d_{deflection}$ is the deflection at a time *t*, *c* is the speed of sound and $t_{timeshift}$ is the timeshift at time *t*.

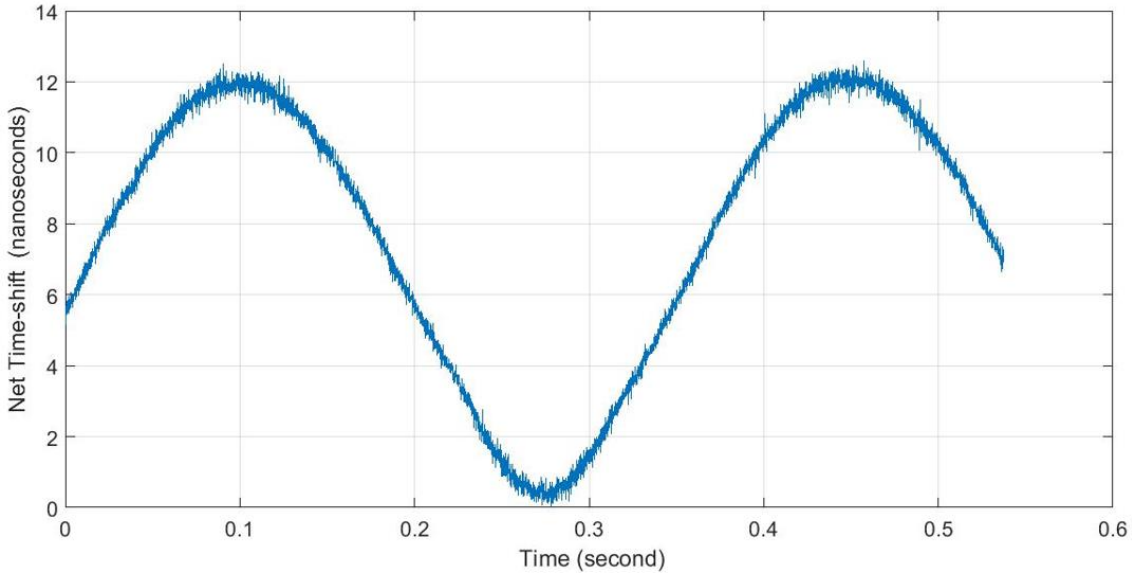

Figure 6.7 Net time shift (3000 kg-25 rpm shaft speed-16RE-EX)

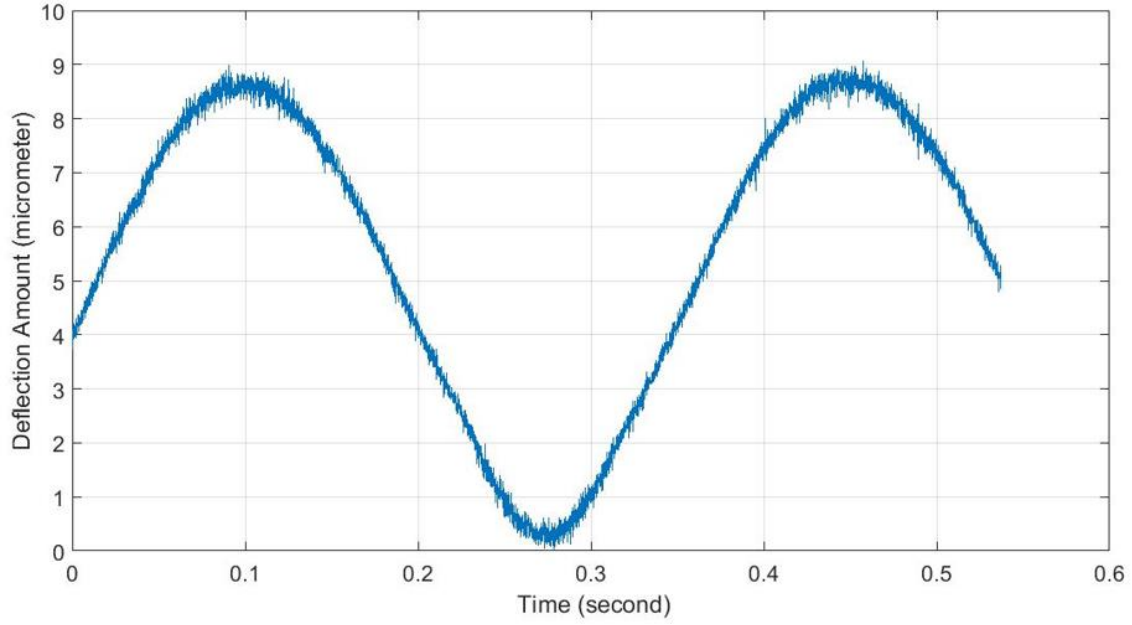

Figure 6.8 Net deflection (3000 kg-25 rpm shaft speed-16RE-EX)

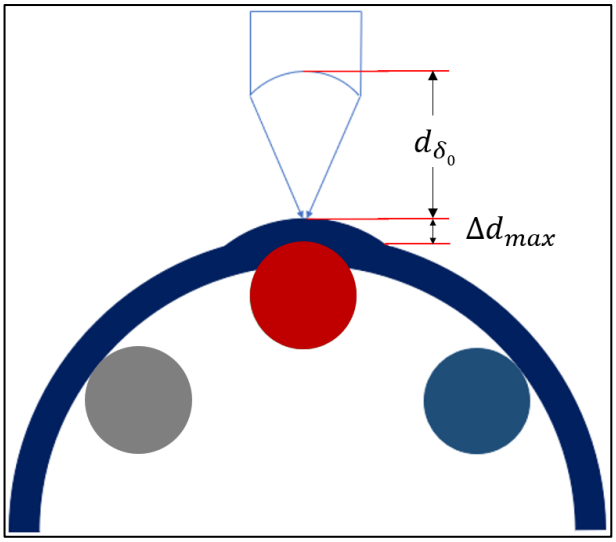

Figure 6.9 Rolling element position under sensor

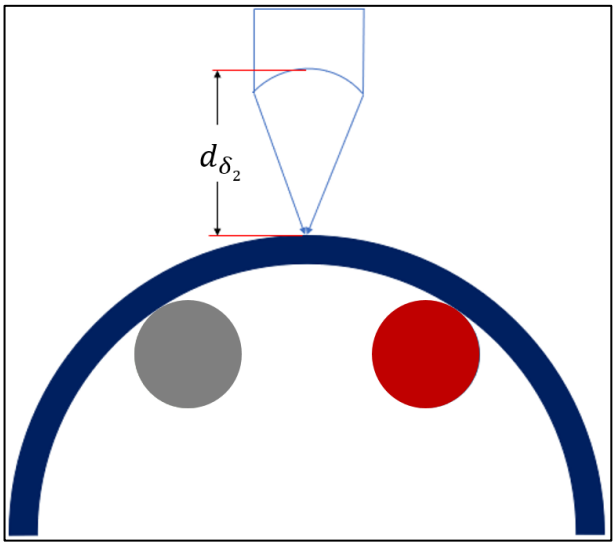

Figure 6.10 Sensor in between two consecutive rolling elements

In this work, all the stages of the rolling element position have been studied. The critical positions of the rolling elements relative to the immersion transducer position have been identified as follows; (i) when the contact occurs underneath the transducer as depicted in Figure 6.9, and (ii) while the sensor is midway between two consecutive rolling elements as shown in Figure 6.10.

These observations show clearly that as the rolling elements pass over the investigated area, the outer race is pushed radially outwards towards the probe and that once the rolling elements are outside the investigated area, the outer race starts moving away from the probe until the midpoint between two consecutive rolling elements. After this point is surpassed, with the subsequent rolling element's approach, the outer race starts to move radially outwards once again until the rolling element is in line with the probe, at which point the shortest path distance is observed. The outer race undergoes this deformation cycle with every passing rolling element.

The deflection cycles obtained in this study are very similar to sine waves – verifying the cyclic behaviour of deflection incurred by the outer race. The cyclic surface displacement of the investigated area for a brand new EX type outer race, having 16 rolling elements and subjected to a 3000 kg radial load and a shaft rotation of 25 rpm can be seen in Figure 6.11.

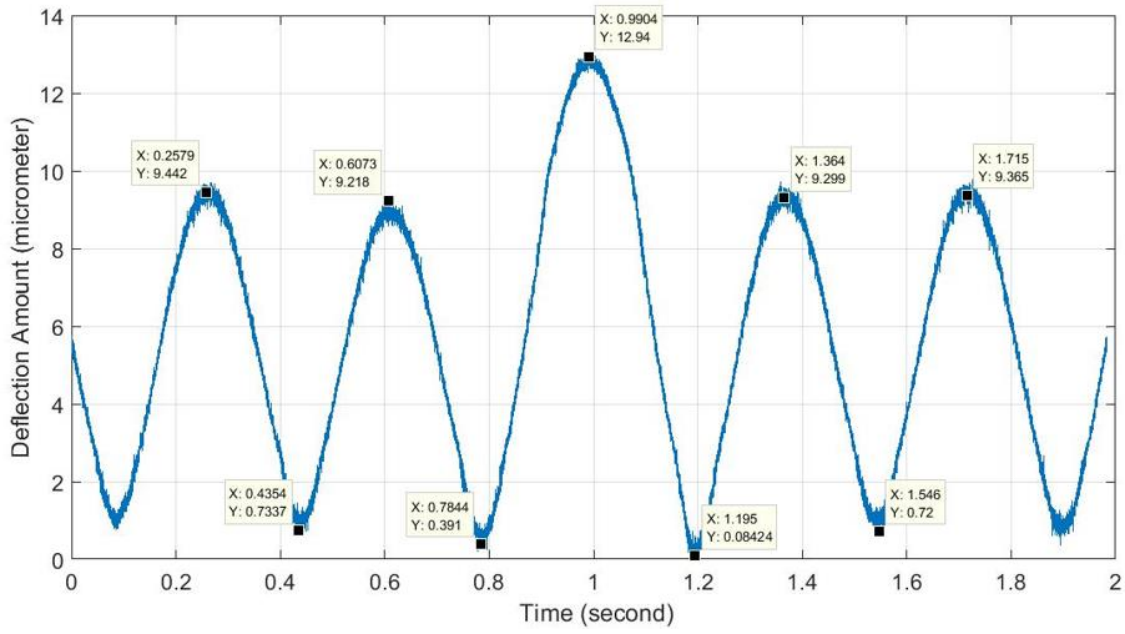

Figure 6.11 Deflection (µm) for 16 RE bearing (3000 kg, 25rpm)

Each cyclic deflection event provides information about the observed point of the outer race movements while rolling elements pass. As can be seen from the Figure 6.11, the peak to peak value of each cycle is almost the same except for the one at the middle. The slight differences in the peaks occur because the rolling elements were not placed tightly and thus some movement within the cage is allowed. Moreover, the surface qualities of each rolling element is slightly different. On the other hand, the cycle which has the higher amplitude and longer duration occurs as a result of the bearing type used: the cage of the split bearing consists of two separate cages, each having 8 rolling elements and the distance between the two adjacent rolling elements located at the cage split point (38.7 mm) is relatively bigger than the distance in between all the others (30.9 mm) as shown in the Figure 6.12. This causes a prolongation of the water path distance, and the cycle takes longer at that point.

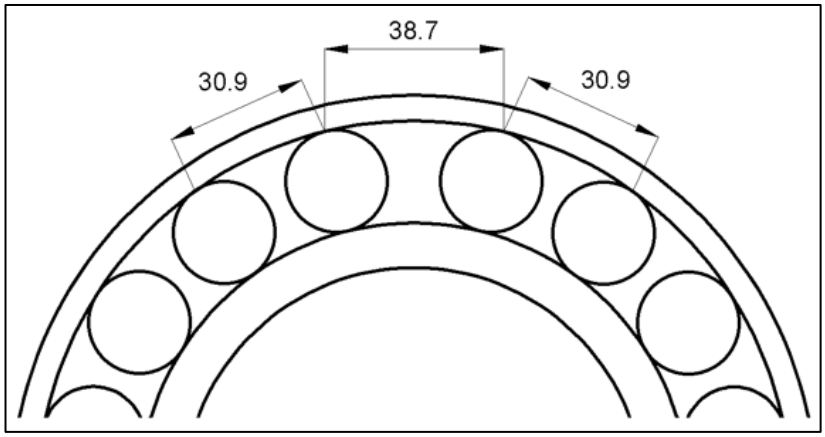

Figure 6.12 Distances, in mm, in between rolling elements at the split point, and otherwise

6.3 Operating parameters and bearing outer race deflection relationship

The operating parameters of the bearing affect the magnitude of the bearing outer race deflection. An increase in the applied radial load results in an increase of the reaction force at the contact and thus the surface displacement increases. On the other hand, an increase in speed does not affect the amount of outer race deflection significantly. In this section the operating parameters and bearing outer race deflection relationship is assessed.

6.3.1 Applied load and experimental procedure

The bearing in the application has been loaded radially through the use of a lever arm – as shown in the schematic below. The radial load applied can be read off the load gauge located at the pivot point. The load acting on the most heavily loaded rolling element can be determined by taking moments about the pivot point, and then using Stribeck's formula discussed in § 3.2.1.

The forces on the test rig bearing are illustrated in Figure 5.2. In order to calculate the reaction force at the contact, moments were taken about the pivot point as shown by Equation 6.3:

$$M = 2xF_r + \text{xmg} - W_r x = 0 \tag{6.3}$$

$$W_r = 2F_r + \text{mg} \tag{6.4}$$

Substituting in Stribeck's formula (Equation 6.5):

$$W_{max} = \frac{5(W_r)}{Z} \tag{6.5}$$

In the table below, radial load reads have been converted to the maximum load incurred by the most heavily loaded rolling element (by using moments and Stribeck's formula) for both 16 rolling element and 8 rolling element cases.

Radial load (kg) (read-out)	Force at heavily loaded RE (16RE) (N)	Force at heavily loaded RE (8RE) (N)
250	1533	3066
500	3066	6132
750	4598	9196
1000	6131	12262
1250	7664	15328
1500	9197	18394

Table 6.1 Radial load (read-out from load gauge) and the force on heavily loaded rolling element

In this study, the load has been incrementally increased from 250 to 1500 kg (equivalent to a radial load increase of 500 to 3000kg), and at each increment, the rig was left running for 45 minutes. This procedure has been repeated for different rotation speeds: 12.5 rpm and 25 rpm. A brand-new EX type outer race was tested with 16 and 8 rolling elements in the cage in order to analyse effect of the distance between rolling elements as well as the effect of the number of rolling elements on the deflection curves. The ultrasound reflections data collected has been post processed using the procedure that has been outlined in § 6.2 to obtain the net time-shift curve of the first reflection – which is directly proportional to bearing outer race surface displacement. Subsequently, the averaged net time shift data for different operating conditions which represents the bearing outer race surface displacement is obtained.

6.3.2 Bearing outer race surface displacement and applied load

Figure 6.13 shows the change in net time shift with increasing radial load of the specified zero-crossing points at the moment when a rolling element is passing through the investigated point on the outer race.

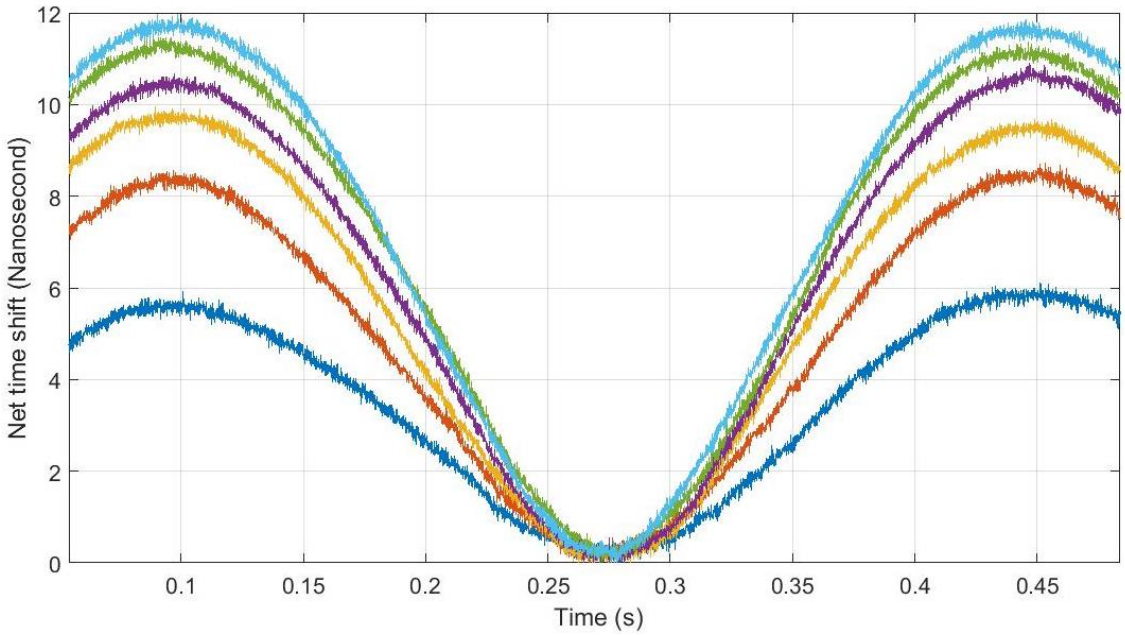

Figure 6.13 Time shift curve of EX type outer race for 16 rolling elements with varied load constant shaft speed (25rpm)

The EX type bearing was loaded from 500 kg to 3000 kg radially and the force acting on the heavily loaded rolling element increased from 1.5 kN to 9.1 kN at a shaft rotation speed of 25rpm – as shown in Table 6.1. The lowest point on the curves represents the time when the rolling element is beneath the transducer and hence incurring the highest load, whereas the peak points represent the moment when the transducer is in the middle of two consecutive rolling elements. The net time shift curves clearly show that time shift increases with applied load: increasing from 5.71 ns to 11.97 ns.

As has already been discussed in § 6.2, the time shift of the first reflection is linear to the deflection incurred by the outer race's outer surface. Hence, by applying the Equation 6.6 that governs this relationship to the time shift curve, the deflection curve can be drawn.

$$d_{deflection}(t) = 0.5ct_{timeshift}(t) \tag{6.6}$$

Where $d_{deflection}$ is the deflection at a time t, c is the speed of sound and $t_{timeshift}$ is the timeshift at time t.

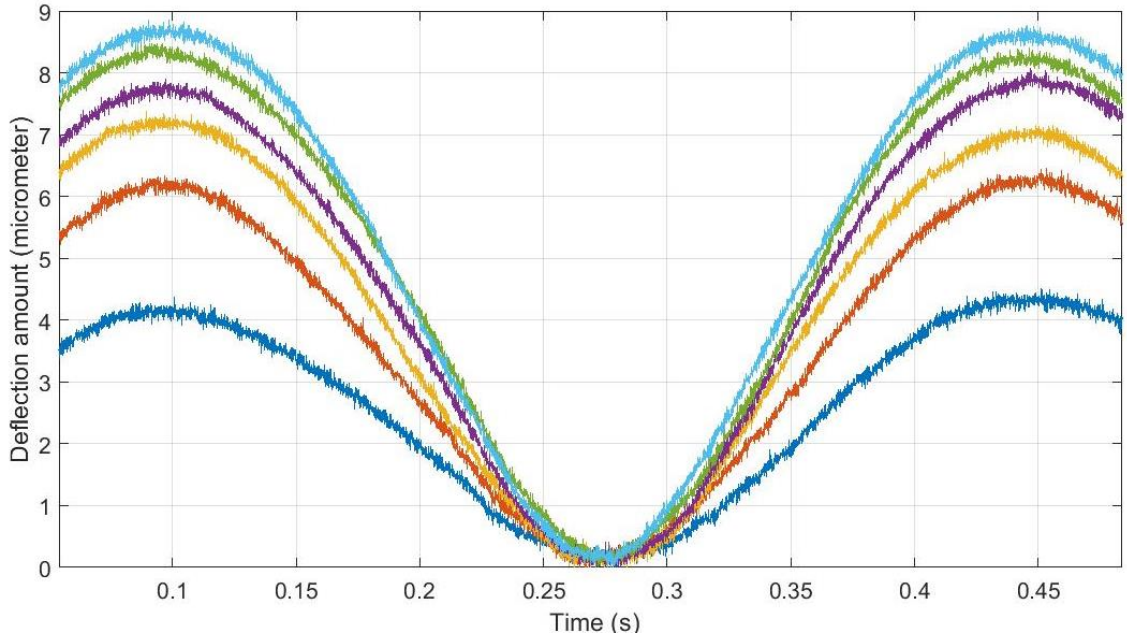

Figure 6.14 Deflection curve of EX type outer race for 16 rolling elements with varied load constant shaft speed (25rpm)

The peak to peak difference in the values of each deflection cycle gives the net bearing outer race deflection value (Figure 6.14). This varies between 4.2 µm and 8.7 µm for the rotation speed of 25 rpm.

6.3.3 Effect of rotating speed on outer race surface displacement

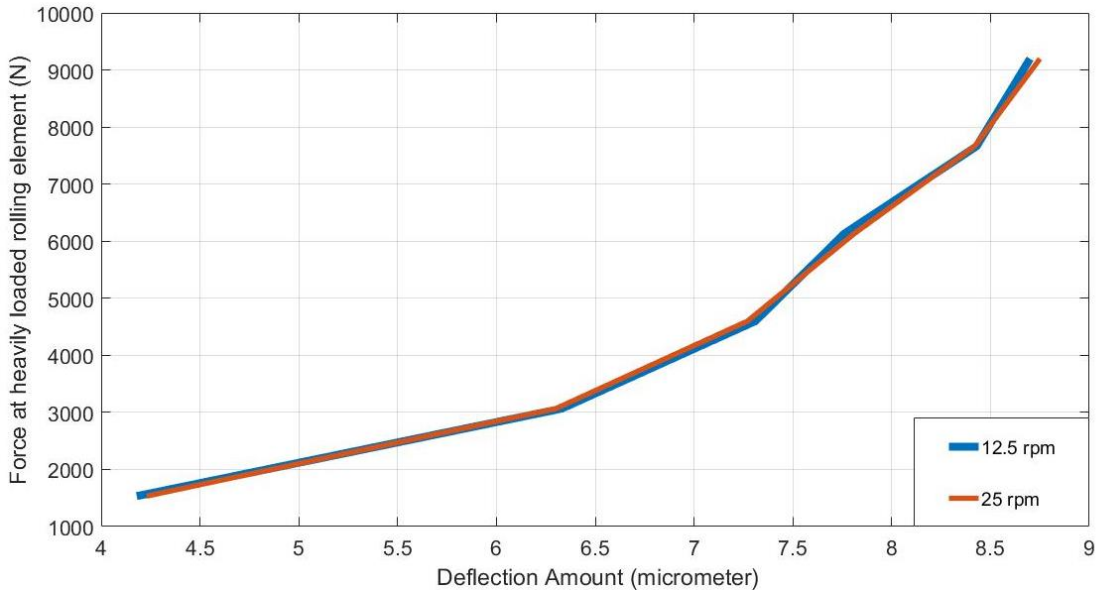

Figure 6.15 EX outer race surface displacement and applied load 12.5 and 25 rpm

Figure 6.15 shows the load-deflection relationship for different rotation speeds (12.5 and 25) for the EX type bearing. As can be seen from the plots, bearing rotation speed does not affect the deflection incurred significantly at relatively low rotation speeds. In order to observe bearing outer race deflection curves in more detail (high horizontal resolution), low rotation speeds were selected to enable the passage of every rolling element to be represented with more data points. However, at higher speeds, such as those over 1000rpm, centrifugal forces would increase the deflection incurred and must therefore be taken into consideration.

6.3.4 Effect of number of rolling elements

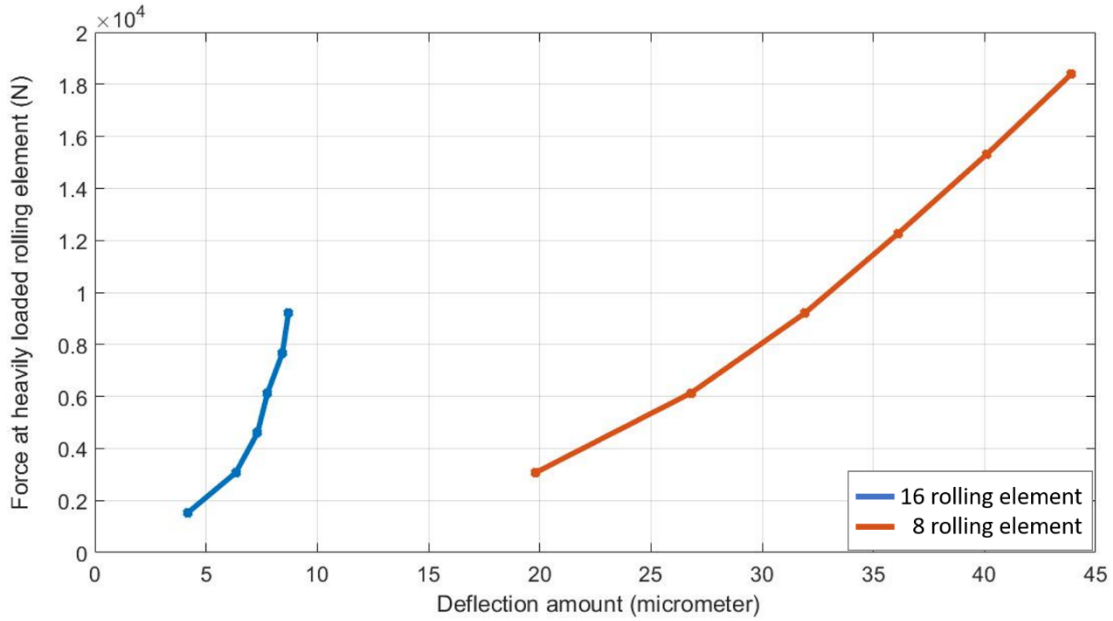

Figure 6.16 EX type outer race displacement for 16 and 8 rolling elements (12.5 rpm)

In the results that have been discussed so far, the bearings under investigation contained 16 rolling elements. However, this work has also studied how the distance between two rolling elements affects the deflection. Hence, tests with 8 rolling elements, instead of 16 have been conducted.

The load-deflection curves shown in Figure 6.16 show that for 8 rolling elements the deflections are much higher than those obtained for 16 rolling element bearings. However, similar to the 16 rolling element, the curves show a non-linear relationship between load and deflection, and that the rotation speed does not affect the deflection greatly.

This difference in deflection quantity between the 16 rolling element bearing and the 8 rolling element one can be explained by taking into consideration the beam deflection theory – which maintains that deflection is directly related to the moment of inertia, the distance between the support points, the elastic modulus, and the applied load and its position.

The rolling elements act as the supports to the radial load applied, and when the probe position is in between two consecutive rolling elements, the radial load acting on the outer race causes a deflection along its radial direction. The larger the distance between the rolling elements, the larger is the deflection incurred. Also, as the number of rolling elements decreases, the force acting on the heavily loaded rolling element is increasing as proposed by the Stribeck Equation.

6.4 Bearing outer race surface displacement real-time monitoring

The produced interface used for recording of ultrasound reflections, has been modified to process data in real time, while the bearing is in operation. In this mode, the data processing methods used were similar to those used in post signal processing, but with some modifications.

In real time mode, the user has the means to view several windows simultaneously: one window contains the first and second reflections, and two others, containing the first and the second reflections in a normalized version. Moreover, the movement of each reflection in the time domain can be monitored and plotted (using the zero crossing method) in real time.

When the system is operating in this mode, the ultrasound waves emitted onto the bearing are not in pulsed form, but in the form of a continuous wave, and in the former mode, the sampling rate is much higher than in the latter. For this reason, the resolution of the real time plots is lower than that which is obtained from post processing of data. Also, the resolution of real time plots is affected by the rotation speed – where the higher the rotation, the lower is the resolution.

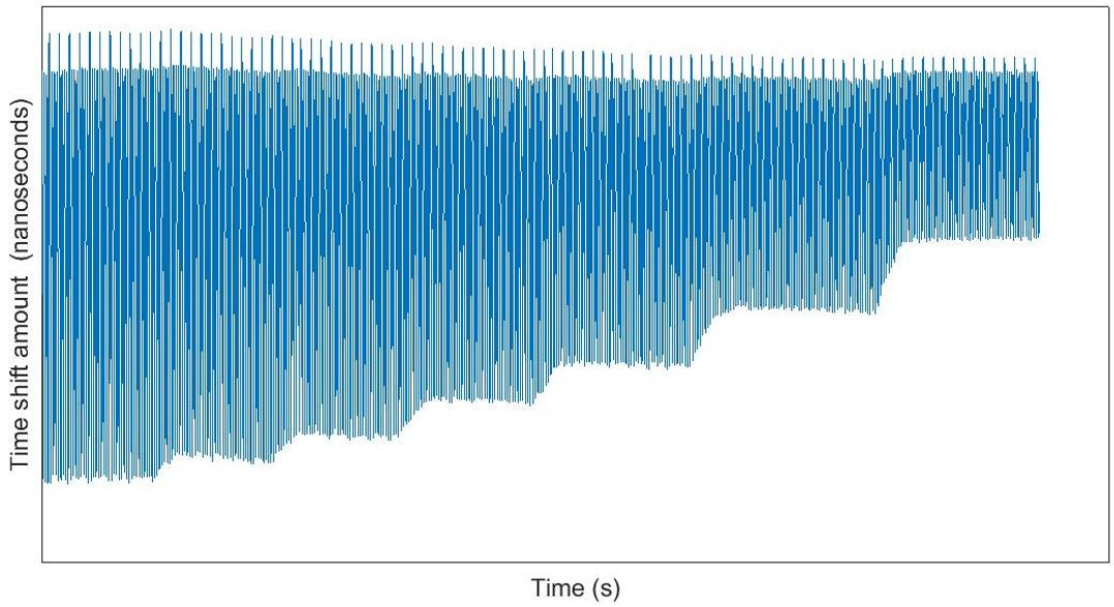

Figure 6.17 Real time time-shift graph (applied load decreasing step-by-step)

In the plot shown in Figure 6.17, it can be seen clearly that as the load was incrementally decreased, the deflection decreased correspondingly. Under the same operating conditions, the time-shift quantities measured in real-time monitoring were similar to those obtained in the post processing method at relatively low shaft speed.

The difference between the time-shift curves (and hence, in the results) lies in the amount of data points that are used in their construction. Whilst in the post processing methods, hundreds of data points are used to represent the contacting interactions, in real-time, the lower amount of data points used result in a less well defined and less accurate contacting representation. Thus, the real-time curve tends to contain noise that reduces the resolution of the measurements. For instance, consider Figure 6.18 that contains 6 net time shift curves for different radial load conditions; starting from 500 kg, with increments of 500 kg, until 3000 kg.

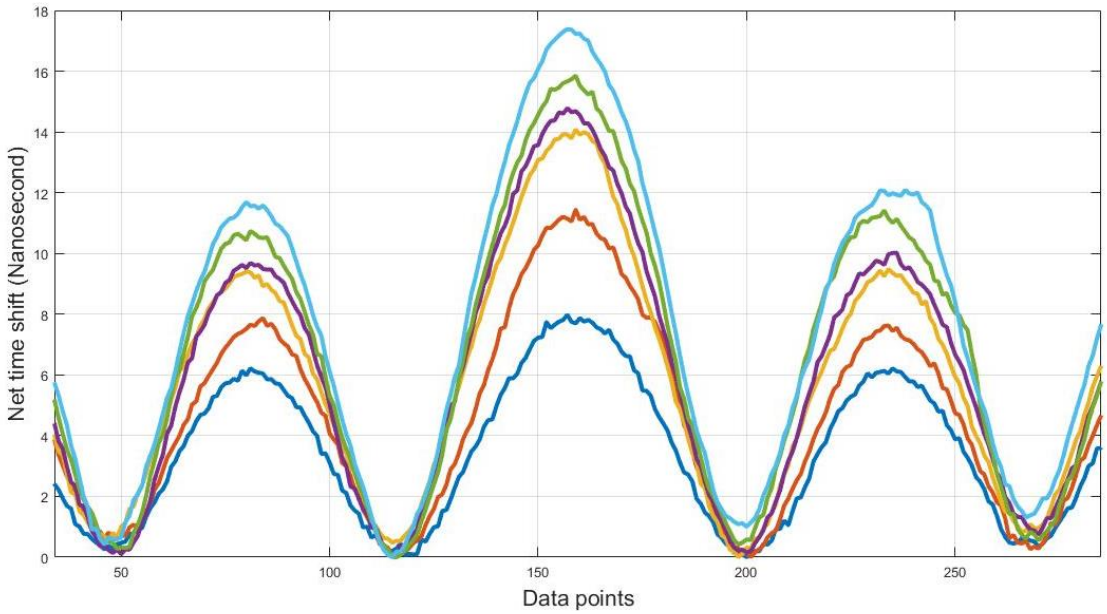

Figure 6.18 Net time shift real time data

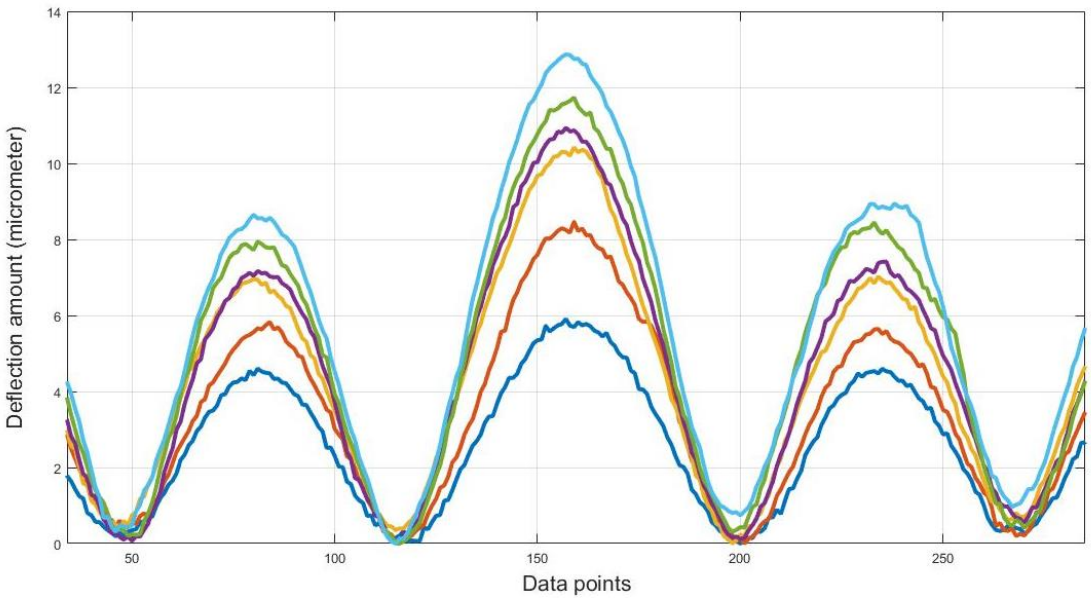

Figure 6.19 Bearing outer race deflection amount real time

Figure 6.19 shows the net time shift converted to outer race deflection amount through Equation 2.7. As can be seen from the plots, the bearing outer race deflection amount increased with radial load. Real-time bearing outer race deflection curves therefore agree with the curves that have been obtained after post signal processing.

Since this real-time method can give instantaneous deflection results at relatively small data sizes (when compared to the data produced in the post processing method), it can be used as a real-time bearing outer race deflection monitoring method.

6.5 Conclusion

In this chapter, the method used to identify and record ultrasound data was explained. Subsequently, the post-signal processing techniques used to deduce bearing outer race movement measurements have been discussed. Finally, the affects of operating conditions on the displacement of the bearing outer are presented and discussed.

The major findings of the work discussed include the following:

- It is understood that ultrasound immersion transducers can be used as proximity transducers for bearing applications;
- Outer race cyclic deflection curves can be obtained both in real-time and by post processing methods;
- While the shaft rotation speed has minor effects on the deflection magnitude of the outer race, the applied radial load and the number of rolling elements (and hence the cage geometry) significantly affect the deformation incurred.

7 ROLLING ELEMENT AND INNER RACE DEFECT DETECTION

This chapter examines the capabilities of the proposed method for inner raceway and rolling element defect detection. Artificial defect implementation on the bearing components, the post signal processing procedure assumed and the bearing kinematics are discussed briefly to facilitate the subsequent discussion on the relationship between defect size and the anomalies observed in the outer race deflection cycle.

7.1 Introduction

In-operation bearing defect diagnosis plays a vital role in preventing excessive failure costs. The desirables for such systems generally include: defect detection, defected bearing component identification, defect location and defect severity evaluation. Non-destructive bearing defect detection sensors such as vibration, acoustic emission and ultrasound sensors and data processing methods have been developed to fulfil these aims. Vibration and acoustic emission methods are generally based on the notion that when a defect comes into contact with a bearing component, an anomaly is observed in the signal collected by the sensor.

In this research, a focused immersion ultrasound transducer was employed to assess the health condition of a bearing. The principle of operation is similar to that of the other mentioned methods – whereby the outer race surface displacement cycles are affected by defects on the bearing components, resulting in anomalies in the bearing outer race deflection curve. In this part of the research, the effects of defects on bearing components (rolling elements and inner race) on the outer race deflection curves will be discussed.

The aim of these tests was to find a relation between signal discontinuity and defect size. Hence, defects in the form of line slots have been generated onto bearing outer races, inner races and rolling elements. Since the line slot width is an indication of defect severity, 3 different line widths: 0.41, 0.59 and 0.72 mm, all having a depth of 0.25 mm have been prepared by Wire-Cut Electrical Discharge Machining (EDM) on 3 different rolling elements. (In this chapter only inner races and rolling element defects are discussed. Defects on the outer race are investigated in Chapter 7). To enable easier

detection, each defective bearing element had only one defect (which means that in total 3 defected outer races, 3 defected inner races and 3 defected rolling elements have been prepared).

In order to observe defect-contact conditions in the rolling elements, the 3 defected ones were placed at known locations within the cage and the first and second ultrasound reflections were observed. Such a setup meant that one full cage revolution would give information on all the three defects. On the other hand, to evaluate the inner race defects, one healthy half of the inner race was changed with one of a known defect size. After recording the reflection signals, these were analysed and the effect of these defects was determined.

These experiments have been performed with a fixed type outer race (GR type) which had been previously used in other studies. This decision was taken to minimize vibration as when rolling elements or inner race were defected, the vibration level increased when the EX type outer race was used.

7.1.1 Generation of the artificial defects

Before the trials of the defect sizes stipulated above have been conducted, a pilot test involving a macroscopic defect was conducted. In this test, a line defect of a couple of millimeters was generated using a hand held Dremel multi tool, on a rolling element, inner race and outer race. The deflection curves obtained from this pilot study clearly showed the detection of such defects and hence a strategy to determine the minimum size defect was established. Moreover, in these preliminary tests, outer race defects were positioned at different and known locations in relation to the transducer position to analyse defect-contact location effects on the bearing outer race deflection curves. Several line defects were produced starting from 0.25mm up to a 0.65 mm width. Although the aimed line defect width sizes were 0.25,0.35, 0.50 and 0.65, these target dimensions were not achieved precisely by EDM.

In the bearing outer race deflection cycle curves, an anomaly was first observed when the 0.41 mm defect was tested. Hence, this was accepted as the minimum detectable defect size by the proposed method. Line widths of 0.59 and 0.72 mm have been further tested to show the relationship between defect size and the discontinuities observed in the deflection curves.

To determine rolling element's defect severity, three defected rolling elements each with a differently sized defect, substituted three healthy rolling elements in the cage at different locations – as shown in the image below. The defected rolling elements have been placed in both halves of the cage and they have been sufficiently spaced so as not to affect each other's deflection waves. One half (shown at the bottom of Figure 7.1) contains the rolling element having the 0.59 mm defect in its 3rd rolling element position and the 0.41 mm defected one in its 7th position, whilst the 0.72 mm defect rolling element is on the other half, in the 4th position (from the right).

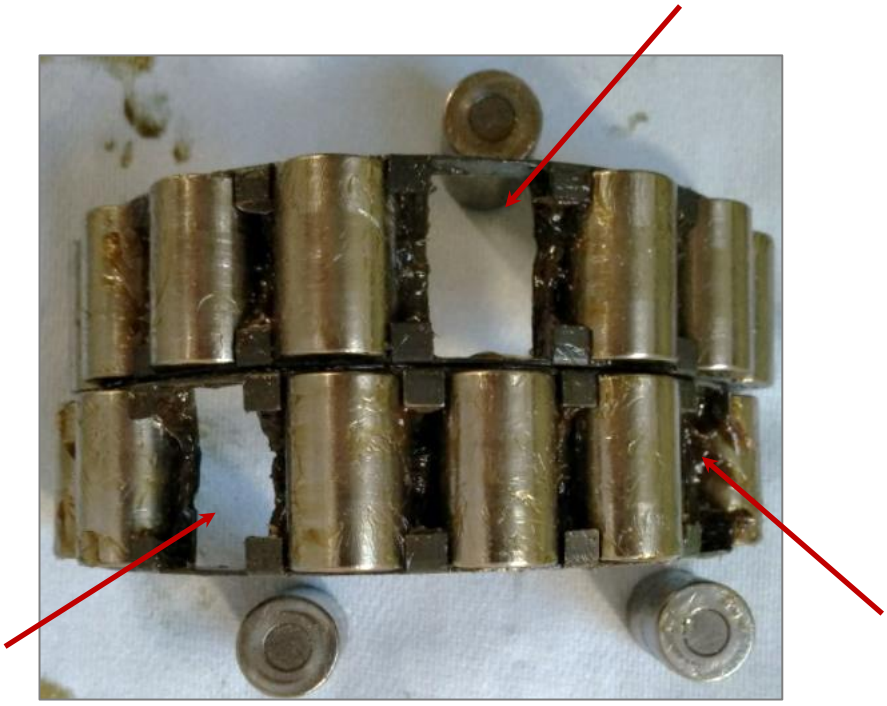

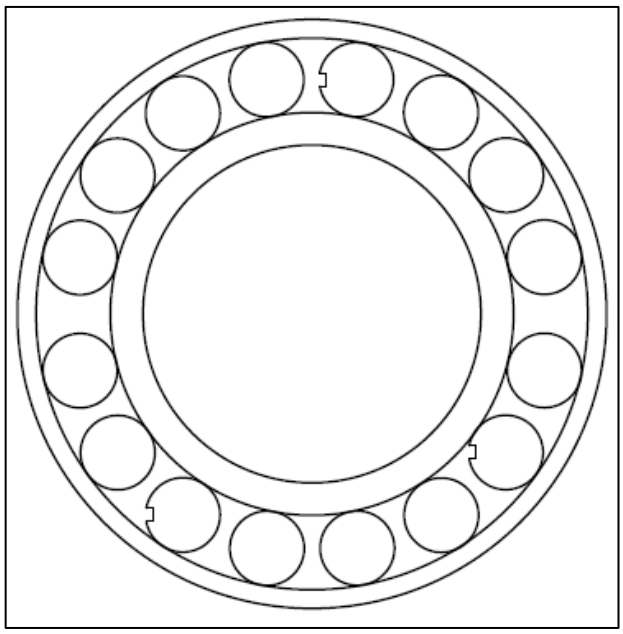

Figure 7.1 Defected rolling elements positions in the cage and sketch of defected rolling elements location

The defects produced have been measured using a Nikon microscope using a X100 times magnification as shown in Figure 7.2.

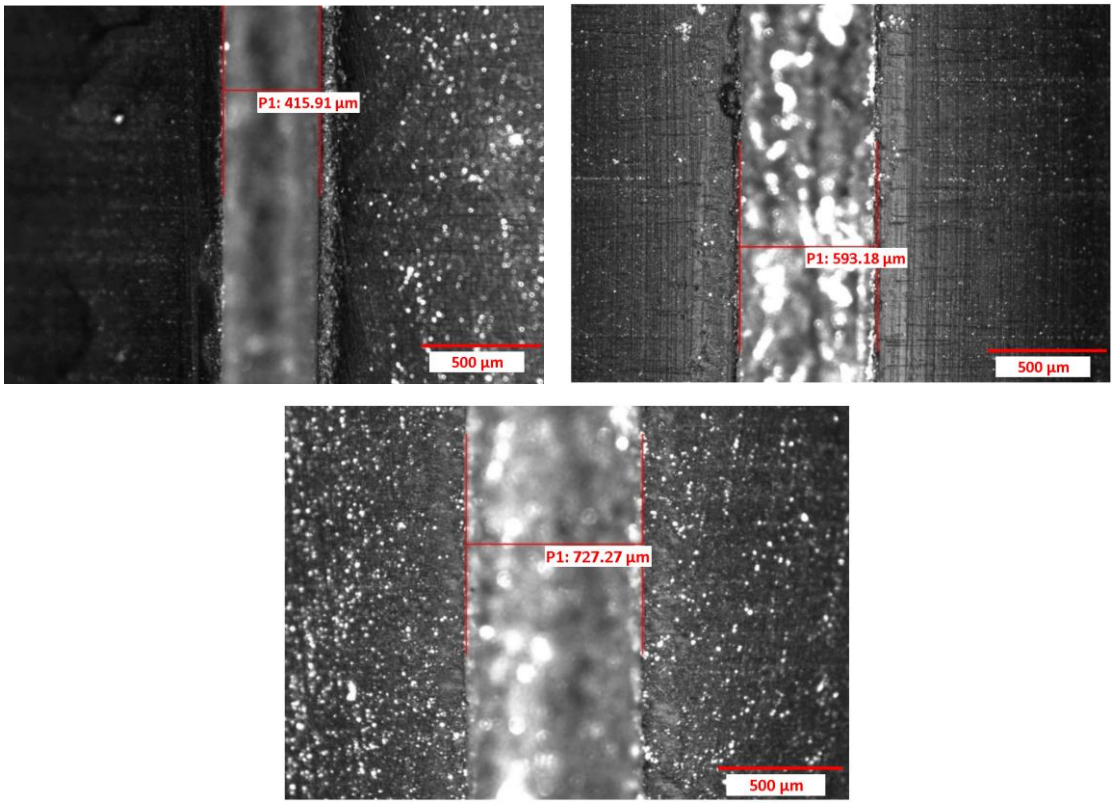

Figure 7.2 Microscope image of slot defects on rolling elements (a) 0.415 mm (b) 0.593 mm (c) 0.727 mm

7.1.2 Data acquisition and post signal processing

The first and second ultrasound reflections were recorded with the highest possible pulse repetition rate (PRR), as permitted by processing abilities of the recording computer. Also, since the post signal processing time depends on the duration of the recorded reflections and the PRR, to obtain a reasonable post signal processing time, a balance between the duration of the recording time and PRR has to be obtained. Hence, after taking these factors into consideration, the PRR was set to 11200Hz for defect detection experiments. This relatively high PRR value provides an adequate (high) resolution for the bearing outer race deflection cycles.

When a defect exists on the bearing outer race, every rolling element will impinge on the defect. However, when a defect is on the inner race or on a rolling element, the defect is not always located at the mating surfaces. Hence, to obtain deflection curves of when the defect/s come into contact the observation of many revolutions was required. Also, since the defected rolling elements were positioned in both halves of cage, to determine the defected rolling element accurately one whole cage rotation should be observed. At the employed shaft rotation speed of 12.5 rpm, one cage revolution takes 11.5 seconds, which subsequently required 3 minutes 30 seconds of post processing for the construction of the deflection curve.

Outer race surface displacement curves were obtained using the zero-crossing method (as explained in § 6.2) in addition to one more signal processing step: the deflection curves needed to be smoother to enable more precise measurements of the defects. In order to remove high frequency noise from the time domain signal low-pass filters such as low-pass FIR filters (Finite Impulse Response) and moving average filters can be applied. The moving average filter, which is the most common denoising filter due to low computational cost (high execution speed) and good performance at edge sharpness was chosen to process the raw outer race deflection curves. Although the defects could be detected from real time monitoring, the relatively small size of the defects and the low sampling rate, made defect size determination less accurate than when post signal processing methods were applied.

The moving average filter is an optimal signal processing method for time domain signals. The mathematics behind the filter can be shown by Equation 7.1.

$$y[i] = \frac{1}{M}\sum_{j=0}^{M-1} x[i+j] \tag{7.1}$$

Where $x[\,]$, is the input data, in this case the selected points which construct the deflection curve, $y[\,]$, is the averaged output data point, and M is the number of selected data points. In this signal processing method, to obtain one output data point, the interested data point and the number of $M-1$ consecutive data points are summed up and divided by M. The noise reduction amount is equal to the square-root of the number of the selected data points (Smith, 1997).

As the filter essentially produces a data point from an average of adjacent data points, whilst reducing the noise, it can also affect the delineation of the signal and its edge sharpness. For this reason, the sample length needs to be chosen carefully. Whilst a low sample length does not change the clarity of the curve, a large sample length (i.e. an average of a large number of adjacent points) can distort the curve utterly – which would lead to loss of defect indication.

For instance, consider Figure 7.3 below, which shows the deflection curve obtained for the defected rolling element having the 0.72 mm width slot. It is operating under a 1500kg radial load and rotating at a 12.5rpm shaft rotation speed. In order to analyse the impact of the sample length, the raw deflection curve and several other moving average curves with different data point lengths are exhibited. The anomaly in the outer race deflection curves caused by the defect impingement is evident.

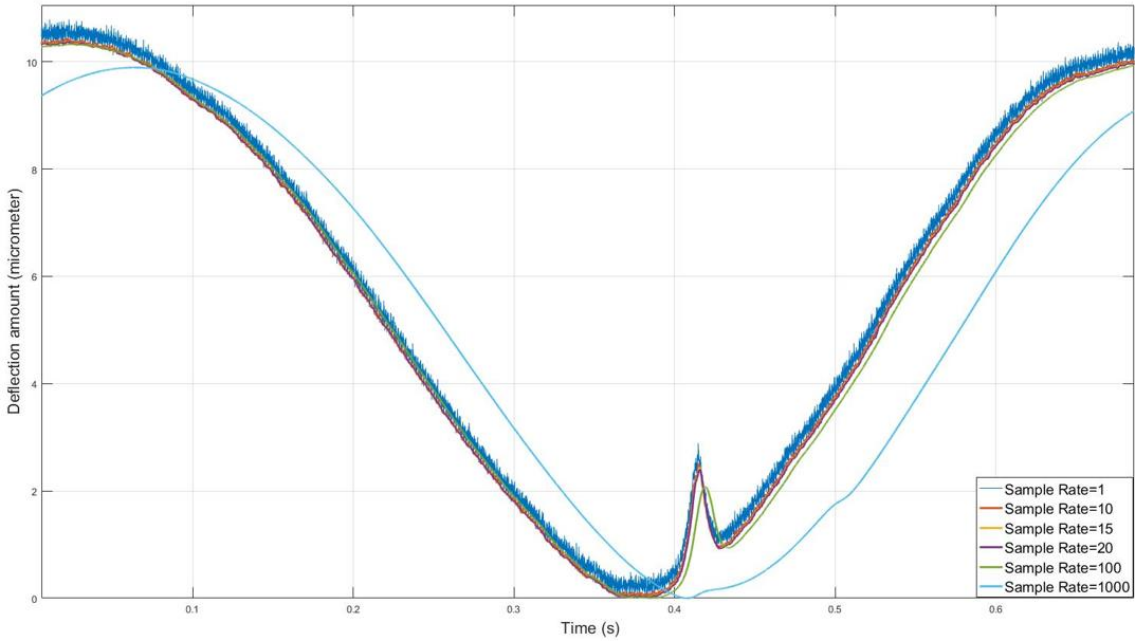

Figure 7.3 Outer race deflection curve including defect indication (discontinuity) smoothed with different sample length values

In order to compare the effect of the moving average filter sample length, consider the critical area where the discontinuity is observed. The following Figure shows a magnified image of this area.

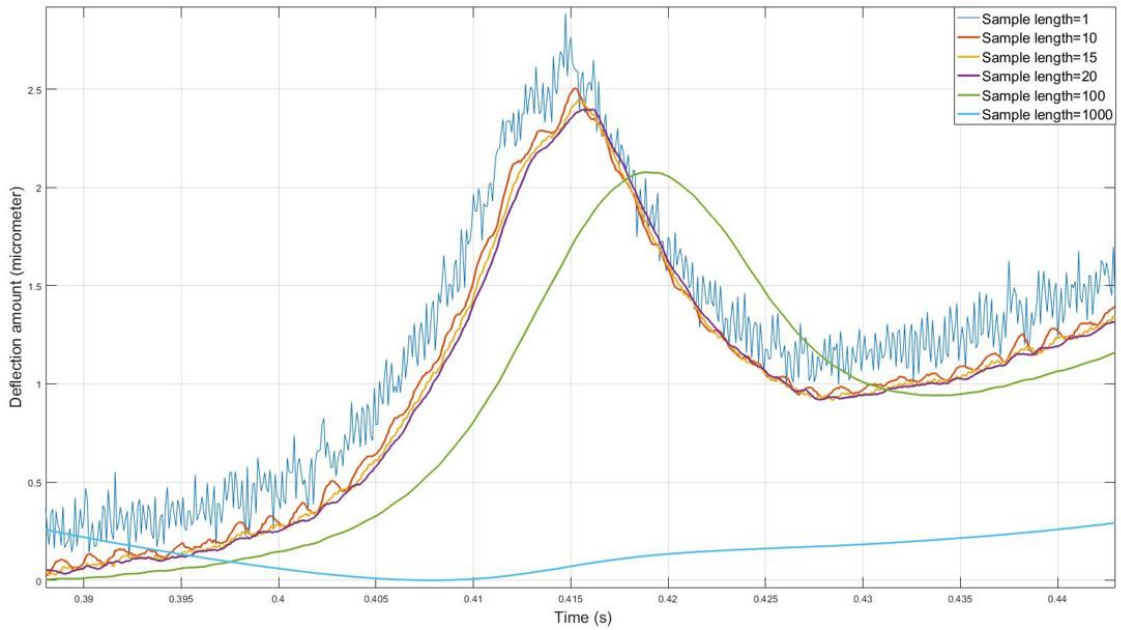

Figure 7.4 Discontinuity properties change with sample length value given to the moving average filter

When the sample length is bigger than 20 data points, the smoothened curve gets distorted: for the 1000 data point sample length curve, the defect is not even observable. Conversely, when the sample length consists of 10 data points, the smoothened curve is very close to the raw curve pattern but still contains significant noise. For the cases when the sample length is lower than 20 data points, de-noised curves are similar to each other. The smoothened curves with 10, 15 and 20 data points sample length, overlap each other at the discontinuity starting and ending points thus these sample lengths do not affect the discontinuity duration measurements. On the other hand, sample length has a slight impact on the discontinuity peak height measurements; the discontinuity peak height of the 10 data point sample length curve is 2.5 μm, for the 15 data points case it is 2.45 μm and for the 20 data point case it is 2.4 μm. Although for a sample length of between 15 and 20 data points, the de-noised discontinuity pattern is close to the raw discontinuity pattern, when using 20 data points the smoothened data curve does not contain bumps and is less noisy. Hence, throughout these defect detection tests the sample length window of 20 data points has been employed to define a discontinuity start and end points without causing disruption to the overall outer race deflection curves.

7.1.3 Bearing Kinematics for Discontinuity and Defect Size Correlation

The deflection curve generated as the rolling element passes through the investigated area gives information about the health of the contact conditions. Observing a discontinuity in a curve indicates that the bearing has a defect in one of its components. As can be seen in Figure 7.3, a discontinuity in the curve has a start point and an end point, which points represent the impingement of the edges of the slots. It has been found that the time difference between the points is correlated to the slot defect width. Furthermore, the slot defect width can be found by using a simple distance-speed-time formula when the rotation speed of the rolling element and the duration of the discontinuity are known. In order to discuss this correlation and the calculations involved, cylindrical rolling element kinematics need to be considered.

The rotation of a motor is conveyed to the gearbox and subsequently this rotary motion is transmitted to the main shaft. Since the bearing inner race is fixed to the main shaft, it rotates at the same angular velocity. The transmission of rotation movement from the inner race to the cage and rolling elements can be found using the following equations.

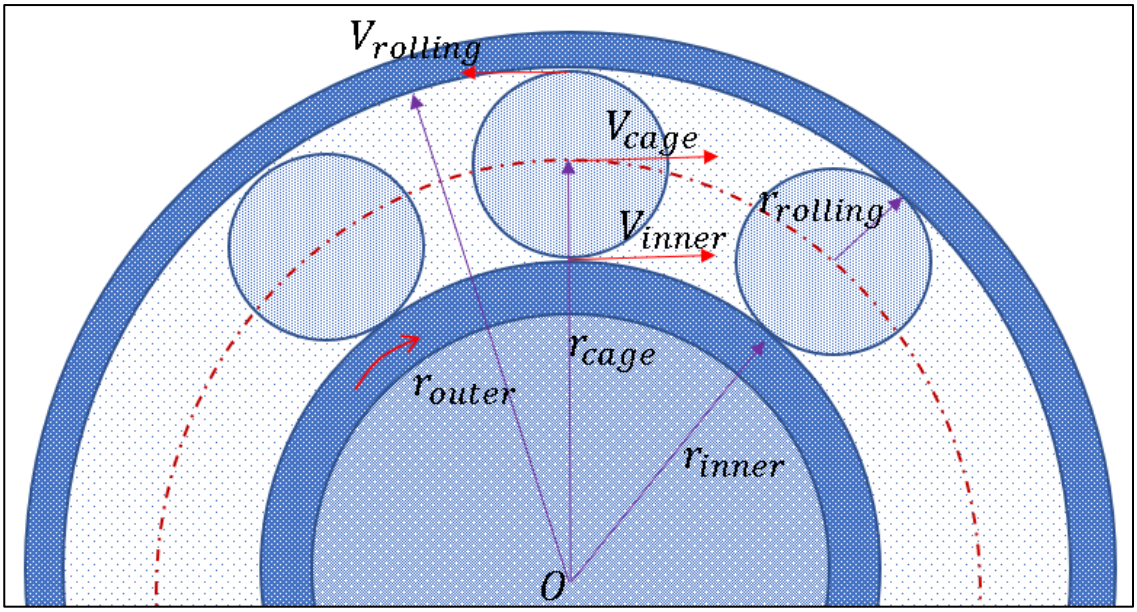

Figure 7.5 Bearing components velocities

The speed of a rotating part is defined in revolutions n per minute (rpm) and is measured by tachometer. The number of revolutions in a minute can be converted to the angular velocity, ω *(rad/s)* by using Equation 7.2:

$$\omega = \frac{2\pi n}{60} \tag{7.2}$$

The angular velocity can be further converted to linear velocity, V *(m/s)*, by multiplying radius, r *(m)*, of the point where linear velocity is measured by Equation 7.3.

$$V = \omega . r \tag{7.3}$$

For the case with a rotating inner-ring, rolling element rotation speed, n_r *(rpm)* can be found using the Equation 7.4, when the inner race rotation speed and bearing geometry are known (Harris and Kotzalas, 2008):

$$n_r = \frac{d_m n_i}{2D}\left(1 - \left(\frac{D cos\alpha}{d_m}\right)^2\right) \tag{7.4}$$

Where d_m is the bearing pitch diameter, D is the rolling element diameter, n_i is the rotation speed of inner race, and α is the contact angle – which has the value of 0 for the cylindrical rolling element bearing. The rolling element linear speed was calculated to be 45.11 *mm/sec*. This value was verified by analysing the outer race deflection curves.

The expected time duration for the defect to go through the investigated point was calculated using the known defect size and the linear velocity of the rolling element as illustrated by Equation 7.5. The expected duration was then converted to data points by multiplying the PRR (11200) to the expected duration time as shown in Table 7.1.

$$defect\ width = v_{rolling} \times duration \tag{7.5}$$

Defect width (mm)	Duration (s)	Data points
0.727	0.016	180
0.593	0.013	147
0.415	0.009	103

Table 7.1 Defect size, expected discontinuity duration and corresponding to data points

7.1.4 Distinguishing defected rolling elements

The deflection curve for the bearing outer race provides information about the contact conditions of the bearing components. If there is no defect in the contacts, a consistent deflection curve is observed. Conversely, if any of the bearing components is defected and the defect is involved in the contact interactions close to the investigated area, a discontinuity is observed.

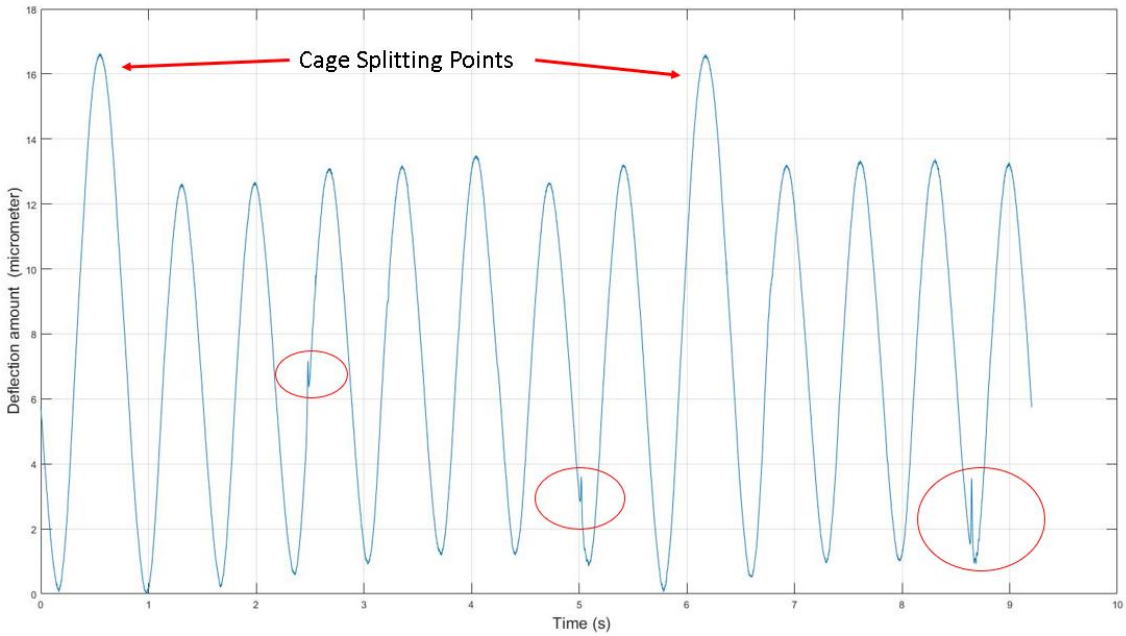

Figure 7.6 Bearing outer race deflection curve showing the passage of rolling elements, 3 of which are defected

Figure 7.6 shows the deflection in the outer raceway as 13 rolling elements pass through the investigated area, whilst the bearing is operating under a load of 1500 kg and a shaft rotation speed of 12.5 rpm. Higher deflections (larger peaks) have been observed at the cage splitting points. This enables an easy identification of each rolling element position: as the splitting points are represented by the larger peak and each trough denotes the contact interactions of a rolling element at the point when it is passing beneath the sensor, the first rolling element passes after 1s, the second rolling element passes after 1.65s, the third at 2.35s and so on.

While the ten healthy rolling elements are passing the investigated area, consistency in the outer race deflection curve is observed. However, when the three defective ones – the 3rd and 7th in the first cage and the 4th from the second cage – pass the investigated area, discontinuities were observed in the bearing outer race deflection curve as indicated in Figure 7.6. The contact interactions of these 3 defected rolling elements are analysed in more detail to investigate the influence of defect-contact positions relative to the transducer position.

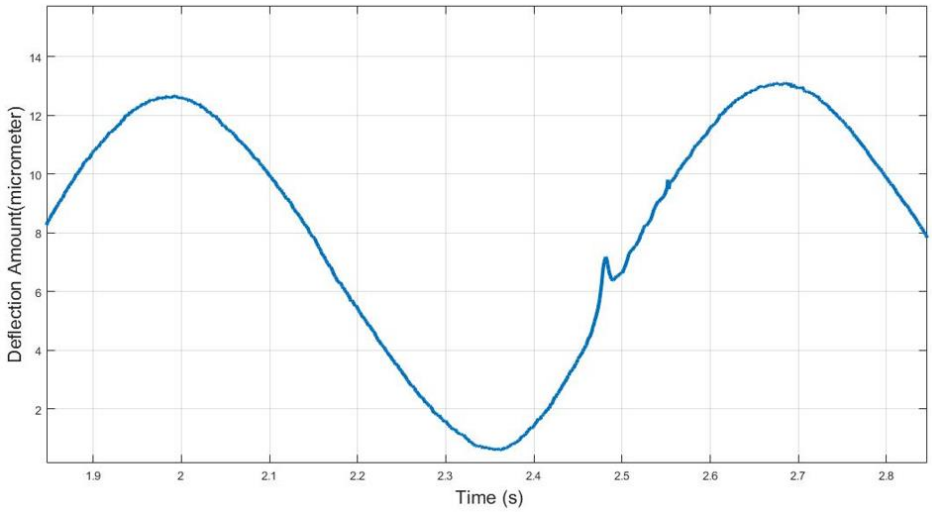
Deflection Amount(micrometer)
Time (s)

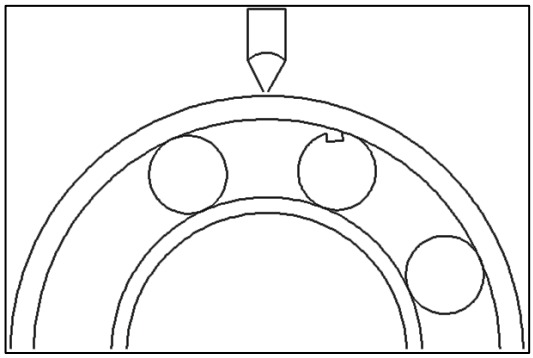

(a)

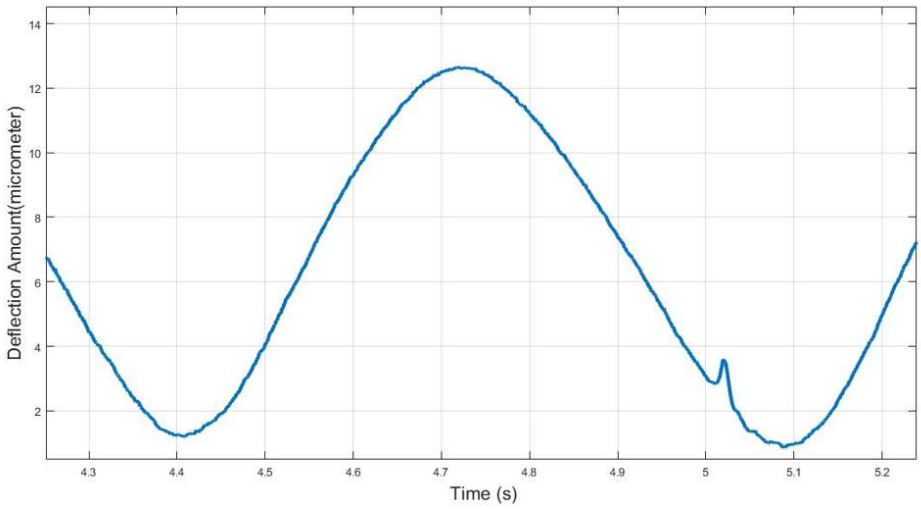
Deflection Amount(micrometer)
Time (s)

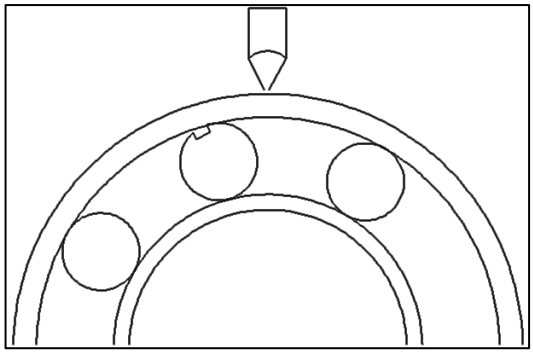

(b)

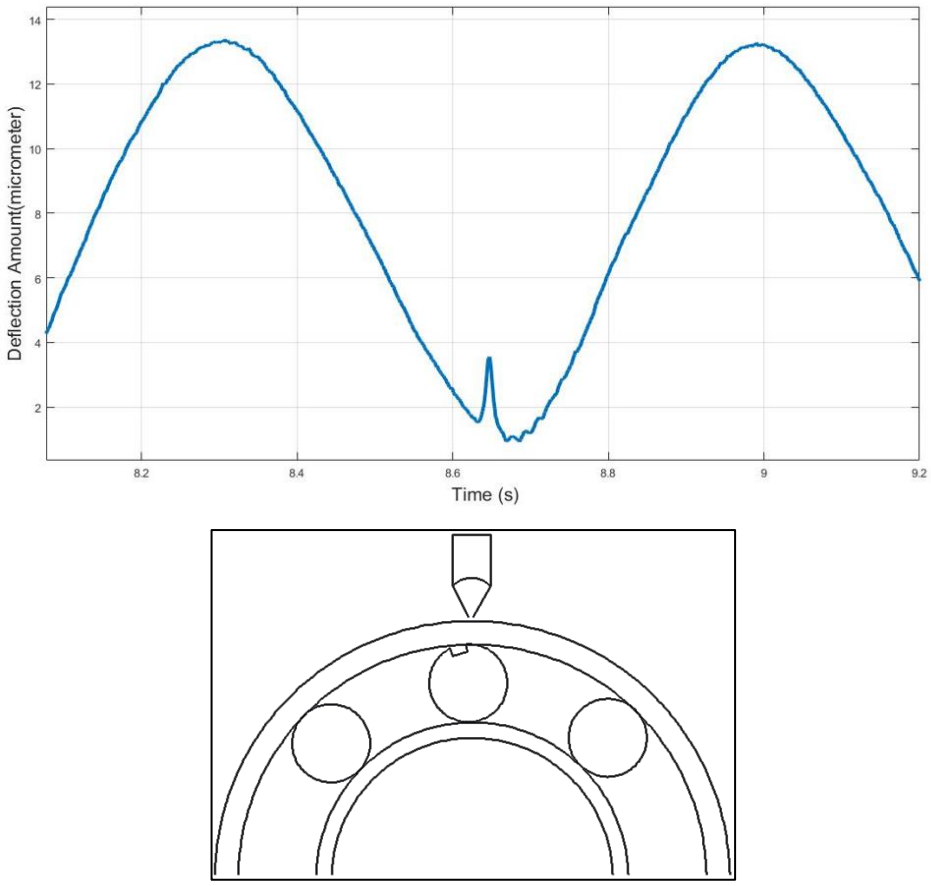

(c)

Figure 7.7 Defect indications of (a) 3rd, (b) 7th and (c) 4th rolling element contact conditions

Figure 7.7 (a) shows the defected 3rd rolling element passing over the investigated area. While the faulty rolling element is directly beneath the sensor, the line defect is contacting neither the inner race nor the outer race. However, as the defected rolling element is leaving the investigated area and before the subsequent rolling element comes into investigated area, the defect impinges the outer race or the inner race and a discontinuity appeared in the deflection cycle.

Figure 7.7 (b) shows the defected 7th rolling element moving across the investigated area. Before the faulty element passes directly beneath the sensor, the line defect impinges to one of the mating surfaces and a spike is observed in the deflection cycle. As the faulty element subsequently passes underneath the sensor, its non-defected surfaces are in contact with the races.

Similarly Figure 7.7 (c) illustrates the defected 4th rolling element (in the other cage) as it cuts across the observed area. In this case, the faulty rolling element's line defect impinges to the mating surface just before the rolling element is directly beneath the sensor.

It is therefore clear that defect detection of rolling elements through outer race deflection curve monitoring is not limited to the point when defect impingement on the mating surfaces is aligned directly under the sensor position, but detection extends over a range about this point. Discontinuities for known defects have in fact been detected all over the range between two consecutive peaks – whereby the peaks represent the midpoint between two consecutive rolling elements as shown in Figure 7.8. This detection range can be determined by using the simple distance-speed-time formula using the same principles employed in the previous section.

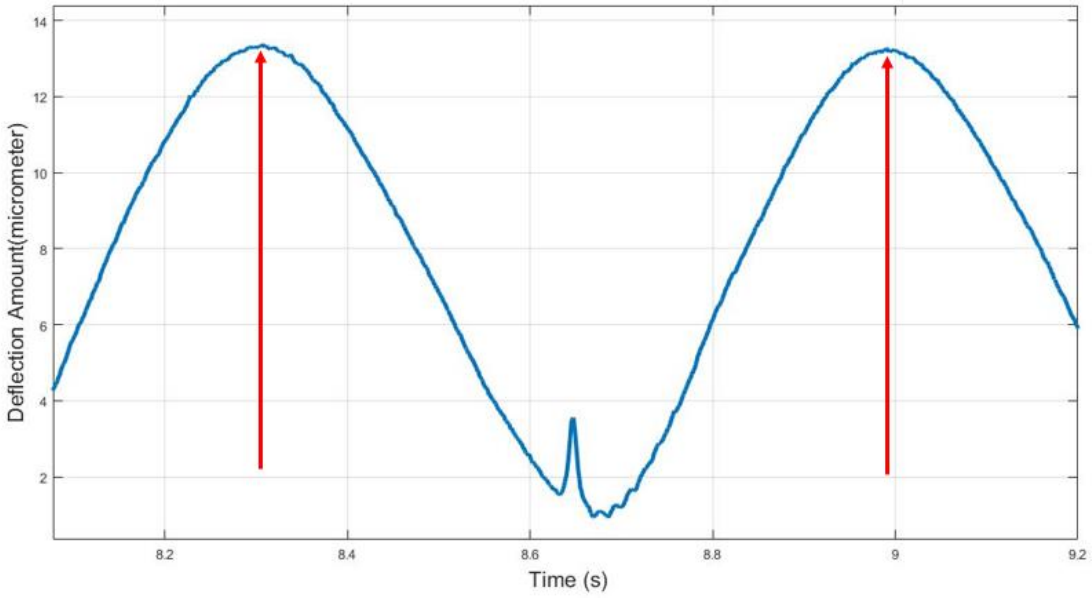

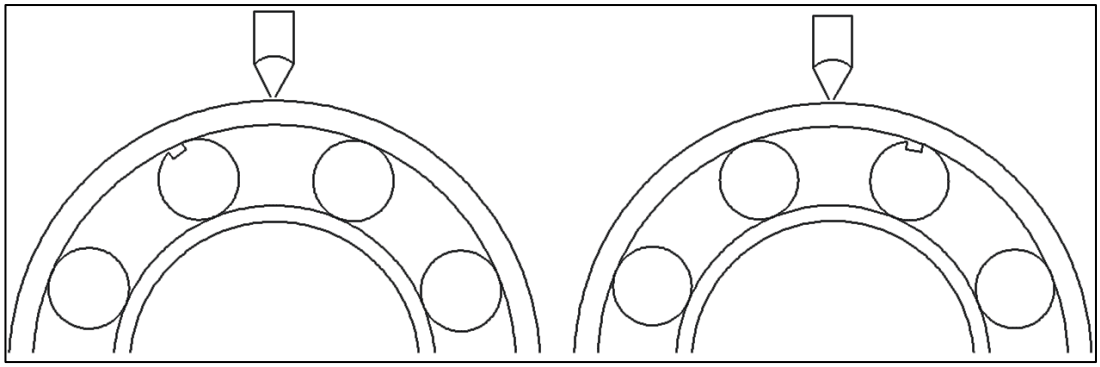

Figure 7.8 Defect indication appearance range in the bearing outer race deflection curves

The time difference between two consecutive peaks (obtained from the number of data points observed on the curves multiplied by the PRR), multiplied by the rolling element rotation speed, gives the detection range. This has been calculated to be 32 mm while the inner race is rotating at a speed of 12.5 rpm.

7.1.5 Measurement of rolling element defect size

A discontinuity in the outer race deflection curve indicates the presence of a defect in the contact areas. Such a discontinuity has two properties: its peak height and the duration as shown in the Figure 7.9.

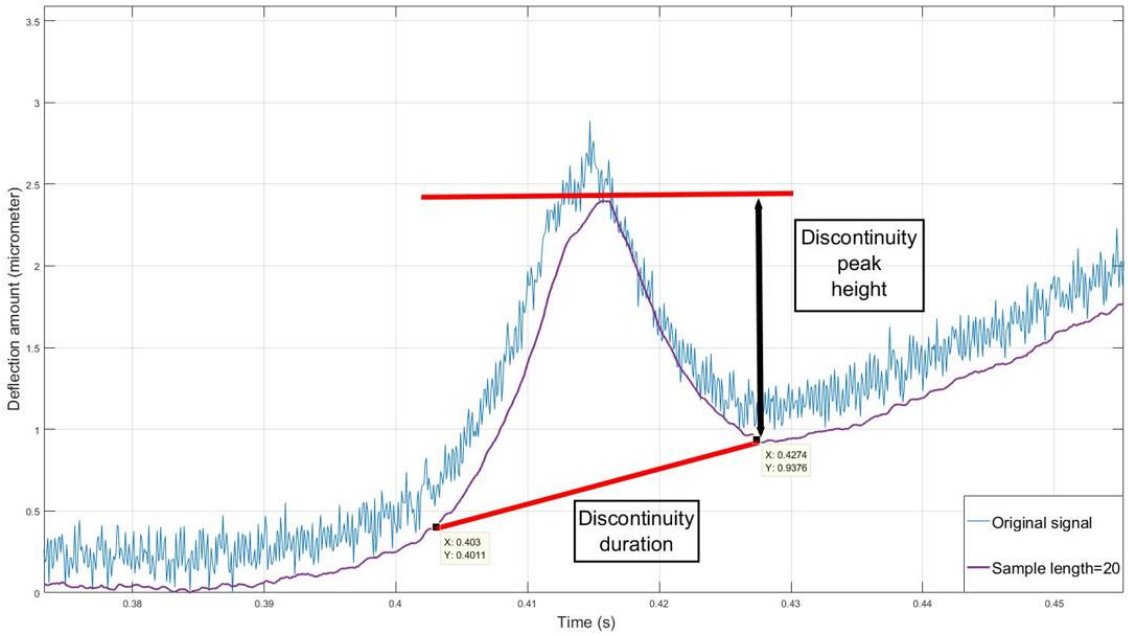

Figure 7.9 Discontinuity parameters of the outer race deflection curve

In the Figure above the original outer race deflection curve and its denoised version are shown. The occurrence for such a discontinuity is explained by the defect-mating surface interactions and the corresponding movement of the bearing outer race. It is thought that when the rolling element defect is in contact with any of the mating surfaces (inner or outer raceway), the acting radial load forces the raceways to partially fill up the gap caused by the defect. In both cases, the outer raceway undergoes a movement in the direction of the acting radial load, as indicated in Figure 7.10.

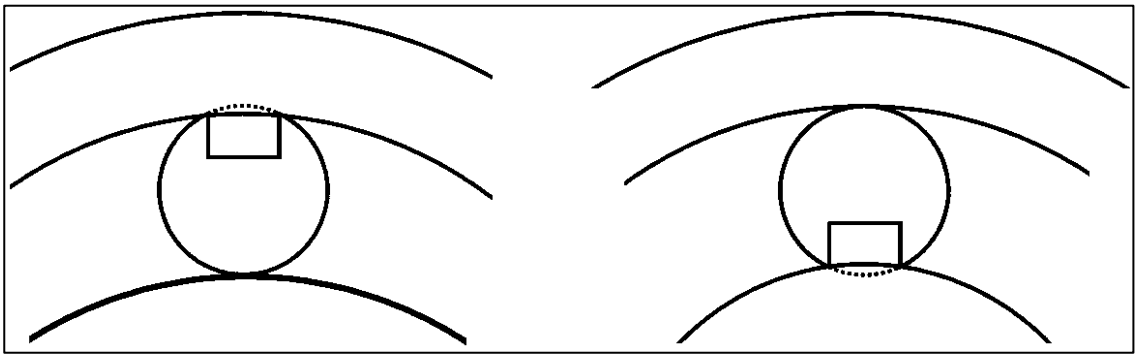

Figure 7.10 Movement of the outer raceway

The magnitude of the peak height and duration vary with the size of the defect but also with the distance of impingement relative to the sensor position. To illustrate this latter point better, consider Figure 7.11, which exhibits several curves for the same rolling element superimposed on each other. When the defect impinges the contacting surfaces right beneath the sensor, the discontinuity appears at the bottom of the trough; however, when the impingement occurs before or after the investigated point (the point in line with the sensor), the discontinuity occurs along the sides of the peaks.

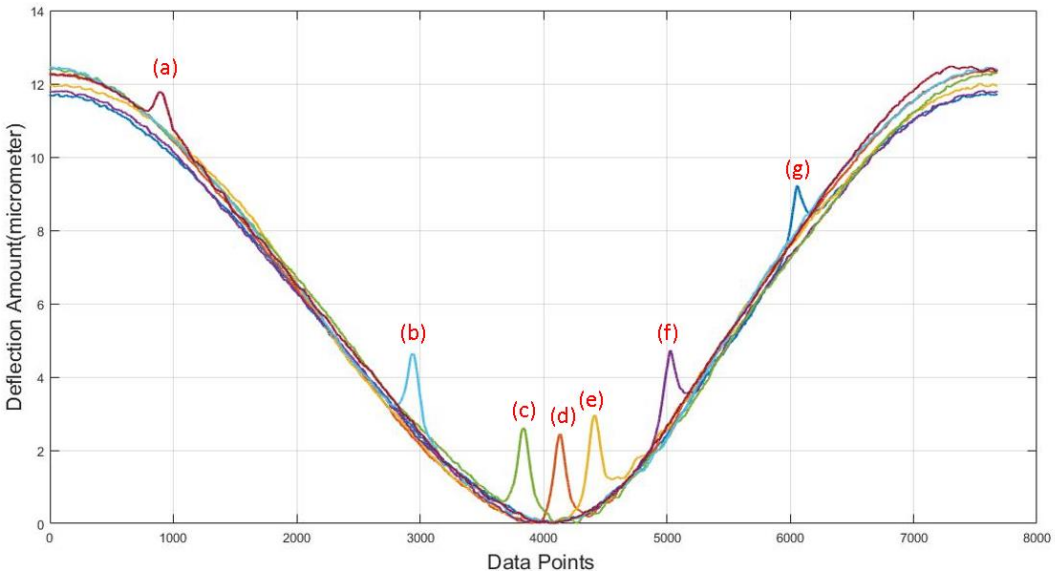

Figure 7.11 4th rolling element different position contact conditions (0.727 mm)

In Figure 7.11 each deflection cycle represents a different impingement location for the 0.727 mm width slot defect. As can be clearly seen from graph, the height and duration of the discontinuity decrease as the contact position of the defect becomes more distant from the sensor. To simplify comparison, the discontinuities have been referenced (a) to (g) starting from the leftmost discontinuity. The peak height and duration of each have been tabulated below.

Discontinuity Number	**Peak Height**	**Measured Discontinuity Duration**	**Measured defect width**
	(µm)	**(Data points)**	**(mm)**
(a)	0.52	209	0.84
(b)	1.38	246	0.99
(c)	2.01	380	1.53
(d)	2.34	333	1.34
(e)	1.68	389	1.56
(f)	1.16	291	1.17
(g)	0.71	223	0.89

Table 7.2 Variations of discontinuity properties with defect-surface contact position

The width of the fourth rolling element defect was measured optically to be 0.727 mm and the expected defect pass duration was calculated to be 180 data points. As can be seen from the Table above the measured discontinuity durations were longer than the expected duration at all the impingement locations. The reason why this happens, is not yet clear, but one possible explanation could be that the deflection cycles are being affected when the edges of the line slot strike the races. This makes the discontinuity start point and end point difficult to identify. Another reason could be that the defect enlarges during operation.

When the defected surface of the faulty 4th rolling element impinges onto either of the races directly underneath the sensor (peak (d)), the discontinuity duration is measured to be 333 data points. As the defect-races contact point becomes more distant from the sensor, the measured discontinuity duration and peak height decrease with distance. In fact, the measurements obtained for (a) and (g) are closer to the expected value of 133 data points. This could be a result of:

(i) geometry: As the sensor measures vertical displacement of the outer raceway, for example, δ, for the case when the rolling element is directly beneath the transducer, when the defect contact occurs at a distance from the sensor, the measured vertical displacement by the sensor, is $\delta\sin\theta$, where θ is the angle between the contact point and the investigated point.

(ii) a lower force acting at that contact point because the load distribution in a bearing varies with rolling element position as explained in § 3.2.1.

Since the rolling elements are rotating within the cage, the probability of a defect occurring in the detection range of the sensor is quite low. Constructing the plot shown in Figure 7.11, that consisted of just seven contact locations, was a laborious exercise that involved the screening of a substantial number of deflection curves. However, since it was desired that the relationship between the measured discontinuity duration and the defect impingement location is studied in further detail, tests involving outer race defects at different known positions have been conducted. In these tests, contact will occur with

every passing rolling element. The changes in the properties of the discontinuities of these tests shall be discussed in the following chapter.

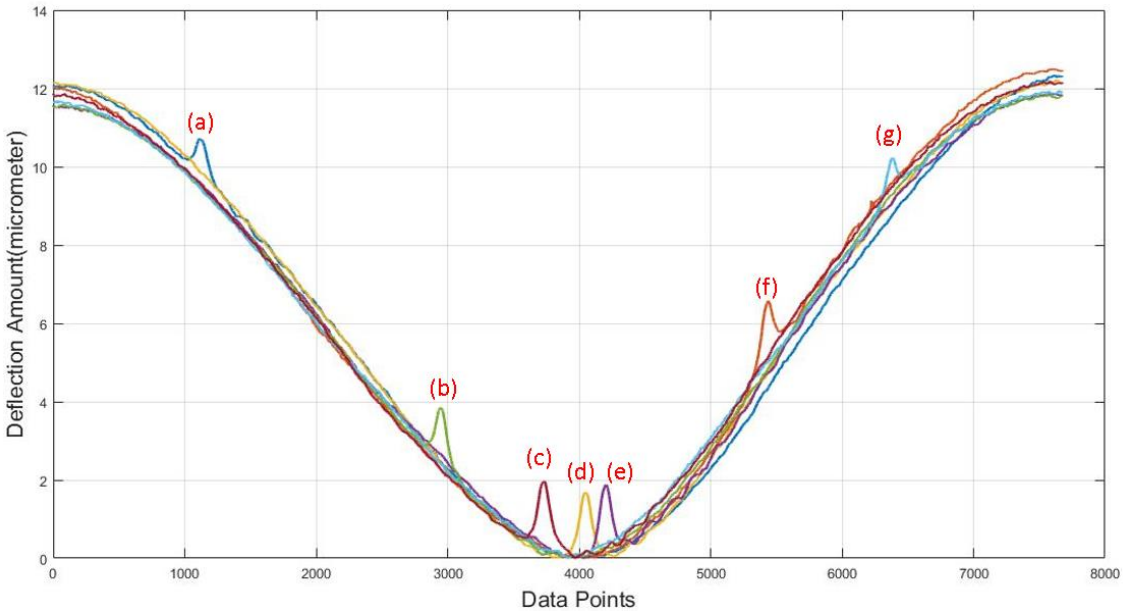

Figure 7.12 3rd rolling element different position contact conditions (0.593 mm)

Figure 7.12 shows seven superimposed deflection curves for the rolling element having the 0.593 mm width slot defect and the calculated expected defect pass duration of 147 data points. Each of the outer race deflection cycles shows the defect contact conditions at a different location with respect to the sensor position. Similar behaviours for the changes of the discontinuities are observed for this smaller defect – namely that as the defect-contact location became more distant from the sensor, the discontinuity duration is decreased. However, the duration and peak height of the discontinuities are smaller than those observed for the previously discussed larger defect, meaning that magnitude of both of these properties may be related to defect severity.

Discontinuity Number	Peak Height	Discontinuity Duration	Measured defect width
	(µm)	(data points)	(mm)
(a)	0.46	195	0.78
(b)	0.94	223	0.89
(c)	1.42	294	1.18
(d)	1.58	280	1.12
(e)	1.4	278	1.11
(f)	0.78	260	1.04
(g)	0.5	198	0.79

Table 7.3 Property variations with defect-surface contact distance from sensor position (0.593mm)

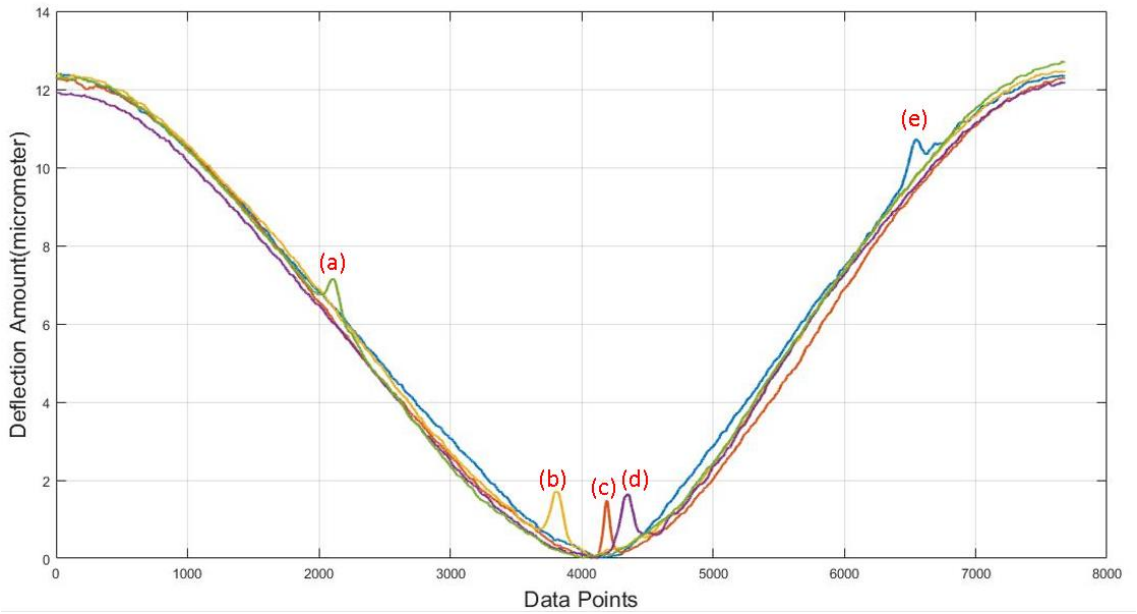

Figure 7.13 7th rolling element different position contact conditions (0.415 mm)

A superimposition of deflection curves for the smallest slot defect of width 0.415 mm and expected defect pass duration of 103 data points is given in Figure 7.13. This defect size is the smallest that can be detected when this method is employed. Once again, the discontinuity duration discontinuity peak height decreases with distance from the sensor and the measured peaks and durations are smaller than those measured for the previous larger defects.

Discontinuity Number	Peak Height	Discontinuity Duration	Measured width
	(µm)	(data points)	(mm)
(a)	0.40	185	0.74
(b)	0.95	255	1.02
(c)	1.32	192	0.77
(d)	0.99	248	0.99
(e)	0.38	177	0.71

Table 7.4 Discontinuities' properties variations with defect-surface contact position (0.415)

When comparing the plots for the three defects, it is clear that the smallest discontinuity peak heights have been observed for the smallest defect and although the measured discontinuity durations vary with the defect-race contact location, it is evident that the durations are directly related to the defect size. It can therefore be concluded that the method is able to detect defects as small as 0.415mm.

7.2 Defect detection and assessment of inner race line defects

In this part of the research, the detection capabilities of inner race defects by the monitoring method under scrutiny shall be discussed. In these experiments, one healthy half of the inner race has been replaced with one having a known defect size. Subsequently, the first and second ultrasound reflections were recorded together for the duration of one revolution of the inner race. By applying the same post signal processing techniques employed in the previous section, deflection curves have been constructed and defect related discontinuities were analysed.

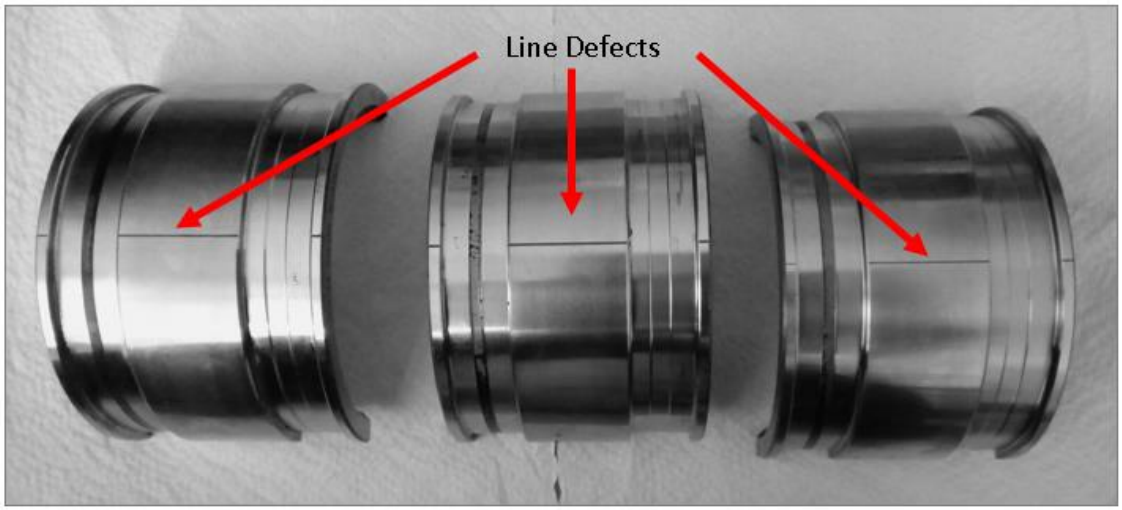

Figure 7.14 Different sizes defects (0.36mm, 0.56mm, 0.63mm)

The artificial line defects that were generated on the inner races by EDM were measured with a stereomicroscope and found to have widths of 0.36mm, 0.56mm and 0.63mm width and a depth of 0.25 mm can be seen in Figure 7.14 and 7.15.

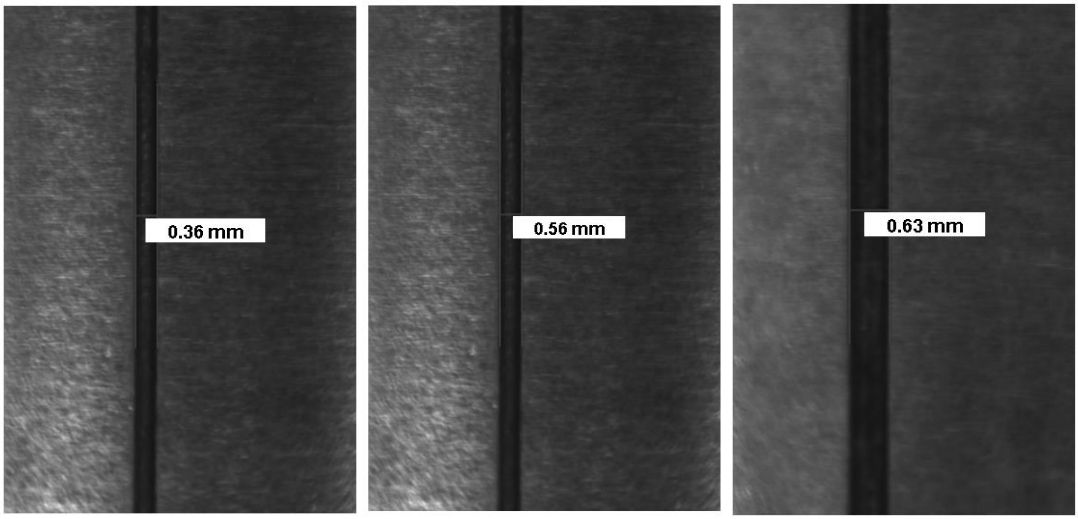

Figure 7.15 Line slot defects images

7.2.1 Identifying the inner race defect

A defect on a rolling element can be detected when the defect impinges onto the contact surfaces – which does not occur at every cycle, but when it occurs, it will be displayed somewhere along the same cycle. For instance, if the 3rd and 7th rolling elements have defects, when the discontinuities are present, they will be somewhere along the 3rd and 7th cycles of the deflection curve respectively. However, a defect on an inner race can be involved in contact interactions with any of the rolling elements and hence on the

deflection curve, the discontinuity generated from such an interaction could lie at any point. Therefore, by observing several curves and assessing the position of the discontinuities given, the defected component (inner race or rolling element) can be identified.

7.2.2 Defect size measurements at different position

The expected inner race defect pass duration and data points for the generated line slot defects, as calculated using the methods described in section 6.1.2, have been presented in Table 7.5. These Figures have been compared to the discontinuity durations measured experimentally. The peak heights and the effect of defect-contact location relative to the sensor position has also been evaluated.

Defect width (mm)	Duration (s)	Data points
0.63	0.0139	156
0.56	0.012	139
0.36	0.0079	89

Table 7.5 Inner race defect sizes and rolling element expected passing duration

For each defective inner race, a number of deflection curves exhibiting the defect discontinuity have been superimposed on each other. For instance, for the defect measuring 0.63 mm, six curves displaying the discontinuity at different locations have been compiled in Figure 7.16. For simplicity, the discontinuities have been referenced (a) through to (f) starting from the leftmost peak in the rightward direction.

The discontinuity peak height and duration were found to decrease as the defect-contact location becomes more distant from the position of the sensor. This behaviour is similar to that observed for rolling element defect detection.

On the other hand, when the inner race's defect contact location is in very close proximity to the sensor, the number of data points for the duration of the peak was observed to be larger than when contact occurred directly beneath the sensor. This phenomenon has also been reported in rolling element defect detection. Although the reason behind this observation is still not clear, the proposition that it might be related to the slot defect edge

hitting the mating components still holds: when the inner race line defect edge hits the rolling element, the transmitted impact effect of the edge is detected by the ultrasound immersion transducer and results in an increase of the discontinuity duration.

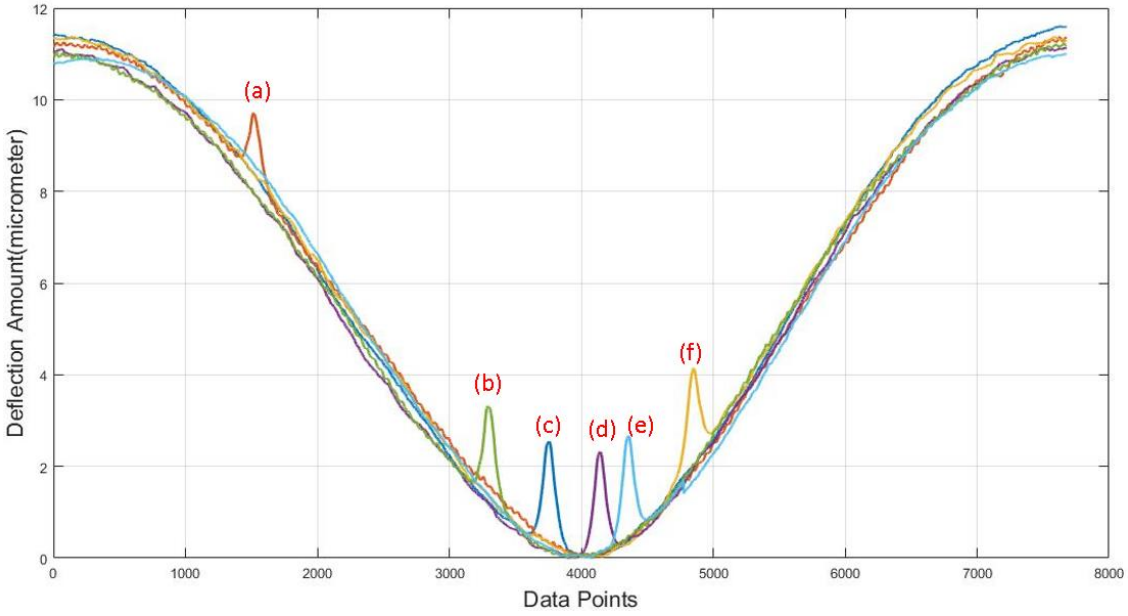

Figure 7.16 Bearing outer race deflection curves' defect indications for different inner race defect contact conditions (0.63mm)

Discontinuity Number	**Peak Height**	**Discontinuity Duration**	**Measured width**
	(µm)	**(data points)**	**(mm)**
(a)	0.94	225	0.90
(b)	1.629	254	1.02
(c)	1.9818	299	1.20
(d)	1.95	285	1.14
(e)	1.82	304	1.22
(f)	1.425	274	1.10

Table 7.6 Variations of the discontinuity properties with defect-surface contact position (0.63 mm defect)

Figure 7.17 exhibits seven superimposed deflection curves for the inner race having the 0.56 mm width slot defect and a corresponding expected defect pass duration of 139 data points. Each of the deflection curves shows the inner race defect contact conditions at a different location with respect to the sensor position.

In general, a similar pattern for the variation of the discontinuities' properties is observed for this smaller width line defect when compared to the larger defect, namely: i) the discontinuity duration decreases when the defect-contact location becomes more distant from the sensor, ii) the discontinuity peak height decreases in a similar way as the discontinuity duration. The latter suggests that both properties of the discontinuity can give an indication of the defect severity.

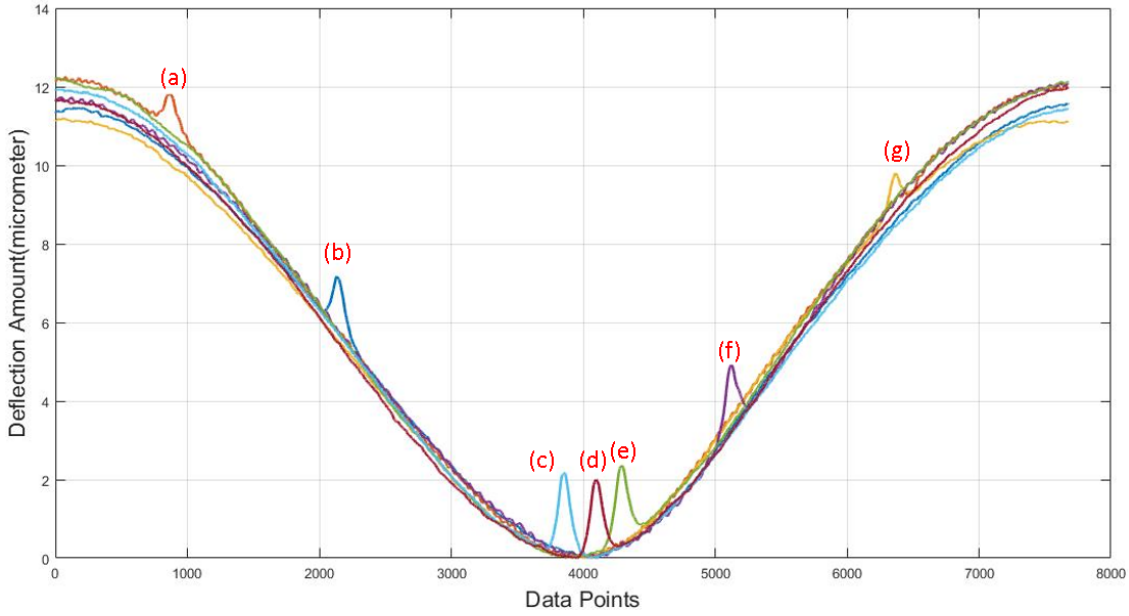

Figure 7.17 Bearing outer race deflection curves' defect indications for different inner race defect contact conditions (0.56mm)

Discontinuity Number	Peak Height	Discontinuity Duration	Measured defect width
	(μm)	(data points)	(mm)
(a)	0.50	221	0.89
(b)	0.85	262	1.05
(c)	1.86	286	1.15
(d)	1.69	261	1.05
(e)	1.48	280	1.12
(f)	1.02	271	1.09
(g)	0.51	230	0.92

Table 7.7 Variations of discontinuity properties with defect-surface contact position (0.56 mm defect)

Although as in previous cases the peak height and duration decrease with distance from the sensor location, the defect was only detected over a distance equal to one fourth of the distance between two consecutive rolling elements. Beyond this point the discontinuity becomes too small for detection, providing evidence that 0.36 mm is the limit for detection.

The smallest inner race slot defect width is 0.36 mm and the expected defect pass duration is 89 data points. The superimposed deflection curves (each showing different defect contact positions) are shown in Figure 7.18 for smallest defect. The measured value that is given by this method is twice the actual value of the defect. Hence, it can be concluded that although the method is able detect an inner race defect, provide information about the defect severity and defect-contact position clearly, it is not able measure defect size.

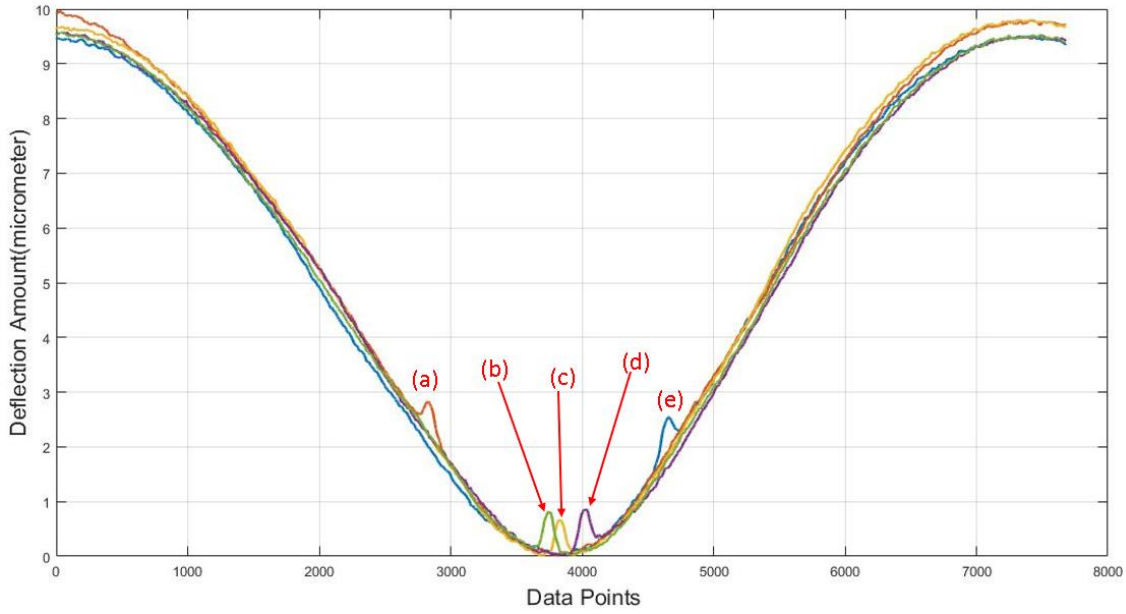

Figure 7.18 Bearing outer race deflection curves' defect indications for different inner race defect contact conditions (0.36mm)

Discontinuity Number	Peak Height	Discontinuity Duration	Measured width
	(µm)	(data points)	(mm)
(a)	0.23	163	0.65
(b)	0.62	191	0.76
(c)	0.60	174	0.70
(d)	0.51	195	0.78
(e)	0.27	170	0.68

Table 7.8 Variations in the discontinuity properties with defect-surface contact position (0.36mm defect)

In order to illustrate the discontinuity peak properties variation with defect-contact position relative to the transducer, the measured discontinuity peak height and peak duration were plotted for each of the different defect sizes and contact positions.

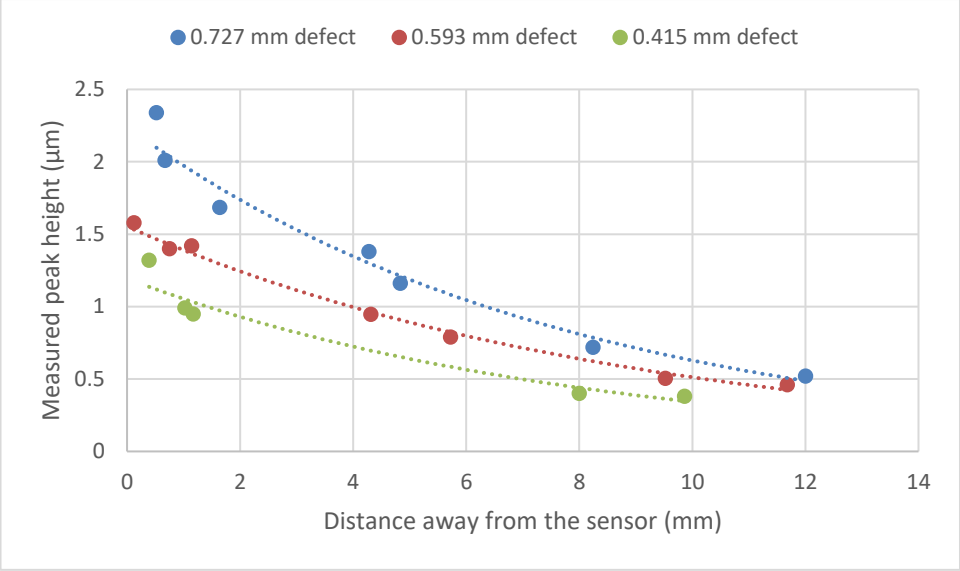

Figure 7.19 Measured peak height (µm) with distance from the sensor (mm) for rolling element defects

Peak height variation with defect-contact position relative to transducer for 3 different rolling element defects can be seen in the Figure 7.19.

As has been explained in § 7.1.2, when any defected component comes into contact with a mating surface, the bearing outer race incurs a movement in the direction of the acting force on the bearing. This is observed as an anomaly in the outer race deflection curves. When this contact condition occurred underneath the sensor, a larger vertical movement is measured than when the defect-mating surface contact occurs at a distance from the sensor, as a result of geometry and load distribution. These phenomena resulted in a discontinuity peak height decrease, as the defect-contact position became more distant from the transducer.

Figure 7.19 clearly shows how the peak height observed for a rolling element defect-contact interaction exhibits an exponential behaviour with distance from the sensor. This means that the method has potential to measure defect size through this parameter, however, more data needs to be collected. If these experiments were extended with a larger number of differently sized defects and different locations, smoother trends would be obtained. A similar pattern has been observed for the inner raceway defects, depicted in Figure 7.20.

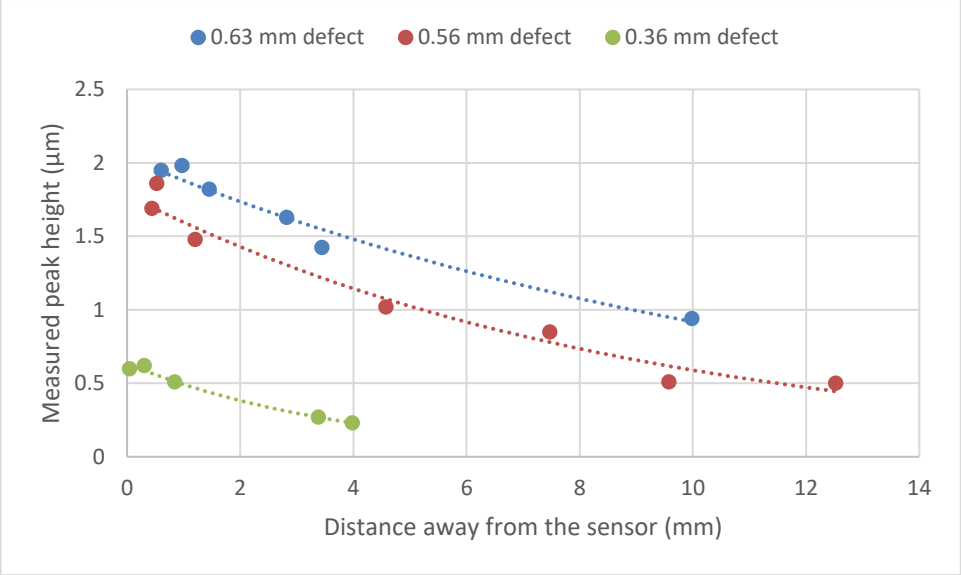

Figure 7.20 Measured peak height (µm) with distance from the sensor (mm) for inner raceway defects

In order to find a correlation between defect width and discontinuity duration, the measured peak durations for the three different rolling element defects were plotted against the defect-mating surface contact positions.

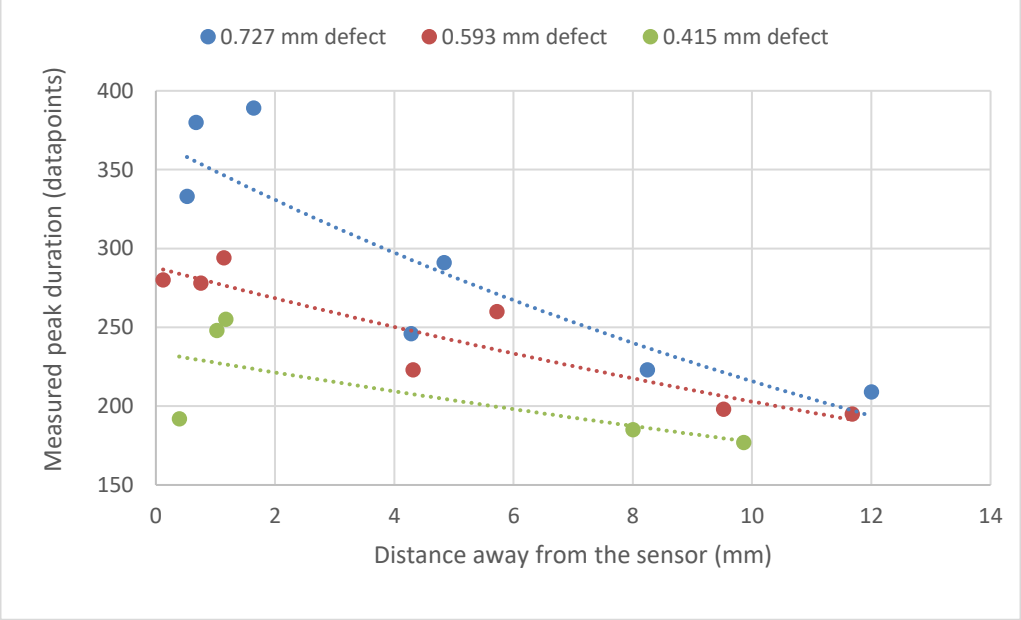

Figure 7.21 Measured peak duration (datapoints) with distance from the sensor (mm) for rolling element defects

The expected discontinuity durations are 180, 147, and 103 data points for the 0.727, 0.593, and 0.415 mm rolling element defects respectively. However, all of the measured discontinuity durations were longer than the expected values. Figure 7.21 shows how the measured discontinuity durations decreased as the contact distance from the sensor increased. As previously discussed, the defect edge impacts onto the mating surface distort end point and start point of the discontinuity. Thus, the measured defect size is not close to the real values.

Similarly, the measured discontinuity durations for the inner race defects were plotted in Figure 7.22 and the same observations as for rolling element defect durations can be drawn. However, for both the rolling element defects and the inner raceway defects, the measured durations correlate to the defect size.

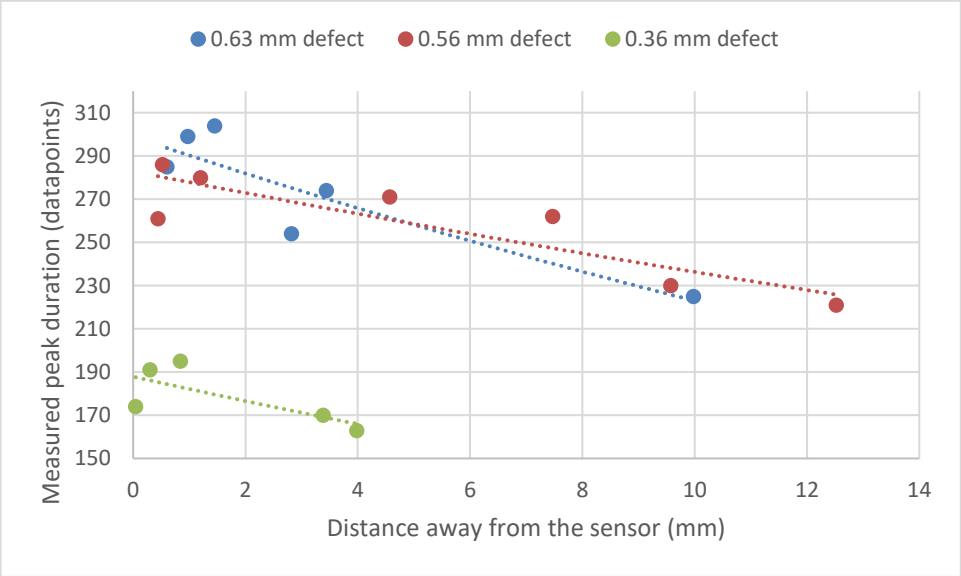

Figure 7.22 Measured peak duration (datapoints) with distance from the sensor (mm) for inner raceway defects

Since both peak height and peak duration measurements for the observed discontinuities show some correlation with defect size, the parameters can be used to give an indication of defect severity.

7.3 Conclusions

This chapter has discussed the relationship between defects in the rolling elements and the inner race. Differently sized line defects have been generated on both bearing components (inner races and rolling elements) and the related ultrasound reflections have been recorded. By applying post signal processing methods, the deflection curves have been constructed. It has been demonstrated how using the moving average filter can improve the signal's noise without significantly distorting the raw signal – allowing for the signal's features, such as dentations, to be analysed adequately. In order to make accurate comparisons, defected components were exposed to the same operating conditions: 12.5 rpm inner race rotation speed under an acting radial load of 1500 kg. Also, the same signal configurations; pulse repetition rate (PRR) and range, were employed to record the ultrasound first and second reflections together during one revolution of component of interest.

The chapter has shown how rolling element defects can not only be detected with ultrasound testing but that the location of the defected rolling element within the bearing can be identified. Furthermore, the proposed method is capable of giving an estimate of the defect severity. In fact, defect severity can be given by two variables: the anomaly duration and the peak height of the anomaly. On the other hand, the abilities of the method to measure defect size need further investigation.

The method has been applied to inner race defects and similar deductions have been drawn: i.e. defects on the inner race can be detected and their location can be determined. However, the defect size cannot be accurately determined.

8 BEARING OUTER RACE DEFECT DETECTION, SIZE MEASUREMENT AND LOCALIZATION

In this chapter, the application of the proposed method to bearing outer race defect monitoring is considered. The discussion will evaluate the ability of the method to: identify a defect on the outer race, determine defect location relative to the investigated area, measure defect size from the deflection curves and establish which of the bearing components is faulty. Since the defect width is of submillimeter dimensions, to obtain high resolution deflection curves, the highest possible pulse rate was used. Subsequently, these deflection curves have been constructed using the post signal processing methods employed (and described) in the previous chapters.

8.1 Defect detection and assessment of outer race line defects

Three line slots of different widths have been cut by EDM at the middle part of three different bearing outer races. The three differently sizes defects of 0.41 mm, 0.65 mm and 0.75 mm widths and 1 mm depth (as shown in Figure 8.1 and 8.2), were then tested under different load conditions and different positions relative to the immersion transducer. The same shaft rotation speed of 12.5rpm was maintained throughout the tests.

Figure 8.1 Line defects on the bearing outer races

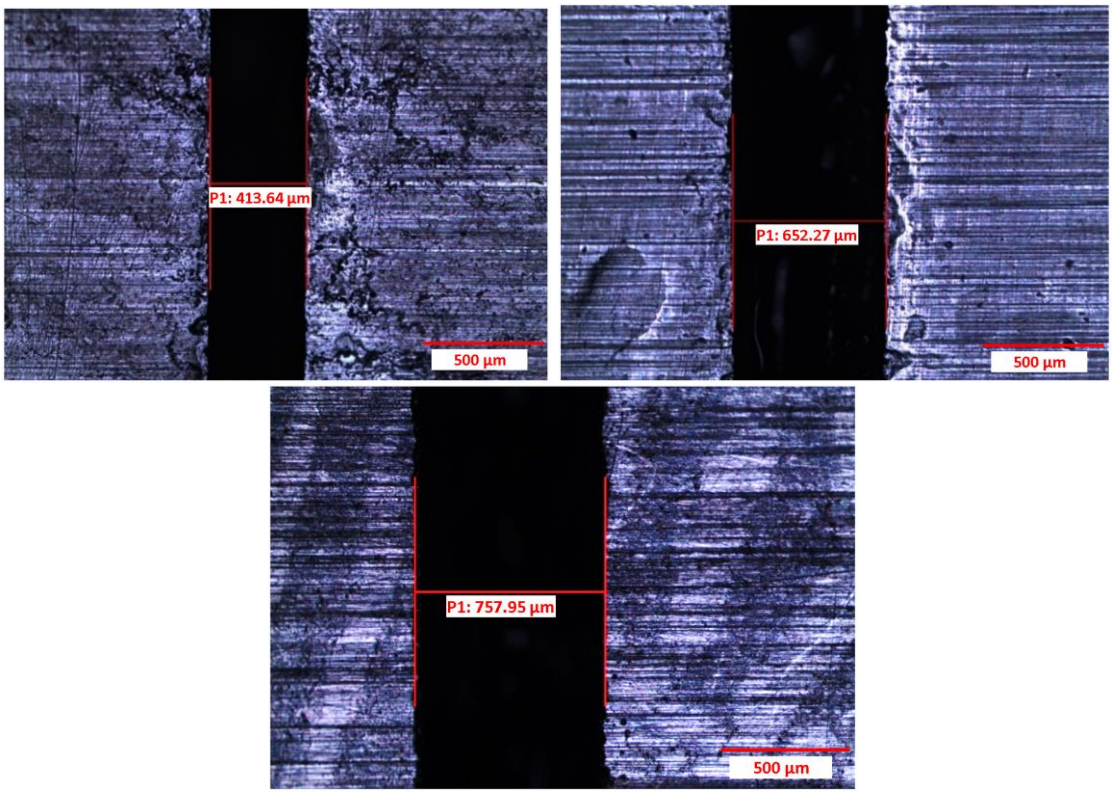

Figure 8.2 Bearing outer race defects microscope images

8.1.1 Data acquisition and post signal processing

In this part of research, the first and second reflections were recorded with the highest possible pulse repetition rate (PRR) (11200 Hz) as permitted by the processing capabilities of the employed computer. Since defect on the outer race appeared in the cyclic deflections curves with each rolling element pass over the defect, a signal recording time of 3s was sufficient to collect the adequate data.

The same post signal processing methods that have been used for inner race and rolling element tests (Chapter 7) have been applied to obtain deflection curves in these tests. Although the presence of a defect can be detected by real time monitoring, it was difficult to analyse the relationship between the defect size and the discontinuity duration. Hence, post signal processing methods were applied to obtain more accurate measurements.

8.2 Outer race defect localisation and defect severity analysis

In the proposed bearing condition monitoring method, the movement of the point where ultrasound waves are aimed is monitored. This point incurs vertical movement as a result of the dynamically varying stress on the bearing outer race that is caused by rolling element passage. While the rolling element is traversing across the investigated point, the outer race moves towards the ultrasound transducer, resulting in the shortest distance between the transducer and outer race to occur when the rolling element is aligned to the investigated point. This instance is represented by the lowest point on the deflection curve in Figure 8.3. While the rolling element is leaving the investigated area, the bearing outer race gradually moves away from the transducer until the point when the investigated area is equidistant from the just-passed rolling element and the subsequent one. The peak points of the deflection curves occur at such points. Subsequently, the distance between the transducer and the bearing outer race starts decreasing again, as the next rolling element approaches the sensor.

While this bearing outer race movement is occurring, rolling element-defect interactions within the investigated area produced anomalies (discontinuities) in the deflection curves as shown in the Figure 8.3.

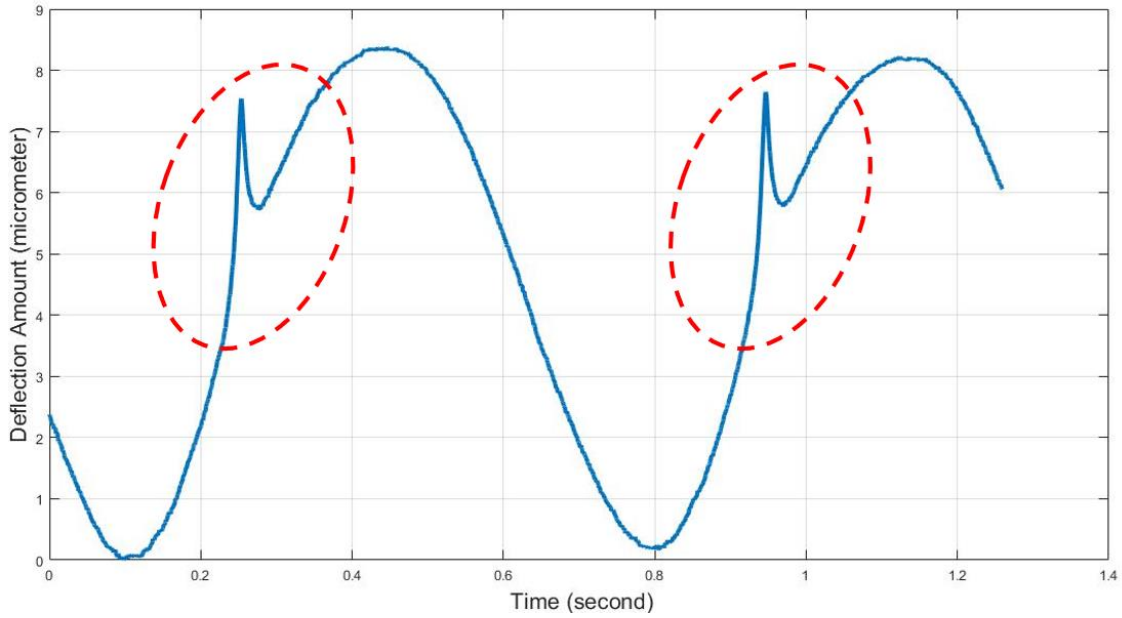

Figure 8.3 Bearing outer race deflection curves of the defected bearing outer race

Defect-rolling element impingement results in a sudden increase in distance between the bearing outer race and the transducer. This sudden increase occurs because while the rolling element is passing the defect, part of the rolling element falls into the defect. However, since the rolling element has restricted motion in the vertical direction, whereas the outer race is acted upon by a radial load, during impingement the outer race is pushed over the rolling element, thereby becoming more distant from the transducer.

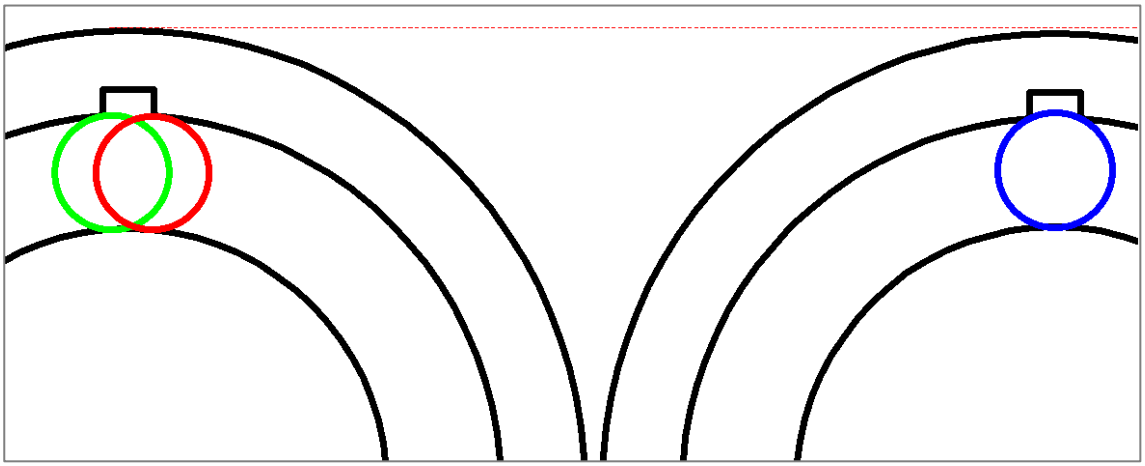

Figure 8.4 Rolling element outer race defect contact conditions

Figure 8.4 provides a visual representation (not scaled) of the defected outer raceway-rolling element contact. While the rolling element is entering the defect (green), it hits first the edge of the line defect and an impact force is transmitted. At this moment, the discontinuity starting point is observed. When the rolling element is aligned to the defect (blue), the bearing outer race moves towards the rolling element due to the applied radial load acting on it. This movement of the raceway is recorded as a spike in the deflection curve. While the rolling element is leaving the defect area (red), it hits the other edge of the line defect, transmitting another impact force. This point would be marked by the ending point in the deflection curve.

This impingement effect was observed clearly when the defect-rolling element contact occurred between two consecutive peaks as shown in the Figure 8.3. In other words, if the defect-rolling element contact occurs at a distance that is equivalent to half of the distance between two consecutive rolling elements away from either side of the sensor, it can be observed clearly. Thus, the proposed defect detection method range is depending on the distance between two consecutive rolling elements.

In order to analyse outer race line defect-rolling element interactions differently sized line defects were positioned at known distances from the transducer and exposed to a varying radial load. The shaft rotation speed was maintained at 12.5 rpm. For better visual comparison, the bearing outer races having 0.75 mm and 0.41 mm line widths (the biggest and the smallest, respectively), have been compared. These defects were positioned directly beneath the transducer and 7 mm and 15 mm away from either side. The recorded ultrasound reflections were then processed and the deflection curves were obtained.

Consistent and stable deflection curves were obtained when the force acting on the heavily loaded rolling element exceeded 3 kN, and for comparison purposes, the deflection curves obtained at 3.07 kN, 6.13 kN and 9.19 kN were evaluated. These forces correspond to a measured 1000 kg, 2000 kg, and 3000 kg radial load, respectively. Since micropitting was observed at the edge of the line defects after some preliminary tests, heavily loading conditions were avoided to prevent further pitting on the edge of the line defects and propagation of the line defect.

In order to find a correlation between discontinuity duration and defect width, the number of expected data points between the discontinuity start point and end point was calculated. This was performed by using the Equations in § 7.1.3 and the known values for defect size, velocity of the rolling element (45.11 mm/s) and pulse repetition rate (11200 Hz). The expected data points of the 0.75 mm and the 0.41 mm defect widths were found to be 186 and 101 data points respectively. These expected values were subsequently compared to the discontinuity duration values which were measured by the proposed method for different defect positions and different load conditions. Another peak parameter that is related to defect severity, peak height, was also compared for the different cases.

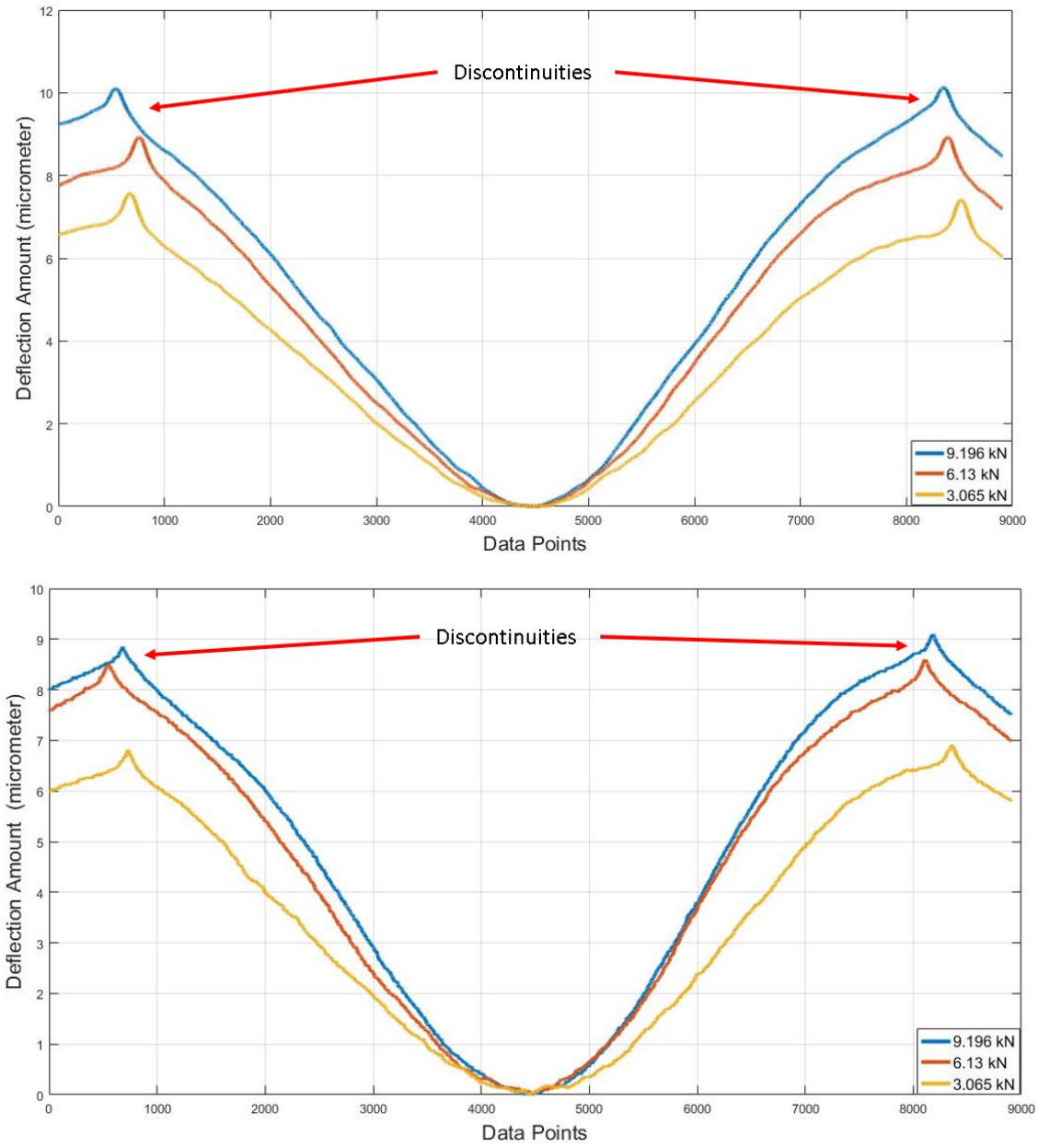

Figure 8.5 Deflection curves for (a) 0.75mm (b) 0.41mm width defects, at a defect position, 15 mm away from the transducer to the left

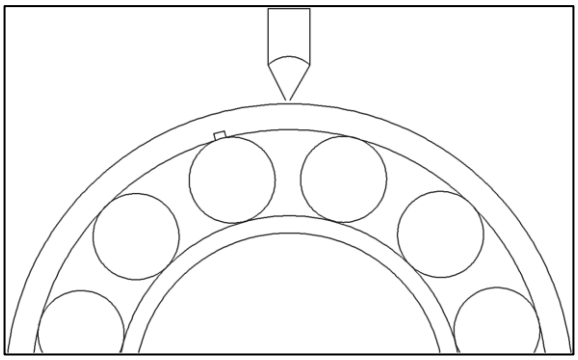

Figure 8.6 Schematic diagram of defect position – 15 mm away from the transducer to the left

The first case to be considered is when the biggest and smallest defects were positioned 15 mm away from the transducer on the left side. The curves given in the Figure 8.5 (a) and (b), show the deflection of the bearing outer race obtained while rolling elements are passing across the 0.75mm defect and the 0.41 mm defect, respectively. The curves show that when the sensor in between two consecutive rolling elements, the rolling element on the left-hand side to it, is interacting with the defect. This interaction results in a discontinuity in the deflection curve. Figure 8.6 shows a schematic representation of this instant. The different radial loads applied: 1000 kg, 2000 kg and 3000 kg are represented by the blue, red and yellow curves respectively.

The number of data points between the starting and ending points of a discontinuity represents a distance, that decreases with increasing load: 360 (1.44 mm), 345 (1.38 mm) and 280 (1.12mm) for 1000, 2000 and 3000 kg respectively, for the 0.75 mm defect. On the other hand, the expected (calculated) number of data points was 186 – revealing a discrepancy between the measured defect widths and the actual values.

Similar to the 0.75 mm case, the measured 0.41 mm defect discontinuity duration decreases with increasing applied load: 275 (1.10 mm), 267 (1.07 mm) and 240 (0.96 mm) for the 1000, 2000 and 3000 kg load, respectively. However, none of these measured durations is close to the expected value of 101 data points.

Since the measured discontinuity duration for both defect sizes is not close to the actual size, discontinuity duration does not provide a good estimation for defect size. Hence, the deduction from this observation is that there is a load dependence of the examined discontinuity parameter and that the discontinuity duration decreases with increasing load. This behaviour has also been observed for other defect positions relative to the sensor.

Variations in the discontinuity peak height have also been considered for both defects. It is observed that this value decreases with increasing radial load: 0.68, 0.66 and 0.46 µm for 1000, 2000 and 3000 kg load, respectively, for the bigger 0.75 mm defect and for the smaller 0.41mm defect: 0.41, 0.38 and 0.25 µm for the same loads. Since the peak height decreases for both defect size and with increasing radial load, this parameter is able to

provide information about the severity of the defect of the outer race, but it cannot predict its size.

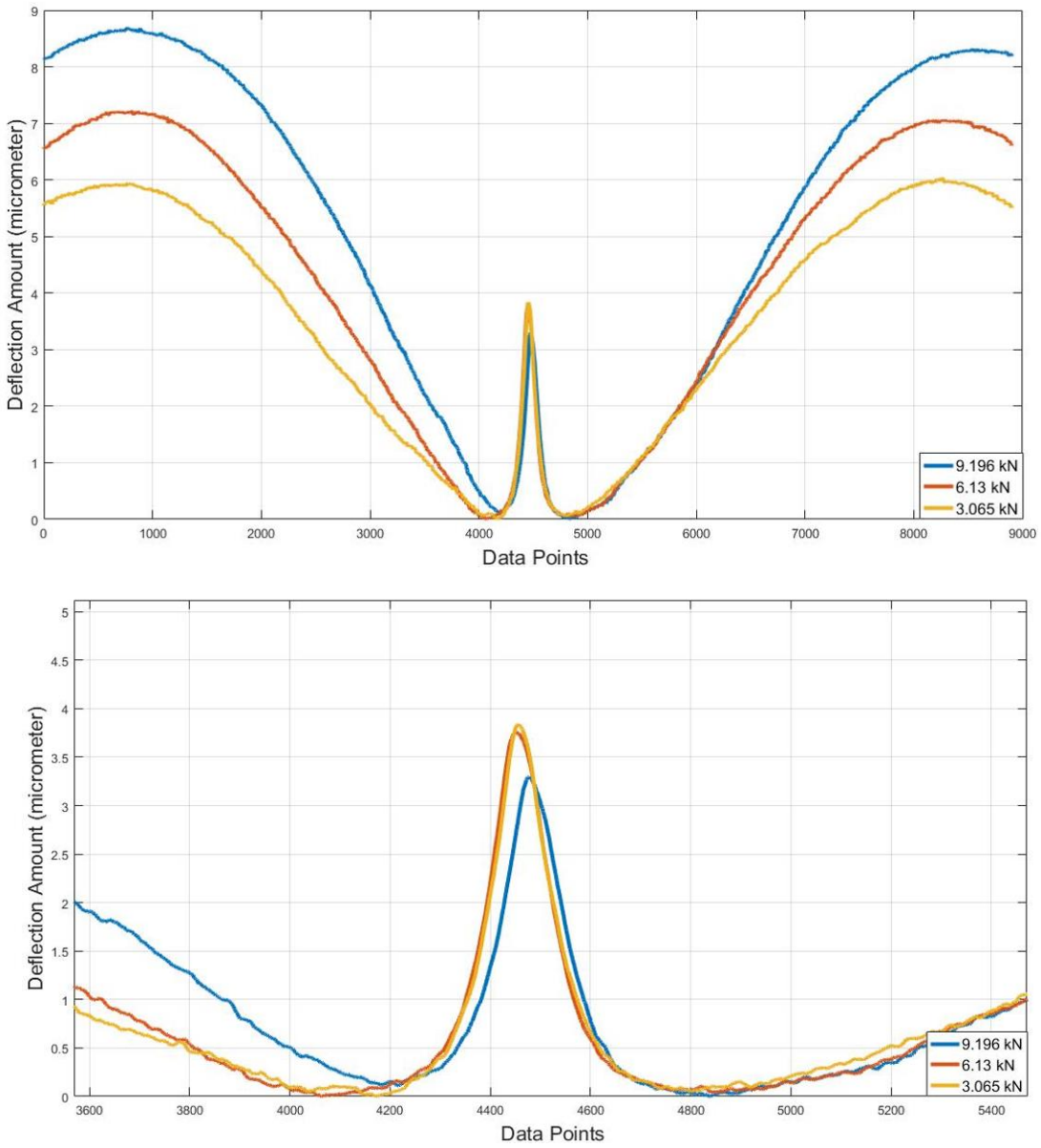

Figure 8.7 (a) Deflection curves for 0.75 mm defect positioned directly beneath sensor (b) magnified peak version

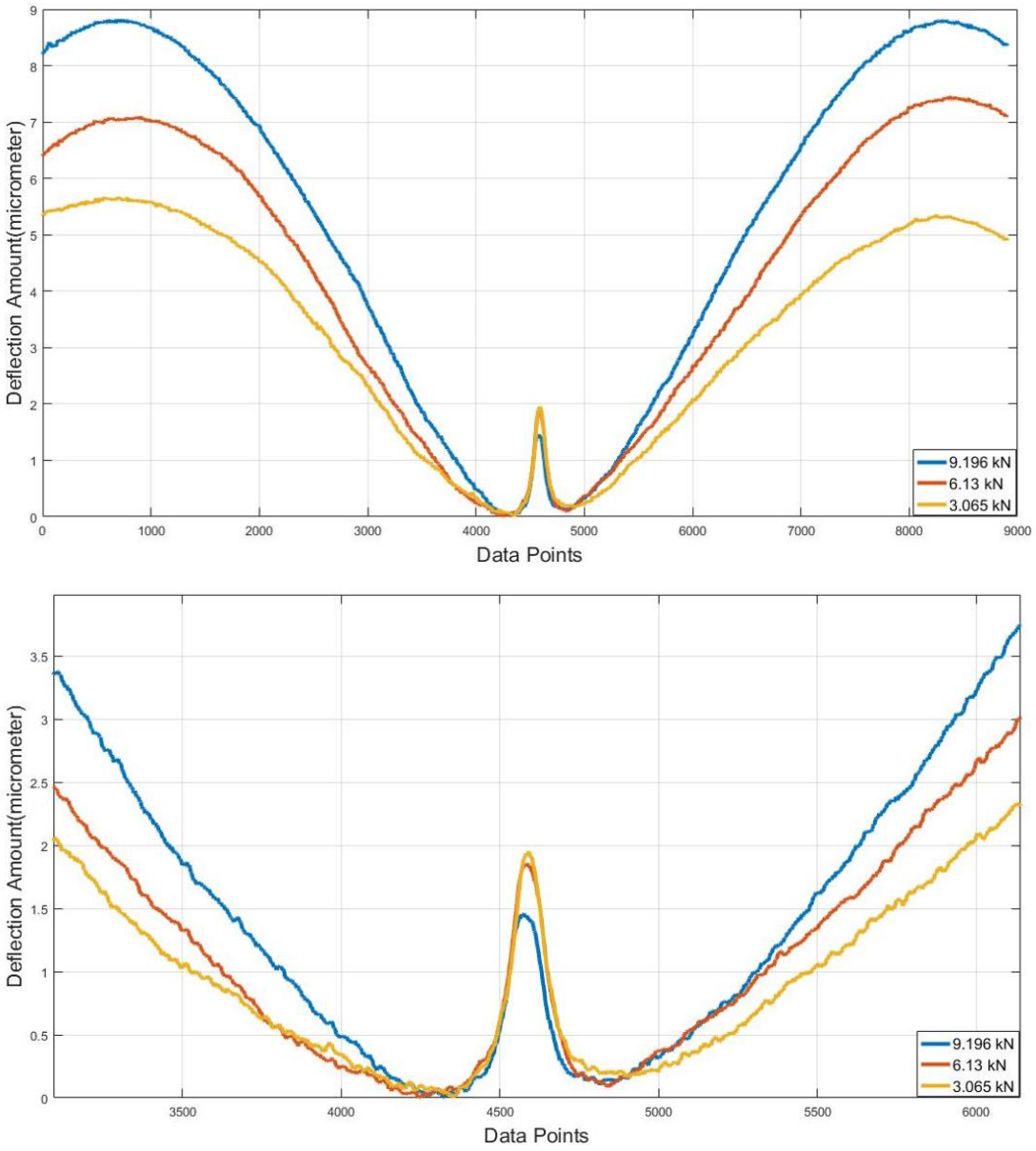

Figure 8.8 (a) Deflection curves for 0.41 mm defect positioned directly beneath sensor (b) magnified peak version

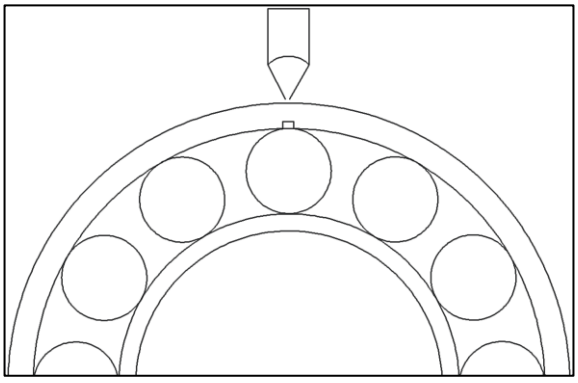

Figure 8.9 Schematic diagram for defect placed directly underneath sensor

Figures 8.7 (a) (and (b)) and 7.8 (a) (and (b)) show the deflection behaviour of the bearing outer race when the defects, 0.75 mm and 0.41 mm, respectively are positioned directly beneath the transducer. In this case, the rolling element – defect interaction takes place directly beneath the sensor as shown in the schematic diagram, Figure 8.9. The discontinuities representing the defects therefore appear at the troughs of the deflection curve. The measured discontinuity durations for the 0.75 mm diameter were: 610, 605 and 577 for the 1000, 2000 and 3000 kg loads respectively, whilst the expected duration was 186 data points. For the smaller defect, the measured data points were 446, 426 and 391 for the same loads, whilst the calculated figure was 101 data points. It can be also noticed that the discontinuities duration decrease with increasing load.

It is immediately evident that there is a significant difference between the measured and expected data point values. The measured values for the defects when these are located underneath the sensor is four times higher the real value. The reason for this could be related to the construction of the bearing type used. The assembly of the bearing involves placing the outer race halves into the cartridge halves at the desired orientation – for example, placing the defect at the mid-point (therefore having the outer race split points and the cartridge split points aligned – since the defect is at the centre of the outer race half). Subsequently, the cartridge halves are held together through four bolts – two at each split point. This tightening of the bolts, may be inducing a compressive force onto the outer race, causing the raceway to incur a deflection. Of course, the maximum deflection incurred by the outer race would be at the mid-point between the cartridge points, i.e. in line with the sensor. Hence, when the defect is placed underneath the sensor, it could be experiencing an enlargement that is caused by the force exerted by the bolts to hold the bearing assembly together. When the outer race defect was placed to the right side or left side of the transducer, the defect still experiences an enlargement due to deflection in the outer race – however, since it would not be placed at the mid-point, the enlargement would be to a lesser extent. The data measured agrees with this explanation as the measured defect enlargement decreased with defect location distance from the sensor. However, defect enlargement due to deflection incurred during assembly cannot justify an increase in size by a factor of four. Hence, it must be concluded that the method is not capable of measuring outer race defect size.

The measured discontinuity peak height, like the peak duration, decreased with increasing load for both defects: 3.84, 3.77 and 3.29 µm for the 0.75 mm defect under an acting radial load of 1000, 2000 and 3000 kg, respectively; and 1.95, 1.84 and 1.42 µm for the 0.41 mm for the same acting loads. The results show that under the same loading conditions, the peak size changed with size of the defect, which suggests that the method is capable of giving an indication of defect severity.

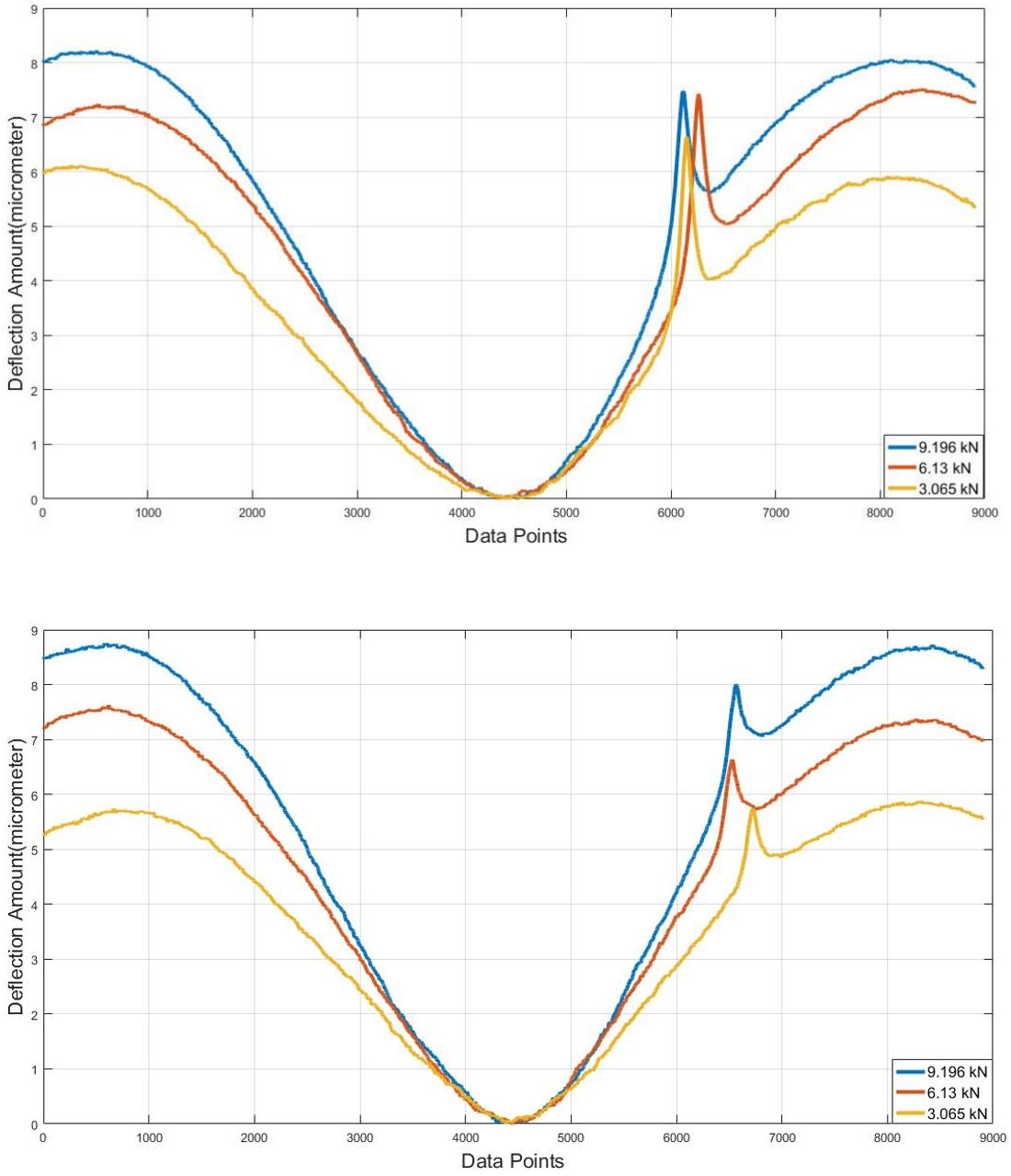

Figure 8.10 Deflection curves for (a) 0.75 mm and (b) 0.41mm width defects (at defect positions, 6.3 and 8.6 mm respectively, away from the transducer to the right)

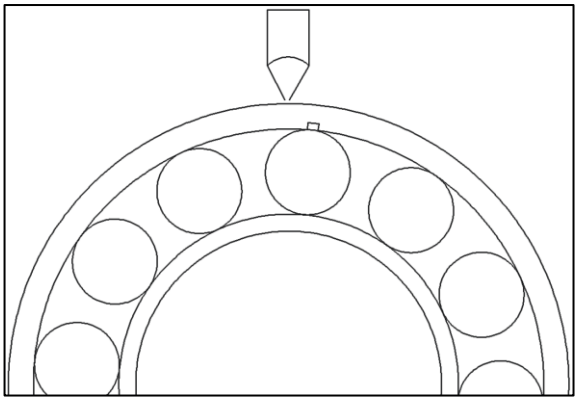

Figure 8.11 Schematic diagram of the defect placed to the right side of the transducer

Figures 8.10 (a) and (b) show the deflection behaviour of the bearing outer race when the 0.75 and 0.41 mm defects were positioned 6.3 mm and 8.62 mm (respectively) away from the transducer, to the right side, as shown in Figure 8.11. The discontinuities appear in the region preceding the peaks of the deflection curve.

The measured discontinuity duration and peak height values obtained by using the proposed method for this defect location follow the same pattern as those obtained for the other defect position cases: both parameters indicate defect severity and both decrease with increasing load. The bigger line defect discontinuity durations are 453, 420 and 386 data points for radial loads 1000, 2000 and 3000 kg respectively; while those for the smaller defect are 312, 285 and 240 data points for the same acting loads. The measured peak height values were 2.61, 2.34 and 1.84 μm for the 0.75 mm, whereas those for the smaller defect were 0.86, 0.81 and 0.74 μm, for the loads 1000, 2000 and 3000 kg, respectively.

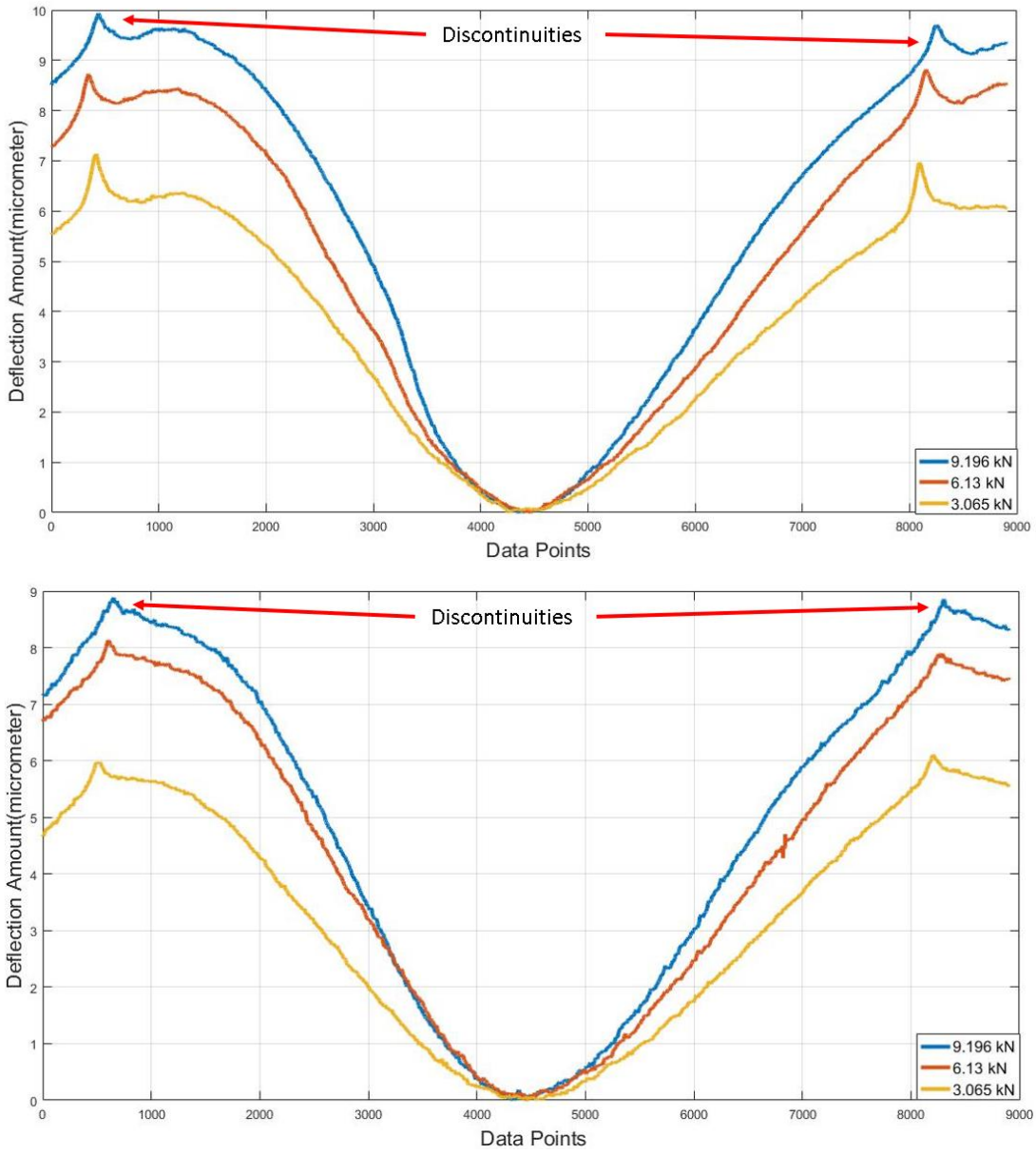

Figure 8.12 Deflection curves for (a) 0.75mm and (b) 0.41mm width defects, at a defect position of 14.2 mm away from the transducer to the right

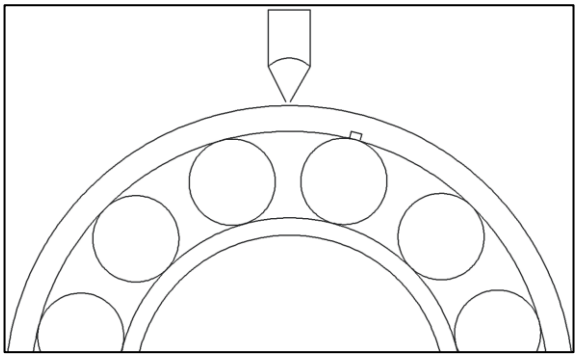

Figure 8.13 Schematic diagram of defect placed 14.2 mm to the right of the transducer

Lastly, the case in which the defects are positioned 14.2 mm away from the transducer to the right side has been evaluated. Similar to all the other tests, the discontinuity duration and peak height decrease with increasing radial load. Also, both parameter values are higher for the more severe line defect. The discontinuity durations for the 0.75 mm line defect were measured to be 419, 343 and 311 data points for radial loads of 1000, 2000 and 3000 kg, respectively, and those for the 0.41 mm line defect – 285, 233 and 198 data points with increasing load. The peak height values were 0.89, 0.59 and 0.48 µm for the larger defect and 0.27, 0.25 and 0.21 µm for the smaller defect for the radial loads of 1000, 2000 and 3000 kg. These parameter values are very similar to those obtained for when the defects were positioned 15 mm away from the transducer on the left side. The minor differences in the figures can be attributed to imprecision in mounting the defects to the predetermined positions.

8.3 Discussion

The results presented have been compiled graphically in Figure 8.14, where the discontinuity durations have been plotted against the applied radial load. The figure includes these variations for the different defect sizes and the different defect positions relative to the transducer.

For all scenarios tested, measured peak duration was larger for the 0.75 mm and smaller for the 0.41 mm. However, Figure 8.14 clearly shows how the measured discontinuity durations were larger than the expected (calculated) values in all cases. This could be due to a defect enlargement that is caused by bearing assembly. It is possible that while the split bearing is being mounted and secured rigidly in place with bolts, the raceway is incurring stress that causes the defect size to enlarge. The dimensions of raceway: 165 mm internal diameter and 5.5 mm thickness and the depth of the defect – 1 mm, would make substantial defect enlargement possible. Moreover, the edge hitting effect, different impact angles, load distribution, and partial cartridge support all contribute to the dynamics of the interaction – with the potential of affecting the measurements.

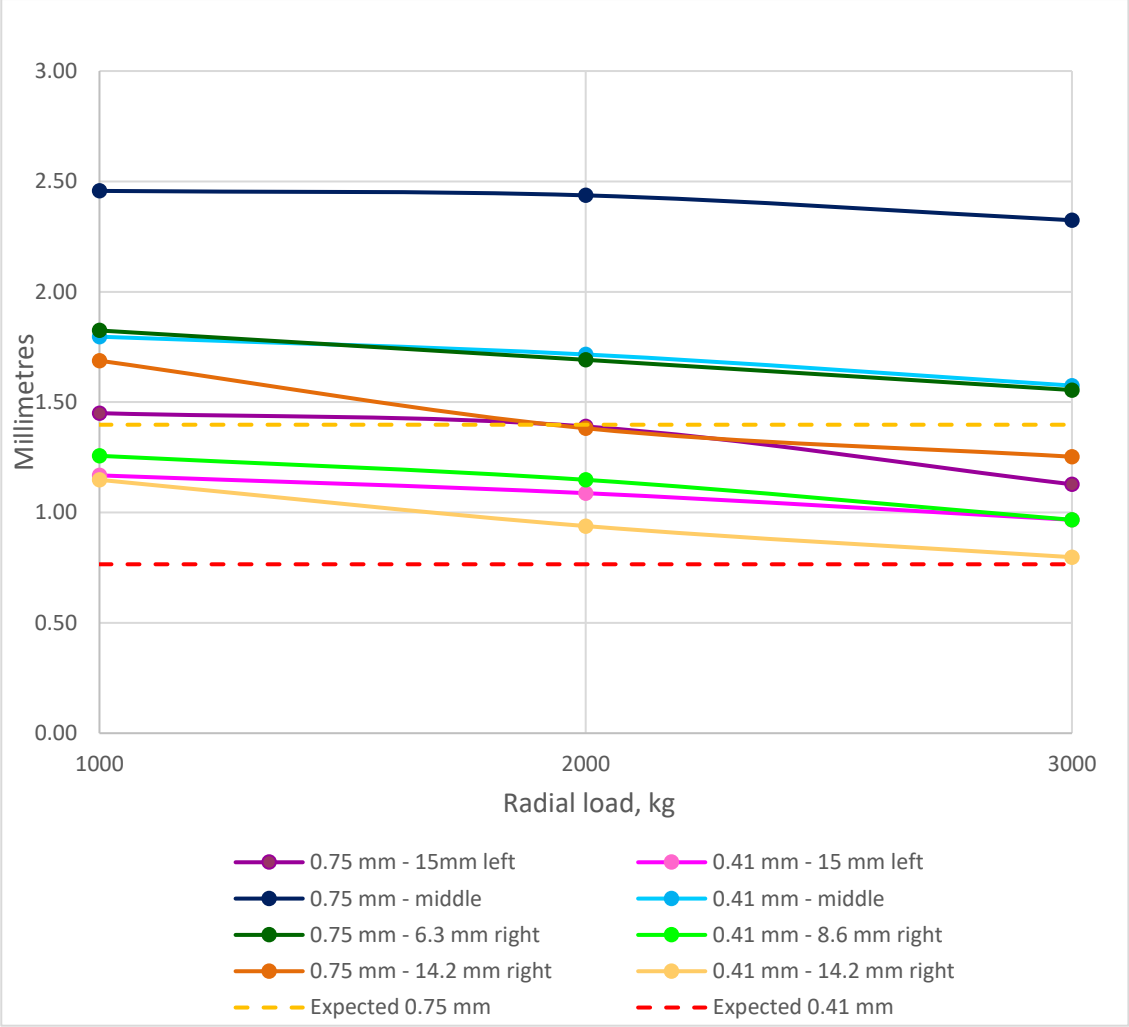

Figure 8.14 Measured defect width variation with applied load for 0.75 and 0.41 mm defect sizes at different locations

Another clear and consistent pattern that was observed in all the cases tested is that the measured parameters decrease as the radial load increases. The reason for this lies in the nature of the setup of the bearing and the way the radial load is applied. As illustrated by Figure 8.15, the radial load distribution would cause the defect width to decrease. Hence, during operation, the defect area is incurring two opposing forces: whilst the radial load pushes the raceway over the rolling element, the defect is caused to increase, but the higher the radial load, the harder it is for the raceway to deform and enclose the rolling element. Thus, as the radial load increases, the defect deformation (enlargement) decreases.

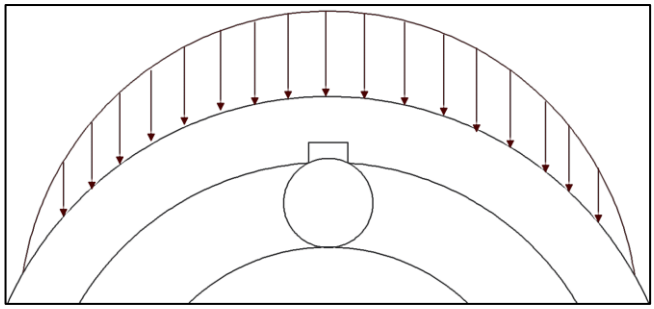

Figure 8.15 Radial load distribution

Also showing the effects of the radial load on the measured defect distribution (and peak height), are the changes in the measurements as the defect moves away from the sensor. The highest values for the parameters were recorded whilst the defect is aligned with the sensor, but the values fall with distance away from the transducer – reflecting the distribution load. The results also show that the load is balanced as very similar values have been reported for when the defects were 14.2 mm to the right and 15 mm to the left of the sensor.

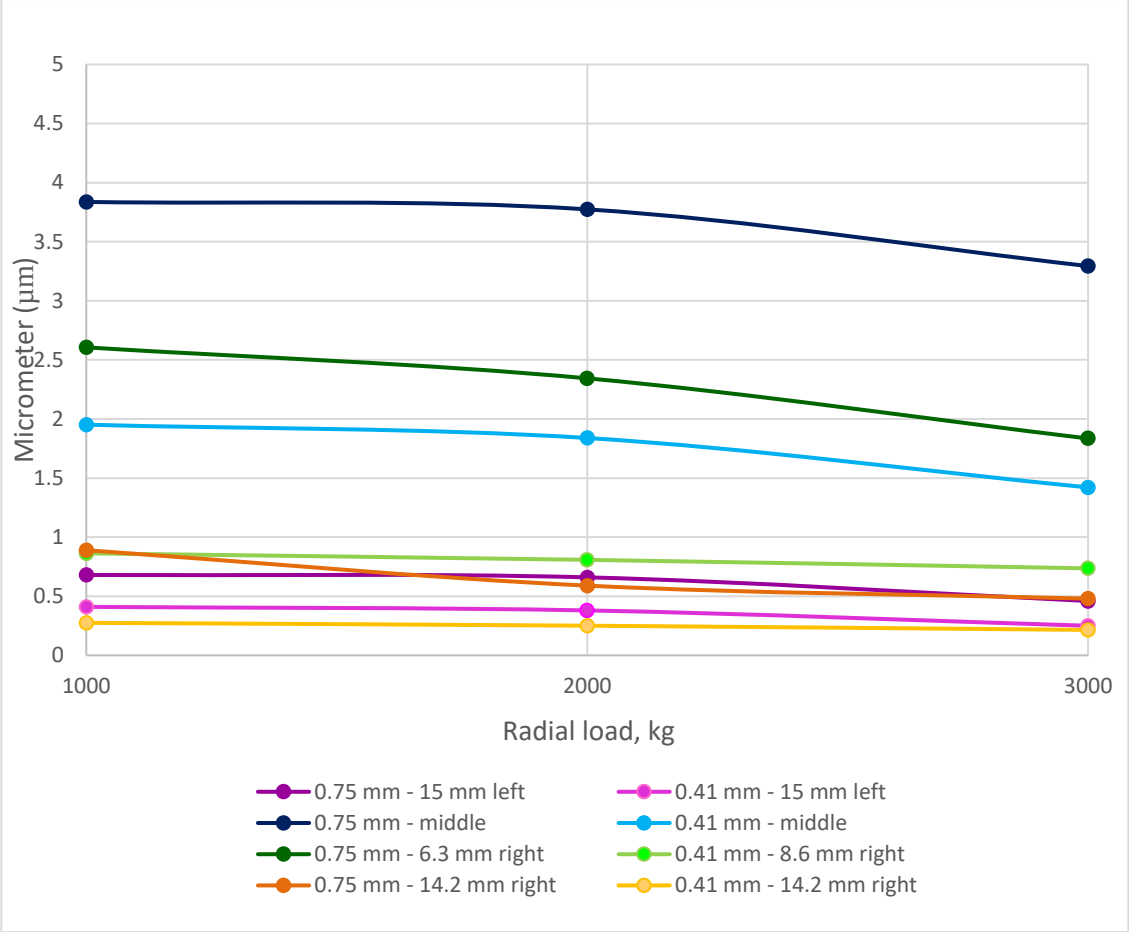

Figure 8.16 Discontinuity peak height variation with applied load for 0.75 and 0.41 mm defect sizes at different locations

Figure 8.16 shows the peak height variation against radial load for all the cases considered. Similar to the results observed for discontinuity peak duration, the same pattern for all defect sizes and positions tested is observed: higher values are recorded for the larger defect and all the parameter values decrease with applied load. This suggests that the parameters are related to each other. Since the deflection curves exhibit the bearing outer race movement, the discontinuity peak heights provide information about how much rolling element is inside of the bearing outer race defect. As the rolling element passes the defect, higher peak heights have been recorded along with larger defect widths. This is because of the geometry of the defect-rolling element contact whereby the rolling element enters further the defect as the defect with increases, as can be visualized in Figure 8.17.

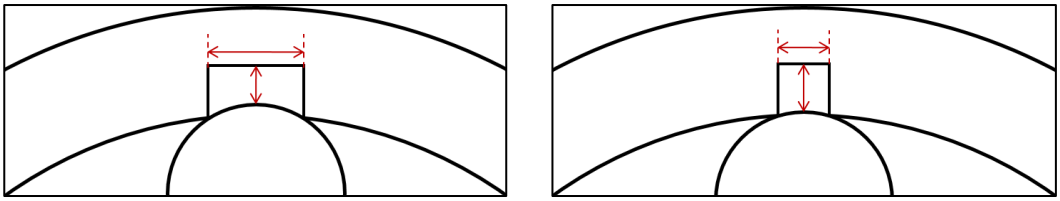

Figure 8.17 Bearing outer race defect-rolling element contact conditions for wide and narrow defect size

8.4 Conclusion

The concluding remarks for this chapter are that the proposed method has been able to detect defects on the outer race. The range across which such defects can be detected is equivalent to half the distance between two consecutive rolling elements, extending to either side of the sensor. Although the measured defect sizes are higher than those expected, the method can still distinguish clearly between the smaller and the larger defects, and hence, with further work, the method could be used to give an estimation of the defect size. The factors affecting the dynamics of the interaction have also been discussed.

9 CONCLUSION

As the wind power generation continues to be an attractive option for countries in pursuit of renewable energy, wind turbine reliability becomes crucial in sustaining the growth of this industry. Very often, wind turbine reliability issues are linked to failure of components on the drive train: the main bearings, the gearbox and some of the bearings within the gearbox. The critical bearings which are most prone to fail have been identified as the planet bearings, the intermediate shaft-locating bearings, the high speed locating bearings, and the main shaft bearing. These bearings are exposed to non-uniform, high and cyclic loads and eventually sub-surface cracks of the bearing components develop and propagate – at which point the bearing fails. Condition monitoring of these critical bearings for defect diagnosis and predictive maintenance improves wind turbine reliability.

In this work, a method to assess the bearing health condition and defect diagnosis has been proposed. This method is applicable to bearings where the bearing inner race rotates and outer race is stationary due to sensor positioning restrictions. The method can be employed to monitor a number of bearings within the wind turbine: the main and intermediate shaft locating bearings, and the gearbox input and output bearings whose inner race rotates and outer race is fixed. The method could also be applied to a vast variety of bearings in other applications and industries, like for example, the bearings in marine propulsion, offshore drilling machines, mining and construction equipment that would require condition monitoring.

9.1 Bearing outer race deflection measurement

In this project, ultrasound waves have been emitted onto the bearing outer race through the use of a spherical focus ultrasound transducer and the time shift in the ultrasound reflections caused by the movement of the outer race has been investigated. To enable measurement of the deflection of the outer race outer surface in both real time and in post signal processing modes, software has been developed. In this software, the zero-cross method has been applied to the first reflection and the time shift amount was calculated and correlated with the applied load and the number of rolling elements. It was found that the bearing outer race deflects more under higher radial loading conditions, when

the distance between rolling elements is bigger (split points) and when the number of rolling elements decreases.

9.2 Defect detection and diagnosis abilities of the method

The defect detection abilities of the proposed method have also been researched and defect interaction has been clearly observed in the cyclic deflection curves. Whilst the outer deflection curves for a healthy bearing exhibit an invariable sinusoidal pattern where the lower points represent the moment when the rolling element is passing through the investigated area, the deflection curves for a defective bearing contain a spike-like discontinuity that represents the interaction of the defect onto the bearing components. When the rotating parts (inner race and rolling elements) of the bearing come into contact with a defect, the distance between the transducer and the outer race increases, which results in a discontinuity in the outer race deflection curves. The anomaly in the deflection curves has been characterized by two parameters: the peak height of the discontinuity and the time difference between start and end points of the discontinuity. In order to determine the correlation between the discontinuity parameters and line defect sizes, defects of known size have been produced on the bearing components and each was tested and monitored.

9.2.1 Inner race defect detection and diagnosis

Three different sizes of line defects were cut on three different inner race halves by electrical discharge machining (EDM). The biggest width defect was 0.63 mm, a medium defect width was 0.56 mm and the smallest defect width was 0.36 mm. The latter was the smallest detectable line defect by the proposed method for the inner race defects (as a smaller defect measuring 0.25 mm did not give satisfactory results during preliminary trials). In each experiment one defected half of the inner race was mounted together with one healthy inner race and the deflection curves were constructed from the collected first reflection time shifts. The defect was detected when it came into contact with the rolling elements within the detectable range, which is equivalent to half of the distance between two consecutive rolling elements. Moreover, defect size and defect-contact location relative to investigated area has been determined. The peak height and the duration of the discontinuity indicated the defect severity, with both height and duration increasing with severity. However, an accurate measurement of the defect was not achieved.

9.2.2 Rolling element defect detection and diagnosis

Three differently sized grooves of widths 0.41 mm, 0.59 mm and 0.72 mm have been cut by EDM on three different rolling elements. All the defected rolling elements have been mounted together, but have been positioned sufficiently spaced in the cage so as not to influence each other's defect interaction effect. Each defect on the rolling elements has been distinguished in the deflection curves and it was shown how the outer race deflection curves can be used to determine the defective rolling element. Similar deductions to inner race defect detection have been drawn, namely that the discontinuity parameters (peak height and peak duration) increase with defect severity.

9.2.3 Outer race defect detection and diagnosis

The line defects cut on three different outer races have dimensions: 0.40 mm, 0.55 mm and 0.74 mm width and 1 mm depth. Although inner race and rolling element defects collide with the outer race randomly, outer race defects impinge on every passing rolling element and hence, discontinuities in the deflection curves were observed more frequently. This enabled the researcher to obtain more information about defect interaction as the defects could be placed at known different locations relative to the sensor position. The defects have been placed directly underneath of the immersion transducer, 7 mm and 15 mm away from to the transducer (both sides). Defect size and location have been determined for every case, but an accurate measurement of the defect size was not achieved.

9.3 Concluding remarks

The proposed method in this study is successful in detecting defects of widths larger than 0.35 mm on the inner race, rolling elements and outer races of a bearing. Moreover, defect size and location of the defect can be determined when the defect falls within the measurable range. This method can be applied to any bearing with rotating inner race and be used to monitor bearing health. Moreover, the method can be used as a real-time monitoring tool and can be combined with other non-destructive monitoring techniques such as vibration and acoustic emission.

The method is able to identify which of the bearing components is defective because each bearing element exhibits the defect at a different frequency. For instance, if the discontinuity is observed for every rolling element, then the defect is located on the outer race. If the discontinuity appears when the same element passes the investigated area, then that particular rolling element is the defective element. If the discontinuity emerges in deflection curves randomly, the inner race would be the defective component.

The capabilities of the method given above make the monitoring of a bearing by the use of a focus ultrasound immersion transducer a potentially effective bearing condition monitoring tool for industrial applications.

9.4 Future works and recommendations

This study has clearly shown that the proposed method can be used to detect defects in bearing components and that despite accurate defect measurements could not be established, it is clear that there a relationship between measured parameters (peak height and peak duration) of a discontinuity in the outer race deflection curve and defect size. In order to get a better understanding of nature of this relationship, more differently sized defects should be tested.

On the other hand, the loading conditions and rotation speeds employed in this study were substantially lower than those typically incurred by the bearings found in the gearboxes of wind turbines. This limitation was imposed by the equipment used. Future work should therefore involve higher loading conditions and faster rotation speeds to better simulate the actual operating conditions of bearings in wind turbine gearboxes.

Although a direct relationship between the applied load and the measured bearing outer race deflection has been observed, a mathematical model has not been derived. In future, this relationship could be determined experimentally for each bearing that can be found in the particular application, e.g. wind turbine. If a bearing which is going to be monitored in an application has the deflection amounts corresponding to the applied loads predetermined, the method can be used to establish the applied load while it is in operation by measuring the deflection quantities, assuming a healthy bearing.

Moreover, numerical models and finite element method (FEM) models that the explain bearing dynamic model can be verified by the proposed method. Comparing the deflection curves of a bearing which is tested under different working conditions using the proposed outer race deflection measurement method to those obtained from a simulation model provides a means to modify and improve the simulation models.

Another opportunity for future work lies in conducting run-to-failure tests with the aim of studying the natural degradation of the bearing. In this study, time was limited and such tests could not be performed. The proposed method could then be used as a deflection based fatigue test method to monitor the natural degradation of the bearing when the deflection amount corresponding to a given radial load is known. As the deflection of a healthy bearing outer race is stable while an applied load is steady, if a substantial increase in deflection is observed whilst the radial load is constant, it is understood that fatigue is occurring and that the bearing is degrading. Also, defect detection and defect assessment capabilities of the proposed method in real-time measurements can be enhanced by developing more powerful digital signal processing techniques for condition monitoring applications.

The proposed method can be applied to naturally degraded bearings from specific applications in order to further validate the defect detection capabilities of the method. Also, comparative studies can be performed with healthy bearings, naturally degraded bearings and artificially defected ones at different stages of failures.

REFERENCES

ABB 355, 2013. Retrieved January 04, 2018, from http://www.apds.co.uk/pdfs/

Advanced NDT Systems. 2004. Retrieved January 04, 2018, from http://www.advanced-ndt.co.uk/ultrasonic_transducers.htm

Al-Ghamd, A. and Mba, D. (2006). A comparative experimental study on the use of acoustic emission and vibration analysis for bearing defect identification and estimation of defect size. Mechanical Systems and Signal Processing, 20(7), pp.1537-1571.

Al-Ghamdi, A., Cole, P., Such, R. and Mba, D. (2004). Estimation of bearing defect size with acoustic emission. Insight - Non-Destructive Testing and Condition Monitoring, 46(12), pp.758-761.

Appleby, M.P., 2010. Wear debris detection and oil analysis using ultrasonic and capacitance measurements (Doctoral dissertation, University of Akron).

Bhushan, B., 2000. Modern tribology handbook, two volume set. CRC press.

Brunskill, H.P., 2013.The Real-Time Characterisation of Dry Machine Element Contacts Using Ultrasonic Reflectometry (Doctoral dissertation, University of Sheffield).

Council, G. W. E. (2016). Global Wind Statistics 2016, 10 February 2017.

Caesarendra, W., 2015. Vibration and acoustic emission-based condition monitoring and prognostic methods for very low speed slew bearing. (Doctoral dissertation, University of Wollongong).

Changsen, W. 1991. Analysis of rolling element bearing. London : Mechanical Engineering.

Tandon, N. and Choudhury, A. (1999). A review of vibration and acoustic measurement methods for the detection of defects in rolling element bearings. Tribology International, 32(8), pp.469-480.

Conkey A P, Juarez JC, Perez R X, Taylor HF, (2003). Detecting loading of roller element bearings using a fiber optic strain sensor. Applied Optics, 42(31), pp.6276-6283.

Cooper Bearing, 2015. Retrieved January 04, 2018, from https://www.cooperbearings.com/downloads.asp

Mat Dan, R., 2013. Multi-view and three-dimensional (3D) images in wear debris analysis (WDA) (Doctoral dissertation, University of Manchester).

Devendiran, S. and Manivannan, K., (2016). Vibration based condition monitoring and fault diagnosis technologies for bearing and gear components-A Review. International Journal of Applied Engineering Research, 11(6), pp.3966-3975.

Devlin, M., Pollard, G., GuevremonT, JM ., Anderson, WB., Ryan, H. (2016). White Etching Formation Due to High Stress Conditions.

Dvorak, P., (2017). What different kinds of bearings are used in wind turbines? Retrieved January 04, 2018, from www.windpowerengineering.com/business-news-projects/misalignment-looseness-and-imbalance-are-all-correctable-problems/

Dwyer-Joyce, R., Drinkwater, B. and Donohoe, C. (2003). The measurement of lubricant-film thickness using ultrasound. Proceedings of the Royal Society A: Mathematical, Physical and Engineering Sciences, 459(2032), pp.957-976.

Echavarria, E., Hahn, B., van Bussel, G. and Tomiyama, T. (2008). Reliability of wind turbine technology through time. Journal of Solar Energy Engineering, 130(3), pp.031005.

Elforjani, M. and Mba, D. (2008). Observations and location of acoustic emissions for a naturally degrading rolling element thrust bearing. Journal of Failure Analysis and Prevention, 8(4), pp.370-385.

Errichello, R., (2004). Another perspective: false brinelling and fretting corrosion. Tribology & Lubrication Technology, 60(4), pp.34.

Eschmann, P. and Hasbargen, L., 1985. Ball and roller bearings: theory, design, and application (No. 621.822 E7 1985).

Fierro, T., (2016). Extending bearing life in wind turbine main shafts. Retrieved January 04, 2018, from http://www.power-eng.com/articles/print/volume-120/issue-8/features/extending-bearing-life-in-wind-turbine-mainshafts.html

Fujii, I., & Kawashima, K. (1995). Digital measurement of ultrasonic velocity. In Review of progress in quantitative nondestructive evaluation, pp. 203-209

Glavatskih, S.B., (2004). A method of temperature monitoring in fluid film bearings. Tribology International, 37(2), pp.143-148.

Gutenberg, P., (2017). Sound speed. Retrieved January 04, 2018, from http://self.gutenberg.org/articles/Sound_speed?View=embedded

Hahn, B., Durstewitz, M., Rohrig, K., (2007). Reliability of wind turbines, experiences of 15 years with 1,500 wind turbines. Wind Energy pp. 464b.

Hamrock, B.J. and Anderson, W.J., 1983. Rolling-element bearings.

Harker, R.G. and Sandy, J.L., (1989). Rolling element bearing monitoring and diagnostics techniques. Journal of Engineering For Gas Turbines and Power, 111(2), pp.251-256.

Harnoy, A., 2002. Bearing design in machinery: engineering tribology and lubrication. CRC press.

Harris, T.A. and Kotzalas, M.N., 2006. Essential concepts of bearing technology. CRC press.

Hawman, M.W. and Galinaitis, W.S., (1988). Acoustic emission monitoring of rolling element bearings. In Ultrasonics Symposium Proceedings., pp. 885-889.

Herr, D. Heidenreich, D., (2014). Understanding the root causes of axial cracking in wind turbine gearbox bearings, Aero Torque Corporation.

Holm-Hansen, B.T. and Gao, R.X., (2000). Vibration analysis of a sensor-integrated ball bearing. Journal of Vibration and Acoustics, 122(4), pp.384-392.

Houpert, L., (2001). An engineering approach to Hertzian contact elasticity—part I. Journal of Tribology, 123(3), pp.582-588.

Houpert, L., 2001. An engineering approach to non-hertzian contact elasticity—Part II. Journal of Tribology, 123(3), pp.589-594.

Howard, T.P., 2016. Development of a novel bearing concept for improved wind turbine gearbox reliability (Doctoral dissertation, University of Sheffield).

Humbert, S., (2008). Detection of electrical discharges in bearings. SKF Maintenance Products.

Ibrahim, M.W., 2013. Lubricant Film Thickness and Contact Measurement in Rolling Element Bearing (Doctoral dissertation, University of Sheffield).

ISO 281: 1990, Rolling bearings: dynamic load ratings and rating life. (International Organisation for Standardisation)

ISO 15243:2004. Rolling bearings- Damage and failures–terms, characteristics and causes. (International Organisation for Standardisation)

IRENA., (2015). Renewable power generation costs in 2014. Retrieved January 04, 2018, from http://www.irena.org/publications/2015/Jan/Renewable-Power-Generation-Costs-in-2014

Li, C.J. and Li, S.Y., (1995). Acoustic emission analysis for bearing condition monitoring. Wear, 185(1-2), pp.67-74.

Jammu, N.S. and Kankar, P.K., (2011). A review on prognosis of rolling element bearings. International Journal of Engineering Science and Technology, 3(10), pp.7497-7503.

Jena, D., Singh, M. and Kumar, R., (2012). Radial ball bearing inner race defect width measurement using analytical wavelet transform of acoustic and vibration signal. Measurement Science Review, 12(4), pp.141-148.

Juarez, J.C., Conkey, A.P., Perez, R.X. and Taylor, H.F., (2002). Fiber optic strain system for ball bearings. In Optical Fiber Sensors Conference Technical Digest. pp. 427-430.

Khonsari, M.M. and Booser, E.R., 2008. Applied tribology: bearing design and lubrication. John Wiley & Sons.

Kim, W., Seo, J. and Hong, D., (2012). Infrared thermographic inspection of ball bearing; condition monitoring for defects under dynamic loading stages. In 18th World Conference on Nondestructive Testing. pp. 4-7

Kinsler, L.E., Frey, A.R., Coppens, A.B. and Sanders, J.V., 1999. Fundamentals of acoustics. John Wiley & Sons.

Kotzalas, M. and Doll, G. (2010). Tribological advancements for reliable wind turbine performance. Philosophical Transactions of the Royal Society A: Mathematical, Physical and Engineering Sciences, 368(1929), pp.4829-4850.

KPMG. (2015). Taxes and incentives for renewable energy. Retrieved January 04, 2018, from https://assets.kpmg.com/xx/en/home/insights/2014/06/taxes-and-incentives-for-renewable-energy.html

Krautkrämer, J. and Krautkrämer, H., 2013. Ultrasonic testing of materials. Springer Science & Business Media.

Lacey, S. J. (2008). An overview of bearing vibration analysis. Maintenance & Asset Management, 23(6), pp.32-42.

Lim, T.C. and Singh, R., (1990). Vibration transmission through rolling element bearings, part I: bearing stiffness formulation. Journal of Sound and Vibration, 139(2), pp.179-199.

Palmgren, A., Lundberg, G., 1947. Dynamic Capacity of Rolling Bearings, Mechanical Engineering Series, 1.

Lundberg, G. and Sjövall, H., (1958). Stress and deformation in elastic contacts, publication no. 4. Institute of Theory of Elasticity and Strength of Materials.

Mason, W.P., 1964. Physical acoustics: principles and methods. Academic press

Mba, D. (2006). Development of acoustic emission technology for condition monitoring and diagnosis of rotating machines: bearings, pumps, gearboxes, engines, and rotating structures. The Shock and Vibration Digest, 38(1), pp.3-16.

Mills, R., Vail, J.R. and Dwyer-Joyce, R., (2015). Ultrasound for the non-invasive measurement of internal combustion engine piston ring oil films. Journal of Engineering Tribology, 229(2), pp.207-215.

Moussa, W., 2014. Thermography-assisted bearing condition monitoring (Doctoral dissertation, University of Ottawa).

Musial, W., Butterfield, S., McNiff, B., (2007). Improving wind turbine gearbox reliability. In European Wind Energy Conference, pp. 7-10.

Nagaraj, H.S., Sanborn, D.M. and Winer, W.O., (1978). Direct surface temperature measurement by infrared radiation in elasto-hydrodynamic contacts and the correlation with the blok flash temperature theory. Wear, 49(1), pp.43-59.

NDT-Resource Center, (2012). AE Signal Properties. Retrieved January 04, 2018, from www.nde-ed.org/EducationResource/CommunityCollege/OtherMethods/AE/AESignal Features.htm

NDT-Resource Center, (2012). Speed of Sound. Retrieved January 04, 2018, from www.nde-ed.org/EducationResources/HighSchool/Sound/speedinmaterials.htm

NDT-Resource Center, (2012). Beam Spread. Retrieved January 04, 2018, from www.ndeed.org/EducationResources/CommunityCollege/Ultrasonics/EquipmentTrans/beamspread.htm

Nohál, L. and Vaculka, M. (2017). Experimental and computational evaluation of rolling bearing steel durability. IOP Conference Series: Materials Science and Engineering, 179, pp.012054.

NTN Corporation, 2001. Ball and Roller Bearings.

Olympus, N.D.T., (2017). Inspections of Wind Turbine Gearboxes. Retrieved January 04, 2018, from https://www.olympus-ims.com/en/applications/rvi-wind-turbine/

Olympus, N.D.T., 2006. Ultrasonic transducers technical notes. Technical brochure: Olympus NDT, Waltham, MA, 2(2.1), pp.2-2.

Palmgren, A., 1959. Ball and roller bearing engineering. SKF Industries Inc.

Patidar, S. and Soni, P.K., (2013). An overview on vibration analysis techniques for the diagnosis of rolling element bearing faults. International Journal of Engineering Trends and Technology, 4(5), pp.1804-1809.

Pao, Y.H., Gajewski, R.R. and Ceranoglu, A.N., (1979). Acoustic emission and transient waves in an elastic plate. The Journal of the Acoustical Society of America, 65(1), pp.96-105.

Quinn, A., Drinkwater, B. and Dwyer-Joyce, R. (2002). The measurement of contact pressure in machine elements using ultrasound. Ultrasonics, 39(7), pp.495-502.

Randall, R.B. and Antoni, J., (2011). Rolling element bearing diagnostics—A tutorial. Mechanical Systems and Signal Processing, 25(2), pp.485-520.

Read, L.J. and Flack, R.D., (1987). Temperature, pressure and film thickness measurements for an offset half bearing. Wear, 117(2), pp.197-210.

Reder, M.D., Gonzalez, E. and Melero, J.J., (2016). Wind turbine failures-tackling current problems in failure data analysis. In Journal of Physics: Conference Series, 753(7), pp. 072027.

RF Cafe, K. B., (2017). Velocity of Sound in Various Media. Retrieved January 04, 2018, from http://www.rfcafe.com/references/general/velocity-sound-media.htm

Ribrant, J. and Bertling, L., (2007). Survey of failures in wind power systems with focus on Swedish wind power plants during 1997-2005. In Power Engineering Society General Meeting, pp. 1-8.

Roylance, B.J. and Raadnui, S., (1994). The morphological attributes of wear particles-their role in identifying wear mechanisms. Wear, 175(1-2), pp.115-121.

Salameh, J., Cauet, S., Etien, E., Sakout, A. and Rambault, L. (2018). Gearbox condition monitoring in wind turbines: A review. Mechanical Systems and Signal Processing, 111, pp.251-264.

Schirru, M., 2017. Development of an Ultrasonic Sensing Technique to Measure Lubricant Viscosity in Engine Journal Bearing In-Situ. (Doctoral dissertation, University of Sheffield).

Schmid, S.R., Hamrock, B.J. and Jacobson, B.O., 2014. Fundamentals of machine elements, CRC Press.

Shell, 2007. Shell Alvania Greases EP (LF) General purpose extreme-pressure industrial grease. pp. 1–2.

Shiroishi, J.Y.S.T., Li, Y., Liang, S., Kurfess, T. and Danyluk, S., (1997). Bearing condition diagnostics via vibration and acoustic emission measurements. Mechanical Systems and Signal Processing, 11(5), pp.693-705.

Silk, M.G., 1984. Ultrasonic transducers for non-destructive testing.

Singh, R. C., Kumar, A., Kumar, N., (2014). Analysis of ball bearings under dynamic loading using non- destructive technique of thermography, 2(4), pp. 781–783.

Smith, S.W., 1997. The scientist and engineer's guide to digital signal processing.

Stachowiak, G. and Batchelor, A.W., 2013. Engineering tribology. Butterworth-Heinemann.

Stolarski, T.A. and Tobe, S., 2000. Rolling contacts. Professional Engineering Publishing.

Suzuki, H., 2016. Bearing surface optimisation on hydrodynamic lubrication film with vibration-assisted machining and ultrasound reflectometry (Doctoral dissertation, University of Sheffield).

Tallian, T.E., 2006. Failure atlas for rolling bearings in wind turbines National Renewable Energy Laboratory (NREL).

Tandon, N., Yadava, G.S. and Ramakrishna, K.M., (2007). A comparison of some condition monitoring techniques for the detection of defect in induction motor ball bearings. Mechanical Systems and Signal Processing, 21(1), pp.244-256.

Tattersall, H.G., (1973). The ultrasonic pulse-echo technique as applied to adhesion testing. Journal of Physics D: Applied Physics, 6(7), pp.819.

Tautz-Weinert, J. and Watson, S.J., (2016). Using SCADA data for wind turbine condition monitoring–a review. IET Renewable Power Generation, 11(4), pp.382-394.

Tchakoua, P., Wamkeue, R., Tameghe, T. A., & Ekemb, G. (2013). A review of concepts and methods for wind turbines condition monitoring. Computer and Information Technology (WCCIT), pp. 1-9.

Thompson, D.O. and Chimenti, D.E. , 2012. Review of progress in quantitative non-destructive evaluation. Springer Science & Business Media.

Timken, 2011. Timken Bearing Damage Analysis with Lubrication Reference Guide. RetrievedJanuary04,2018,fromwww.timken.com/pdf/5892_Bearing%20Damage%20Analysis%20 Brochure.pdf

Tra, V., Kim, J., Khan, S. and Kim, J. (2017). Incipient fault diagnosis in bearings under variable speed conditions using multiresolution analysis and a weighted committee machine. The Journal of the Acoustical Society of America, 142(1), pp.EL35-EL41.

Tripp, J.H., 1985. Hertzian contact in two and three dimensions.

Union, E. (2009). Directive 2009/28/EC of the European Parliament and of the Council of 23 April 2009 on the promotion of the use of energy from renewable sources and amending and subsequently repealing Directives 2001/77/EC and 2003/30/EC. Official Journal of the European Union, 5, 2009.

Vaishakh, R. and Jigar, P., (2015). A review on bearing defects analysis of rolling bearing using vibration response.

Wang, L. and Gao, R.X., (2006). Condition monitoring and control for intelligent manufacturing. Springer Science & Business Media.

Wang, W. and Zhang, W., (2005). A model to predict the residual life of aircraft engines based upon oil analysis data. Naval Research Logistics (NRL), 52(3), pp.276-284.

Wardle, F., 2015. Ultra-precision bearings. Elsevier.

Watson, M.J., Byington, C.S. and Behbahani, A., (2007). Very high frequency monitoring system for engine gearbox and generator health management. SAE Technical Paper.

Williams, T., Ribadeneira, X., Billington, S. and Kurfess, T., (2001). Rolling element bearing diagnostics in run-to-failure lifetime testing. Mechanical Systems and Signal Processing, 15(5), pp.979-993.

Yagi S., 2004.Bearings for wind turbine. NTN Technical Review no. 71, pp. 40–47

Yang, Y., Danyluk, S. and Hoeprich, M., (2000). A study on rolling element skew measurement in a tapered roller bearing with a specialized capacitance probe. Journal of Tribology, 122(3), pp.534-538.

Yang, Y., Kurfess, T., Liang, S. and Danyluk, S., (1999). Application of a specialized capacitance probe in bearing diagnosis. Wear, 225, pp.1215-1221.

Yang, W., Tavner, P., Crabtree, C., Feng, Y. and Qiu, Y. (2012). Wind turbine condition monitoring: technical and commercial challenges. Wind Energy, 17(5), pp.673-693.

Yoshioka, T., Korenaga, A., Mano, H. and Yamamoto, T., (1999). Diagnosis of rolling bearing by measuring time interval of AE generation. Journal of Tribology, 121(3), pp.468-472.

Yu, J.J., Bently, D.E., Goldman, P., Dayton, K.P. and Van Slyke, B.G., (2002). Rolling element bearing defect detection and diagnostics using displacement transducers. Journal of Engineering For Gas Turbines and Power, 124(3), pp.517-527.

Zantopulos, H., (1988). An alternate solution of the deformation of a cylinder between two flat plates. Journal of Tribology, 110(4), pp.727-729.

Zaretsky, E.V., 1992. STLE life factors for rolling bearings. Stle Special Publication SP.

Zhang, J., Drinkwater, B.W. and Dwyer-Joyce, R.S., (2006). Acoustic measurement of lubricant-film thickness distribution in ball bearings. The Journal of the Acoustical Society of America, 119(2), pp.863-871.